Low Temperature Kinetic Studies using a Pulsed Laval Nozzle Apparatus

Rebecca Louise Caravan

Submitted in accordance with the requirements for the degree of
Doctor of Philosophy

The University of Leeds
School of Chemistry

March 2015

The candidate confirms that the work submitted is her own, except where work which has formed part of jointly-authored publications has been included. The contribution of the candidate and the other authors to this work has been explicitly indicated below. The candidate confirms that appropriate credit has been given within the thesis where reference has been made to the work of others.

R.L. Caravan, R.J. Shannon, T. Lewis, M.A. Blitz and D.E. Heard, “Measurements of Rate Coefficients for Reactions of OH with Ethanol and Propan-2-ol at Very Low Temperatures”, *The Journal of Physical Chemistry A*, ASAP, DOI: 10.10121/JP505790M, 2014.

RLC wrote the manuscript and performed all the experimental work and data analysis. RJS and MAB provided laboratory assistance and advice. TL helped with some of the experimental work. DEH assisted in preparing the manuscript and provided scientific advice.

J.C. Gomez Martin, R.L. Caravan, M.A. Blitz, D.E. Heard and J.M.C. Plane, “Low Temperature Kinetics of the CH_3OH + OH Reaction”, *The Journal of Physical Chemistry A,* **118**, 2693-2701, 2014.

RLC performed the Laval apparatus measurements and data analysis. JCGM performed the flowtube measurements, chemical modelling and data analysis. JCGM wrote the manuscript with assistance from all authors. RLC and MAB performed the chemiluminescence experiments. MAB provided scientific advice and assistance. DEH and JMCP provided scientific advice.

K. Acharyya, E. Herbst, R.L. Caravan, R.J. Shannon, M.A. Blitz and D.E. Heard, “The Importance of OH-Radical-Neutral Low Temperature Tunnelling Reactions in Interstellar Clouds using a New Model”, *Molecular Physics,* Accepted, 2015. DOI: 10.1080/00268976.2015.1021729

K.A and E.H constructed the chemical model and wrote the manuscript. RLC and RJS performed the experiments with assistance from MAB– the results of which are included in the model. DEH provided scientific advice and coordinated the collaboration.

R.J. Shannon, R.L. Caravan, M.A. Blitz and D.E. Heard, “A Combined Experimental and Theoretical Study of Reactions Between the Hydroxyl Radical and Oxygenated Hydrocarbons Relevant to Astrochemical Environments”, Physical Chemistry Chemical Physics, **16**, 3466, 2014.

RJS, RLC and DEH wrote the manuscript. RJS and RLC performed the experimental work with assistance from MAB. RJS performed the theoretical work. DEH provided scientific advice.

Acknowledgements

First and foremost, I would like to express my immense gratitude to my supervisors Professors Dwayne Heard and John Plane for giving me this wonderful opportunity to join their research groups. In particular I would like to thank my primary supervisor, Dwayne, for his unfailing enthusiasm, kindness and attention to detail, and for all the opportunities he has afforded me throughout my PhD – thanks Dwayne !

I am very grateful to Mark, Mike, Paul, Daniel and Robin for all of their help and advice throughout my PhD. I have learned a great deal from all of them, including some interesting phrases from Mark.

Thanks to Andy and Chris for their help with LabVIEW, and to Francis for always delivering my gas cylinders with impeccable timing and cheeriness. Thanks to Lavinia for her help with deriving some of the complex fitting equations.

I have been very fortunate to have met some wonderful people during my time in Leeds. Thank you in particular to James, Sami, Robin, Claire, Fred, Jess, Daniel, Lisa, Tom, Charlotte, Tamsin, JC, Tom C. and Jo. A special thank you to Daniel, Lisa, Tamsin and Charlotte who always made sure I had enough coffee/food when writing up.

I am very grateful for the love and support of my parents Catherine and William, and my grandparents Bernadette and Dennis. My parents have always been incredibly supportive of my decision to go to university and have almost never asked when I am going to get a real job. Thanks guys !

Lastly, and most importantly, I would like to thank my best friend and husband Timothy, who has somehow survived the last three and a half years of listening to me talk almost exclusively about kinetics. I can’t begin to put into words the gratitude I have for your love, support and encouragement.

Abstract

Laboratory kinetic studies of reactions relevant to interstellar environments have been performed using a pulsed Laval nozzle apparatus coupled with pulsed laser photolysis-laser induced fluorescence spectroscopy in the temperature range 54-148 K.

Rate coefficients for the reactions of the hydroxyl radical with several oxygenated organic molecules are reported in Chapters 3 and 4. At low temperatures, the rate coefficients for these reactions are found to be significantly enhanced despite barriers to hydrogen abstraction. A common mechanism has been identified involving the initial formation of a weakly bound complex (~ 15-30 kJ mol^{-1}), which has an extended lifetime at lower temperatures. The extended lifetime of the complex facilitates two competing channels: collisional stabilisation into the pre-barrier well, or quantum mechanical tunnelling through the hydrogen abstraction barrier. The role of these channels is assessed through studies of pressure dependence. The mechanism is also found to be operative for even very weakly bound complexes, such as in the reaction of OH with ammonia as reported in Chapter 5. Pressure dependence and product detection studies enable the low temperature yield of NH_2 radicals from this reaction to be quantified. The potential interstellar implications of these reactions in light of the rate coefficients obtained in this work are reported.

In Chapter 6, the reaction of the postulated products from the OH + methanol and ethanol reactions, methoxy and ethoxy radicals, with NO are studied for the first time at low temperatures. The role of pressure stabilization of the complex, RONO, versus bimolecular product formation is investigated through pressure dependence studies and detection of the NO + methoxy radical product, HCHO, via laser induced fluorescence spectroscopy.

The low temperature high pressure limiting rate coefficients of the OH + oVOC and OH + NH_3 reactions are explored in Chapter 7 using the proxy method of Jaffer, Smith, Quack and Troe. Rate coefficients for the reactions are obtained at different quanta of vibrational excitation of OH, and the validity of the proxy method for weakly bound complexes at low temperatures is considered with regards to efficient intramolecular vibrational relaxation.

Contents

Figures

3. The low temperature reaction kinetics of OH with alcohols: The role of a weakly bound complex .....

5. The reaction of OH with ammonia at low temperatures: Rapid bimolecular product formation via a very weakly bound complex .....

6. Radical-radical reactions at low temperatures: Kinetics of nitric oxide with alkoxy radicals .....

7. Experimental determination of the high pressure limiting rate coefficient at low temperatures via the proxy method .....

Chapter 1. Introduction

1.1 Low temperature environments – the interstellar medium

The interstellar medium (ISM) is the name given to the diverse regions of space located between stars, where temperatures and densities have been found to vary by orders of magnitude, from 10-200 K and from 10^{-4} to 10^{9} molecule cm^{-3}.[1,2] Chemical models (also known as networks) of these regions which are constructed from the results of observational studies have identified significant deficiencies in the knowledge of the mechanisms and rate coefficients by which molecules react with one another at the extreme temperatures of space.[3,4] However, symbiosis within the astrochemical community through laboratory, modelling and observational studies via telescopes has greatly enhanced understanding about the origins of several molecules. The chemistry occurring within interstellar environments can be grouped into three classifications: gas, dust and ice, and the role of each will be briefly covered.

Gas phase species dominate the interstellar medium, with ~ 99 % of interstellar cloud mass being in the gas phase.[5,6] Around 180 molecules (excluding their isotopologues) have been discovered within the gas phase of interstellar environments to date including organic molecules, metal atom containing species and recently, rare gas atom containing species.[2,5] Organic molecules dominate the species detected thus far, from small molecules such as methanol, to large structures such as polycyclic aromatic hydrocarbons (PAHs) and a selection of the smaller species detected as summarised in Table 1. 1 [5]

The detection of these species has largely been facilitated by rotational spectroscopy in the mm to sub-mm range, and the relative intensities of the rotational lines have also been exploited to obtain local temperatures.[2,5] Vibrational spectroscopy is also employed, primarily for the detection of molecules on grains and non-polar species in the gas phase such as methane.[5]

Table 1. 1 : Selection of some C, N, O and H containing neutral molecules detected in interstellar environments. Bold typeface indicates a radical species. Adapted from Smith, and Herbst and van Dishoeck.[7,8] CH_3O detected by Cernicharo *et al.*[9]

H-containing	O-containing	N-containing
CH	**OH**	**NH**
CN	H_2O	**NO**
CH_2	**HCO**	HNO
C_2H	H_2CO	**NH_2**
HCCH	**CH_3O**	**H_2CN**
c-C_3H_2	HCOOH	HNCO
C_5H	CH_3OH	CH_3NH_2
C_4H	CH_3CHO	CH_3C_3N
C_2H_4	CH_3OCH_3	NH_2CH_2CN
CH_2C2H	C_2H_5OH	C_2H_5CN
CH_3CHCH_2	$CH_3C(O)CH_3$	NH_2CHO
CH_3C_6H	CH_3COOH	C_2H_3CN
C_6H_6	$HOCH_2CHO$	CH_3CONH_2
	C_2H_5CHO	

The majority of molecules are found within so-called interstellar (or molecular) clouds, which can be partitioned into two categories: diffuse and dense. Diffuse clouds are very low pressure environments with around 100 molecule cm^{-3}, and as such UV radiation can penetrate the clouds leading to the destruction of molecules.[6] Dense clouds are the sites of star formation and is where the majority of chemical interest lies, particularly in the cold regions where temperatures are between 10-100 K. The most abundant molecule detected in interstellar clouds is H_2, with CO following behind with a relative concentration of ~ 0.01 % of that of H_2.[7] Saturated organic molecules can act as a chemical marker for hot cores which are higher density regions towards protostars (regions in the early stages of star formation).[2,10] Conversely, unsaturated long chain carbon species are primarily found within the cold and dark regions where star formation is yet to begin.[5] As such, the abundance and functional groups of detected molecules can be used as an indicator of the age of the cloud.

The role of gas phase chemistry in interstellar environments has long been recognised, with emphasis placed on ion-molecule reactions which have large rate coefficients even at very low temperatures.[2] The development of new experimental techniques which enable low temperature rate coefficient measurements of neutral-neutral reactions (see Chapter 2) has shone light on the role of barrierless reactions which often have weak temperature dependencies and thus persist at conditions relevant to interstellar clouds. Whilst gas phase chemistry has been shown to be important to the formation of many complex molecules, existing knowledge was unable to rationalise the abundance of molecular hydrogen. The low density of interstellar clouds means that mechanisms which proceed via third body stabilisation are not usually viable, and so another pathway must be considered.

The widely accepted major route for the formation of molecular hydrogen in interstellar environments is the recombination of hydrogen atoms on the surface of what are known as grains.[6,11-14] Grains (also known as dust) are particles of amorphous silicon or carbon which are typically 0.001 – 1 μm in size. Grains are thought to act as a 'reservoir' for gas phase species at very low temperatures (~ 10 K). The heterogeneous formation of molecules on the surface of grains proceeds via the initial adsorption of the gaseous species on the surface of the grain. The enhanced contact time between the molecules, which can 'hop' around the surface of the grain via diffusion, leads to a higher probability of reaction and the grain itself acts as a third body for the removal of excess energy following bond formation.[2] Molecules can then be released into the gas phase immediately (in the case of molecular hydrogen) or following a temperature increase or shock wave.[7,15] In the very cold regions of interstellar clouds the grains are covered by ices which largely comprise water. Other species including methanol, CO, CO_2, HCHO, NH_3 and CH_4 have also been detected in ices, with summed abundances of ~ 5-50 % of that of water ices.[5]

Ice and grain related chemistry has been able to establish the formation pathways of some small organic molecules, for example HCHO and methanol are thought to be produced on the surface of grains and ices from the successive hydrogenation of CO.[7] However, the formation of some of the species detected within the ISM cannot be rationalised thus far by these mechanisms. The methoxy radical (CH_3O) which has recently been detected in interstellar space for the first time by Cernicharo *et al.*, could not be produced in a laboratory simulation experiment of UV and ion irradiation of ices.[9] It was found in the case of methanol ices, it is exclusively the isomer

of methoxy, CH_2OH, which is produced. The authors concluded that the observed interstellar methoxy must be formed by gas-phase reactions, and hence the focus of studies on new pathways to complex molecule formation has come full circle.

Detection of radicals such as OH (which is known in Earth's atmosphere for its reactivity towards volatile species [16]) in interstellar molecular clouds close in proximity to organic species such as methanol,[17] alludes to a pathway by which species such as methoxy may be formed. Indeed, a recent study on the OH + methanol reaction in the gas phase at low temperatures reported an enhanced rate coefficient at low temperatures despite a significant barrier to reaction. This reaction is thought to proceed via a mechanism involving quantum mechanical tunnelling, and at 100 K yields ~ 80 % methoxy radical products according to master equation modelling.[18] Quantum mechanical tunnelling pathways have also been the subject of recent interest for grain and ice chemistry. Evidence has been found in laboratory experiments for the rapid diffusion of oxygen atoms on ice and silicate grain surfaces, which Minisalle and Congiu *et al.* rationalised by quantum tunnelling through the barriers to diffusion.[19-21] Oba *et al.* have recently observed rapid reaction of H atoms with solid H_2O_2 ices despite barriers to reaction.[22] A significant kinetic isotope effect was also observed when deuterated studies were performed, and the authors interpreted their results as evidence for the reaction operating via quantum mechanical tunnelling.[22]

Gas phase reactions such as OH + methanol have previously been disregarded in astrochemical models due the presence of the barrier to reaction on the potential energy surface. Extrapolation of the rate coefficient for such reactions using the Arrhenius equation (see section 1.2.2) would lead to a much lower rate coefficient than has recently been experimentally measured, and as such has previously been termed too slow to be of importance in cold interstellar environments. The laboratory and theoretical study of the reactions of neutral species, such as the detected organic species with OH, is therefore important to developing a better understanding of the temporal development of the ISM.[23]

In the following sections, the theoretical basis of elementary reaction kinetics will be outlined as well as some kinetic theories which are often used to rationalise and predict the behaviour of neutral reactions. In this work the kinetics of radicals such as OH with several species known to be present in interstellar environments has been studied. Many of the rate coefficients

obtained in this work and reported here are measured below 200 K for the first time.

1.2 Reaction kinetics

To rationalise and predict experimentally observed phenomena, many kinetic theories have been developed over time. The forthcoming sections will outline some of these theories and the approximations which are made in their formulation. However, to understand the relative importance of a given reaction and to subsequently examine its agreement with theoretical predictions, the rate coefficient firstly needs to be extracted from experimental data. The rate equations of two types of elementary reactions will be derived below.

Considering first the unimolecular reaction of species A (R1.1), which proceeds with a rate coefficient, $k_{1.1}$.

$$A \xrightarrow{k_{1.1}} Products \qquad \text{R1.1}$$

From R1.1, it can be seen that the rate coefficient is directly proportional to the change in concentration of A with time, which yields the differential equation E1.1.

$$\frac{d[A]}{dt} = -k_{1.1}[A] \qquad \text{E1.1}$$

Integration of E1.1 yields E1.2 which shows that concentration of the reactant in a first order reaction decays exponentially with time.

$$[A]_t = [A]_0 \exp(-k_{1.1}t) \qquad \text{E1.2}$$

Therefore, the rate coefficient for R1.1 can be obtained experimentally by measuring the temporal evolution of the concentration of *A*, or some property proportional to it (such as fluorescence, phosphorescence or conductivity), and fitting its concentration-time profile with an expression for exponential decay.

The kinetic scheme for an elementary bimolecular reaction between species A and B is given in R1.2.

$$A + B \xrightarrow{k_{1.2}} Products \qquad \text{R1.2}$$

where $k_{1.2}$ is the bimolecular rate coefficient for the reaction. The rate equation for the reaction can be expressed as shown in E1.3.

$$\frac{d[A]}{dt} = -k_{1.2}[A][B] \qquad \text{E1.3}$$

Integration of E1.3 yields E1.4, and it can be seen that for the rate coefficient to be known, the concentrations of both A and B with time must be followed.

$$[A]_t = \frac{[A]_0[B]t}{[B]_0} \exp\left(-([B]_0 - [A]_0)k_{1.2}t\right) \quad \text{E1.4}$$

One way to overcome this experimental challenge is to put one reactant in such large excess that its concentration can be considered to be constant throughout the reaction. Therefore the second order rate equation (E1.4) can be reduced to a pseudo first order one (E1.5) and the reaction is therefore said to be performed under pseudo first order conditions.

$$\frac{d[A]}{dt} = -k_{obs}[A] \quad \text{E1.5}$$

where

$$k_{obs} = k_{1.2}[B] \quad \text{E1.6}$$

Pseudo first order conditions are routinely employed for laboratory kinetic studies and have been utilised for the kinetic studies of bimolecular reactions in this work.

1.2.1 The pressure dependence of association reactions: Lindemann-Hinshelwood theory.

It has been observed that association reactions, for example the reaction of OH + ethene, exhibit a pressure dependence upon their rate coefficient, which then reaches a plateau at high pressures.[24-26] The Lindemann-Hinshelwood mechanism rationalises this behaviour by the formation of the association complex with a large degree of internal excitation. The excited association complex will either be stabilised via collisions with an unreactive bath gas, M, or it will dissociate back to reactants. Whilst the Lindemann-Hinshelwood mechanism was originally developed to describe the activation and subsequent reaction of a unimolecular reactant, it can be adapted, as it has been in this work, to describe the pressure dependence of an association reaction (reverse of a unimolecular dissociation) species A and B.

$$A + B \xrightarrow{k_a} AB^* \quad \text{R1.3}$$

$$AB^* \xrightarrow{k_{-a}} A + B \quad \text{R1.4}$$

$$AB^* + M \xrightarrow{k_s} AB + M \quad \text{R1.5}$$

In the above scheme, species A and B can associate to form an activated complex, AB*, which has two fates: redissociation to reactants (R1.4) or

stabilisation via collisions with the bath gas, M, to yield the stabilised adduct (R1.5).

The rate expression for the activated complex is described by E1.7 and given it is a short lived energetically excited intermediate, the steady state approximation can be applied, so that after an initial induction period, its concentration does not change with time.

$$\frac{d[AB^*]}{dt} = -k_{-a}[AB^*] + k_a[A][B] - k_s[AB^*][M] \approx 0 \qquad \text{E1.7}$$

and therefore

$$[AB^*] = \frac{k_a[A][B]}{k_s[M]+k_{-a}} \qquad \text{E1.8}$$

The rate expression for the stabilised adduct, AB, can be described by E1.9 assuming the steady state approximation for the energised adduct.

$$\frac{d[AB]}{dt} = k_s[AB^*][M] = \frac{k_s k_a[A][B][M]}{k_s[M]+k_{-a}} \qquad \text{E1.9}$$

Two limiting cases can be observed from E1.9. At low pressures where k_s[M] << k_{-a} and the rate of stabilisation is therefore less than the rate of dissociation, it can be assumed that k_s[M] + k_{-a} is approximated by k_{-a}, yielding E1.10. In the low pressure regime the overall rate coefficient for the reaction of species A with B to form the stable adduct AB, is linearly dependent on pressure and is a third order process.

$$\frac{d[AB]}{dt} = \frac{k_s k_a[A][B][M]}{k_{-a}} \qquad \text{E1.10}$$

At the high pressure limit, where [M] is large so that k_s[M] >> k_{-a}, E1.9 can be simplified to E1.11. In the high pressure limit, the rate of formation of the energised adduct AB* is the rate determining step and the rate coefficient is independent of pressure so that it is a second order process.

$$\frac{d[AB]}{dt} = \frac{k_s k_a[A][B][M]}{k_s[M]} = k_a[A][B] \qquad \text{E1.11}$$

The overall pressure dependence of a reverse unimolecular (or association) process as described by the Lindemann-Hinshelwood mechanism is illustrated by Figure 1. 1.

The Lindemann-Hinshelwood mechanism is able to qualitatively predict the pressure dependence of an association process but the model is too simplistic to be able to reproduce experimentally obtained results. A key reason for this, which was first identified by Hinshelwood, is that the model does not account for the energy dependence of the processes. Rice Ramsperger Kassel Marcus theory (see section 1.3.3) builds on the basic

principles of Lindemann-Hinshelwood theory but considers the energy dependence of rate coefficients for a given process.[27]

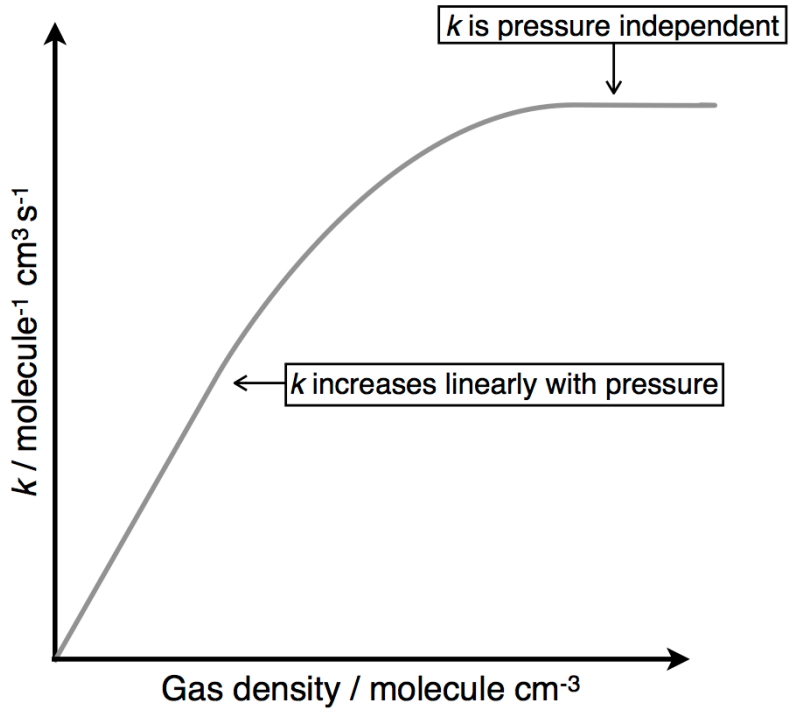

Figure 1. 1: Pressure dependence of the rate coefficient for an association (reverse unimolecular) process as described by the Lindemann-Hinshelwood mechanism.

An extended Lindemann-Hinshelwood model has been utilised in this work to obtain the relative contributions for collisional stabilisation and bimolecular channels following an association process. For further details of this work, see Chapter 3.

1.2.2 Temperature dependence: The Arrhenius equation

Developed in 1889 by Svante Arrhenius, the Arrhenius equation (E1.12) is based on experiments performed by Arrhenius in which the reaction rate coefficients were found to increase with temperature.[28]

$$k = Aexp\left(\frac{-E_a}{RT}\right) \qquad \text{E1.12}$$

A is the pre-exponential factor, which corresponds to the collision frequency of the reactant molecules. E_a is the activation energy of the reaction, which is related to the relative energy between the transition state (the maximum on the minimum energy pathway of a reaction) and the reactants. The difference in these is a result of the energy required to rearrange the atoms and break bonds within the reactants. *R* and *T* are the gas constant (J K^{-1}

mol^{-1}) and the temperature (K) respectively. Whether or not a reaction conforms to Arrhenius behaviour can be verified by plotting ln(k), versus 1/T (as shown in Figure 1. 2). If the plot yields a straight line, Arrhenius type behaviour is observed over that temperature range. The intercept of the plot is the logarithm of the pre-exponential factor (ln A) and the gradient ($-E_a/R$) yields the activation energy of the reaction.

Whilst the rate coefficients for many reactions conform to Arrhenius type behaviour over a small temperature range, numerous exceptions have been observed, in particular at high or very low temperatures.[29-36] Two commonly considered reasons for deviation from Arrhenius type kinetics are the temperature dependence of the pre-exponential factor A (high temperatures) and quantum mechanical tunnelling (low temperatures), leading to a temperature dependent activation energy.[37]

A recent perspective article by Ian Sims highlighted three extremes of temperature dependencies for neutral exothermic reactions. Using the illustration of Sims, these will be briefly summarised below.[38]

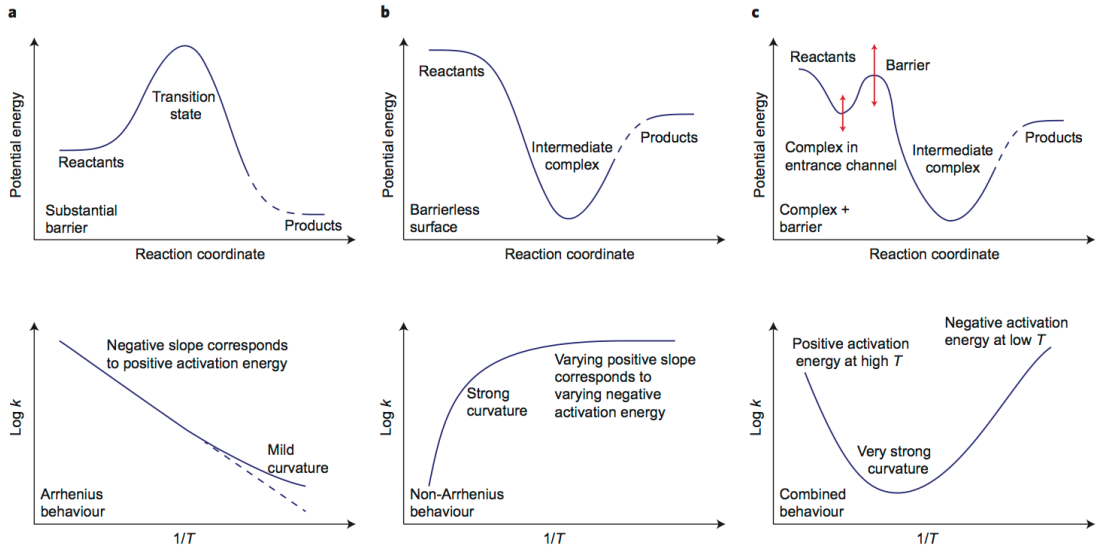

Figure 1. 2: The temperature dependence (bottom) of neutral-neutral exothermic reactions for different potential energy surfaces (top), reproduced from Sims.[38]

Figure 1. 2(a) shows the potential energy surface for a reaction with an overall barrier, such as the reaction of OH with butane.[39,40] The temperature dependence adheres to Arrhenius-type behaviour, perhaps with some curvature at lower temperatures for reactions where tunnelling may play a role. Figure 1. 2(b) illustrates a typical potential energy surface for a barrierless reaction, such as the reaction of CN with O_2.[41-44]The formation of an association complex below the reactant energy leads to distinctly non-Arrhenius behaviour.

The complicated temperature dependence for a reaction which has a weakly bound complex followed by a barrier (which may be positive or submerged below the reactant energy) on the potential energy surface (Figure 1. 2(c)) has been observed for the reaction of CN with C_2H_6 through low temperature kinetic measurements by Sims *et al.*[45] Theoretical work by Georgievskii and Klippenstein was able to rationalise the observed unusual temperature dependence by a two transition state model.[46] At high temperatures, the rate determining step is traversing the submerged barrier to reaction to yield the bimolecular products HCN and C_2H_5 and so the transition state is the barrier to reaction. Whereas at low temperatures, the bottleneck to the reaction becomes the initial formation of the weakly bound complex between CN and C_2H_6 prior to the submerged barrier. Similar temperature dependencies have been observed by Brown *et al.* for the OH + HNO_3 reaction, by Shannon *et al.* at low temperatures and also in this work for reactions whereby the barrier following complex formation is positive with respect to reactant energy.[18,47-52]

1.3 Kinetic theories

1.3.1 Simple collision theory

Simple collision theory (SCT) is a method of estimating the rate coefficient for a reaction by treating the reacting species, A and B, as hard spheres with no intermolecular forces.[27] The rate coefficients predicted by SCT are dependent on two components: the number of collision events between species A and B, and the probability that a collision between A and B will lead to a reaction.

$$\sigma = \pi {b_{max}}^2 \qquad \text{E1.13}$$

The collision cross section (σ), which is defined in E1.13, determines the probability of a collision between species A and B and is dependent on the maximum intermolecular separation between species A and B that can result in a collision (b_{max}) the value of b_{max} is taken to be the sum of the radii of species A and B.

The total number of collisions per volume per unit time is taken to be dependent on the number of each molecule A and B, the collision cross section and the relative velocities of the molecules. At a given temperature, the species A and B are assumed to travel at a Maxwell-Boltzmann distribution of velocities, and the mean relative velocity of the colliding species is calculated by E1.14

$$v = \left(\frac{8k_BT}{\pi\mu}\right)^{0.5} \quad \text{E1.14}$$

where k_B is the Boltzmann constant, T is the temperature, and μ is the reduced mass of A and B. The probability of reaction following collision is dependent on the number of molecules which have sufficient energy to overcome the barrier to reaction (E_0) and so combining this with E1.13 and E1.14, the overall SCT rate coefficient is given by E1.15

$$k = \left(\frac{8k_BT}{\pi\mu}\right)^{0.5} \pi {b_{max}}^2 exp\left(\frac{-E_0}{k_BT}\right) \quad \text{E1.15}$$

At best, SCT is able to qualitatively predict the temperature dependence of a reaction.[53] However, in addition to neglecting intermolecular forces, this simplistic model disregards that species may only react with one another in a particular orientation and additionally the vibrational and rotational motions of the molecules.[53] Therefore, to obtain a more realistic prediction of reaction rate coefficients, these parameters need to be accounted for – the steric factor, ρ , is included in SCT to account for differences between the observed and calculated rate coefficients.

1.3.2 Transition state theory

Transition state theory (TST), developed by Evans, Polanyi and Eyring examines the rate coefficient of a reaction by considering trajectories (a path taken by the reactants over the potential energy surface with time) of atoms or molecules over the potential energy surface for the reaction.[54,55] The theory is based around the formation of a transition state (or activated complex) between the reactants, which is positioned at the maximum of the minimum energy pathway on the potential energy surface. The transition state is a high energy complex and is considered to be transient, and acts as a dividing surface between reactants and products. Trajectories which pass through the dividing surface on the potential energy surface are assumed to proceed straight to products without reverting back to reactants. This is known as the no-recrossing assumption.[56] TST assumes the reactants are equilibrated either in a canonical (fixed temperature) or microcanonical (fixed exact energy) ensemble and thus either the k(T) or the k(E) values are obtained.[37,56]

The rate coefficient can be obtained using the one way local flux over the dividing surface, where the probability of the trajectory proceeding over the dividing surface is determined by the Boltzmann distribution. The expression for the transition state theory rate coefficient is shown in E1.16.

$$k = \frac{k_B T}{h} \frac{Q^+}{Q} \exp\left(\frac{-E_0}{k_B T}\right) \quad \text{E1.16}$$

where E_0 is the critical minimum energy of the transition state, Q and Q^+ are the partition functions for the reactants and transition state respectively, h is Planck's constant, k_B is the Boltzmann constant and T is the temperature in Kelvin. The vibrational frequency corresponding to motion along the reaction co-ordinate is removed when calculating the partition function of the transition state species and is known as the imaginary frequency.

As it is assumed that all of the trajectories crossing into the products region cannot re-cross, the rate coefficient yielded from this method is the upper bound to the real rate coefficient.[37,57] There have been several developments based on the principles of TST. For example, in variational TST, the position of the dividing surface is varied to minimise the one way flux crossing the dividing surface.[56] Variational TST is particularly valuable for calculating the rate coefficients of a barrierless reaction where the transition state is not well defined.[37]

1.3.3 RRKM theory

RRKM theory is a statistical rate theory which can be considered a microcanonical version of transition state theory.[56] RRKM theory is the descendant of the earlier RRK theory, which had been developed by Rice and Ramsperger in 1927 and additionally by Kassel in 1928.[58-60] The improvement that RRK theory made on Lindemann-Hinshelwood theory was to account for the energy dependence of the rate coefficients for the energisation (R1.6) and reaction of the complex (R1.7), so that the rate coefficients were microcanonical. For a unimolecular process, an example of this is given below, whereby R1.8 proceeds with a rate coefficient of $k_2(E)$.

$$AB + M \xrightarrow{\delta k_1\,(E \to E+\delta E)} AB^*(E \to E+\delta E) + M \quad \text{R1.6}$$

$$AB^* + M \xrightarrow{k_{-1}} AB + M \quad \text{R1.7}$$

$$AB^* \to products \quad \text{R1.8}$$

Quantum RRK theory assumes that there are a number of identical oscillators within the molecule and all with identical associated frequencies. For R1.6, instead of energisation occurring within in a range of energies, E→E+δE, it is thought of as occurring by partitioning energy in to a particular quantum state of an oscillator.[61] To acquire the overall rate coefficient, the contribution from each quantised level is summed from the minimum energy required to overcome the barrier to reaction. Whilst this theory was a

significant progression on the Lindemann-Hinshelwood mechanism, it is not realistic to consider the oscillators of a molecule as identical with identical frequencies.

Rudolph Marcus refined the theory further in 1952 by establishing the distinction between an energised molecule (AB*), and an activated molecule ($AB^{‡}$) which is otherwise known as the transition state (TS).[62-64] The activated molecule is located at the top of the barrier between reactants and products. The energised molecule has sufficient internal energy to proceed over the barrier to reaction, and thus has sufficient energy to become an activated molecule, but needs to undergo vibrations in order to redistribute the energy in the correct vibrational mode which corresponds to the reaction coordinate.[61]

$$AB + M \xrightarrow{\delta k_1\,(E^* \rightarrow E^* + \delta E)} AB^*(E^* \rightarrow E^* + \delta E) + M \qquad \text{R1.9}$$

$$AB^* + M \xrightarrow{k_{-1}} AB + M \qquad \text{R1.7}$$

$$AB^*(E^*) \xrightarrow{k_2(E^*)} AB^{‡} \xrightarrow{k^{‡}} products \qquad \text{R1.11}$$

The overall expression for a first order rate expression from RRKM theory is given in E1.17.[61]

$$k = -\frac{1}{[AB]}\frac{d[AB]}{dt} = \int_{E^*=E_0}^{\infty} \frac{k_2(E^*)dk_1(E^* \rightarrow E^* + \delta E)/k_{-1}}{1 + k_2(E^*)/k_{-1}[M]} \qquad \text{E1.17}$$

As RRKM theory is primarily concerned with how energy can be distributed amongst the modes of a molecule, it is important to be able to know the number of modes and energy spacing between them. In the case of RRK theory, the modes were assumed to be of equal energy. All the vibrational and rotational modes are considered to be active and so the number of energy levels and their spacing can be obtained from the vibrational frequencies and rotational constants. Advances in *ab initio* calculations means these properties can be readily computed and so a more accurate depiction of how energy is partitioned amongst the modes of a molecule can be obtained. Therefore, for the reaction step shown in R1.11, the microcanonical rate coefficient k_2(E*) can be thought of as being related to the sum of vibrational and rotational states (W($E^{‡}$)) in the TS with an energy less than or equal to $E^{‡}$, compared to the density of states (ρ(E*)) of the energised molecule AB* (which is defined as the number of quantum states in a given energy range). The overall RRKM result is presented in E1.18.[57]

$$k_2(E^*) = \frac{W(E^{‡})}{h\rho(E^*)} = \frac{\sum_0^{E^{‡}} P(E^{‡})}{h\rho(E^*)} \qquad \text{E1.18}$$

There is one key assumption of RRKM theory – that statistical redistribution of vibrational energy around the modes of the molecule is assumed to be rapid on the timescale of reaction, and this is known as the ergodicity principle. This assumption has been shown to be valid for many systems, but breaks down where the modes are uncoupled from one another by having significantly different frequencies.

The strong collision assumption was previously also utilised in RRKM theory, whereby deactivation is considered to occur by one collision encounter and that a large amount of energy is transferred through collisions. In the master equation implementation of RRKM theory (discussed below), this assumption is removed by accounting for stepwise energy transfer.

1.4 Computational implementation of RRKM theory : the energy grained master equation

In Chapters 4 and 5 of this thesis, results from master equation calculations performed by Dr Robin Shannon and Dr Arne Bunkan respectively using the MESMER code are presented to rationalise and investigate the experimental results obtained in this work and by Shannon *et al.*[50,65] A full detailed discussion of master equation calculations is beyond the scope of this thesis and as such only a brief outline of how RRKM energy grained master equation methods such as MESMER operate is given.[65] Further details can be seen in the publication regarding the MESMER code by Glowacki *et al.*[65]

The master equation (ME) uses the result of RRKM theory (E1.18) to deduce microcanonical rate coefficients for unimolecular processes by evaluating the temporal evolution of a population of molecules with a specific internal energy. For ease of obtaining a numerical solution, the energy states are grouped into ‘grains’ of a given energy width, and it is the temporal evolution of the grains populations which is calculated. The smaller the grain size, the more representative the model is. However, below a given grain size for a particular system, the results will converge. For a unimolecular reaction of a species, *i* (following the barrierless association of A and B) a schematic illustrating the processes considered in a master equation analysis is shown in Figure 1. 3.

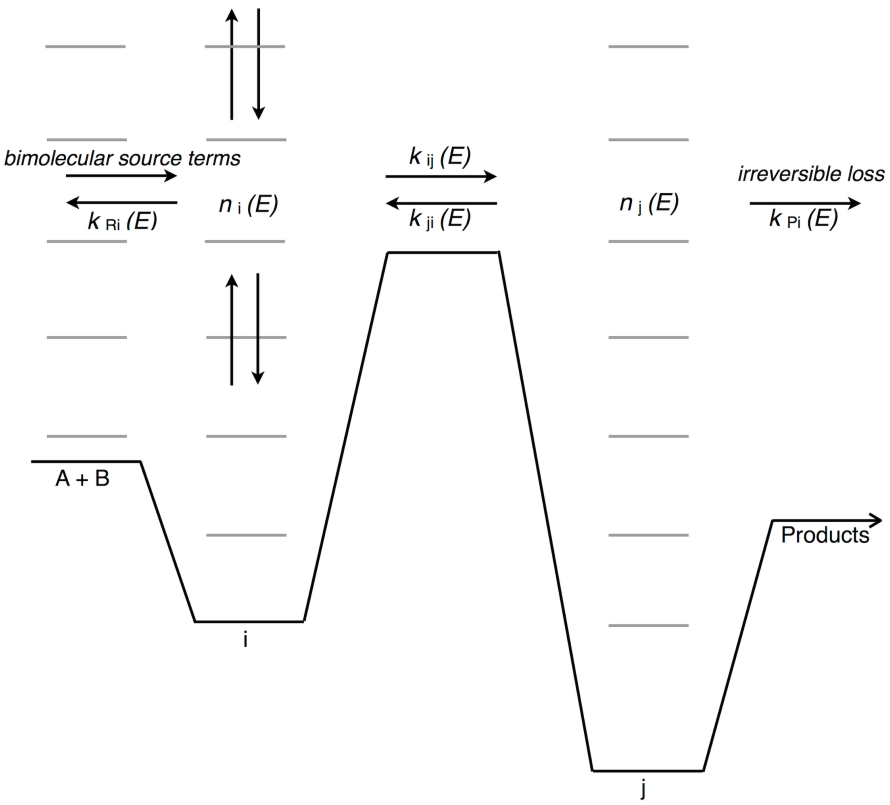

Figure 1. 3: The unimolecular processes considered in the computational implementation of energy grained master equation calculations, where the grey lines represent the grains. Based on diagrams by Shannon and by Glowacki *et al*.[65,66] The various terms and symbols are described in the text.

The master equation for the process illustrated in Figure 1. 3 is shown in its algebraic form in E1.19 and can be broken down into four parts which are described below.

$$\frac{dn_i(E)}{dt} = \omega \int_{E_{0_i}}^{\infty} P(E|E')n_i(E')dE' - \omega n_i(E) - \sum_{i\neq j}^{M} n_i(E)k_{ji}(E) + \sum_{i\neq j}^{M} n_j(E)k_{ij}(E) - k_{Pi}(E)n_i(E) - k_{Ri}(E)n_i(E) + K_{Ri}^{eq}k_{Ri}(E)\frac{\rho_i(E)e^{-E/k_BT}}{Q_i(T)}[A]n_B \qquad \text{E1.19}$$

a) The first two terms describe the gain and loss, respectively, of the population of molecules *i* with a specific internal energy (*E*) by collisional energy transfer from and to other energy levels, respectively. $P(E|E')$ is the probability that collision will result in transfer from a grain with energy E' to a grain with energy E. ω is the Lennard-Jones collision frequency. $n_i(E')$ is the

population of isomer *i* with energy (*E'*), and $n_i(E)$ is the population of isomer *i* with energy E. The probability of transfer from one grain to another of lower energy $P(E|E')$ can be approximated by the exponential down model, where the probability is related to the energy difference between the grains (ΔE) and the average energy transferred in a downward direction, $<\Delta E_{down}>$. This is shown in E1.20 where *C* is a normalisation constant.[61,65]

$$P(E|E') = Cexp\left[-\left(\frac{\Delta E}{<\Delta E_{\mathrm{down}}>}\right)\right] \qquad \text{E1.20}$$

The probability for transfer to a higher energy grain is related by detailed balance.[57] Transfer via collisions to a lower energy grain is favoured over collisional energy transfer in an upward direction due to the density of states (number of energy levels in a given energy range) increasing with energy as the energy levels tend towards a continuum. Hence it is easier to transfer energy in a downward direction rather than an upward direction. The detailed balance constraint ensures that at long times, a Boltzmann distribution of energy levels is occupied.[61]

b) The third and fourth terms of the ME are the contributions to the change in the population of *i* in a grain with energy *E* by the loss and gain via isomerisation to and from other species on the potential energy surface with the same internal energy, *E*. The contributions of these terms are determined by the rate coefficients for isomerisation to species *i* from species *j* and vice-versa and the population of each of these species with energy *E*. $k_{ji}(E)$ and $k_{ij}(E)$ are the microcanonical rate coefficients for the population transfer of isomer *i* to *j*, and *j* to *i*, respectively, both with energy, *E*.

c) The 5th term represents the irreversible loss of the population of *i* from a grain with energy *E* to products with the microcanonical rate coefficient, $k_{Pi}(E)$. Considering product formation as in irreversible sink of the reactants echoes the no re-crossing rule of TST, but is not considered suitable for all reactions.

d) The final two terms are the bimolecular source terms. For reactions where species *i* is formed by the initial association of reactants *A* and *B* (collectively denoted *R*) , and where reactant *A* is in great excess of reactant *B* (under pseudo first order conditions), the 6th term describes gain of the collective population of reactants *R* via dissociation of *i* and the 7th term describes the gain in populations of species *i* from the association reaction of the reactants, *R*. In the work by Shannon and Bunkan discussed in this thesis,[50]

the bimolecular source term rate coefficients have been calculated using an inverse Laplace transform method, which is described in Appendix A.

The master equation is computationally solvable using the matrix formulation E1.21, where ***M*** is the master equation matrix and *i* is the population of the reactant summed over all energies.[65]

$$\frac{di}{dt} = \boldsymbol{M}i \qquad \text{E1.21}$$

The solution to this matrix yields several eigenvalues which are negative, as the population of the reactant, *i*, decreases with time. For a one well system the bimolecular rate coefficient is obtained from the chemically significant eigenvalue, which is the least negative of these eigenvalues.

1.4.1 Quantum mechanical tunnelling

Tunnelling is the quantum mechanical phenomenon of a wavefunction having a non-zero probability of passing through a barrier.[27,67] The tunnelling probability is inversely dependent on the mass of the tunnelling species, and so it was previously thought that only light atoms such as hydrogen have a significant probability of tunnelling.[27] However, recent work by Minisalle and Congiu *et al*. related to grain processes in interstellar environments have found evidence for tunnelling of atoms as large as oxygen.[19-21]

Quantum mechanical tunnelling can contribute significantly to the rate coefficient of hydrogen transfer processes at low temperatures where the internal energy of the reactants is insufficient for the barrier to the process to be traversed. The probability of tunnelling through a reaction barrier can be calculated and this probability used in rate theory calculations such as those reported in this work.

Tunnelling probability calculations consider the probability of tunnelling either one- or multi-dimensionally. The former considers transmission through the barrier only on the reaction coordinate and the latter accounts for tunnelling which may occur on pathways not directly along the reaction coordinate. Calculation of multidimensional tunnelling probabilities is a more rigorous approach, but ultimately is significantly more computationally expensive. An example of a multidimensional tunnelling theory is the small curvature semi-classical tunnelling (SCT) method developed by the group of Donald Truhlar. SCT is based on the observations by Marcus and Coltrin that tunnelling can occur through a pathway which is slightly deviated from the reaction co-ordinate.[68-70] To obtain the tunnelling probability via Truhlar's

method, *ab initio* energy calculations need to be performed along the minimum energy pathway. At each point an energy optimisation and frequency calculation is required, thus making it computationally demanding.

One dimensional tunnelling calculations are currently more widely used and have been employed for the master equations performed by Shannon and Bunkan which are used to support the experimental work presented in Chapters 4 and 5, respectively. As such the method utilised by Shannon and Bunkan will be briefly overviewed hereafter.

The probability of tunnelling occurring is dependent on the shape of the barrier. The thinner and lower the barrier, the higher the probability that tunnelling will occur. It should be noted that the probability of tunnelling exhibits a quadratic dependence on the barrier width, but only a linear dependence on the height.[27] The shape of the barrier can be approximated in some way using a function or it can be calculated by several stationary point calculations along the minimum energy pathway of a reaction via *ab initio* methods. Whilst the latter method can yield more accurate results (depending on the level of theory used) it can be computationally expensive.

The method developed by Miller utilises the Eckart function to approximate the shape of the potential barrier.[67,71] The imaginary frequency, which is the frequency corresponding to the vibration along the reaction coordinate, is used to approximate the width of the barrier. Using the imaginary frequency and the relative barrier height (compared to both reactants and products) the probability of tunnelling (P_{tun}) can be calculated. The overall expression for the Miller/Eckart method is given in E1.22-E1.25.

$$P_{tun} = \frac{\sinh(a)sinh(b)}{sinh^2\left(\frac{a+b}{2}\right)+cosh^2(c)} \qquad \text{E1.22}$$

$$a = \frac{4\pi}{\hbar\omega_b}\sqrt{E_1 + V_0}({V_0}^{-0.5} + {V_1}^{-0.5})^{-1} \qquad \text{E1.23}$$

$$b = \frac{4\pi}{\hbar\omega_b}\sqrt{E_1 + V_1}({V_0}^{-0.5} + {V_1}^{-0.5})^{-1} \qquad \text{E1.24}$$

$$c = 2\pi\sqrt{\frac{V_0+V_1}{(\hbar\omega_b)^2} - \frac{1}{16}} \qquad \text{E1.25}$$

where $\hbar=h/2\pi$ (h is Planck's constant), ω_b is the imaginary frequency, V_0 is the barrier height relative to the reactant energy and V_1 is the barrier height relative to the product energy.

A shortcoming of this method is that *ab initio* calculations of vibrational frequencies often suffer significant errors and are highly sensitive to the level of theory used to calculate them. Therefore, for rate theory calculations in

which the Eckart/Miller method is employed, the imaginary frequency corresponding to the barrier width, is often varied to explore the sensitivity of the obtained rate coefficient to this parameter. Despite the limitations of this method, Eckart/Miller tunnelling corrections are widely employed in the literature, suggesting that sufficiently accurate results can be yielded to obtain a reasonable tunnelling probability.[46,72-74] An example of a system to which this method has been applied is the reaction of OH + CO.[72]

1.5 References

1 van Dishoeck, E. F. B., Geoffrey A.; Draine, B. T.; Lunine, J. I. The chemical evolution of protostellar and protoplanetary matter. *Protostars and planets* **III**, 163-241 (1993).

2 Van Dishoeck, E. F. Astrochemistry of dust, ice and gas: introduction and overview. *Faraday Discussions* **168**, 9-47 (2014).

3 Hebrard, E., Dobrijevic, M., Benilan, Y. & Raulin, F. Photochemical kinetics uncertainties in modeling Titan's atmosphere: A review. *Journal of Photochemistry and Photobiology C: Photochemistry Reviews* **7**, 211-230 (2006).

4 Hebrard, E., Dobrijevic, M., Benilan, Y. & Raulin, F. Photochemical kinetics uncertainties in modeling Titan's atmosphere: First consequences. *Planetary and Space Science* **55**, 1470-1489 (2007).

5 Herbst, E. Three milieux for interstellar chemistry: gas, dust, and ice. *Physical Chemistry Chemical Physics* **16**, 3344-3359 (2014).

6 Herbst, E. Concluding remarks: astrochemistry of dust, ice and gas. *Faraday Discussions* **168**, 617-634 (2014).

7 Herbst, E. & van Dishoeck, E. F. Complex Organic Interstellar Molecules. *Annual Review of Astronomy and Astrophysics* **47**, 427-480 (2009).

8 Smith, I. W. The Liversidge Lecture 2001–02. Chemistry amongst the stars: reaction kinetics at a new frontier. *Chemical Society Reviews* **31**, 137-146 (2002).

9 Cernicharo, J. *et al.* Discovery of the Methoxy Radical, CH_3O, toward B1: Dust Grain and Gas-phase Chemistry in Cold Dark Clouds. *The Astrophysical Journal Letters* **759**, L43 (2012).

10 Charnley, S. in *Encyclopedia of Astrobiology* 763-763 (Springer, 2011).

11 Dulieu, F. *et al.* How micron-sized dust particles determine the chemistry of our Universe. *Scientific reports* **3** (2013).

12 Duley, W. & Williams, D. The formation of interstellar H_2 on amorphous silicate grains. *Monthly Notices of the Royal Astronomical Society* **223**, 177-182 (1986).

13 Cazaux, S. & Tielens, A. H_2 formation on grain surfaces. *The Astrophysical Journal* **604**, 222 (2004).

14 Biham, O., Furman, I., Katz, N., Pirronello, V. & Vidali, G. H_2 formation on interstellar grains in different physical regimes. *Monthly Notices of the Royal Astronomical Society* **296**, 869-872 (1998).

15 Smith, I. W. M., Herbst, E. & Chang, Q. Rapid neutral–neutral reactions at low temperatures: a new network and first results for

TMC-1. *Monthly Notices of the Royal Astronomical Society* **350**, 323-330 (2004).

16 Heard, D. E. *Analytical techniques for atmospheric measurement*. (John Wiley & Sons, 2006).

17 Szymczak, M. & Kus, A. J. New detections of OH sources towards the 6.7 GHz methanol masers. *Astron. Astrophys. Suppl. Ser.* **147**, 181-185 (2000).

18 Shannon, R. J., Blitz, M. A., Goddard, A. & Heard, D. E. Accelerated Chemistry in the Reaction between the Hydroxyl Radical and Methanol at Interstellar Temperatures Facilitated by Tunnelling. *Nature Chem.* **5**, 745-749 (2013).

19 Minissale, M., Congiu, E. & Dulieu, F. Oxygen diffusion and reactivity at low temperature on bare amorphous olivine-type silicate. *The Journal of Chemical Physics* **140**, 074705 (2014).

20 Minissale, M. *et al.* Quantum tunneling of oxygen atoms on very cold surfaces. *Physical review letters* **111**, 053201 (2013).

21 Congiu, E. *et al.* Efficient diffusive mechanisms of O atoms at very low temperatures on surfaces of astrophysical interest. *Faraday Discussions* **168**, 151-166 (2014).

22 Oba, Y., Osaka, K., Watanabe, N., Chigai, T. & Kouchi, A. Reaction kinetics and isotope effect of water formation by the surface reaction of solid H_2O_2 with H atoms at low temperatures. *Faraday Discussions* **168**, 185-204 (2014).

23 Herbst, E. Chemistry of Star-Forming Regions. *The Journal of Physical Chemistry A* **109**, 4017-4029 (2005).

24 Taylor, S. E. *Reaction Kinetics at Very Low Temperatures Measured Using a Pulsed Laval Nozzle System*, University of Leeds, (2007).

25 Taylor, S. E., Goddard, A., Blitz, M. A., Cleary, P. A. & Heard, D. E. Pulsed Laval nozzle study of the kinetics of OH with unsaturated hydrocarbons at very low temperatures. *Physical Chemistry Chemical Physics* **10**, 422-437 (2008).

26 Vakhtin, A. B., Murphy, J. E. & Leone, S. R. Low-Temperature Kinetics of Reactions of OH Radical with Ethene, Propene, and 1-Butene. *The Journal of Physical Chemistry A* **107**, 10055-10062 (2003).

27 Pilling, M. J. & Seakins, P. W. *Reaction kinetics*. (Oxford University Press, 1995).

28 Arrhenius, S. On the reaction velocity of the inversion of cane sugar by acids. *J. Phys. Chem* **4**, 226 (1889).

29 Zellner, R. Non-Arrhenius behavior in bimolecular reactions of the hydroxyl radical. *Journal of Physical Chemistry* **83**, 18-23 (1979).

30 Sharkey, P. & Smith, I. W. M. Kinetics of elementary reactions at low temperatures: rate constants for the reactions of OH with HCl ($298 \geq T/K \geq 138$) , CH_4 ($298 \geq T/K \geq 178$) and C_2H_6 ($298 \geq T/K \geq 138$). *Journal of the Chemical Society, Faraday Transactions* **89**, 631-637 (1993).

31 Plane, J. M. A kinetic study of the reaction lithium + nitrous oxide: non-Arrhenius behavior over the temperature range 363-900 K. *Journal of Physical Chemistry* **91**, 6552-6557 (1987).

32 Mozurkewich, M., Lamb, J. J. & Benson, S. W. Negative activation energies and curved Arrhenius plots. 2. Hydroxyl + carbon monoxide. *The Journal of Physical Chemistry* **88**, 6435-6441 (1984).

33 McGillen, M. R., Baasandorj, M. & Burkholder, J. B. Gas-phase rate coefficients for the OH + n-, i-, s-, and t-butanol reactions measured between 220 and 380 K: non-Arrhenius behavior and site-specific reactivity. *The Journal of Physical Chemistry A* **117**, 4636-4656 (2013).

34 Lamb, J. J., Mozurkewich, M. & Benson, S. W. Negative activation energies and curved Arrhenius plots. 3. Hydroxyl + nitric acid and hydroxyl+ peroxynitric acid. *The Journal of Physical Chemistry* **88**, 6441-6448 (1984).

35 Grotheer, H. H., Riekert, G., Walter, D. & Just, T. Non-arrhenius behavior of the reaction of hydroxymethyl radicals with molecular oxygen. *The Journal of Physical Chemistry* **92**, 4028-4030 (1988).

36 Chen, C.-J., Back, M. & Back, R. The thermal decomposition of methane. II. Secondary reactions, autocatalysis and carbon formation; non-Arrhenius behaviour in the reaction of CH_3 with ethane. *Canadian Journal of Chemistry* **54**, 3175-3184 (1976).

37 Laidler, K. J. *Chemical kinetics*. (McGraw-Hill, 1977).

38 Sims, I. R. Low-temperature reactions: Tunnelling in space. *Nature chemistry* **5**, 734-736 (2013).

39 Tully, F. P., Goldsmith, J. & Droege, A. T. Hydrogen atom abstraction from alkanes by hydroxyl. 4. Isobutane. *The Journal of Physical Chemistry* **90**, 5932-5937 (1986).

40 Bravo-Pérez, G., Alvarez-Idaboy, J. R., Jiménez, A. G. & Cruz-Torres, A. Quantum chemical and conventional TST calculations of rate constants for the OH + alkane reactions. *Chemical physics* **310**, 213-223 (2005).

41 Klippenstein, S. J. & Kim, Y. W. Variational statistical study of the CN + O_2 reaction employing *ab initio* determined properties for the transition state. *The Journal of Chemical Physics* **99**, 5790-5799 (1993).

42 Sims, I. *et al.* Ultra−low temperature kinetics of neutral–neutral reactions: The reaction CN + O_2 down to 26 K. *The Journal of Chemical Physics* **97**, 8798-8800 (1992).

43 Sims, I. *et al.* Ultralow temperature kinetics of neutral–neutral reactions. The technique and results for the reactions CN + O_2 down to 13 K and CN + NH_3 down to 25 K. *The Journal of chemical physics* **100**, 4229-4241 (1994).

44 Sims, I. R. & Smith, I. W. Rate constants for the radical-radical reaction between CN and O_2 at temperatures down to 99 k. *Chemical Physics Letters* **151**, 481-484 (1988).

45 Sims, I. R. *et al.* Rate constants for the reactions of CN with hydrocarbons at low and ultra-low temperatures. *Chemical Physics Letters* **211**, 461-468 (1993).

46 Georgievskii, Y. & Klippenstein, S. J. Strange Kinetics of the C_2H_6 + CN Reaction Explained. *The Journal of Physical Chemistry A* **111**, 3802-3811 (2007).

47 Caravan, R. L., Shannon, R., Lewis, T., Blitz, M. A. & Heard, D. E. Measurements of Rate Coefficients for Reactions of OH with Ethanol and Propan-2-ol at Very Low Temperatures. *The Journal of Physical Chemistry A* (2014).

48 Brown, S. S., Burkholder, J. B., Talukdar, R. K. & Ravishankara, A. R. Reaction of Hydroxyl Radical with Nitric Acid: Insights into Its Mechanism. *The Journal of Physical Chemistry A* **105**, 1605-1614 (2000).

49 Brown, S. S., Talukdar, R. K. & Ravishankara, A. Reconsideration of the rate constant for the reaction of hydroxyl radicals with nitric acid. *The Journal of Physical Chemistry A* **103**, 3031-3037 (1999).

50 Shannon, R. J., Caravan, R. L., Blitz, M. & Heard, D. E. A combined experimental and theoretical study of reactions between the hydroxyl radical and oxygenated hydrocarbons relevant to astrochemical environments. *Phys. Chem. Chem. Phys.* **16**, 3466-3478 (2014).

51 Shannon, R. J., Taylor, S., Goddard, A., Blitz, M. A. & Heard, D. E. Observation of a Large Negative Temperature Dependence for Rate Coefficients of Reactions of OH with Oxygenated Volatile Organic Compounds Studied at 86-112 K. *Phys. Chem. Chem. Phys.* **12**, 13511-13514 (2010).

52 Gomez Martin, J. C., Caravan, R. L., Blitz, M. A., Heard, D. E. & Plane, J. M. C. Low Temperature Kinetics of the CH_3OH + OH Reaction. *J. Phys. Chem. A* **118**, 2693-2701 (2014).

53 Fernández-Ramos, A., Miller, J. A., Klippenstein, S. J. & Truhlar, D. G. Modeling the kinetics of bimolecular reactions. *Chemical reviews* **106**, 4518-4584 (2006).

54 Eyring, H. The activated complex in chemical reactions. *The Journal of Chemical Physics* **3**, 107-115 (1935).

55 Evans, M. G. & Polanyi, M. Some applications of the transition state method to the calculation of reaction velocities, especially in solution. *Trans. Faraday Soc.* **31**, 875-894 (1935).

56 Truhlar, D. G., Garrett, B. C. & Klippenstein, S. J. Current status of transition-state theory. *The Journal of Physical Chemistry* **100**, 12771-12800 (1996).

57 Gilbert, R. G. & Smith, S. C. *Theory of unimolecular and recombination reactions*. (Blackwell Scientific, 1990).

58 Rice, O. K. & Ramsperger, H. C. Theories of unimolecular gas reactions at low pressures. *Journal of the American Chemical Society* **49**, 1617-1629 (1927).

59 Rice, O. K. & Ramsperger, H. C. Theories of Unimolecular Gas Reactions at Low Pressures. II. *Journal of the American Chemical Society* **50**, 617-620 (1928).

60 Kassel, L. S. Studies in Homogeneous Gas Reactions. I. *The Journal of Physical Chemistry* **32**, 225-242 (1928).

61 Holbrook, K. A., Pilling, M. J. & Robertson, S. H. *Unimolecular reactions*. (Wiley, 1996).

62 Wieder, G. M. & Marcus, R. Dissociation and isomerization of vibrationally excited species. II. Unimolecular reaction rate theory and its application. *The Journal of Chemical Physics* **37**, 1835-1852 (1962).

63 Marcus, R. & Rice, O. The Kinetics of the Recombination of Methyl Radicals and Iodine Atoms. *The Journal of Physical Chemistry* **55**, 894-908 (1951).

64 Marcus, R. Unimolecular dissociations and free radical recombination reactions. *The Journal of Chemical Physics* **20**, 359-364 (1952).

65 Glowacki, D. R., Liang, C.-H., Morley, C., Pilling, M. J. & Robertson, S. H. MESMER: an open-source master equation solver for multi-energy well reactions. *The Journal of Physical Chemistry A* **116**, 9545-9560 (2012).

66 Shannon, R. J. *Experimental and computational studies of hydroxyl radical kinetics at very low temperatures* PhD thesis, University of Leeds, (2012).

67 Bell, R. P. *The Tunnel Effect in Chemistry*. (Chapman and Hall, 1980).

68 Marcus, R. & Coltrin, M. E. A new tunneling path for reactions such as $H+H_2 \rightarrow H_2+H$. *The Journal of Chemical Physics* **67**, 2609-2613 (1977).

69 Skodje, R. T., Truhlar, D. G. & Garrett, B. C. A general small-curvature approximation for transition-state-theory transmission coefficients. *The Journal of Physical Chemistry* **85**, 3019-3023 (1981).

70 Fernández-Ramos, A., Truhlar, D. G., Corchado, J. C. & Espinosa-García, J. Interpolated Algorithm for Large-Curvature Tunneling Calculations of Transmission Coefficients for Variational Transition State Theory Calculations of Reaction Rates. *The Journal of Physical Chemistry A* **106**, 4957-4960 (2002).

71 Miller, W. H. Tunneling corrections to unimolecular rate constants, with application to formaldehyde. *Journal of the American Chemical Society* **101**, 6810-6814 (1979).

72 Golden, D. M. *et al.* OH(OD) + CO: Measurements and an Optimized RRKM Fit. *The Journal of Physical Chemistry A* **102**, 8598-8606 (1998).

73 Senosiain, J. P., Klippenstein, S. J. & Miller, J. A. The Reaction of Acetylene with Hydroxyl Radicals. *The Journal of Physical Chemistry A* **109**, 6045-6055 (2005).

74 Sabbah, H. *et al.* Understanding Reactivity at Very Low Temperatures: The Reactions of Oxygen Atoms with Alkenes. *Science* **317**, 102-105 (2007).

Chapter 2. Experimental methods

2.1 Measuring rate coefficients at low temperatures

2.1.1 Cryogenic cooling

Cryogenic cooling is a widely used method for low temperature kinetic studies. A specially designed cell or flowtube is utilised, whereby the cooling agent is circulated in a chamber surrounding the reaction cell. The bath gas is cooled by collisions with the wall between the chamber containing the cooling agent and the reaction cell and subsequently, the reagents themselves are cooled through collisions with the bath gas. A wide range of temperatures can be reached with this method, and temperatures as low as 212 and 195 K are routinely achieved using chloroform/dry ice and acetone/dry ice, respectively.[1,2] Below this temperature, condensation of the gaseous reagents onto the cooled reaction cell walls becomes problematic, leading to a large uncertainty in the concentration of reactant remaining in the gas phase. However, wall losses can be accounted for through careful characterisations and modelling, as long as they are not a dominant loss for the reagent.

2.1.2 Free jet expansions

Free jet expansions are produced by the pinhole expansion of high-pressure gas, and if a molecular beam is desired, the jet is subsequently collimated using skimmers. For kinetic studies relevant to interstellar chemistry, free jet expansions provide the distinct advantage over cryogenic cooling in that considerably lower temperatures can be attained (1 K).[3] However, free jet expansions are subject to significant temperature and density gradients along the axis of the jet. Whilst kinetic studies are not impossible to perform, to obtain an overall rate coefficient, careful and complex data analysis must be undertaken. This difficult task was undertaken by Mazley and Smith, who derived a model based on the thermal conduction model of Beijerinck and Vester to obtain rate coefficients for ion-molecule reactions from their free-jet expansion studies.[4,5] Additionally, the rate coefficient for the electronic quenching of OH $A^2\Sigma^+(v'=0)$ by air was measured at 26 ± 4 K in a free jet expansion by Creasey *et al.*, who used a combination of detailed laser induced fluorescence spectroscopy measurements and computational fluid dynamics calculations to elucidate the temperature and density profile of the jet.[6]

2.1.3 The Laval nozzle apparatus

The Laval nozzle apparatus enables the study of low temperature gas phase reactions in thermally equilibrated conditions without the risk of wall effects, and was first developed by Rowe and Marquette in 1984 for the study of ion-molecule reactions.[7] The technique, which employs the isentropic expansion of gas, was later adapted by Sims *et al.* to enable kinetic studies of neutral species.[8] The experiment is also known as CRESU (Cinétique de Réactions en Ecoulement Supersonique Uniforme), a French acronym which translates as reaction kinetics in a uniform supersonic expansion.

A high density flow of gas is expanded through a convergent-divergent shape nozzle, as shown in Figure 2. 1 forming a low temperature collimated jet upon entry into a reaction chamber where kinetics measurements can be recorded.

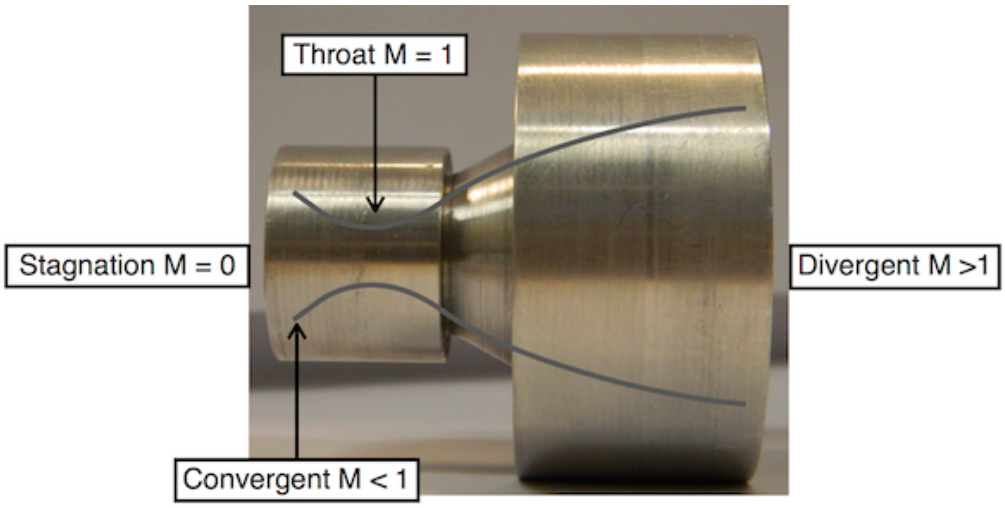

Figure 2. 1: Annotated photograph of a Laval nozzle which yields a jet of T~ 146 K and is used in the University of Leeds pulsed Laval nozzle apparatus. The grey line signifies the internal shape of the Laval nozzle. The flow of the gas is from left to right.

The profile of a Laval nozzle utilised in this work is also illustrated in Figure 2. 1 and the regions within and prior to the Laval nozzle are labelled. The flow in the convergent region has a Mach number (defined in E2.1) of less than 1 and hence is subsonic. As the gas is compressed into the throat section, the Mach number increases to 1 and the velocity of the flow increases to sonic levels. In the divergent region the gas accelerates further upon expansion, its Mach number increases to above 1 and the velocity becomes supersonic in the laboratory frame of reference (although it should be noted that the molecules within the jet are moving slowly with respect to one another). The temperature, pressure and density of the flow decrease in

relation to that in the convergent region. The shape of the divergent section is specifically designed to give cylindrically symmetric expansion and to remove waves caused by this expansion that would otherwise perturb the flow. High densities in the jet (on the order of 10^{16} - 10^{17} molecule cm^{-3}) ensure that the gas is thermally equilibrated and of a uniform density and velocity distribution.[7]

The cooling of the gas in the divergent region of the nozzle is a result of the Joule-Kelvin effect where the thermal component of the internal energy is reduced upon expansion and as a result the gas is cooled. The cooling of the gas upon expansion can also be thought of in terms of the ideal gas law, whereby the temperature is proportional to the pressure. Given that upon expansion the pressure is reduced, the temperature must do so also. The temperature of the expanded gas flow is related to its post-expansion temperature via a property called the Mach number, *M*, a dimensionless number which is defined in E2.1

$$M = v/a \qquad \text{E2.1}$$

where *v* is the velocity of the gas and *a* is the local speed of sound of the medium in which the gas is travelling. The local speed of sound is related to the temperature by E2.2

$$a = (\gamma RT)^{\frac{1}{2}} \qquad \text{E2.2}$$

where *R* is the gas constant, *T* is the temperature in Kelvin and γ is the ratio of the heat capacities of the bath gas (in these experiments, N_2 or Ar) and is a measure of how a molecule can distribute energy amongst its rotational, translational and vibrational degrees of freedom (E2.3). C_p is the heat capacity at a constant pressure and C_v is the heat capacity at constant volume.

$$\gamma = \frac{C_p}{C_v} \qquad \text{E2.3}$$

$$C_v = (a + b)\frac{R}{2} \qquad \text{E2.4}$$

where *a* is the number of translational degrees of freedom (3), and *b* is the number of rotational degrees of freedom (2 for a linear molecule and 0 for a monoatomic).

$$C_p = C_v + R \qquad \text{E2.5}$$

For a diatomic molecule such as N_2, C_v = (5R/2) and from E2.5 a value of (7R/2) is obtained for C_p and therefore γ = 7/5. For a monoatomic species such as Ar, C_v = (3R/2) and so C_p is (5R/2), hence γ = 5/3. The ratio of the

heat capacities, γ, is inversely proportional to the temperature of the gas (E2.2), so as the ratio of the heat capacities increases, the temperature of the flow will decrease for a given value of the local speed of sound. For this reason, it is important that the temperature of the jet for a given nozzle must be ascertained using only one gas (so the γ value, and therefore the temperature is straightforward to calculate) and that this must be the predominant gas in experiments where these conditions will be used.[9] To minimise the chance of perturbing the jet by affecting the overall γ value, the other gases used in these experiments make up less than ~ 2% of the total flow density, which is a conservative value chosen based on the work of Atkinson and Smith.[10] The relative pressures of the expanded gas flow (impact) and reservoir (stagnation) regions are linked with the Mach number by the Rayleigh equation E2.6

$$\frac{P}{P_0} = \left[\frac{(\gamma+1)M^2}{(\gamma-1)M^2+2}\right]^{\left(\frac{\gamma}{\gamma-1}\right)} \left(\frac{\gamma+1}{2\gamma M^2-\gamma+1}\right)^{\left(\frac{1}{\gamma-1}\right)} \qquad \text{E2.6}$$

where P is the expanded gas flow pressure and P_0 is the stagnation pressure.

Each Laval nozzle is designed to give an expanded flow with a specific Mach number and therefore a specific temperature. Although many stable jets with various densities (of the same temperature) can often be yielded from one nozzle, many nozzles need to be designed and characterised to study the temperature dependence of the rate coefficient for a reaction. The temperature and density of the jet produced from gas expansion are characterised utilising the Rayleigh equation and a method known as impact pressure measurements. The experimental procedure for this is described in section 2.3.2.

The advent of the Laval nozzle apparatus has facilitated low temperature kinetic studies for a number of reaction types, including ion-molecule, radical-radical, barrierless association and neutral bimolecular reactions.[9,11-24] The breadth of temperatures attainable using the Laval technique is now significant, with the lowest temperature reached thus far being 7 K where cryogenic pre-cooling of the gas mixture (He bath gas) by liquid nitrogen was utilised.[25] There have been a number of experimental developments, perhaps the most impactful being the development of a pulsed apparatus.[26] The pioneering CRESU experiments at the University of Rennes, require a large throughput of reactant and bath gases through the Laval nozzle to create a continuous jet. Consequently, the pumping requirements are also

significant which is both restrictive financially and in terms of laboratory space. In 1995 Atkinson and Smith developed a pulsed CRESU experiment, whereby the gas is expanded through the Laval nozzle in 6-20 ms pulses using two pulsed solenoid valves.[10,27]. Recently, a new pulsed CRESU experiment has been developed by the Jiménez group at the University of Castilla-La Mancha whereby a spinning disk is utilised instead of pulsed valves. In addition to the University of Castilla-La Mancha apparatus, there are a number of pulsed CRESU experiments in operation around the world including at the University of Gottingen (Abel group), Lawrence Berkeley National Laboratory (LBNL, Leone and Wilson groups), the University of Rennes (Canosa group) and the University of Leeds (Heard group). The latter is utilised in this work and will be described in detail later in the chapter. There is also a mini-continuous CRESU experiment at the University of Bordeaux (Hickson and Bergeat groups) which has reported rate coefficients down to 50 K and has the advantage of lower gas usage of the pulsed instruments without the necessity for pulsed valves.[28,29]

2.2 Detection methods for the measurement of rate coefficients

Having established some methods for reaching low temperatures, focus will now turn to some experimental techniques which can be employed for the measurement of reaction rate coefficients. As this work primarily concerns the kinetics of radical-neutral reactions whereby the reaction is initiated using flash photolysis, this method will be outlined. Following this, some detection methods which can be coupled to flash photolysis will be covered, including laser induced fluorescence spectroscopy which has been utilised in this work.

The study of reaction kinetics presents the experimental challenge of allowing the reactants to mix sufficiently prior to recording kinetic measurements.[30] The development of the flash photolysis technique by Norrish and Porter in 1949, which exploited the recent advent of the flash lamp devised for photography, presented a phenomenal advantage over previous methods in that it eradicated the necessity for a mixing period prior to measurements.[31] For the reactions of transient species, such as atoms, radicals and excited states, a precursor to the transient species and the co-reactant were pre-mixed in the reaction cell before the reaction was initiated by photolysis using a flash lamp. The flash lamp provided a uniform light source, creating a homogenous mixture of the transient and co-reactant species in the reaction cell, so that kinetic measurements could be recorded

immediately following photolysis. This development, which made Norrish and Porter Nobel Laureates in 1967, has since been furthered following the introduction of the excimer laser as a photolysis light source. Using a laser to initiate the chemical reaction provides several advantages over flash lamps: they can be operated with high pulse repetition rates, short pulse durations and high energies, and they have a narrow line width and a defined spatial profile.[30] Flash photolysis is now a very widely used technique for both kinetics and dynamics studies. In this work this method (otherwise known as pulsed laser photolysis, PLP) has been employed using an excimer laser.

2.2.1 Laser induced fluorescence spectroscopy

Laser induced fluorescence (LIF) spectroscopy is a powerful and highly sensitive technique which is routinely employed for kinetic studies of reaction of radicals and atoms, as well as for atmospheric measurements. This method utilises the specific energy gaps between ground and excited rovibronic energy levels of a species to selectively detect different chemical species using a frequency matched laser light source. Following excitation, the species emits a photon via fluorescence with a frequency which is either the same as (on-resonance) or red-shifted (off-resonance) with respect to the excitation wavelength. The fluorescence scheme commonly utilised for laboratory based LIF detection of hydroxyl radicals is illustrated in Figure 2. 2.

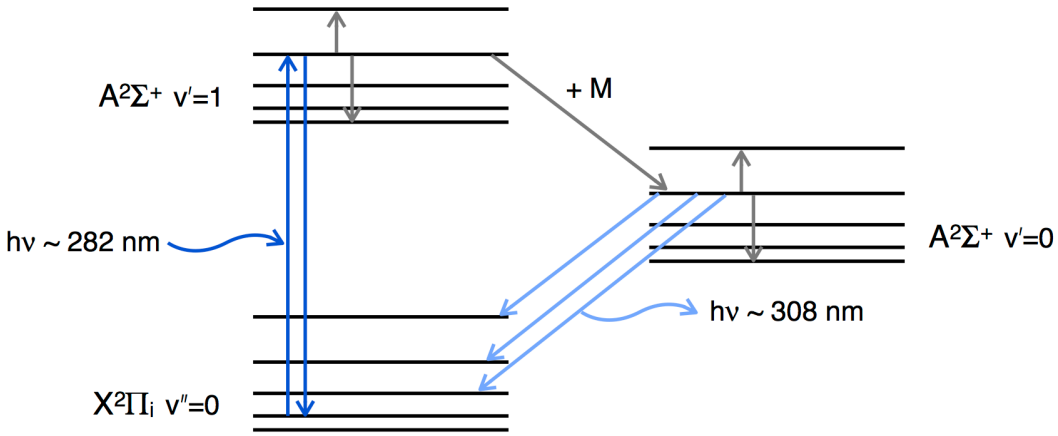

Figure 2. 2: The OH $A^2\Sigma^+(v'=1) \leftarrow X^2\Pi_{3/2}(v''=0)$ laser induced fluorescence scheme commonly utilised for the laboratory detection of OH radicals, including in this work. The grey lines represent collisional energy transfer to different rovibronic levels, the dark blue upward arrow represents the laser excitation wavelength utilised to excite OH to its first electronically excited state and M represents the bath gas. Some on resonance fluorescence can occur (dark blue downward arrow). The light blue arrow represents the red shifted (off resonance) fluorescence following collisional transfer to the v'=0 level. For clarity only one transition is shown for each fluorescence step.

The emitted photons can be detected by a photomultiplier tube positioned orthogonally to the photolysis and excitation laser beams to minimise detection of scattered laser light. The fluorescence wavelength can be selected prior to being imaged by the detector either using a monochromator or a suitable interference filter. The main requirement for detection of a given species by LIF is that the electronically excited state must be bound (i.e. non-dissociative). For sensitive detection, the species should have a reasonable absorption coefficient and the excited state should have a good quantum yield for fluorescence. The major advantage of LIF spectroscopy is that it is a “zero” background technique in the absence of scattered light. In other words, it is analogous to detecting a candle being lit outdoors at night. To obtain a rate coefficient using PLP-LIF, the temporal profile of a given species must be constructed by monitoring the fluorescence signal as a function of the time delay between the photolysis and probe lasers. It should be noted that LIF is a relative method and absolute concentrations cannot be retrieved, unless a prior calibration has been carried out.

LIF spectroscopy has been employed in this work for the detection of both reactant and product species: the hydroxyl radical (Chapters 3,4,5 and 7), the amidogen radical (Chapter 5), the methoxy radical (Chapter 6), the ethoxy radical (Chapter 6) and formaldehyde (Chapter 6). The selectivity of LIF spectroscopy to specific rovibronic transitions means that it can also be utilised to obtain rotationally resolved spectra (section 2.3.3) and probe specific vibrational states of radicals (Chapter 7), subject to adequately narrow spectral line width of the laser.

2.2.2 Absorption techniques

Whilst LIF spectroscopy is a relative method, absorption spectroscopy is able to retrieve direct concentrations of species if the wavelength dependent absorption cross section (σ_λ) and the path length of the reaction cell (l) are known, using the Beer Lambert law (E2.7) where I is the intensity after absorption, I_0 is the initial intensity prior to reaction initiation (and hence absorption) by the photolysis laser.

$$I = I_0 \exp\left(-\sigma_\lambda c l\right) \qquad \text{E2.7}$$

A broadband light source, for example a xenon arc lamp, can be used to irradiate the reaction cell, and a detector (fitted with a filter or monochromator) placed at the opposite end is used to measure the absorption intensity. An entire kinetic trace can be obtained from a single photolysis laser shot, however signal averaging is usually required to

optimise the signal-to-noise ratio. Absorption methods typically have poorer sensitivity compared to LIF spectroscopy. For low concentrations and typical values of l and σ_λ, the value of I/I_0 can be very close to the value of I. Furthermore, it can be difficult to accurately determine the path length, l. Therefore, the ability to detect a small change to a relatively large signal is required – an analogy is perhaps being able to notice a candle being extinguished in broad daylight. Higher sensitivity can be achieved by increasing the path length, l, of the reaction cell by multi-passing the light source through the chamber using highly reflective mirrors. Absorption methods often suffer from poorer selectivity compared to LIF spectroscopy as more than one reactant or product species may absorb at a given wavelength. This can be overcome by using a tuneable laser light source with a narrow line width. Alternatively, multiplexed detection can be employed to distinguish between chemical species, such as the instruments recently developed by Sheps and by Lewis *et al.,* whereby a spectrograph coupled with a detector such as a CCD camera can be utilised to monitor all wavelengths output by a broadband light source as a function of reaction time.[32-34] Thus both the absorption spectrum as well as the kinetic profile can be obtained.

2.2.3 Mass spectrometry

Mass spectrometry is a powerful and universal detection method, which is particularly beneficial for the detection of reaction products and in order to determine branching ratios. However, it is difficult to implement mass spectrometry detection for high pressure reaction systems. Gas sampled from a reaction cell by a pinhole is ionized by an electron or vacuum ultraviolet (VUV) beam prior to detection by a mass spectrometer based on the mass-to-charge (m/z) ratio. Photoionization, as opposed to electron impact, leads to less fragmentation upon ionization and therefore is usually the preferred method for chemical kinetics. The ability to detect a chemical species by mass spectrometry is dependent on the Franck-Condon overlap between the neutral and ionized states and attaining the photoionization energy threshold for the species of interest.

Pioneering work by Osborn and Taatjes (Sandia National Laboratories) on the development of a multiplexed photoionization mass spectrometer coupled to a slow flow quartz reactor and interfaced with VUV synchrotron radiation from the Advanced Light Source (LBNL) has yielded the first direct detections of two highly important and elusive reaction intermediates – a

QOOH and a Criegee biradical.[33,35-38] Gas is sampled from the reactor by a pinhole orifice in the wall of the reactor and the tuneable VUV radiation of the synchrotron is used to ionise the resultant molecular beam. Mass spectra are constructed as a function of m/z ratio, kinetic time and photoionization energy. By obtaining the signal as a function of photoionization energy, discrimination between isomers is possible by comparison with *ab initio* calculations or by experimentally obtaining photoionization energy curves for chemical standards. This has facilitated the discrimination of, for example, the QOOH species from the RO_2 isomer.[33]

Coupling a mass spectrometer to a Laval nozzle apparatus presents a substantial challenge. The jet produced in the Laval expansion is at a pressure too high for direct sampling by a mass spectrometer so needs to be skimmed, however the skimming method must not perturb the stability of the jet. This challenge has been met by the Leone group. Soorkia *et al.* have constructed an airfoil to skim the Laval jet into a quadrupole mass spectrometer which is also interfaced with tuneable synchrotron ionization radiation from the Advanced Light Source (ALS), thus allowing isomer resolution of product species.[17] For example, in the study of the reaction of C_2H with propyne conducted by Bouwman *et al.* at 79 K, it was found the reaction primarily proceeded (85 %) to yield CH_3 + C_4H_4 products with a 15 % yield of the H + C_5H_6 channel.[39] The contributions of relative isomers for each channel were resolved using photoionization energy curves, and it was found that the C_4H_4 channel comprised only vinyl acetylene, whilst the C_5H_6 channel comprised 3 isomers and the contribution of each was resolved.[39]

2.3 The University of Leeds pulsed Laval nozzle apparatus

In the following section, the apparatus used for the kinetic studies reported in this thesis will be outlined and experimental details given. First, details of the reaction chamber and instrumentation are given. Secondly, the experimental procedures utilised for jet characterization are discussed and results presented. Thirdly, the experimental method used for measuring rate coefficients via pulsed laser photolysis-laser induced fluorescence is described.

2.3.1 The reaction chamber and instrumentation

The overall setup of the University of Leeds pulsed Laval nozzle apparatus is illustrated in Figure 2. 3. Details about the setup are given below.

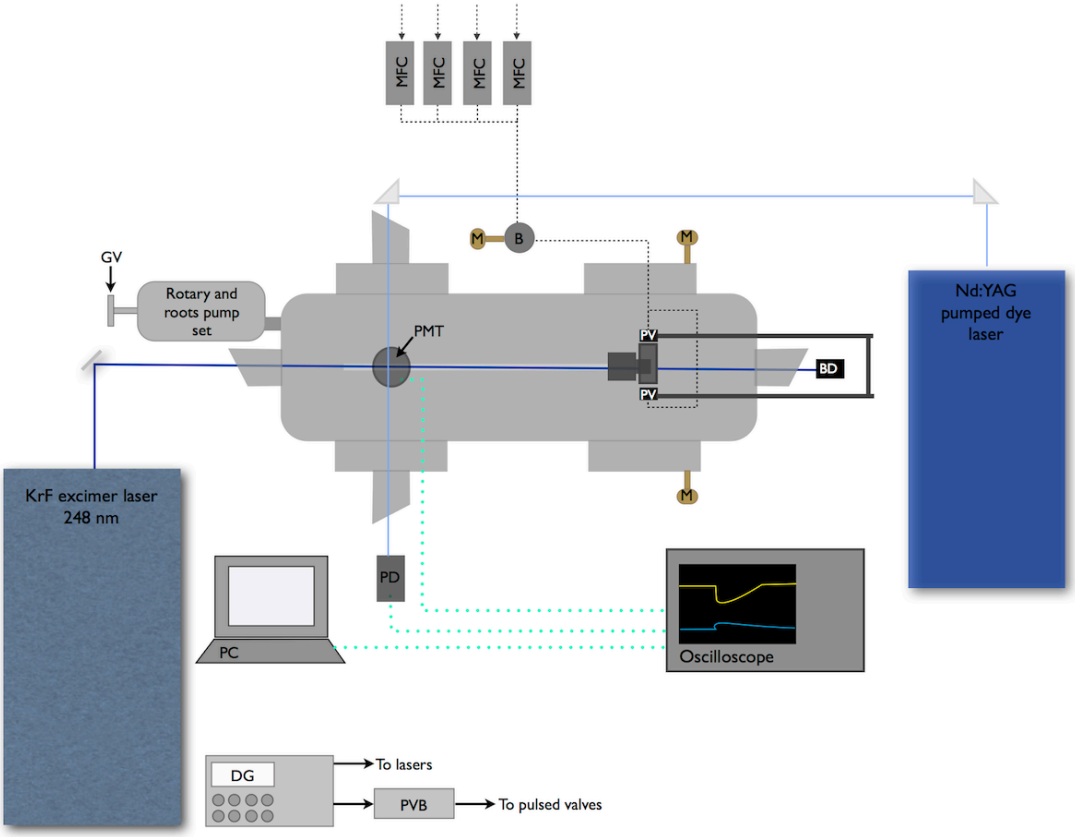

Figure 2. 3: Overall setup of the University of Leeds pulsed Laval nozzle apparatus. DG = delay generator, PVB = pulsed valve control box. GV= adapted gate valve. PC = personal computer. BD = beam dump. PMT = photomultiplier tube. PD = photodiode. PT = differential pressure transducers. PV = pulsed valve. M = manometer. B = ballast tank. MFC = mass flow controller.

The Laval nozzle is housed in a 774 mm cylindrical stainless steel chamber that has nine flanges for access. Four of the flanges have windows mounted at Brewster's angle for the entry and exit of laser beams. The chamber is evacuated using two pumps in series (Leybold D65B Rotary and Leybold RUVAC 251 Roots pumps) via the flange under the optics rail (Figure 2. 4) and PMT. The pumps can give a combined pumping capacity of 210 m^3 hr^{-1} and the chamber pressure is selected and maintained using a gate valve which has been adapted to allow selection of the chamber pressure to increments of 0.01 Torr (Leybold DN63150-F H). A second pump set, comprising an Edwards ED660 Rotary and an Edwards EH250 Roots pump in series, can be attached via an additional flange for attaining lower chamber pressures. An Edwards Speedivalve (SP16K N 9bar) connected to atmosphere is fitted to the chamber to allow it to be returned to atmospheric pressure when not in use. The chamber pressure is monitored by two capacitance manometers (Leybold Ceravac CTR 90 0-1000 Torr and Leybold Ceravac CTR 90 0-10 Torr).

The Laval nozzle is held in place by a yoke, which is mounted on two threaded rods and a third non-threaded rod. The longitudinal position of the nozzle along the chamber can be adjusted by the movement of the yoke back and forth along these threaded rods. This is controlled by a stepper motor (McLennan) which allows movement to a 0.01 cm level of accuracy and a maximum distance of 25.00 cm. The position of the yoke, and hence that of the nozzle, is moveable to achieve the most stable conditions to produce a supersonic expansion. This will be further discussed in section 2.3.2. The movement of the stepper motor is controlled by a custom LabVIEW virtual instrument (VI) written by Dr Andrew Goddard (formerly of the University of Leeds).

A gas manifold used for preparing cylinders (see section 2.3.4) and also as a vacuum reference source for impact pressure measurements (see section 2.3.2) is served by a vacuum pump (Edwards RUCAC Roots pump) and two pressure gauges (MKS Baratron pressure transducers , 0-1000 Torr and 100 PSI). Gas is delivered to the Laval nozzle via a set of mass flow controllers (MKS Instruments Mass-Flo® Controller, MFC) which enable maximum flow rates of 0.5, 2, 5 and 20 SLM (standard litre per minute). The mass flow controllers are calibrated regularly using a Drycal DC-Lite primary flow meter. For the reactions of OH where $(CH_3)_3COOH$ (*t*-BuOOH) was utilised as the photolytic precursor, a glass bubbler has been used to deliver the vapour pressure (23 Torr at 293 K) to the relevant mass flow controller. The reactant and bath gases are premixed the stainless steel delivery line and in a 2 L stainless steel ballast tank before being delivered to the 1 cm^3 pre-expansion reservoir of the Laval nozzle. The pressure in the ballast tank is monitored by a manometer (MKS 0-5000 Torr). The inlet of gas from the ballast tank through the nozzle is controlled by two pulsed solenoid valves (Parker series 9). The frequency and duration of the pulses are controlled by a delay generator (Berkeley Nucleonics Corporation (BNC) box, pulse/delay generator, model 555) and an in-house built pulse control box. The pressure of the pre-expansion region prior to the nozzle is monitored by a piezo-resistive pressure transducer (Omega, PX170 DE 28 Inch H_2O).

The kinetic data were obtained by PLP-LIF spectroscopy, the procedure for which will be discussed further in section 2.2. A KrF 248 nm excimer laser is utilised for the photolysis of the radical precursor. A Lambda Physik LPX 200 laser operating at a pulse repetition frequency of 5 Hz , and with an energy of 60-340 mJ per pulse, was aligned along the axis of the jet, through the centre of the reaction chamber and Laval nozzle. A HeNe laser aligned

through the centre of the reservoir and chamber was used to aid the alignment of the excimer laser. The excimer laser beam was reduced to a diameter of 1 cm to match the diameter of the Laval nozzle exit.

A 532 nm Nd:YAG laser (Litron LPY664-10) was aligned into a dye laser (Sirah Gmbh Cobra stretch) using a periscope optics setup. The output of the Nd:YAG pumped dye laser was frequency doubled using a KDP (KH_2PO_4) crystal and compensator, and the resultant UV laser light was separated from the non-doubled light via four quartz Pelin-Broca prisms aligned in a self compensating configuration. The UV light was aligned into the reaction chamber perpendicularly to the excimer beam, and the beam diameter was reduced to 0.6 cm to optimise the signal-to-noise ratio and reduced scattered light. The optics utilised for the collection of fluorescence are mounted on two rails perpendicular to the length of the chamber. Two lenses and a back reflecting mirror are used to focus the fluorescence onto the photomultiplier tube (Thorn EMI 9813QB), as illustrated in Figure 2. 4.

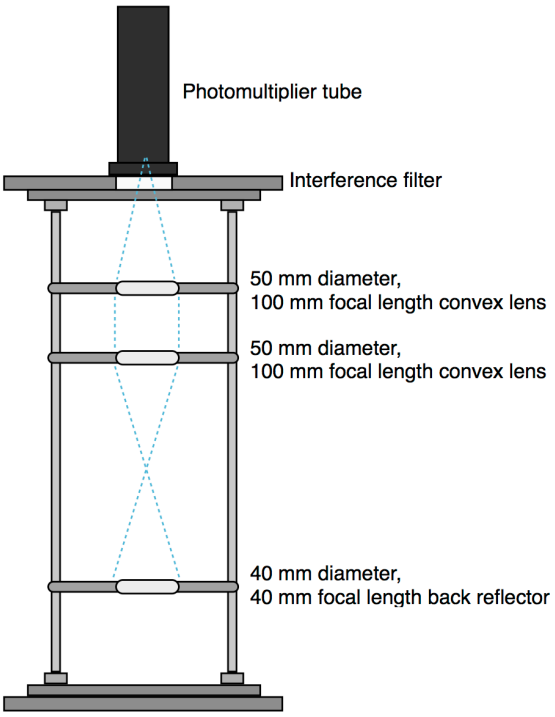

Figure 2. 4: Optics setup utilised in the Leeds pulsed Laval nozzle apparatus to focus the fluorescence onto the photomultiplier tube. The blue dotted lines indicate the focussing action of the optics. The cooled jet from the Laval nozzle is travelling into the page with respect to the optical setup. For impact pressure measurements, a piezo-resistive pressure transducer on a custom designed mount is attached to the rails in alignment with the centre of the Laval nozzle.

2.3.2 Jet characterisation via impact pressure measurements

For the pulsed Laval nozzle apparatus to be utilised for low temperature kinetic studies, pressure and temperature fluctuations along the flow must be minimised for the maximum length possible. The distance of the nozzle from the rail bearing the optics used for fluorescence collection can be controlled using a stepper motor (McLennan) which allows movements to a 0.01 cm level of accuracy and a maximum distance of the nozzle exit from the fluorescence collection region of 25.00 cm. The larger the distance between the nozzle exit and the optics, the longer the amount of time allowed for reaction to occur before fluorescence collection. The longer the length of the jet, the smaller the change in radical concentration and subsequently, the slower the rate coefficient which can be measured. For this reason it is desirable that conditions be found which give a long region of stable flow.

To establish optimum conditions for the flow of the nozzle to be stable with respect to temperature and pressure for the longest possible distance, a series of impact pressure measurements are taken. The ‘impact’ pressure of the flow at the fluorescence collection region is measured and from this, properties such as the temperature of the flow can be obtained using the equations described below.

To carry out impact pressure measurements, two piezo-resistive differential pressure transducers (Omega PX170-28BV) are positioned in the apparatus: one in the reservoir region of the Laval nozzle, which measures the stagnation pressure, and one is positioned on a mount on the rails amongst the optics where fluorescence collection occurs (as shown in Figure 2. 4) which measures the impact pressure of the flow. The impact pressure transducer is aligned to the centre of the Laval nozzle using a He-Ne laser which traverses the centre of the reaction chamber. The pressure transducers are also connected to vacuum to provide a reference pressure. The experimental setup is illustrated in Figure 2. 5.

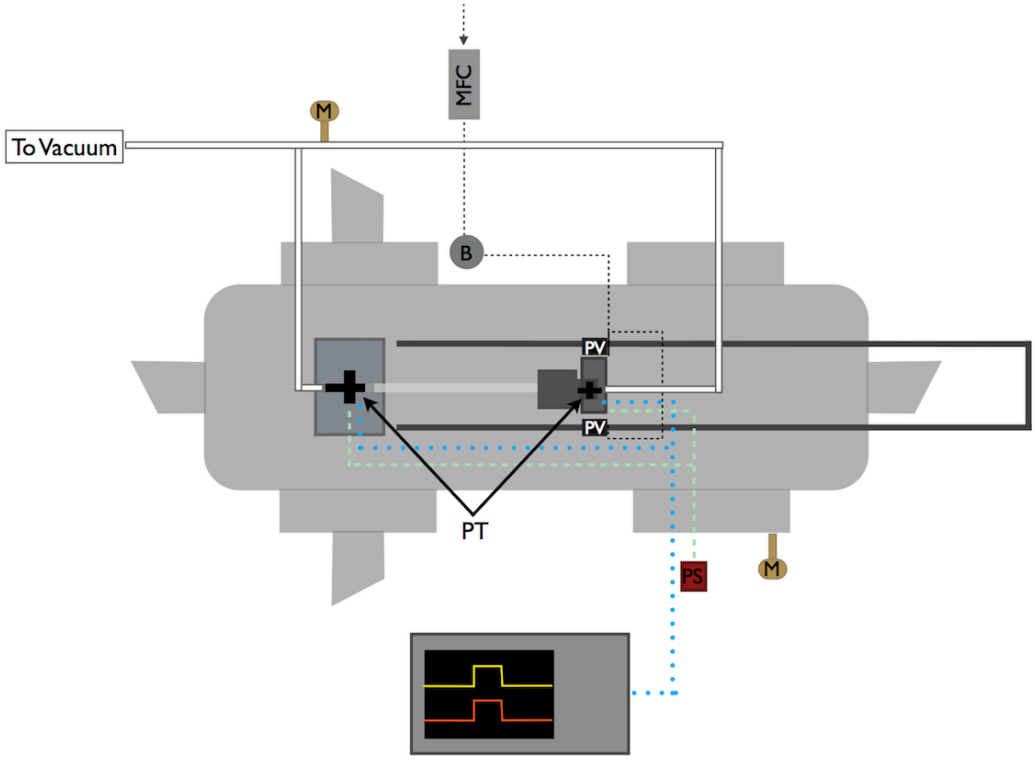

Figure 2. 5: Setup utilised for impact pressure measurements. PT = differential pressure transducers. PV = pulsed valve. PS = power supply to the pressure transducers. M = manometer. B = ballast tank. MFC = mass flow controller.

To ensure accuracy of the impact pressure measurements, both differential pressure transducers are calibrated to their full pressure range. This is done by assessing the response of the pressure transducers to increasing pressure by slowly opening the chamber to atmospheric pressure using an Edwards Speedivalve (SP16K N 9bar). Two capacitance manometers, Leybold Ceravac CTR, 0-10 Torr and 0-1000 Torr, are used to monitor the pressure of the vacuum and the chamber respectively during the calibration. The vacuum acts as a reference pressure for the differential pressure transducers. A calibration factor for each pressure transducer is obtained, and is subsequently incorporated in to the custom LabVIEW VI (written by Dr Andrew Goddard, formerly of the University of Leeds) in which the impact pressure data is collected.

For each set of impact pressure measurements, the position of the gate valve (which controls how open the chamber is to the pump set) and the gas flow rate are selected and the yoke bearing the nozzle is positioned immediately next to the optics used for fluorescence collection. The pulsed valves are set to a fire at a frequency of 5 Hz and the pulse duration is set to a fixed value between 8-20 ms so that the pulse profile does not exhibit significant pressure fluctuations . The mean pressure throughout the entire gas pulse is recorded both in the stagnation and impact regions with

readings averaged 50 times per point. Impact and stagnation pressures are recorded at a rate of 10 Hz, so pressure readings can be obtained for when the pulsed valves are open and closed to account for the non-instantaneous response of the pressure transducers to the increased chamber pressure. The averaged pressures at each yoke position measured by the stagnation and impact pressure transducers are recorded and analysed using a custom LabVIEW VI (Dr Andrew Goddard), where they are converted to the Mach number, *M*, by solving the Rayleigh equation for isentropic flows iteratively (E2.6).

$$\frac{P}{P_0} = \left[\frac{(\gamma+1)M^2}{(\gamma-1)M^2+2}\right]^{\left(\frac{\gamma}{\gamma-1}\right)} \left(\frac{\gamma+1}{2\gamma M^2-\gamma+1}\right)^{\left(\frac{1}{\gamma-1}\right)} \quad \text{E2.6}$$

The obtained Mach number is then used to obtain the jet temperature and density using E2.8 and E2.9 respectively.

$$\frac{T_0}{T} = 1 + \frac{(\gamma-1)}{2}M^2 \quad \text{E2.8}$$

$$\frac{\rho_0}{\rho} = \left(\frac{T_0}{T}\right)^{\left(\frac{1}{\gamma-1}\right)} \quad \text{E2.9}$$

where T_0 and T are the temperatures in the reservoir and jet respectively, γ is the ratio of heat capacities (defined in E2.3-E2.5), ρ_0 and ρ are the gas densities in the reservoir and jet, respectively, and M is the Mach number, as defined in E2.1.

This process is repeated as the yoke is moved further away from the fluorescence collection region at 0.2-1 cm intervals and a flow temperature versus distance plot is constructed. Measurements are taken at increasing distances until it is evident that the temperature and pressure in the flow is no longer uniform, which is characteristic of the jet losing stability. An example of a pressure and temperature profile of a stable jet obtained from impact pressure measurements is shown in Figure 2. 6.

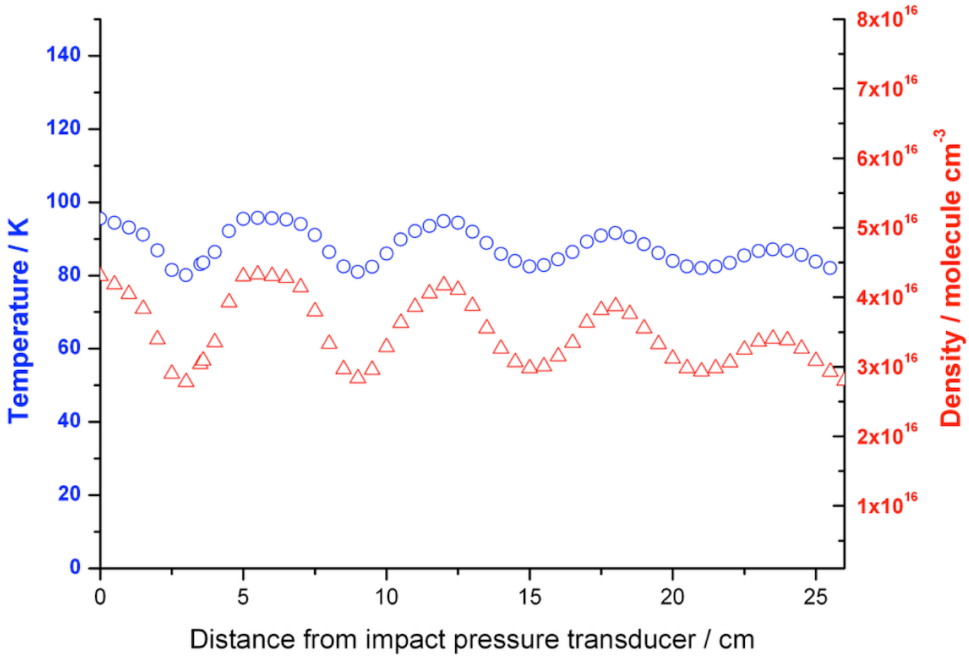

Figure 2. 6: Temperature profile (blue circles) and gas density profile (red triangles) as a function of distance of the nozzle from the impact pressure transducer obtained for a stable jet using N_2 bath gas. The resultant mean jet temperature, Mach number and density of the jet was found to be 88 ± 5 K, 3.49 ± 0.47 and (3.5 ± 0.5) × 10^{16} molecule cm^{-3}, respectively. The total stable jet length is 25.5 cm, corresponding to a kinetic time of ~ 337 μs.

Impact pressure measurements have been carried out using a range of total gas flow rates and chamber pressures to obtain jet profiles whereby the fluctuations in temperature along the flow are deemed small enough for the flow to be considered stable. Usually where the standard deviation in the temperature, density and Mach number is less than 10 %. In this work, a number of different stable flows have been identified from each nozzle used which yield the same jet temperature (within the error range) but different flow densities, and so this allows for the study of the pressure dependent kinetics of a reaction. The stable jets obtained in this work through impact pressure measurements and used for kinetic measurements are summarised in Table 2. 1. The temperature profiles of all the jets characterised and utilised in this work are shown in Appendix B.

Table 2. 1: Mean temperature, gas density and Mach number of the stable jets obtained and utilised in this work for kinetic studies. The jets were characterised via impact pressure measurements and the errors in the values are the standard deviation of the mean over the stable jet length. The chamber and ballast pressure at which the stable jets were obtained were measured by capacitance manometers.

T/K	Density / 10^{16} molecule cm^{-3}	Bath gas	Mach number	Stable jet length / cm	Chamber pressure / Torr	Total flow rate / sccm	Ballast pressure / Torr
56 ± 4	4.4 ± 0.5	Ar	3.62 ± 0.17	11.6	0.46	1250	646
54 ± 6	8.0 ± 1.4	Ar	3.7 ± 0.3	14.2	0.90	2426	1085
53 ± 9	15 ± 4	Ar	3.76 ± 0.35	12.0	1.82	4776	2213
88 ± 5	3.5 ± 0.5	N_2	3.49 ± 0.47	25.5	0.47	1156	612
90 ± 6	4.1 ± 0.6	N_2	3.39 ± 0.15	16.8	0.38	1738	1027
89 ± 3	6.5 ± 0.6	N_2	3.43 ± 0.09	20.0	0.81	2297	1067
86 ± 3	6.8 ± 0.6	N_2	3.51 ± 0.09	14.0	0.86	1600	698
88 ± 4	7.4 ±0.8	N_2	3.47 ± 0.10	17.6	0.77	3373	1912
91 ± 4	8.3 ± 0.9	N_2	3.37 ± 0.11	17.0	1.10	3060	1360
88 ± 8	9.4 ± 1.3	Ar	2.68 ± 0.17	3.7	2.25	1511	631
89 ± 4	11 ± 1	N_2	3.42 ± 0.11	16.0	1.13	5025	2721
88 ± 4	11 ± 1	N_2	3.46 ± 0.11	16.0	1.31	3822	1880
84 ± 4	12 ± 2	N_2	3.57 ± 0.12	15.0	1.42	3150	1289
82 ± 3	16 ± 2	N_2	3.65 ± 0.10	15.0	1.74	4694	1870
138 ± 9	8 ± 1	N_2	2.42 ± 0.15	4.6	2.25	1511	580
148 ± 15	10 ± 2	N_2	2.26 ± 0.07	5.0	2.90	1604	635
133 ± 10	13 ± 3	N_2	2.49 ± 0.17	3.5	3.64	3004	1051
144 ± 15	18 ± 2	N_2	2.32 ± 0.09	4.0	5.16	3149	1270
146 ± 15	26 ± 4	N_2	2.29 ± 0.12	4.0	7.36	4694	1880

The pulse profiles can also be recorded at different distances from the impact pressure transducer so that the most uniform section of the pulse can be sampled for kinetic measurements. The pulse profile for the stable jet shown in Figure 2. 6 as a function of distance is shown in Figure 2. 7. The region of the jet sampled for kinetic measurements is denoted in Figure 2. 8.

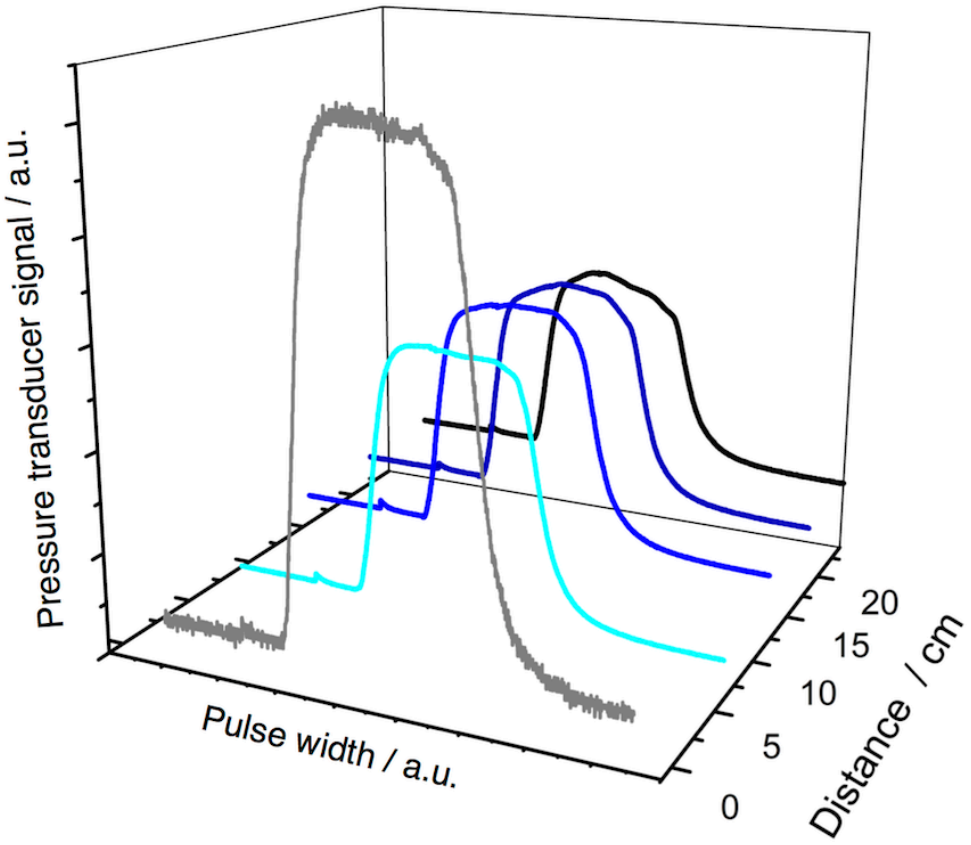

Figure 2. 7: Pulse profile of the jet presented in Figure 2. 6 as a function of distance from the impact pressure transducer : 0.0 cm (grey line), 6.0 cm (cyan line), 12.0 cm (blue line), 18.0 cm (dark blue line) and 24.0 cm (black line).

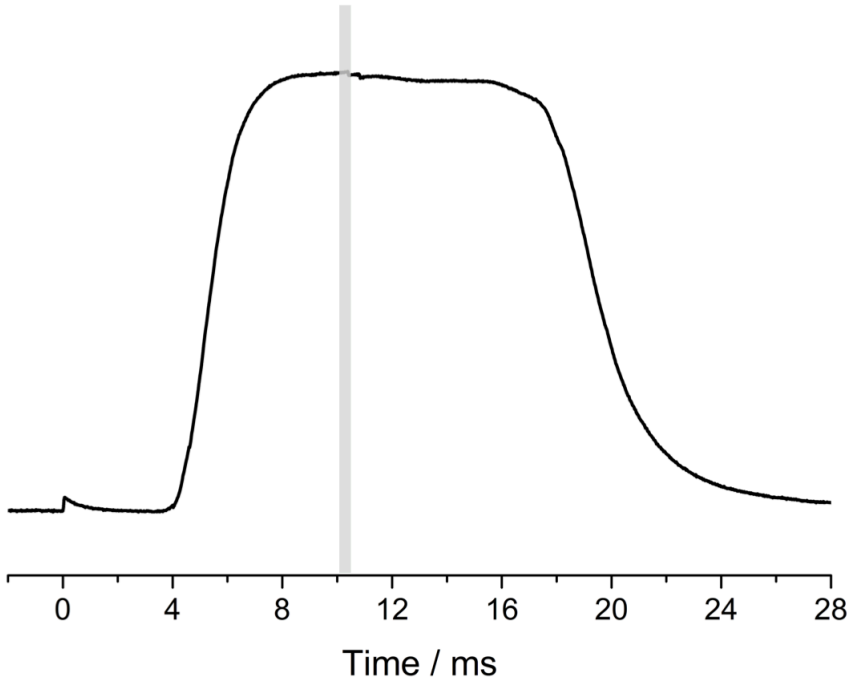

Figure 2. 8: Pulse profile at 6.0 cm showing the section of the jet sampled (~ 300 μs) for kinetic measurements (grey line).

2.3.3 Rotationally-resolved laser induced fluorescence spectroscopy for obtaining jet temperatures

The measurement of impact pressures is a widely used technique for assessing the stability of a jet and to enable the temperature, density and pulse profiles of a given jet to be obtained in just one experiment. However, LIF can be exploited to act as an independent method of obtaining the temperature of the jet, by recording rotationally-resolved laser induced fluorescence spectra of the hydroxyl radical and other species. The probe laser wavelength is scanned and the resultant off-resonance fluorescence signal recorded. The relative signal areas for each peak, which correspond to individual rotational transitions within a vibronic transition, can be related to the population of the rotational state using the Boltzmann distribution (E2.10), and from the relative populations of each rotational state, the temperature can be obtained.

$$\frac{N_{J''}}{N_0} = g_{J''} exp\left(-\frac{E_{J''}}{k_B T}\right) \qquad \text{E2.10}$$

where $N_{J''}$ is the population of the J[th] rotational level, N_0 is the population of the ground rotational level, $g_{J''}$ is the degeneracy of the energy level and is defined in E2.11, J'' is the rotational quantum number $E_{J''}$ is the energy of the J[th] level and is defined in E2.12 for a rigid rotor, k_B is the Boltzmann constant and T is the temperature in Kelvin.

$$g_{J''} = 2J + 1 \qquad \text{E2.11}$$

$$E_{J''} = hcBJ(J+1) \qquad \text{E2.12}$$

where *h* is Planck's constant and *c* is the speed of light. To assign the energy levels, and hence calculate their energies, the most relevant Hund's coupling case must be applied. Hund's coupling cases a and b are ways in which the sources of angular momentum (spin and orbital angular momentum and nuclear rotation) are coupled with one another. The most appropriate case for low temperature systems, where only low rotational levels are occupied, is Hund's case a, which is applied to all calculations in this work. [40]

The relative population of the J[th] level is proportional to the peak area, $S_{J''}$ (E2.13), for a given transition, which is obtained by analysis of the spectrum using Origin 7 software.

$$S_{J''} = CB_{J''}\phi_{J'}g_{J''}\exp\left(-\frac{E_{J''}}{k_B T}\right) \qquad \text{E2.13}$$

where *C* is a rotational state independent constant accounting for experimental parameters such as laser power, the solid angle of

fluorescence collection, the transmission of the interference filter and the PMT efficiency. $B_{J''}$ is the Einstein B coefficient for absorption for a given rotational level, the values of which are obtained from the spectral simulation software LIFBASE.[41] $\phi_{J'}$ is the quantum yield from a given excited vibronic level. A plot constructed from E2.14 yields a gradient containing the jet rotational temperature, *T*.

$$\ln\left(\frac{S_{J''}}{g_{J''}B_{J''}}\right) = \ln(C\phi_{J''}) - \left(E_{J''}\frac{1}{k_B T}\right) \qquad \text{E2.14}$$

y = c + *x* m

Rotationally resolved LIF spectra of OH have been performed in this study to verify the characterisations by impact pressure measurements. The experimental setup used for recording rotationally-resolved LIF spectra is illustrated in Figure 2. 9. The experimental procedure used for verifying the temperature of the stable jet shown in Figure 2. 6 is given and the results will be presented thereafter.

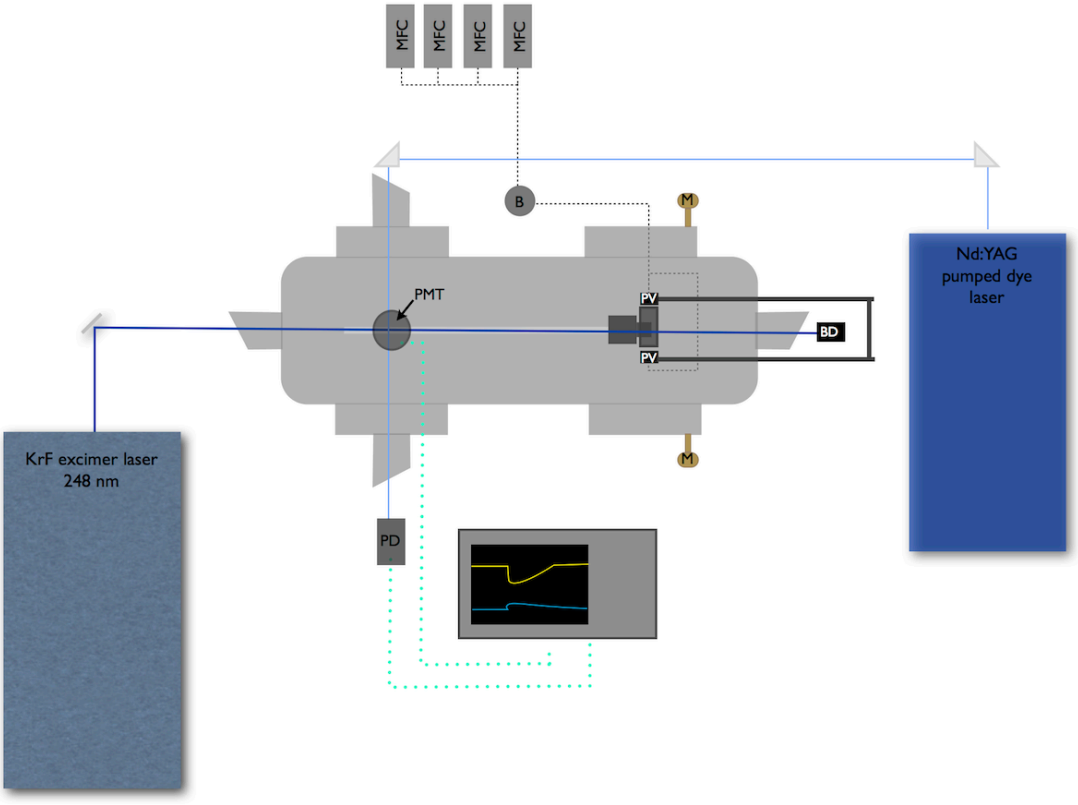

Figure 2. 9: Experimental setup utilised for recording rotationally resolved LIF spectra and for kinetic measurements. The excimer beam (dark blue line) is aligned collinearly with the jet axis and collected by a beam dump (BD).The probe laser beam (light blue line) is aligned perpendicular to the excimer and jet axis and the power is monitored by a photodiode (PD). Two capacitance manometers (M) are used to monitor the chamber pressure. PMT = photomultiplier tube. MFC = mass flow controller. PV = pulsed valve. B = ballast tank.

The nozzle was positioned at a given distance from the optics mount used for fluorescence collection and nitrogen bath gas (BOC, OFN) and the photolytic OH precursor $(CH_3)_3COOH$ (Aldrich 70 % wt. in H_2O) were expanded through the Laval nozzle via the pulsed valves operating at a frequency of 5 Hz. The total gas flow rate, pulse duration and the chamber pressure were set to values found to a stable jet via the impact pressure measurements. The OH precursor was photolysed at 248 nm using an excimer laser aligned collinearly with the jet to produce an approximately uniform OH density along the jet (corresponding the density profile from the impact pressure measurements). After a delay time of 55 μs, the probe laser, aligned orthogonally to the jet axis, was fired at a wavelength selected to be close to, or coincident with a rotational transition within the OH $A^2\Sigma^+(v'=1)\leftarrow X^2\Pi_{3/2}(v''=0)$ vibronic band. The delay time of 55 μs was selected to ensure that the OH which is produced rotationally hot from photolysis of the precursor had undergone sufficient collisions with the bath gas to ensure a Boltzmann distribution of rotational states were occupied. The off-resonant fluorescence is imaged and collected via a PMT fitted with a suitable interference filter (Barr associates Inc. 50 mm diameter, 3 mm thickness, λ_{max}=308.5 nm, 5 nm FWHM) using the optics setup shown in Figure 2. 4. The probe wavelength is scanned over a given range so that the fluorescence signal following excitation of several rovibronic transitions can be recorded. The probe laser wavelength is scanned at 0.0005 nm increments and for each point the signal obtained following excitation of each wavelength is averaged over two laser shots. The fluorescence signal collected via the PMT is imaged via an oscilloscope (LeCroy Waverunner) before being transferred to a PC for analysis. Instrument control and data acquisition is achieved using a custom LabVIEW VI constructed by Dr Andrew Goddard interfaced with a delay generator (Berkeley Nucleonics corporation) used to control the pulsed valves and the lasers.

Three rotationally resolved laser excitation spectra recorded when the nozzle was positioned at 5.0, 15.0 and 25.5 cm from the optics are presented in Figure 2. 10, Figure 2. 11 and Figure 2. 12, respectively alongside the corresponding Boltzmann plot for each spectrum constructed using E2.14 from the peak areas. The assigned rotational lines in each spectrum were used in the respective Boltzmann plots.

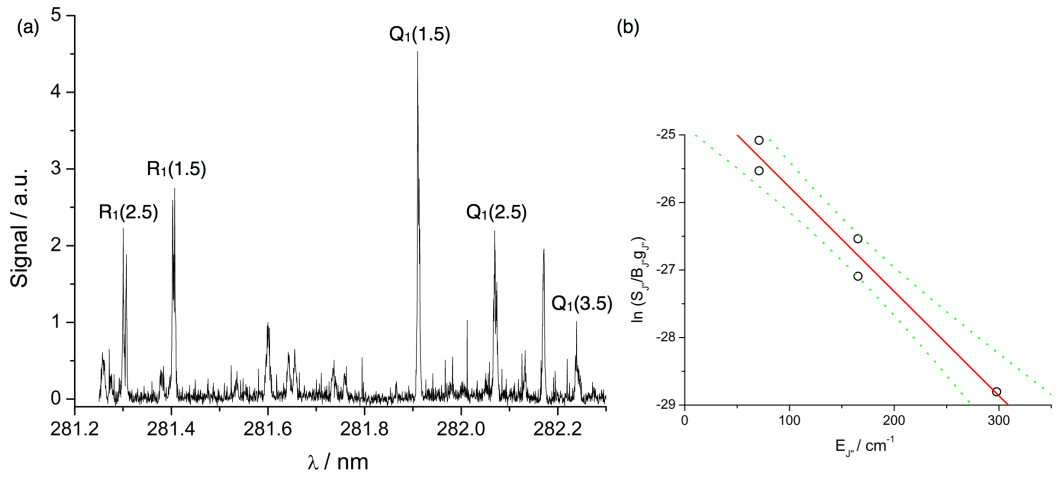

Figure 2. 10: (a)Rotationally resolved LIF excitation spectrum of the OH $A^2\Sigma^+(v'=1)\leftarrow X^2\Pi_{3/2}(v''=0)$ vibronic transition obtained for the jet presented in Figure 2. 6, obtained at a distance from the impact pressure transducer of 5.0 cm. (b) The corresponding Boltzmann plot constructed from the assigned transitions in figure (a), where the red line is the linear least squares best fit which gave 93 ± 22 K and the green dotted lines represent the 90 % confidence limits to the fit.

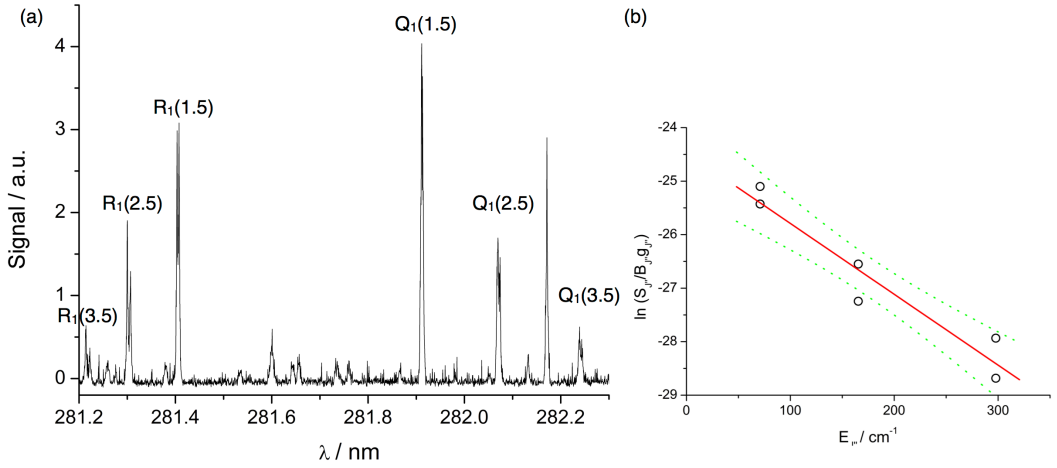

Figure 2. 11: (a)Rotationally resolved LIF excitation spectrum of the OH $A^2\Sigma^+(v'=1)\leftarrow X^2\Pi_{3/2}(v''=0)$ vibronic transition obtained for the jet presented in Figure 2. 6, obtained at a distance from the impact pressure transducer of 15.0 cm. (b) The corresponding Boltzmann plot constructed from the assigned transitions in figure (a), where the red line is the linear least squares best fit which gave T= 108 ± 33 K and the green dotted lines represent the 90 % confidence limits to the fit.

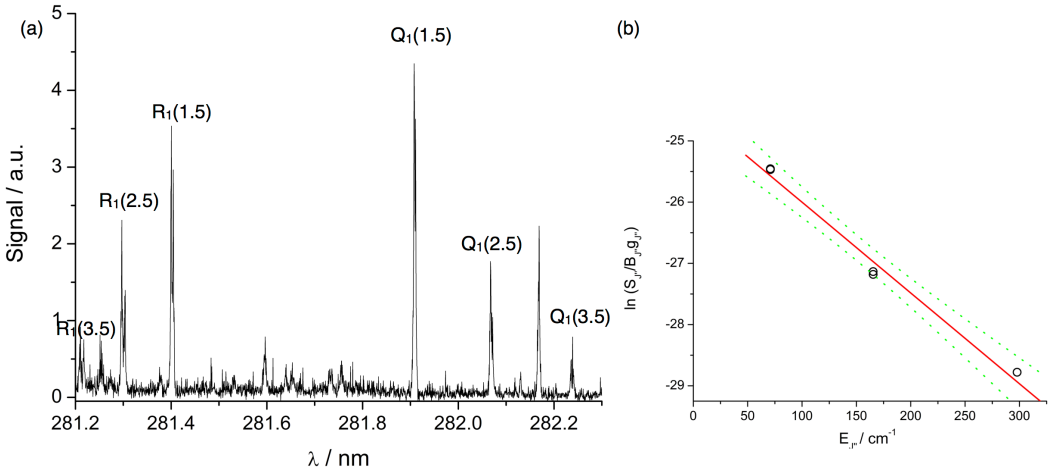

Figure 2. 12: (a) Rotationally resolved LIF excitation spectrum of the OH $A^2\Sigma^+(v'=1)\leftarrow X^2\Pi_{3/2}(v''=0)$ vibronic transition obtained for the jet presented in Figure 2. 6, obtained at a distance from the impact pressure transducer of 25.5 cm. (b) The corresponding Boltzmann plot constructed from the assigned transitions in figure (a), where the red line is the least squares best fit which gave T= 97 ± 16 K and the green dotted lines represent the 90 % confidence limits to the fit. Note that points are overlapping in the Boltzmann plot.

The 90 % confidence limits of the Boltzmann plot gradient were used to obtain the error in the jet temperature. The obtained temperature as a function of distance is plotted alongside the temperature profile obtained from impact pressure measurements in Figure 2. 13.

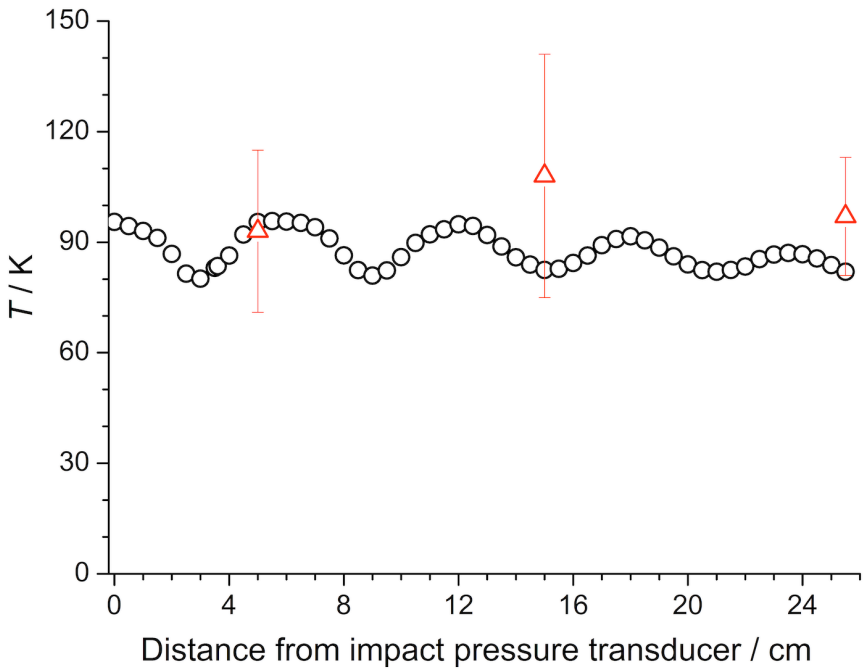

Figure 2. 13: Temperatures obtained from Boltzmann analysis of the rotationally resolved LIF spectra shown above (red triangles) where the errors are propagated from the 90 % confidence limits to the Boltzmann plot. These are plotted alongside the temperature profile obtained from impact pressure measurements (black circles), as previously presented in Figure 2. 6.

It can be seen from Figure 2. 13 that the temperatures obtained from rotationally revolved LIF spectroscopy of OH are in agreement within the error of the temperatures obtained by impact pressure measurements. However, the temperatures obtained via LIF spectroscopy have a significant error, which is due in part to the small number of rotational lines analysed to obtain the temperature. At low temperatures, only a small number of rotational levels are occupied and therefore fewer lines (corresponding to different rovibrational transitions) are present in the spectrum for analysis, which is exacerbated by the relatively large rotational constant for OH. Furthermore, this method is subject to a number of possible errors, a few of which are listed hereafter. Some of the lines in the spectra (such as those in the R_1 branch) overlap with other rovibronic transitions (such as the R_{21} branch) and so one has to distinguish where each peak ends and the other begins. The spectra quality also rely on the accuracy of the wavelength increments and signal averaging which is performed – if the wavelength steps are too large, then the fine structure of the spectra will not be obtained and this may cause errors in obtaining the signal area of each peak. The signal-to-noise ratio must be sufficiently high that the peaks can be distinguished from the background noise. Care must be taken to ensure that the transitions are not optically saturated so that the peak heights scale with probe laser energy.

The rotationally resolved LIF spectra obtain the rotational temperature of the jet, whereas the impact pressure measurements obtain the translational jet temperature – for valid kinetics studies the temperatures need to be the same and therefore, it is instructive to perform both types of characterisation. However, rotationally resolved LIF measurements are not used for the initial jet characterisation as it would be a comparatively time inefficient method.

2.3.4 PLP-LIF technique

Following the identification of stable jets through impact pressure measurements, the impact pressure transducer mount is removed from the chamber and the nozzle is positioned as far back from the optics as the jet remains stable so the longest possible kinetic time is accessed. Typical kinetic timescales obtained from stable jets in this work were between 100 and 400 μs.

As discussed previously, the jet must largely comprise the bath gas used to characterise the jets due to the heat capacity of the gas determining the jet

temperature (see section 2.1.3). In these experiments, the bath gas comprised a minimum of ~ 98 % of the jet density.

The pressure of an evacuated cylinder was recorded using two pressure gauges (MKS Baratron pressure transducers , 0-1000 Torr and 100 PSI) attached to a stainless steel gas manifold. The vapour pressure of the co-reactant of the radical was admitted into the evacuated cylinder and the resultant cylinder pressure recorded. The contents were then diluted with the bath gas and a final pressure reading was recorded. The contents of the cylinder allowed to mix overnight before use and the pressure readings used to calculate the co-reagent concentration in the cylinders.

For the reactions of OH radicals, the primary hydroxyl radical precursor used was $(CH_3)_3COOH$ (Aldrich, 70 % wt. in H_2O) which is a liquid at room temperature. The vapour pressure (23 Torr at 293 K) of the precursor was entrained into a flow of the bath gas using a glass bubbler prior to the mass flow controller. The radical precursor concentration was kept as low as possible to prevent side reactions and to maintain pseudo first order conditions. The radical precursor, co-reagent/bath gas mixture and the bath gas were flowed through a set of calibrated mass flow controllers into a stainless steel mixing manifold followed by a stainless steel 2 L ballast tank at the total flow rate found to yield a stable jet via the impact pressure measurement characterisations. The chamber pressure was adjusted to the optimum value using the adapted gate value.

A 248 nm excimer laser used for photolysis of the radical precursor was aligned along the axis of the Laval nozzle using a HeNe laser to aid alignment. The diameter of the excimer laser was reduced to 1 cm using an iris, so that the diameter matched that of the Laval nozzle exit. The frequency doubled output of an Nd:YAG pumped dye (probe) laser was aligned perpendicularly to the excimer laser and the power monitored via a photodiode positioned by the opposite Brewster's angle window. The dye laser beam was irised to a 0.6 cm diameter to minimise scatter. The probe laser wavelength was tuned to be coincident with a rovibronic transition of the relevant radical spectrum . For the OH $A^2\Sigma^+(v'=1)\leftarrow X^2\Pi_{3/2}(v''=0)$ band, the $Q_1(1.5)$ rotational line was used as this yielded the strongest fluorescence signal, as shown in, for example, Figure 2. 10(a).

Instrument control was achieved using a delay generator and a pulse valve control box interfaced to a custom build LabVIEW VI designed by Dr Andrew Goddard. The experiments were performed at a pulse repetition rate of 5 Hz. The lasers were arranged to fire near the middle of the jet pulse as

shown in Figure 2. 8 – only one photolysis and one probe laser shot is fired per jet pulse. The excimer laser was fired synchronously with the probe laser, defining time zero in the kinetic trace. The off-resonance fluorescence following excitation of the radical species was collected by a PMT aligned orthogonally to the laser beams and the jet via the optics setup shown in Figure 2. 4. A suitable interference filter was placed prior to the PMT to minimise detection of reflected laser light. The signal from the PMT and the photodiode were visualised on an oscilloscope (LeCroy Waverunner-2 DSO) and the signal integration window (typically 0.5-8 μs) to optimise data collection and minimise the effect of laser scatter. Data acquisition was accomplished using the LabVIEW VI. The time delay between the photolysis and probe lasers was increased at 1 μs increments to obtain the temporal profile of the radical, and each data point was averaged around 12-20 times. The signal acquired when the probe laser was fired prior to the photolysis laser was used to subtract the baseline of the traces.

The time evolution of OH (kinetic traces) were recorded at different co-reactant concentrations and each trace was individually analysed to obtain pseudo first order rate coefficients. For the majority of experiments performed in this thesis, the traces were fitted with either a single exponential decay function (E2.15) or an exponential growth-exponential loss function (E2.16), where the growth following the instantaneous production at t=0 is due to rotational relaxation of the photolytically produced radical into the laser probed level.

$$[OH]_t = [OH]_0 e^{-k_{obs}t} \qquad \text{E2.15}$$

$$[OH]_t = \left(\frac{k'_{rel}}{k_{obs}-k_{rel}}\right)[OH^*]_0(e^{-k'_{rel}t} - e^{-k_{obs}t}) + [OH]_0 e^{-k_{obs}t} \qquad \text{E2.16}$$

where OH* is the initially rotationally excited hydroxyl radical formed from its photolytic precursor, k'_{rel} is the pseudo first order rate coefficient for rotational relaxation of the rotationally excited OH into the laser probed level and k_{obs} is the observed pseudo first order rate coefficient (E2.17) for reaction with the reagent and k_{loss} is the pseudo first order rate coefficient for reaction with the precursor and diffusional loss out of the detection region.

$$k_{obs} = k_{bimolecular}[co-reagent] + k_{loss} \qquad \text{E2.17}$$

Further details about the fitting equations used are given in each results chapter and where relevant, the derivations are presented in Appendix C. An example fitted decay trace of OH in the presence of ethene, which was used as a test reaction, is shown in Figure 2. 14.

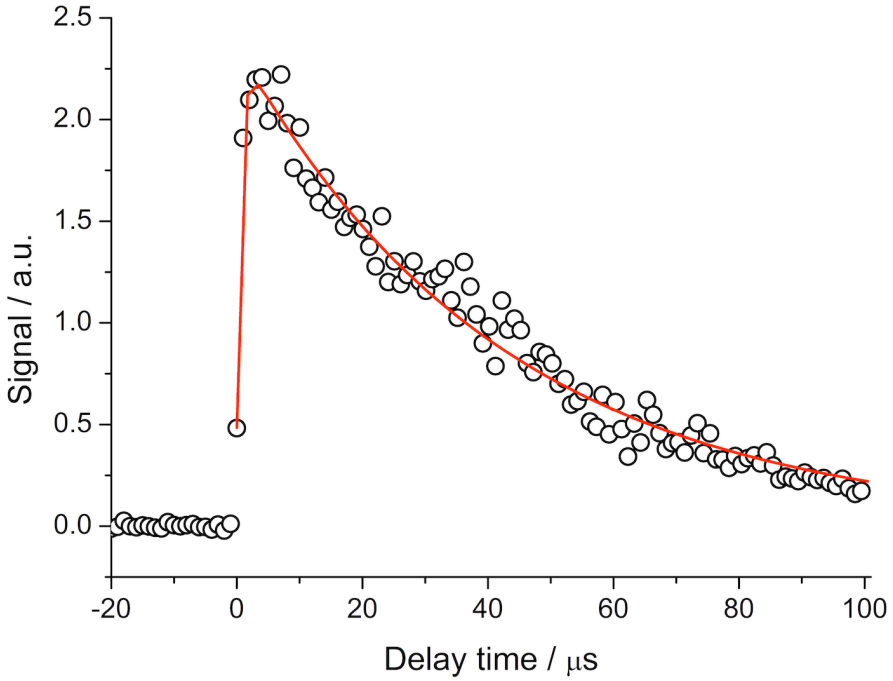

Figure 2. 14: LIF trace of OH recorded under pseudo first order conditions together with the non linear least squares fit of E2.16 to the data from the 248 nm photolysis of $(CH_3)_3COOH$ in the presence of ethene (1.0×10^{15} molecule cm^{-3}) at 144 ± 15 K and a total gas of (18 ± 2) × 10^{16} molecule cm^{-3} using N_2 bath gas. The least squares fit of E2.16 yields a pseudo first order rate coefficient of k_{obs} = 23623 ± 489 s^{-1}.

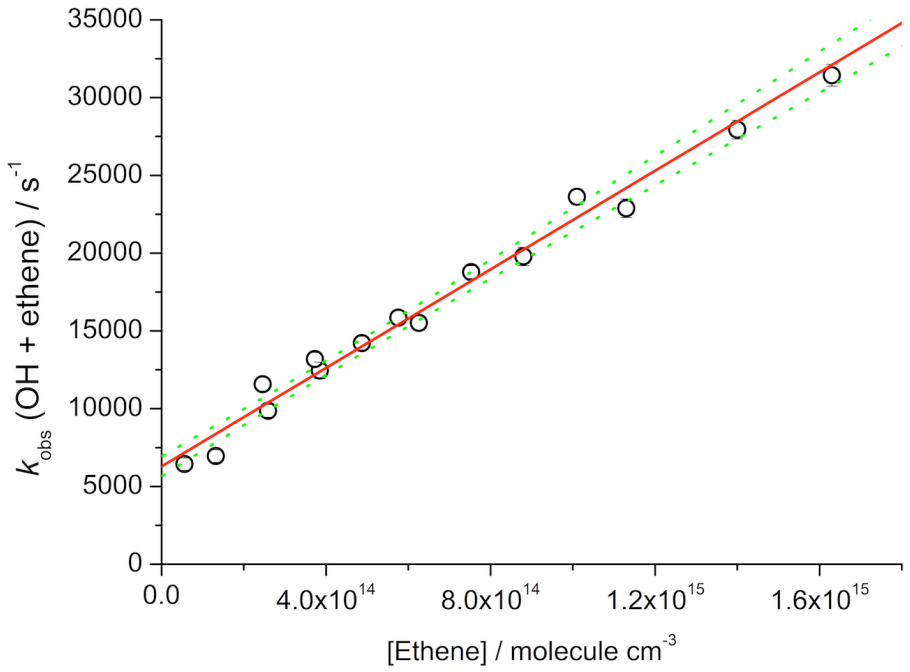

Figure 2. 15: Variation of k_{obs} with ethene concentration obtained at 144 ± 15 K and a total gas density of (18 ± 2) × 10^{16} molecule cm^{-3} using N_2 bath gas, together with a weighted linear least squares fit to the data, the gradient of which yields the bimolecular rate coefficient of (1.58 ± 0.05) × 10^{-11} $molecule^{-1}$ cm^3 s^{-1}. The green dashed lines represent the upper and lower 95 % confidence limits.

The pseudo first order rate coefficients were plotted against the co-reagent concentration to construct a bimolecular plot. The bimolecular rate coefficient at the given jet temperature and gas density is the gradient of the plot, and the intercept is the pseudo first order loss of the radical due to reaction with the precursor and diffusional loss. The bimolecular rate coefficients reported in this work are an average of the values obtained from multiple bimolecular plots (typically between 3 to 8) each comprising several pseudo first order rate coefficients (typically in the range of 8 to 25). An example bimolecular plot obtained in this work for the reaction of OH with ethene is shown in Figure 2. 15. The rate coefficient for the reaction of OH with ethene obtained from the bimolecular plot (Figure 2. 15) is in good agreement of the value predicted at this temperature (1.62×10^{-11} molecule^{-1} cm^3 s^{-1}) by Vakhtin *et al.* from their low temperature measurements using a pulsed Laval nozzle apparatus.[11] Measurement of a rate coefficient previously reported in the literature is also a useful method of confirming the jet temperature.

This chapter has summarised some experimental approaches utilised for the study of reaction kinetics at low temperatures, including methods of generating suitable low temperature conditions and techniques by which rate coefficients can be measured. In the following chapters the results obtained using the experimental setup described in this chapter will be presented and discussed.

2.4 References

1 Lockhart, J., Blitz, M. A., Heard, D. E., Seakins, P. W. & Shannon, R. J. Mechanism of the Reaction of OH with Alkynes in the Presence of Oxygen. *The Journal of Physical Chemistry A* **117**, 5407-5418 (2013).

2 Lockhart, J., Blitz, M., Heard, D., Seakins, P. & Shannon, R. Kinetic Study of the OH + Glyoxal Reaction: Experimental Evidence and Quantification of Direct OH Recycling. *The Journal of Physical Chemistry A* **117**, 11027-11037 (2013).

3 Miller, T. A. Chemistry and chemical intermediates in supersonic free jet expansions. *Science* **223**, 545-553 (1984).

4 Mazely, T. & Smith, M. Kinetic analysis in thermally anisotropic systems: Application to supersonic free jet expansions. *The Journal of Chemical Physics* **89**, 2048-2062 (1988).

5 Beijerinck, H. & Verster, N. Absolute intensities and perpendicular temperatures of supersonic beams of polyatomic gases. *Physica B+C* **111**, 327-352 (1981).

6 Creasey, D. J. *et al.* Visualisation of a supersonic free-jet expansion using laser-induced fluorescence spectroscopy: Application to the

measurement of rate constants at ultralow temperatures. *Applied Physics B* **65**, 375-391 (1997).

7 Rowe, B. R., Dupeyrat, G., Marquette, J. B. & Gaucherel, P. Study of the reactions $N^{+2}+2N_2$ --> $N^{+4}+N_2$ and $O^{+2}+2O_2$ --> $O^{+4}+O_2$ from 20 to 160 K by the CRESU technique. *The Journal of Chemical Physics* **80**, 4915-4921 (1984).

8 Sims, I. *et al.* Ultra−low temperature kinetics of neutral–neutral reactions: The reaction CN + O_2 down to 26 K. *The Journal of Chemical Physics* **97**, 8798-8800 (1992).

9 Rowe, B. & Marquette, J. CRESU studies of ion/molecule reactions. *International journal of mass spectrometry and ion processes* **80**, 239-254 (1987).

10 Atkinson, D. B. & Smith, M. A. *Design and characterization of pulsed uniform supersonic expansions for chemical applications*. Vol. 66 (AIP, 1995).

11 Vakhtin, A. B., Murphy, J. E. & Leone, S. R. Low-temperature kinetics of reactions of OH radical with ethene, propene, and 1-butene. *The Journal of Physical Chemistry A* **107**, 10055-10062 (2003).

12 Vakhtin, A. B., McCabe, D. C., Ravishankara, A. & Leone, S. R. Low-temperature kinetics of the reaction of the OH radical with hydrogen peroxide. *The Journal of Physical Chemistry A* **107**, 10642-10647 (2003).

13 Vakhtin, A. B., Lee, S., Heard, D. E., Smith, I. W. & Leone, S. R. Low-temperature kinetics of reactions of the OH radical with propene and 1-butene studied by a pulsed Laval nozzle apparatus combined with laser-induced fluorescence. *The Journal of Physical Chemistry A* **105**, 7889-7895 (2001).

14 Vakhtin, A. B., Heard, D. E., Smith, I. W. & Leone, S. R. Kinetics of reactions of C_2H radical with acetylene, O_2, methylacetylene, and allene in a pulsed Laval nozzle apparatus at T= 103 K. *Chemical Physics Letters* **344**, 317-324 (2001).

15 Vakhtin, A. B., Heard, D. E., Smith, I. W. & Leone, S. R. Kinetics of C_2H radical reactions with ethene, propene and 1-butene measured in a pulsed Laval nozzle apparatus at T= 103 and 296 K. *Chemical Physics Letters* **348**, 21-26 (2001).

16 Soorkia, S. *et al.* Reaction of the C_2H Radical with 1-Butyne (C_4H_6): Low-Temperature Kinetics and Isomer-Specific Product Detection. *The Journal of Physical Chemistry A* **114**, 3340-3354 (2010).

17 Soorkia, S. *et al.* Airfoil sampling of a pulsed Laval beam with tunable vacuum ultraviolet synchrotron ionization quadrupole mass spectrometry: Application to low-temperature kinetics and product detection. *Review of Scientific Instruments* **82**, 124102 (2011).

18 Daugey, N. *et al.* Kinetic measurements on methylidyne radical reactions with several hydrocarbons at low temperatures. *Phys Chem Chem Phys* **7**, 2921-2927 (2005).

19 Daranlot, J. *et al.* Revealing atom-radical reactivity at low temperature through the N + OH reaction. *Science* **334**, 1538-1541 (2011).

20 Daranlot, J. *et al.* Elemental nitrogen partitioning in dense interstellar clouds. *Proceedings of the National Academy of Sciences of the United States of America* **109**, 10233-10238 (2012).

21 Daranlot, J. *et al.* Gas−Phase Kinetics of Hydroxyl Radical Reactions with Alkenes: Experiment and Theory. *ChemPhysChem* **11**, 4002-4010 (2010).

22 Taylor, S. E., Goddard, A., Blitz, M. A., Cleary, P. A. & Heard, D. E. Pulsed Laval nozzle study of the kinetics of OH with unsaturated hydrocarbons at very low temperatures. *Phys Chem Chem Phys* **10**, 422-437 (2008).

23 Rowe, B., Marquette, J., Dupeyrat, G. & Ferguson, E. Reactions of He+ and N+ ions with several molecules at 8 K. *Chemical Physics Letters* **113**, 403-406 (1985).

24 Bouwman, J., Fournier, M., Sims, I. R., Leone, S. R. & Wilson, K. R. Reaction Rate and Isomer-Specific Product Branching Ratios of C_2H+ C_4H_8: 1-Butene, cis-2-Butene, trans-2-Butene, and Isobutene at 79 K. *The Journal of Physical Chemistry A* **117**, 5093-5105 (2013).

25 James, P. L., Sims, I. R., Smith, I. W., Alexander, M. H. & Yang, M. A combined experimental and theoretical study of rotational energy transfer in collisions between NO ($X\ ^2\Pi_{1/2}$, v= 3, J) and He, Ar and N_2 at temperatures down to 7 K. *The Journal of Chemical Physics* **109**, 3882-3897 (1998).

26 Atkinson, D. B. & Smith, M. A. Design and characterization of pulsed uniform supersonic expansions for chemical applications. *Review of Scientific Instruments* **66**, 4434-4446 (1995).

27 Lee, S., Hoobler, R. J. & Leone, S. R. A pulsed Laval nozzle apparatus with laser ionization mass spectroscopy for direct measurements of rate coefficients at low temperatures with condensable gases. *Review of Scientific Instruments* **71**, 1816-1823 (2000).

28 Bergeat, A., Hickson, K. M., Daugey, N., Caubet, P. & Costes, M. A low temperature investigation of the N(^{4}S°) + NO reaction. *Phys Chem Chem Phys* **11**, 8149-8155 (2009).

29 Shannon, R. J. *et al.* The fast C(^{3}P)+ CH_3OH reaction as an efficient loss process for gas-phase interstellar methanol. *RSC Advances* **4**, 26342-26353 (2014).

30 Pilling, M. J. & Seakins, P. W. *Reaction kinetics*. (Oxford University Press, 1995).

31 Norrish, R. & Porter, G. Chemical reactions produced by very high light intensities. *Nature* **164**, 658 (1949).

32 Sheps, L., Scully, A. M. & Au, K. UV absorption probing of the conformer-dependent reactivity of a Criegee intermediate CH_3CHOO. *Phys. Chem. Chem. Phys.* **16**, 26701-26706 (2014).

33 Savee, J. D. *et al.* Direct observation and kinetics of a hydroperoxyalkyl radical (QOOH). *Science* **347**, 643-646 (2015).

34 Lewis, T. R., Blitz, M. A., Heard, D. E. & Seakins, P. W. Direct evidence for a substantive reaction between the Criegee intermediate, CH_2OO, and the water vapour dimer. *Physical Chemistry Chemical Physics* (2015).

35 Welz, O. *et al.* Direct kinetic measurements of Criegee intermediate (CH_2OO) formed by reaction of CH_2I with O_2. *Science* **335**, 204-207 (2012).

36 Taatjes, C. A. *et al.* Direct measurements of conformer-dependent reactivity of the Criegee intermediate CH_3CHOO. *Science* **340**, 177-180 (2013).

37 Taatjes, C. A. *et al.* “Imaging” combustion chemistry via multiplexed synchrotron-photoionization mass spectrometry. *Physical Chemistry Chemical Physics* **10**, 20-34 (2008).

38 Osborn, D. L. *et al.* The multiplexed chemical kinetic photoionization mass spectrometer: A new approach to isomer-resolved chemical kinetics. *Review of Scientific Instruments* **79**, 104103 (2008).

39 Bouwman, J., Goulay, F., Leone, S. R. & Wilson, K. R. Bimolecular Rate Constant and Product Branching Ratio Measurements for the Reaction of C2H with Ethene and Propene at 79 K. *The Journal of Physical Chemistry A* **116**, 3907-3917 (2012).

40 Taylor, S. E. *Reaction Kinetics at Very Low Temperatures Measured Using a Pulsed Laval Nozzle System* PhD thesis thesis, University of Leeds, (2007).

41 Luque, J. & Crosley, D. R. LIFBASE: Database and spectral simulation, Version 1.5. *SRI International Report MP 99-009* (1999).

Chapter 3. The low temperature reaction kinetics of OH with alcohols: The role of a weakly bound complex.

3.1 Background and previous studies of OH + alcohol reactions

The reaction kinetics of OH with alcohols have been extensively studied at ambient and high temperatures owing to their relevance to atmospheric and combustion chemistry.

Methanol is emitted into the Earth's atmosphere via biomass burning and its use as a fuel additive, ethanol has been investigated as a potential biofuel and propanol, which has been detected in both oceanic and urban environments, is suspected to be released from oceans and also from biogenic sources such as windscreen wiper fluid. [1-8] The primary removal pathway of these species is expected to be via reaction with OH, one of the most important oxidation species in Earth's atmosphere. [9]

Gas phase methanol is highly abundant in low temperature interstellar environments. It was first detected in 1970 by Ball *et al.* in Sgr B2 and Sgr A molecular clouds and since then has been detected in a variety of regions including star forming regions, cold and dark molecular clouds and post-star forming regions (HII regions).[10] Gas phase abundances of methanol relative to H_2 in these regions range from 10^{-9} (in cold dark pre-star forming clouds) to 10^{-6} (in star forming regions).[11-18] The interstellar formation pathway for methanol has been the subject of many studies, and it is expected that methanol is formed via the heterogeneous hydrogenation of CO on the surface of grains and ices.[19-21] Methanol is then postulated to be released into the gas phase by shock waves and heating events.

In addition, ethanol has been detected with an abundance relative to H_2 ranging from 10^{-8} to 10^{-6} in interstellar molecular clouds and star forming regions (hot and cold cores) such as W3(OH) and Sgr B2, where temperatures can reach as low as 40 K. [22-26] However the formation pathways of ethanol are not currently well defined.[25,27] Interestingly, the hydroxyl radical is almost ubiquitous in interstellar environments, including the areas where both methanol and ethanol have been detected.[26,28] As such, Millar *et al.* suggested that ethanol could potentially be used as a chemical clock for hot cores if the kinetics of its reactions with species including the hydroxyl radical were better understood at temperatures pertinent to such environments. Therefore conducting kinetic studies with species known to be present in these cold environments is important for the

advancement of chemical models of these regions.[25] However, recent low temperature studies of neutral-neutral reactions have shown that the temperature dependence of their rate coefficients is often complex and poorly understood, and so kinetic data close to ambient temperatures cannot simply be extrapolated.[29-32]

From previous studies it is acknowledged that at temperatures above 200 K, the reactions of OH with alcohols appear to proceed via a direct, bimolecular hydrogen abstraction mechanism (R3.1). [4-8,33-35]

$$OH + ROH \xrightarrow{k_{3.1}} products \qquad \text{R3.1}$$

Such reactions exhibit parallel product channels depending on the moiety from which hydrogen abstraction occurs. For the reactions of OH with methanol, ethanol or propan-2-ol, there is more than one possible channel:

$$OH + CH_3OH \xrightarrow{k_{3.2}} products \qquad \text{R3.2}$$

$$OH + CH_3OH \longrightarrow CH_2OH + H_2O \qquad \text{R3.2a}$$

$$OH + CH_3OH \longrightarrow CH_3O + H_2O \qquad \text{R3.2b}$$

$$OH + CH_3CH_2OH \xrightarrow{k_{3.3}} products \qquad \text{R3.3}$$

$$OH + CH_3CH_2OH \longrightarrow CH_2CH_2OH + H_2O \qquad \text{R3.3a}$$

$$OH + CH_3CH_2OH \longrightarrow CH_3CHOH + H_2O \qquad \text{R3.3b}$$

$$OH + CH_3CH_2OH \longrightarrow CH_3CH_2O + H_2O \qquad \text{R3.3c}$$

$$OH + CH_3CH(OH)CH_3 \xrightarrow{k_{3.4}} products \qquad \text{R3.4}$$

$$OH + CH_3CH(OH)CH_3 \longrightarrow CH_2CH(OH)CH_3 + H_2O \qquad \text{R3.4a}$$

$$OH + CH_3CH(OH)CH_3 \longrightarrow CH_3C(OH)CH_3 + H_2O \qquad \text{R3.4b}$$

$$OH + CH_3CH(OH)CH_3 \longrightarrow CH_3CH(O)CH_3 + H_2O \qquad \text{R3.4c}$$

Kinetic studies of various deuterated analogues of the above species have previously been employed to determine the branching ratios for these reactions. Hess and Tully observed a significant kinetic isotope effect (KIE) on the rate coefficient for the OH + CD_3OH reaction when compared to OH + CH_3OH data between 290-860 K, indicating that the primary pathway operating is R3.2a.[34] This is supported by direct room temperature measurements using mass spectrometry by Meier *et al.*, who determined the branching for this channel to be 0.83 ± 0.13.[35] However, Hess and Tully

found that the KIE decreased with increasing temperature, which suggests increasing abstraction from the hydroxyl group, R3.2b.[34] This behaviour can be rationalized by consideration of calculations of the potential energy surface (PES) by Xu and Lin at the CCSD(T)/6-311+G(3df,2p) level of theory, and at the CCSD(T)/6-311G(d,p)//BHandHLYP/6-311++G(d,p) level by Galano *et al.*, which show that the barrier for R3.2a is lower than that for R3.2b by around 4-13 kJ mol^{-1}. [36,37]

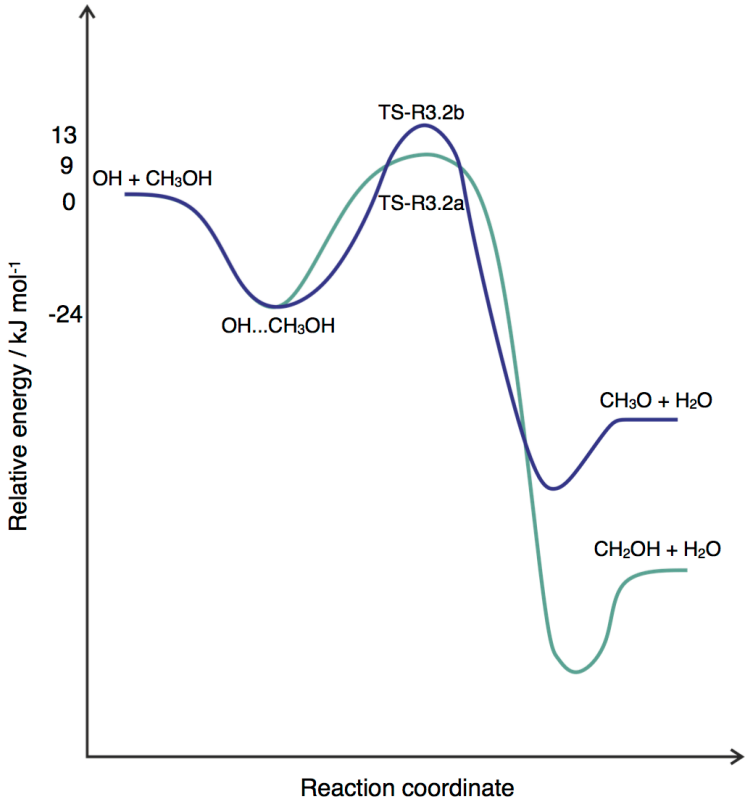

Figure 3. 1: To-scale potential energy surface for the reaction of OH + methanol (with relevant relative energies) based on *ab initio* calculations by Galano *et al.* at the CCSD(T)/6-311G(d,p)//BHandHLYP/6-311++G(d,p) level of theory.[37]

Rigorous studies of deuterated analogues of OH + ethanol by Carr *et al.* from 298-523 K have revealed that at ambient and high temperatures, abstraction from the methylene centre (R3.3b) is the dominant pathway.[8] Theoretical studies on this system have shown that this pathway has the lowest barrier to hydrogen abstraction and R3.3c the highest.[36-39] Carr *et al.* demonstrated that at room temperature, whilst alpha abstraction via R3.3b is dominant (~90 %), as the temperature increases, the branching fraction via R3.3b is reduced and abstraction from the alcohol group (R3.3c) yielding ethoxy radicals becomes dominant at high temperatures (branching fraction of ~0.47-0.53 at 865 K).[8]

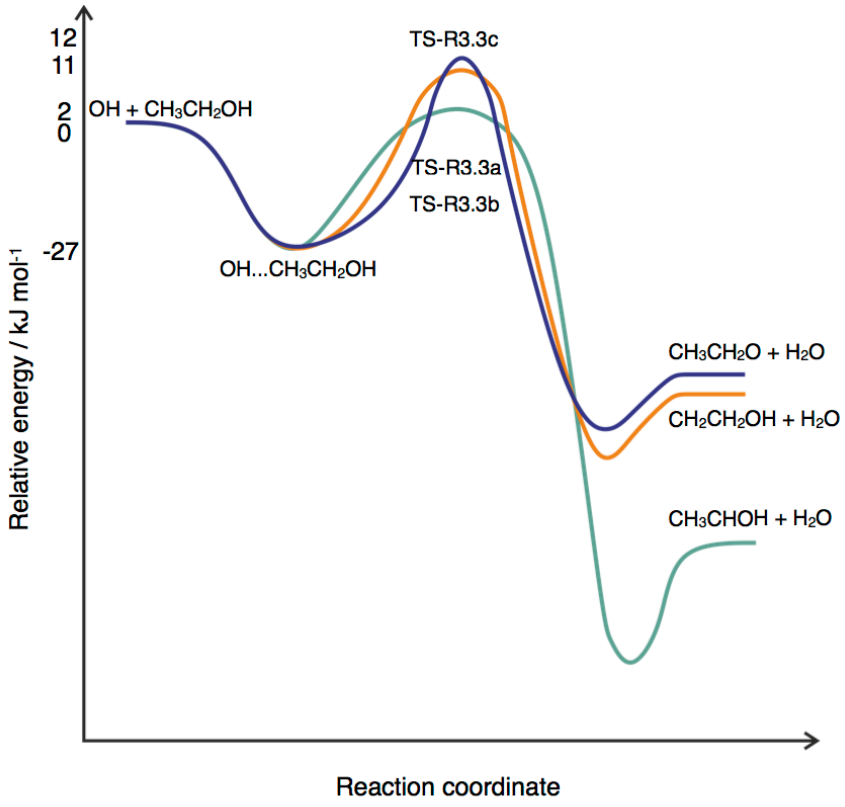

Figure 3. 2: To-scale potential energy surface for the reaction of OH + ethanol (with relevant relative energies) based on *ab initio* calculations by Galano *et al.* at the CCSD(T)/6-311G(d,p)//BHandHLYP/6-311++G(d,p) level of theory.[37]

Kinetic studies of the reaction of OH with various deuterated analogues of propan-2-ol were performed by Dunlop and Tully between 293-502 K.[6] Analysis of the observed kinetic isotope effects demonstrated that abstraction of the alpha hydrogen (R3.4b) dominated, with increasing contribution from the beta abstraction channel (R3.4a) at increasing temperatures. The overall bimolecular rate coefficient for the OH + propan-2-ol reaction exhibits little dependence on temperature, which is supportive of the reaction proceeding largely via a barrierless pathway. *Ab initio* stationary point calculations by Galano *et al.* on this system showed that abstraction from the CH group (R3.4b) is barrierless, whereas channels R3.4a and R3.4c exhibited barriers, which is in agreement with the experimental observations by Dunlop and Tully.[6,37] Nevertheless, the rate coefficient is around two orders of magnitude below the gas kinetic limit across the temperature range at which this reaction has until now been studied, indicating that channels with positive barriers are also contributing to the overall rate coefficient.

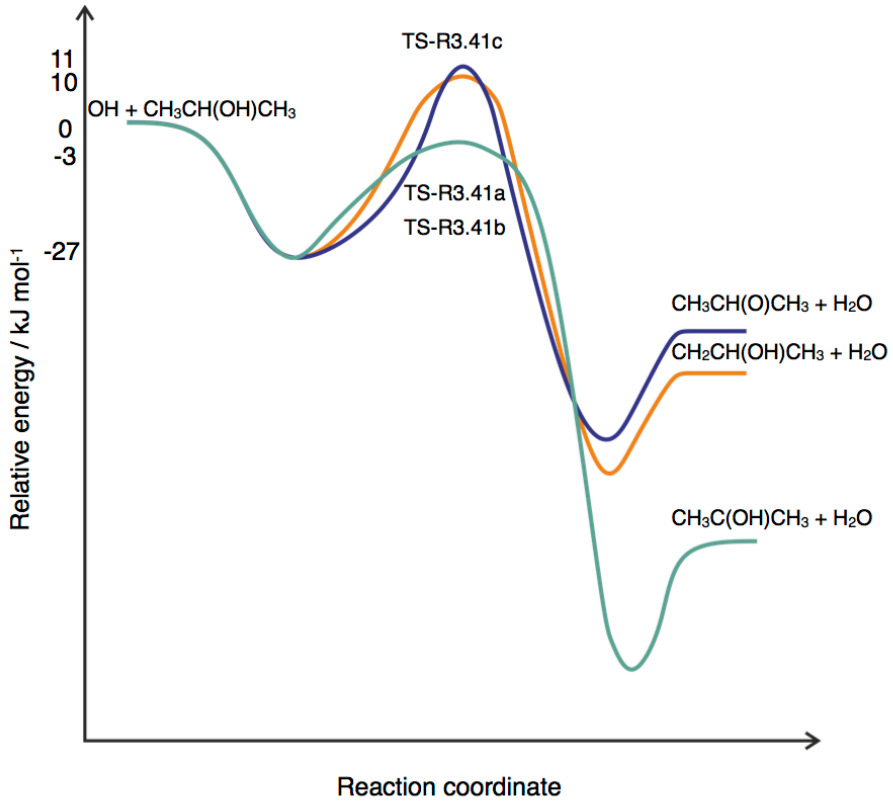

Figure 3. 3: To-scale potential energy surface for the reaction of OH + propan-2-ol (with relevant relative energies) based on *ab initio* calculations by Galano *et al.* at the CCSD(T)/6-311G(d,p)//BHandHLYP/6-311++G(d,p) level of theory.[37]

Recent low temperature kinetic studies by Shannon *et al.* performed in this laboratory on the reaction of OH with methanol have shown that, unusually, the rate coefficient increases by around a factor of 50 between 298 and 65 K despite the presence of barriers.[32] This very large increase in the rate coefficient is attributed to a mechanism involving the formation of a weakly bound complex between the reactants (binding energy of 20.5 kJ mol^{-1} from calculations by Xu and Lin[36]) followed by quantum mechanical tunnelling through the reaction barrier. The increased lifetime of the complex at lower temperatures is found to enhance the probability of tunnelling through the barrier, which in turn causes the rate coefficient to be dramatically enhanced. Under the experimental conditions, the rate coefficient was shown to be independent of pressure and thus the complex was not stabilized into the pre-barrier well. Master equation modelling and direct product detection using laser induced fluorescence spectroscopy demonstrated that at low temperatures, the reaction instead proceeds via R3.2b to yield water vapour and the methoxy radical (CH_3O).[32] It is notable that the observed low temperature products are obtained via the higher, but narrower reaction barrier.[32]

Due to the presence of methanol and OH in common interstellar environments, it is expected that the enhanced rate coefficient for the reaction of these species could have potential implications on their predicted abundances in cold interstellar environments. However, to accurately deduce the implications of this reaction using interstellar chemical models, the rate coefficient needs to be well defined at several temperatures, in particular very low temperatures (towards 20 K) which are most pertinent to regions where methanol and OH have been detected, and higher temperatures (between 100-200 K), so that the turnaround in the rate coefficient from the apparent low and high temperature regimes can be better understood. As such, further low temperature rate coefficients for the OH + methanol system have been measured in this work using the pulsed Laval apparatus. Additionally, in collaboration with Gomez Martin and Plane, a cryogenically cooled flow tube apparatus was also used, allowing for an intercomparison between the two experimental techniques.[40] Following on from the comments made by Millar *et al.*,[25] the reaction kinetics of OH with ethanol have been studied between 56-146 K. To explore the mechanism of this class of reactions further, the kinetics of OH + propan-2-ol have been studied between 89-146 K. The low temperature kinetic behaviour of the three alcohol reactions will also be compared and contrasted. The work presented in the following section is the subject of three publications.[40-42]

3.2 Experimental procedure

The apparatus and experimental procedure has been described fully in Chapter 2 of this thesis and thus only a brief outline is given here.

The vapour pressure of the alcohol co-reactant (methanol (Sigma-Aldrich ≥ 99.9 %) ethanol (Sigma-Aldrich, ethanol absolute ≥ 99.8 %) or propan-2-ol (Fischer scientific, 99.5 %)) was admitted to an empty cylinder at room temperature via a gas manifold, and the cylinders were subsequently diluted to a total pressure of ~ 5000 Torr with the bath gas (nitrogen (BOC, OFN) or argon (99.998 %, BOC)). The cylinder, which typically contained 0.5-2 % alcohol, was allowed to mix overnight before use.

The alcohol/bath gas mixture, $(CH_3)_3COOH$ (Aldrich, 70 % wt. in H_2O) and the bath gas (nitrogen (BOC, OFN) or argon (99.998 %, BOC)) were delivered to the pre-expansion reservoir via a set of calibrated mass flow controllers (MKS instruments). $(CH_3)_3COOH$ was seeded in a flow of nitrogen (OFN) or argon (99.998 %, BOC)) via a glass bubbler. All

experiments were carried out under pseudo first order conditions and in addition the reagent concentration did not exceed 2 % of the total gas flow.

The mixture of reagent and bath gases was expanded supersonically in ~ 10-20 ms pulses, depending on the nozzle used, through the convergent-divergent shaped Laval nozzle into a low pressure stainless steel chamber producing a thermally equilibrated, low temperature jet. The short gas pulses were achieved using two pulsed solenoid valves (Parker 9 series), which control the flow of gas from a 1 cm^3 reservoir region through the Laval nozzle.

The rate coefficients of the OH + methanol, OH + ethanol or OH + propan-2-ol reaction were measured by monitoring the temporal decay of the hydroxyl radical via pulsed laser photolysis-laser induced fluorescence (PLP-LIF). The experiments were performed under pseudo first order conditions so that the concentration of the co-reagent is in great excess (around a factor of 100 or more) of the OH concentration. The OH precursor ($(CH_3)_3COOH$) was photolysed at 248 nm using an excimer laser (KrF Lambda Physik LPX 200), with typical laser energy of 60-160 mJ per pulse, along the axis of the expanded gas flow producing a uniform OH density. The subsequent decay of OH due to reaction and other loss processes was measured by probing the $A^2\Sigma^+ \leftarrow X^2\Pi_i$ (1,0) $Q_1(1.5)$ transition at ~ 282 nm using a Nd:YAG (Litron LPY 664-10) pumped dye laser (Sirah Gmbh Cobra stretch with Rhodamine 6G dye). The off-resonant fluorescence at ~ 308 nm was monitored using a photomultiplier tube (Thorn EMI 9813QB) fitted with a 308 nm interference filter (Barr associates λ_{max} = 308.5 nm, FWHM = 5 nm) positioned above the axis of the jet and laser beams. The temporal evolution of the OH radicals was recorded by varying the time delay between the photolysis and probe lasers. At very short times following photolysis, probe laser excitation scans revealed the presence of rotationally excited OH, which rapidly relaxes to the temperature of the jet, the temperature being obtained independently by impact pressure measurements.

The reaction scheme for the formation and removal of OH is given by:

$$(CH_3)_3COOH + h\upsilon \longrightarrow OH, OH^* + co - products \qquad \text{P3.1}$$

$$OH^* + M \xrightarrow{k_{rel}} OH + M \qquad \text{R3.5}$$

$$OH + ROH \xrightarrow{k_{3.1}} products \qquad \text{R3.1}$$

where *OH** is an initially rotationally excited hydroxyl radical, formed in v″= 0 from photolysis of the precursor, and k_{rel} is the rate coefficient for rotational relaxation of the rotationally excited hydroxyl radical into the laser probed level, OH . For pseudo first order conditions [*ROH*]>>[*OH*] and also [*M*] >> [*OH**] the temporal evolution of OH is given by E3.1 (see Appendix C for derivation).

$$[OH]_t = \left(\frac{k_{rel}}{k_{obs}-k_{rel}}\right)[OH^*]_0\left(e^{-k'_{rel}t} - e^{-k_{obs}t}\right)+[OH]_0 e^{-k_{obs}t} \qquad \text{E3.1}$$

and

$$k_{obs} = k_{3.1}[ROH] + k_{loss} \qquad \text{E3.2}$$

where k_{obs} is the pseudo first order rate coefficient and k_{loss} is the rate coefficient for the loss of OH out of the detection region via diffusion and reaction with the precursor.

3.3 Results and discussion

Examples of the temporal evolution of the OH LIF signal following 248 nm photolysis of $(CH_3)_3COOH$ in the presence of methanol, ethanol and propan-2-ol are shown in Figures 3.4-3.6, together with non-linear least squares fits of (E3.1) to the data which yielded k_{obs}.

Experiments were repeated for a variety of concentrations of either methanol, ethanol or propan-2-ol, and Figures 3.7-3.9 show the variation of k_{obs} with [alcohol], the gradients of which yield the bimolecular rate coefficients. The rate coefficients obtained in this study are summarized in Table 1, and the temperature dependence of $k_{3.2}$, $k_{3.3}$ and $k_{3.4}$ are shown in Figures 3.10-3.12.

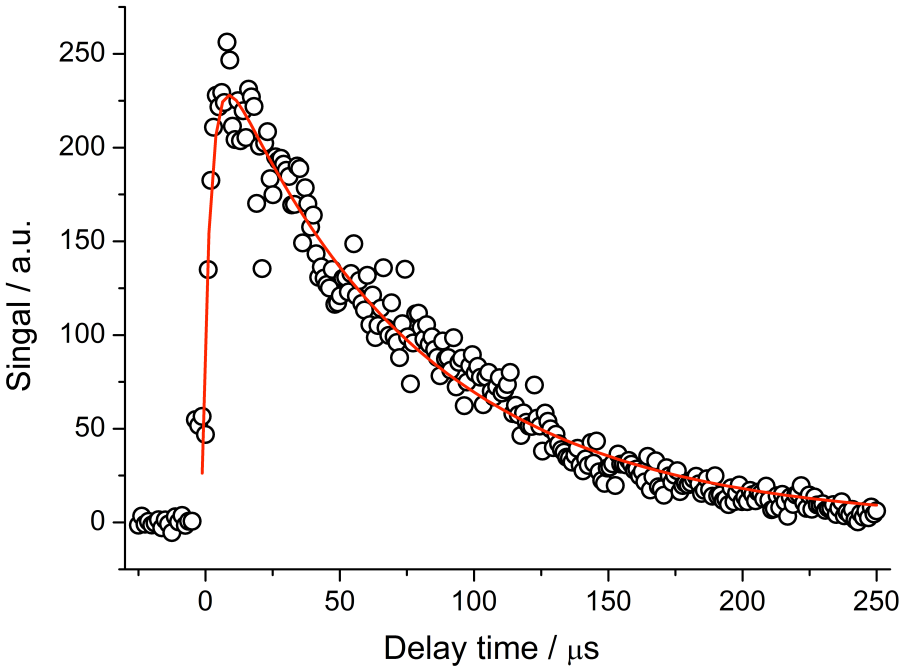

Figure 3. 4: Pseudo first order LIF profile of OH (open circles) together with the non-linear least squares fit of E3.1 to the data (red line) from the 248 nm photolysis of $(CH_3)_3COOH$ in the presence of methanol (2.2×10^{14} molecule cm^{-3}) at 56 ± 4 K and a total density (4.4 ± 0.5) × 10^{16} molecule cm^{-3}, using Ar bath gas The least squares fit of E3.1 to the data yields a pseudo first order rate coefficient of 13479 ± 235 s^{-1}.

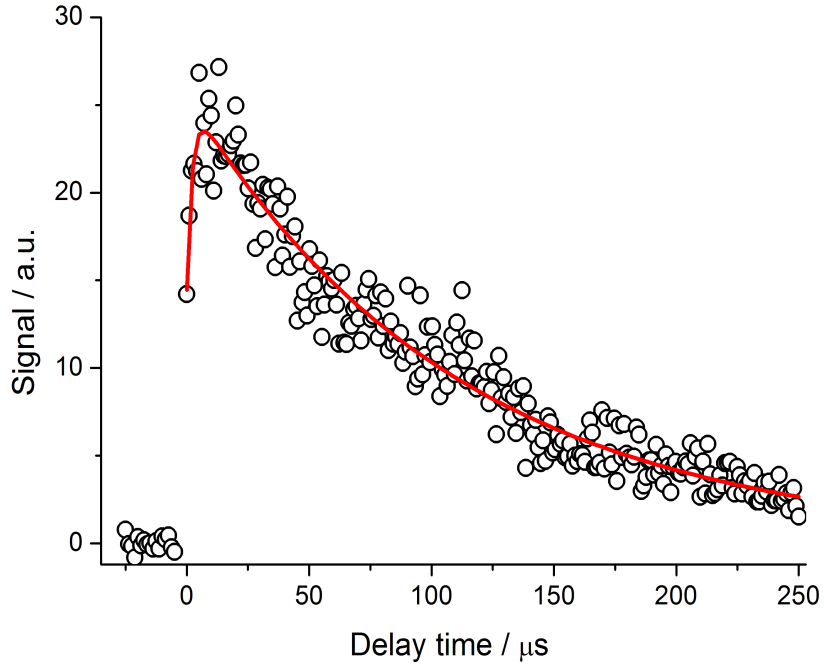

Figure 3. 5: Pseudo first order LIF profile of OH (open circles) together with the non-linear least squares fit of E3.1 to the data (red line) from the 248 nm photolysis of $(CH_3)_3COOH$ in the presence of ethanol (8.4×10^{13} molecule cm^{-3}) at 56 ± 4 K and a total density (4.4 ± 0.5) × 10^{16} molecule cm^{-3} using Ar bath gas. The least squares fit of E3.1 to the data yields a pseudo first order rate coefficient of 9342 ± 181 s^{-1}.

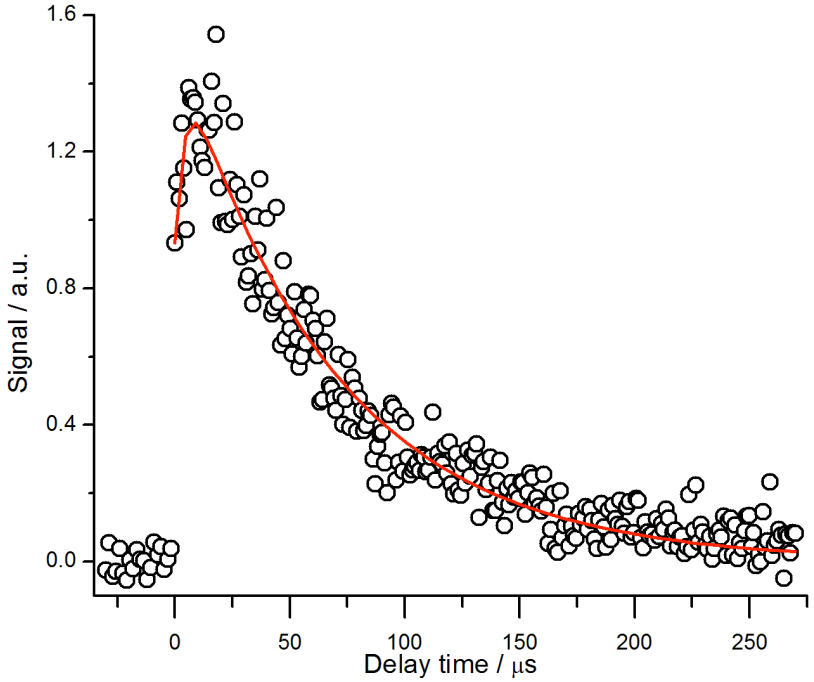

Figure 3. 6: Pseudo first order LIF trace of OH (open circles) together with the non-linear least squares fit of E3.1 to the data (red line) from the 248 nm photolysis of $(CH_3)_3COOH$ in the presence of propan-2-ol (1.22×10^{14} molecule cm^{-3}) at 91 ± 4 K, and a total density ($8.3 \pm 0.9) \times 10^{16}$ molecule cm^{-3} using N_2 bath gas. The least squares fit of E3.1 to the data yields a pseudo first order rate coefficient of 14767 ± 347 s^{-1}.

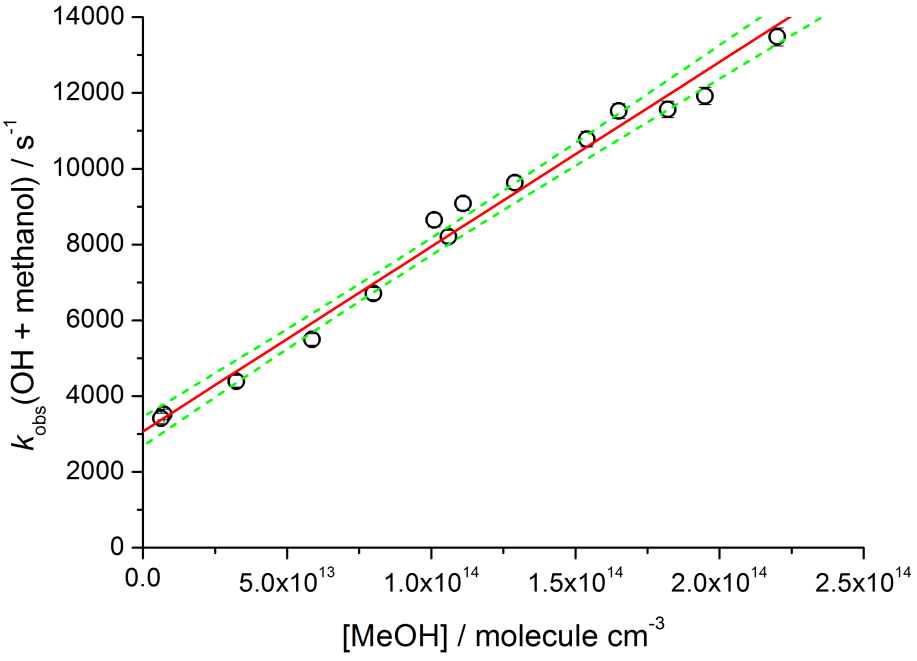

Figure 3. 7: Variation of k_{obs} with methanol concentration obtained at 56 ± 4 K and a density of $(4.4 \pm 0.5) \times 10^{16}$ molecule cm^{-3} using Ar bath gas, together with a weighted linear least squares fit of E3.2 to the data, the gradient of which yields the bimolecular rate coefficient, $k_{3.2}$= $(4.9 \pm 0.8) \times 10^{-11}$ molecule^{-1} cm^3 s^{-1}. The green dashed lines represent the upper and lower 95 % confidence limits. The error bars on the pseudo first order rate coefficients result from the error in the fit of E3.1 to the data, and in this case the error bars are obscured by the symbol. The overall error in the bimolecular rate coefficient is the 95% confidence limits propagated with the error in the determination of the total density from the impact pressure measurements.

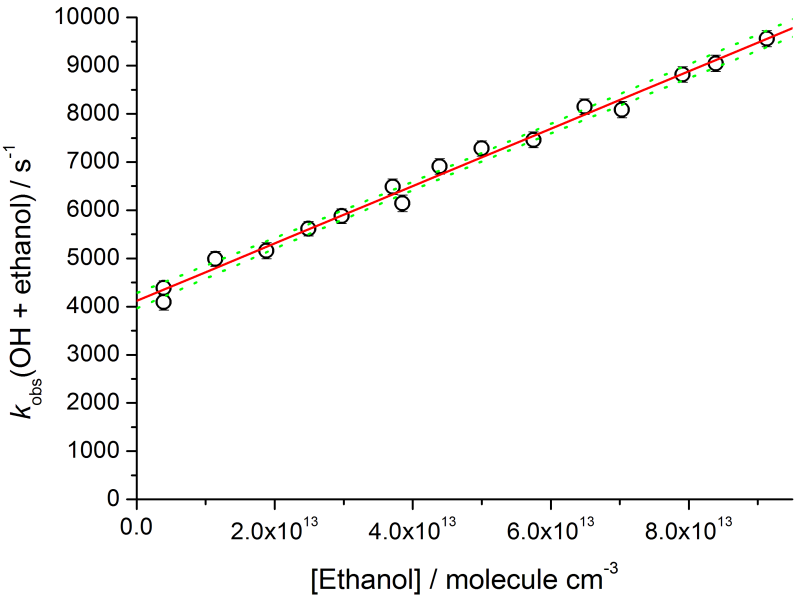

Figure 3. 8: Variation of k_{obs} with ethanol concentration obtained at 56 ± 4 K and a density of (4.4 ± 0.5) × 10^{16} molecule cm^{-3} using Ar bath gas, together with a weighted linear least squares fit of E3.2 to the data, the gradient of which yields the bimolecular rate coefficient, $k_{3.3}$= (6.0 ± 0.5) × 10^{-11} molecule^{-1} cm^3 s^{-1}. The green dashed lines represent the upper and lower 95 % confidence limits. The error bars on the pseudo first order rate coefficients result from the error in the fit of E3.1 to the data, and in this case the error bars are obscured by the symbol. The overall error in the bimolecular rate coefficient is the 95% confidence limits propagated with the error in the determination of the total density from the impact pressure measurements.

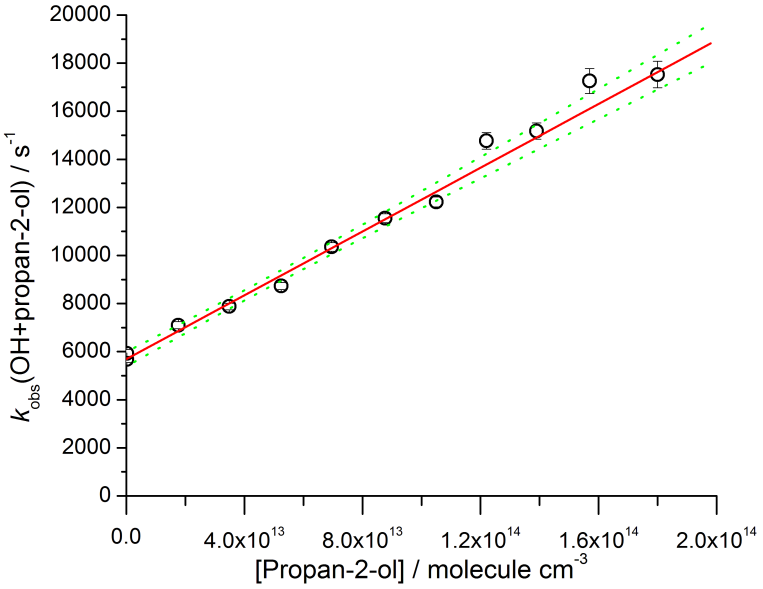

Figure 3. 9: Variation of k_{obs} with propan-2-ol concentration obtained at 91± 4 K and a density of (8.3 ± 0.9) × 10^{16} molecule cm^{-3} using N_2 bath gas, together with a weighted linear least squares fit of E3.2 to the data, the gradient of which yields the bimolecular rate coefficient, $k_{3.4}$= (6.7 ± 0.7) × 10^{-11} molecule^{-1} cm^3 s^{-1}. The green dashed lines represent the upper and lower 95 % confidence limits. The error bars on the pseudo first order rate coefficients result from the error in the fit of E3.1 to the data, and in this case the error bars are obscured by the symbol. The overall error in the bimolecular rate coefficient is the 95% confidence limits propagated with the error in the determination of the total density from the impact pressure measurements.

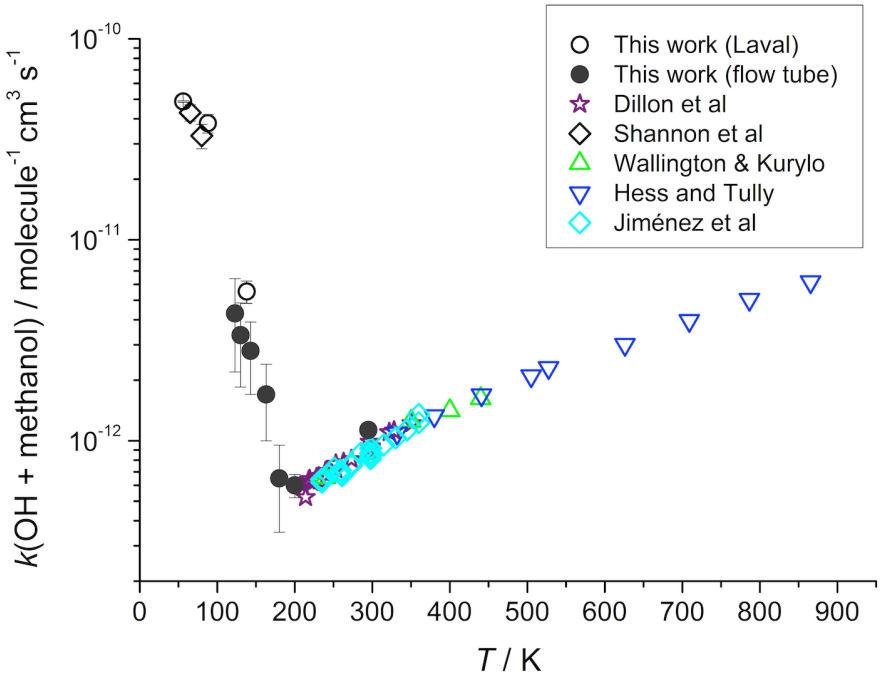

Figure 3. 10: Temperature dependence of $k_{3.2}$, the OH + methanol rate coefficient from this work and other studies.[4,5,7,32,34,40]

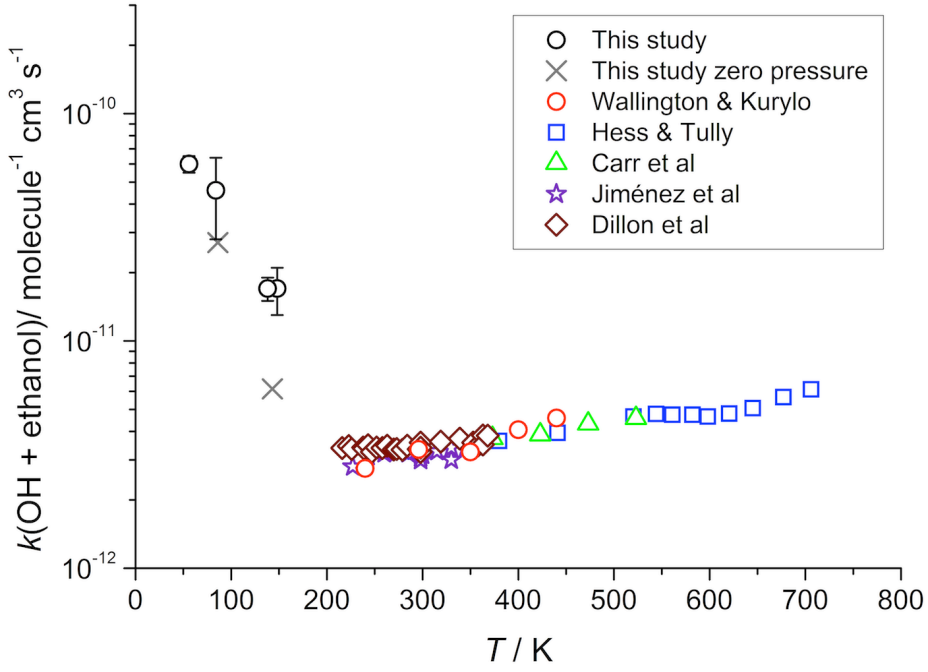

Figure 3. 11: Temperature dependence of $k_{3.3}$, the OH + ethanol rate coefficient from this work and other studies.[4,5,7,8,43]

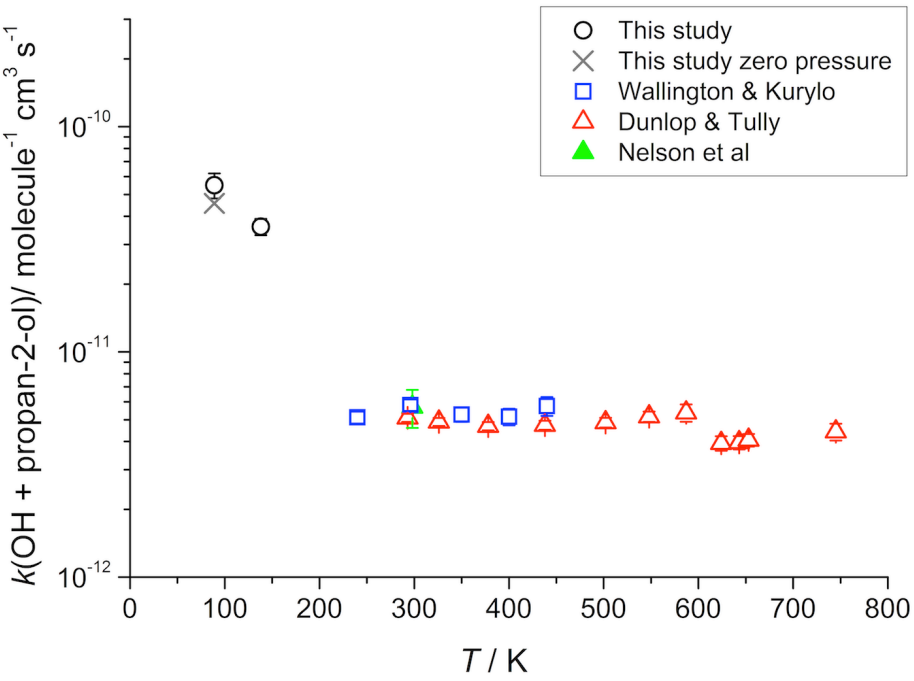

Figure 3. 12: Temperature dependence of $k_{3,4}$, the OH + propan-2-ol rate coefficient from this work and other studies.[6,7,44]

The rate coefficient for the reaction of OH + methanol measured at 56 K is found to be a factor of 55 higher than the value reported at 298K by Dillon *et al.*, continuing the trend observed by Shannon *et al.* down to 65 K.[4,32] There is also reasonable agreement at ~ 140 K between the independent Laval nozzle apparatus and flow tube measurements. The flowtube measurements by Gomez-Martin are in good agreement with the ambient temperature data obtained by Dillon *et al.*, and indicate a turnaround of the rate coefficient from the Arrhenius-type behaviour to the low temperature regime around 180 K. [4,40] The rate coefficient for the reaction of OH + ethanol measured at 56 K is found to be a factor of 18 higher than the value reported at 293 K by Hess and Tully,[43] signifying a strong inverse temperature dependence at lower temperatures. The rate coefficient for OH + propan-2-ol is also found to exhibit a notable inverse temperature dependence below 240 K, increasing by around an order of magnitude between 296 and 88 K.[7]

Table 3. 1: Measured rate coefficients of OH + alcohol reactions obtained in this study, together with the temperatures, Mach numbers and total gas densities of the flows generated by the pulsed Laval nozzles utilised in this work. Errors have been calculated by propagation of the 95 % confidence limits in the bimolecular rate coefficients with the errors in the expansion densities.

T/K	Bath gas (M)	[M] / 10^{16} molecule cm^{-3}	$k_{3.2}$ / 10^{-11} molecule^{-1} cm^3 s^{-1}	$k_{3.3}$ / 10^{-11} molecule^{-1} cm^3 s^{-1}	$k_{3.4}$ / 10^{-11} molecule^{-1} cm^3 s^{-1}
56 ± 4	Ar	4.4 ± 0.5	4.9 ± 0.8	6.0 ± 0.5	-
54 ± 6	Ar	8 ± 1	-	5.5 ± 0.7	-
88 ± 5	N_2	3.5 ± 0.5	-	4.0 ± 0.6	5.5 ± 0.7
89 ± 3	N_2	6.5 ± 0.6	-	4.2 ± 0.2	5.7 ± 0.7
86 ± 3	N_2	6.8 ± 0.6	-	5 ± 2	-
91 ± 4	N_2	8.3 ± 0.9	-	-	6.7 ± 0.7
88 ± 8	Ar	9.4 ± 1.3	3.8 ± 0.4	-	-
88 ± 4	N_2	11 ± 1	-	5.5 ± 0.6	7 ± 1
84 ± 4	N_2	12 ± 2	-	6 ± 2	-
82 ± 3	N_2	16 ± 2	-	7 ± 3	-
138 ± 9	N_2	8 ± 1	0.5 ± 0.2	1.7 ± 0.2	3.6 ± 0.3
148 ± 15	N_2	10 ± 2	-	1.7 ± 0.4	-
133 ± 10	N_2	13 ± 3	-	3.6 ± 0.3	4.7 ± 0.4
144 ± 15	N_2	18 ± 2	-	3.6 ± 0.8	-
146 ± 15	N_2	26 ± 4	-	4 ±1	-

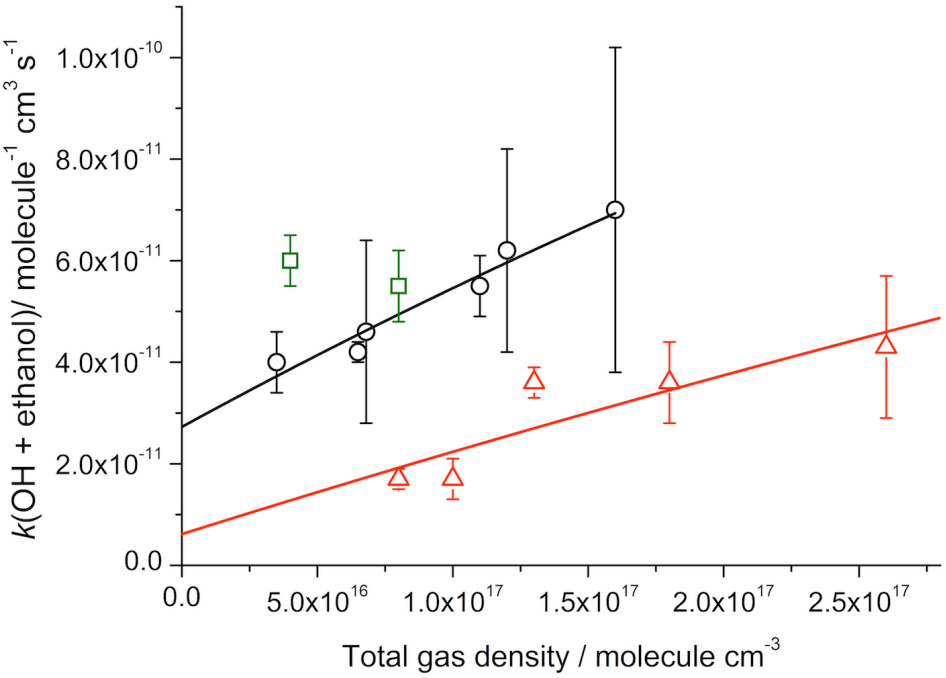

Figure 3. 13: Pressure dependence of $k_{3.3}$, the OH + ethanol rate coefficient at 54-56 K (green open squares, Ar bath gas), 82-89 K (N_2 bath gas, black open circles) and 133-148 K (N_2 bath gas, red open triangles). The black and red lines are the extended Lindemann-Hinshelwood fits (E3.8) to the experimental data obtained at 88-89 K and 133-148 K, respectively. The error bars are the result of propagation of the 95 % confidence limits in the bimolecular rate coefficients with the errors in the expansion densities.

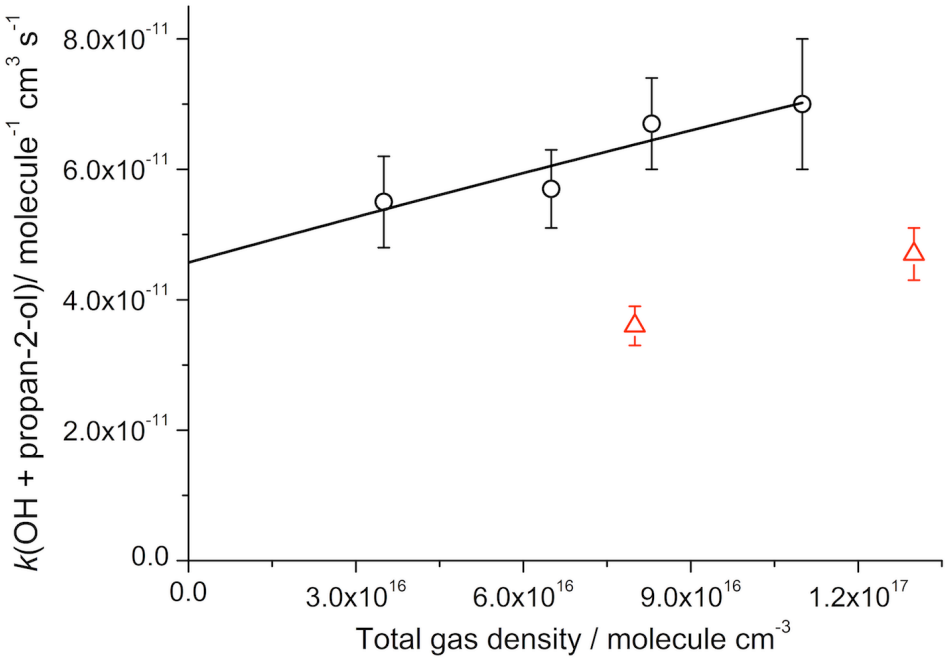

Figure 3. 14: Pressure dependence of $k_{3.4}$, the OH + propan-2-ol rate coefficient at 88-91 K (N_2 bath gas, black open circles) and 133-148 K (N_2 bath gas, red open triangles). The black line is the extended Lindemann-Hinshelwood fit (E3.8) to the experimental data obtained at 88-91 K. The error bars are the result of propagation of the 95 % confidence limits in the bimolecular rate coefficients with the errors in the expansion densities.

Previous work by Shannon *et al.* demonstrated that the rate coefficient for the reaction of OH with methanol was independent of pressure.[32] In this study, the rate coefficients $k_{3.3}$ and $k_{3.4}$ were measured over a range of total bath gas densities and, in contrast to the reaction of OH with methanol, the measured rate coefficients demonstrate a pressure dependence at the low temperatures studied in this work, as shown in Figures 3.13 and 3.14. [32]

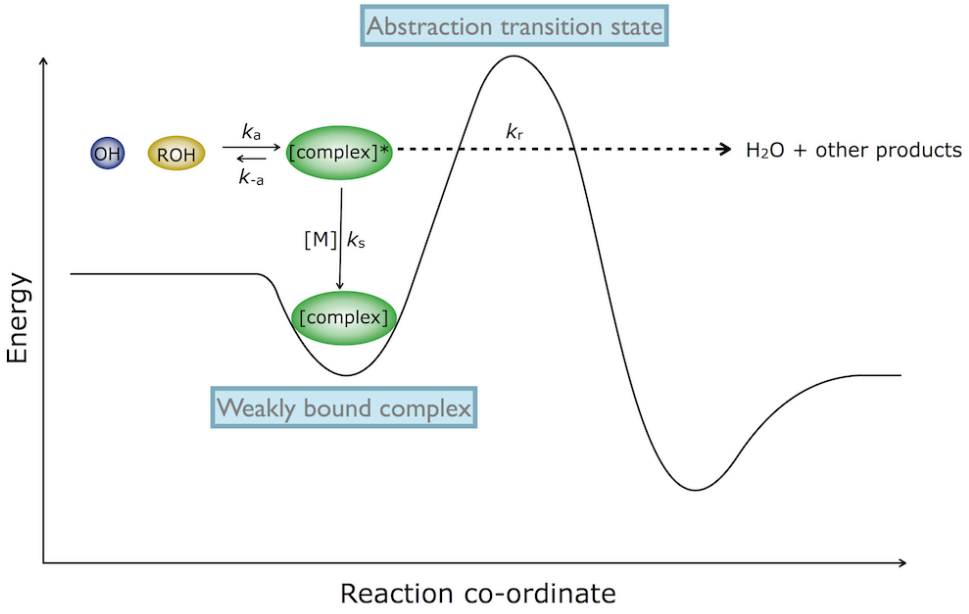

Figure 3. 15: Generic potential energy surface for the reaction of OH + alcohols outlining the possible reaction pathways at low temperatures, where k_r is the rate coefficient for bimolecular reaction, and k_s is the rate coefficient for collisional stabilisation of the OH-alcohol complex into the pre-barrier well. For the reaction of OH with propan-2-ol, there is also a barrierless channel possibly in operation – see individual PES diagrams for more information.

The observed experimental results for $k_{3.3}$ and $k_{3.4}$ can be interpreted by examining the generic potential energy surface for the reaction of OH with alcohols. Figure 3. 15 shows a simplified generic PES for such reactions based on *ab initio* calculations reported in the literature by Galano *et al.* and Sivamakrishnan *et al.*[37,38] It can be observed that a weakly bound complex between the alcohol and OH, typically bound by ~ 18 - 27 kJ mol^{-1}, is formed prior to the barrier(s) to reaction. The overall reaction is therefore described by an extended Lindemann-Hinshelwood type mechanism:

$$OH + ROH \xrightarrow{k_a} [complex]^* \qquad \text{R3.1a}$$

$$[complex]^* \xrightarrow{k_{-a}} OH + ROH \qquad \text{R3.1b}$$

$$[complex]^* + M \xrightarrow{k_s} [complex] + M \qquad \text{R3.1c}$$

$$[complex]^* \xrightarrow{k_r} products \qquad \text{R3.1d}$$

The enhancement in the rate coefficients $k_{3.3}$ and $k_{3.4}$ with total gas density (as show in Figures 3.13 and 3.14) is a result of the increasing collisional stabilization of the complex, a channel which is not observed for the reaction of OH + methanol at low temperatures.[32]

From this scheme, the rate of change of OH and the complex are given by:

$$\frac{-d[OH]}{dt} = k_a[OH][ROH] - k_{-a}[complex]^* \qquad \text{E3.3}$$

$$\frac{d[complex]^*}{dt} = k_a[OH][ROH] - k_{-a}[complex]^* \qquad \text{E3.4}$$

$$-k_s[M][complex]^* - k_r[complex]^*.$$

Applying the steady state approximation to the complex gives:

$$[complex]^* = \frac{k_a\,[OH][ROH]}{k_{-a}+k_s[M]+k_r} \qquad \text{E3.5}$$

and hence:

$$\frac{-d[OH]}{dt} = \left(k_a\ - \frac{k_{-a}k_a}{k_{-a}+k_s[M]+k_r}\right)[OH][ROH] \qquad \text{E3.6}$$

The experimental rate law for the loss of OH via reaction with ROH is defined by;

$$\frac{-d[OH]}{dt} = k_{3.1}[OH][ROH] \qquad \text{E3.7}$$

and comparing terms with E3.6 leads to:

$$k_{3.1} = \frac{k_a\,(k_{-a}+k_s[M]+k_r)}{k_{-a}+k_s[M]+k_r} - \frac{k_{-a}k_a}{k_{-a}+k_s[M]+k_r} = \frac{k_a\,k_s[M]}{k_{-a}+k_s[M]+k_r} + \frac{k_a\,k_r}{k_{-a}+k_s[M]+k_r}$$

which is equivalent to:

$$k_{3.1} = \frac{[M]}{\frac{k_{-a}}{k_a\,k_s}+\frac{[M]}{k_a}+\frac{k_r}{k_a\,k_s}} + \frac{1}{\frac{k_{-a}}{k_a\,k_r}+\frac{k_s[M]}{k_a\,k_r}+\frac{1}{k_a}} \qquad \text{E3.8}$$

The expression E3.8 enables the Lindemann-Hinshelwood parameters to be obtained by fitting to observations of $k_{3.3}$ or $k_{3.4}$ as a function of [M], as shown in Figures 3.13 and 3.14.[45] The rate coefficient for the pressure independent abstraction channel is given by $k_{3.1}$ at [M]=0 (when only the second term in E3.8 remains) which is $k_{3.1} = (k_a k_r)/(k_{-a}+k_r)$, and the ratio k_r/k_s (previously referred to as the chemical activation ratio[45]) can be obtained from the ratio of the value of $k_{3.1}$ at [M]=0 to the low pressure limiting gradient of $k_{3.1}$ versus [M]$(k_a k_r)/(k_{-a}+k_r)$. To deduce the chemical activation ratio and the rate coefficient for the pressure independent abstraction

channel, the high pressure limit, $k_{3.1} = k_a$, was fixed at values obtained experimentally at ~ 89 K using the proxy method in which the loss of vibrationally excited OH following collisions with the alcohol is monitored. [46,47] The complete results and methodology for the proxy method will be reported in Chapter 7. The same high pressure limiting value was used for both the ~89 K and ~140 K data, as the barrierless association reaction which k_a is expected to be relatively independent of temperature. The values of k_a used and the values of k_r/k_s, and $k_1(M \rightarrow 0) = (k_a k_r)/(k_{-a}+k_r)$ obtained from the fits are displayed in Table 2.

Table 3. 2: Parameters obtained from the fit of the extended Lindemann-Hinshelwood expression (E3.8) to the experimental pressure dependent data.

System	T / K	High pressure limit* k_a / molecule^{-1} cm^3 s^{-1}	Chemical activation ratio (k_r/k_s)/ molecule cm^{-3}	Zero pressure rate coefficient $\frac{k_a k_r}{k_{-a}+k_r}$ / molecule^{-1} cm^3 s^{-1}
OH+ ethanol	82-91	4.5×10^{-10}	$(1.0\pm0.8)\times10^{17}$	$(2.7\pm0.8)\times10^{-11}$
	133-148	4.5×10^{-10}	$(3.6\pm5.9)\times10^{16}$	$(6.2\pm8.1)\times10^{-12}$
OH+ propan-2-ol	88-91	4.7×10^{-10}	$(1.8\pm0.7)\times10^{17}$	$(4.6\pm0.5)\times10^{-11}$

* High pressure limits obtained experimentally using the proxy method of monitoring the decay of vibrationally excited OH, the details of which will be presented in Chapter 7.

From Figures 3.13 and 3.14 it can be seen that at low temperatures the rate coefficient extrapolated to [M]=0 is significant, indicative of a pressure independent product channel. In the case of ethanol (Figure 3. 13) , for which all product channels proceed via a significant activation barrier, this provides evidence for quantum mechanical tunnelling, as observed for the reaction of OH with methanol.[32] For propan-2-ol, although the abstraction channel R3.4b is calculated to be barrierless,[37] and hence could proceed at very low temperatures, the rate coefficient between 250 – 750 K is only ~ 5×10^{-12} cm^3 molecule^{-1} s^{-1} (see Figure 3. 12) and relatively independent of temperature, whereas as shown in Figure 3. 14, the intercept at [M] =0 for 89 K gives a value that is almost 10 times higher. This finding provides evidence for a further mechanism that is operating at very low temperatures, namely, once again the formation of a longer-lived complex which facilitates

quantum mechanical tunnelling through one of the positive barriers to reaction, as observed for OH + methanol.[32]

$$k_{3.1} = \frac{[M]}{\frac{k_{-a}}{k_a k_s} + \frac{[M]}{k_a} + \frac{k_r}{k_a k_s}} + \frac{1}{\frac{k_{-a}}{k_a k_r} + \frac{k_s[M]}{k_a k_r} + \frac{1}{k_a}}$$

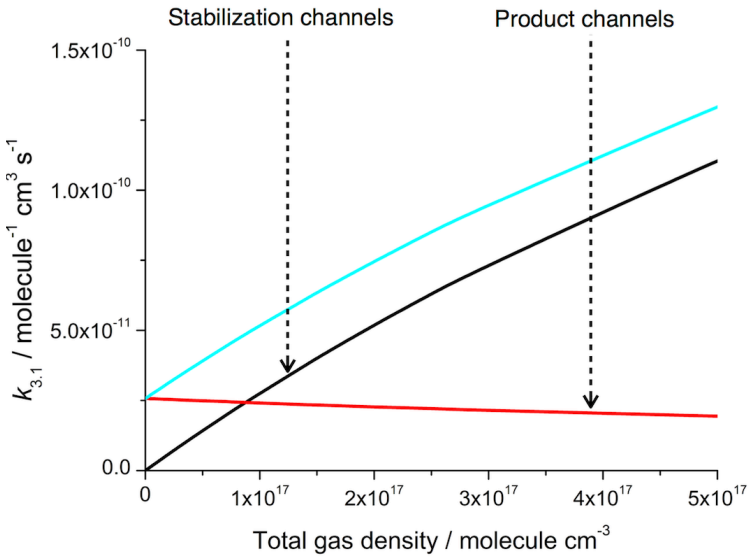

Figure 3. 16: The extended Lindemann-Hinshelwood expression (E3.8) for $k_{3.1}$ as a function of [M] using the best fit parameters from fitting to the 82-89 K OH + ethanol experimental data (cyan line), together with the calculated contributions to $k_{3.1}$ from the pressure dependent first term (black line) and the approximately pressure independent second term (red line) as a function of total gas density.

As [M] increases, this pressure independent contribution to $k_{3.1}$ becomes less significant and the first term in E3.8 begins to dominate, representing the collisional stabilization of the hydrogen-bonded OH-alcohol complex. Figure 3. 16 shows the best-fit of the extended Lindemann-Hinshelwood expression E3.8 to pressure dependent data for the reaction of OH with ethanol at 82-89 K (as shown in Figure 3. 13), together with the individual contributions towards $k_{3.1}$ of the two right-hand-side terms of E3.8 as a function of pressure. Using the mechanism above, in the limit of low pressure, $k_{3.1}$ ([M]→0)=($k_a k_r$)/(k_{-a}+k_r) and when there is a barrier to forming products, k_r, and hence $k_{3.1}$ will be small, even though k_{-a} will decrease significantly at low temperatures. However, when quantum mechanical tunnelling is significant (for example in hydrogen transfer reactions such as these), the value of k_r is significant (and independent of temperature), and hence at low temperatures the value of $k_{3.1}$ can increase significantly. The pressure independent rate coefficient, estimated by fitting E3.8 to the experimental data as shown in Figure 3. 13, is significantly larger at ~ 82-89 K for ethanol compared with ~ 133-148 K, consistent with this mechanism

(see Table 3. 2). Although at 56 K there are only two data points which overlap within experimental uncertainties, there is evidence for a larger pressure independent rate coefficient.

At high temperatures where there is sufficient energy to surmount the barrier to reaction, there is rapid formation (R3.1a) and dissociation (R3.1b) of the complex and so the bottleneck for reaction (R3.1d) is location at the barrier itself. The complex has a short lifetime and collisional stabilization is not able to compete with dissociation, and consequently only the pressure independent abstraction channel (R3.1d) is observed. Only at low temperatures is k_{-a} sufficiently reduced such that the lifetime of the complex is long enough for collisional stabilization to compete with dissociation. [30,48,49]

In the case of OH + propan-2-ol, the bimolecular abstraction reaction can occur via a submerged barrier for channel R3.4b.[37] The observed increase in the rate coefficient for this bimolecular channel at low temperatures is due to the reduction in k_{-a} (R3.1b) and hence an extended complex lifetime with decreasing temperature, resulting in a higher probability of the complex proceeding to products either via the submerged barrier or by tunnelling through one of the other positive barriers to hydrogen abstraction. Furthermore, the lifetime of the complex is sufficiently long that collisional stabilization is competitive, as evident from Figure 3. 14.

In the case of the ethanol system, there is uncertainty in the literature as to whether the lowest barrier to H-abstraction (R3.3b) is submerged or not. Work by Sivaramakrishnan *et al.* at the QCISD(T)/CBS//B3LYP/6-311++G(d,p) level of theory indicates a slightly submerged or energetically neutral barrier, with an error larger than the energy by which the barrier is submerged being placed on the value. [38] The findings of Xu and Lin using theory at the CCSD(T)/6-311+G(3df,2p) level support this. [36] Conversely, calculations by Galano *et al*.[37] at the CCSD(T)/6-311G(d,p)//BHandHLYP/6-311++G(d,p) level yield a small positive barrier as indicated schematically in Figure 3. 15. From the Arrhenius type behaviour of the experimental data currently in the literature at higher temperatures, as shown in Figure 3. 11, it is expected that this barrier is indeed positive or that the transition state is sufficiently tight so that the kinetic behaviour appears as if there is a positive barrier. Considering the low temperatures at which the experiments reported here have been undertaken and its demonstrated role in the OH + methanol reaction for a similar temperature range, the contribution of quantum

mechanical tunnelling in the OH + ethanol reaction (and perhaps to certain channels of the OH + propanol-2-ol reaction) must be considered. [32,40]

At higher temperatures, where there is sufficient energy to surmount the barriers to reaction, the contribution from quantum mechanical tunnelling is reduced and the relative heights of the barriers to hydrogen atom abstraction from the different moieties on ethanol or propan-2-ol influence the branching ratios of the products. However, at low temperatures when the quantum mechanical tunnelling mechanism dominates reaction, the product branching ratios are predominantly influenced by the shape of the vibrationally adiabatic reaction path, in other words, the barrier widths.[32,50,51] Therefore, in the case of OH + ethanol it is likely that hydrogen atom abstraction process is not occurring through the lowest energy barrier, which corresponds to abstraction from the CH_2 moiety (R3.3b) to form CH_3CHOH, but instead through the barrier which has the largest imaginary frequency (~2300-2900 cm^{-1}), which is abstraction from the hydroxyl group (R3.3c) resulting in ethoxy radical formation, CH_3CH_2O.[36-38] Although this channel has been experimentally and theoretically determined to be relatively inactive at ambient temperatures, previous work by Shannon *et al.* on the OH + methanol reaction has shown that abstraction via the barrier with the largest imaginary frequency (also the OH group, to form CH_3O) dominates at low temperatures. [8,32,38] An unsuccessful attempt has been made in this work to detect both CH_3O and CH_3CH_2O products of the methanol and ethanol reactions respectively via laser induced fluorescence spectroscopy, which will be further discussed in the following section. We postulate that the inability to observe this product is in part due to fast secondary reactions of the CH_3CH_2O radical with other radicals such as OH and H, which were abundant in the experiments where product detection was attempted, resulting in chemiluminescence which obscured the laser induced fluorescence signal. This is further discussed in the next section. [40]

Although there is a barrierless abstraction channel for the OH + propan-2-ol reaction (R3.4b), quantum mechanical tunnelling through the barrier associated with abstraction from the OH group of propanol-2-ol (R3.4c) may be competitive at low temperatures, due to the high imaginary frequency.[37] Consequently, the distribution of products at low temperatures may differ from the room temperature branching ratios. The pressure independent rate coefficients for the reactions of OH with ethanol and propan-2-ol increase by around a factor of 8 between 298 and 84 K, obtained from extrapolations of the Lindemann-Hinshelwood fits to [M]=0 and corresponding to the product

formation channels. These product channels are of potential relevance to star forming regions and molecular clouds in the interstellar medium as the low gas density (~ 10^2 - 10^4 molecule cm^{-3}) in these environments means that collisions are very infrequent and hence collisional stabilization of the complex (R3.1c) is precluded.[24]

For the mechanism outlined above, $k_{3.1}$ (M→0)=($k_a k_r$)/(k_{-a}+k_r) and hence at the very low temperatures present in these regions, when $k_{-a} \rightarrow 0$, $k_{3.1} = k_a$ and the bimolecular reaction to form products will be encounter controlled and approach the gas kinetic limit. Hence reactions of this type, involving the formation of pre-barrier hydrogen-bonded complexes, may be important in these interstellar environments.

3.4 Attempts of product detection from the reactions of OH with methanol and ethanol

Recent work by Shannon *et al.*, as well as work in this study has shown that the rate coefficients for many reactions of OH with OVOCs exhibit a large negative temperature dependence below 200 K.[29,32,40,52] Further exploration of the mechanisms of these reactions via pressure dependence studies and master equation calculations have demonstrated that for some of these reactions, particularly in the case of the alcohol systems, the increase in the rate coefficient at low temperatures is due to a quantum tunnelling mechanism. In the case of OH + methanol, it has been theoretically determined that the low temperature product of this reaction is not CH_2OH, the dominant high temperature product, but the methoxy radical which is obtained favourably via tunnelling due to the higher imaginary frequency associated with the barrier to this hydrogen abstraction site. This was further quantified by Shannon *et al.*[32,52] via the detection and kinetics of the methoxy radical product by LIF at ~ 297.6 nm via the $\tilde{A}^2A_1$-$\tilde{X}^2E$, $\boldsymbol{\nu}$=3 ← 0 transition.[32,52]

As discussed in the previous section, it is hypothesised that the ethoxy radical will be the dominant low temperature product from the OH + ethanol reaction at low temperatures. Attempts have been made in this work to both detect the products from the ethanol reaction and to repeat the methoxy detection work by Shannon *et al.* from the reaction of OH + methanol. Whilst both studies have been unsuccessful, the experimental procedures undertaken will be described and suggestions for why the alkoxy products could not be detected will be outlined.

3.4.1 Experimental procedure – Pulsed Laval nozzle apparatus

Photolytic precursors for the alkoxy radicals (methyl and ethyl nitrite) were prepared as previously described in the literature (and as described in Chapter 6) in order to aid tuning of the dye laser to a strong transition of the relevant alkoxy spectra.[53] Once synthesised, the vapour pressure of the relevant alkoxy radical precursor was admitted to an empty cylinder, then diluted with nitrogen (BOC, OFN). A slow flow of the relevant precursor was entrained into a flow of nitrogen (BOC, OFN) bath gas at a total flow rate found to yield a stable jet with a temperature of 88 ± 5 K and a total gas density of (3.5 ± 0.5) × 10^{16} molecule cm^{-3}. The gas mixture was allowed to mix in a 2 L stainless steel ballast tank prior to expansion through the Laval nozzle via two pulsed solenoid valves firing at a pulse repetition frequency of 5 Hz. The alkyl nitrite precursor was photolysed at 248 nm using an excimer laser aligned collinearly with the jet (pulsed excimer laser, KrF, Lambda-Physik). At a delay time of ~ 30 μs, the probe laser was fired (Sirah Cobra stretch dye laser pumped by Nd:YAG Litron LPY 664-10) and was tuned to an approximate wavelength corresponding to an electronic transition of the alkoxy radical known from the literature (methoxy radical: $\tilde{A}^2A_1 \leftarrow \tilde{X}^2E, \boldsymbol{\nu}_3 = 1 \leftarrow 0$, ethoxy radical: $\tilde{A}^2A_1 \leftarrow \tilde{X}^2A'', \boldsymbol{\nu}_{10} = 3 \leftarrow 0$).[54,55] The wavelength of the probe laser was scanned at small increments (0.002 or 0.005 nm) over a small wavelength range (~ 1 nm) where the transition maximum was reported to occur in the literature. The resultant fluorescence signal from excitation at each wavelength (6 shots per point) was collected by a PMT (Thorn EMI 9813QB) fitted with a wide bandpass filter (Thor labs, 400 ± 40 nm), before being integrated and visualised on the oscilloscope (LeCroy waverunner-2) and transferred to the PC for analysis. The concentrations of the alkoxy radical precursors were 1.3 × 10^{13} and 8.3 × 10^{12} molecule cm^{-3} for methoxy and ethoxy radicals respectively, yielding approximately 2.2 × 10^{12} and 2.3 × 10^{12} methoxy and ethoxy radicals following photolysis at 248 nm.[56,57]

For the direct detection of methoxy and ethoxy radicals from the OH + alcohol reactions, the experimental setup was as previously described for the PLP-LIF experiments, except details that will be given below. A higher concentration of OH was required to attempt product detection and so ozone was used as the hydroxyl radical precursor via the reactions shown below.

$$O_3 \xrightarrow{248\ nm} O(^1D) + O_2 \qquad \text{P3.2}$$

$$O(^1D) + H_2 \longrightarrow OH\ (v \geq 0) + H \qquad \text{R3.6}$$

$$OH\ (v \geq 0) + M \longrightarrow OH\ (v = 0) + M \qquad \text{R3.7}$$

Ozone has a higher absorption cross section at 248 nm than $(CH_3)_3COOH$ by around a factor of 500, and has a quantum yield of 0.9 to produce $O(^1D)$.[58,59] It was confirmed that more OH was indeed produced via this method by the magnitude of the 308 nm on-resonance OH laser induced fluorescence signal from the photolysis of ozone/H_2 being around a factor or 20 larger than from the photolysis of $(CH_3)_3COOH$.

The ozone was prepared via electrical discharge of oxygen (BOC 99.999 %) through an ozone generator (Fischer technology Ozon-generator 500) and was diluted with nitrogen (BOC, OFN) in a set of stainless steel cylinders (10 L) then left for a short mixing period. The ozone concentration was estimated at ~ 2 % in the cylinders and was monitored periodically by offline UV absorption measurements (Agilent Technologies, Cary series UV-vis spectrophotometer) . The vapour pressure of methanol (Sigma-Aldrich ≥ 99.9 %) or ethanol (Sigma-Aldrich ≥ 99.8 %) was delivered to the mass flow controller via a bubbler system using nitrogen (BOC, OFN) as the carrier gas. Hydrogen (BOC), the ozone/N_2/O_2 mixture, nitrogen bath gas (BOC, OFN) and alcohol vapour pressure entrained into a nitrogen flow were delivered to the ballast tank via a set of calibrated mass flow controllers (MKS). The gas was expanded through a Laval nozzle into the reaction chamber held at low pressure with a set of pumps (Leybold), via two pulsed solenoid valves (Parker series 9) firing at a pulse repetition frequency of 5 Hz. The chemical production of OH was initiated by the photolysis of ozone along the jet via a pulsed 248 nm excimer (KrF, Lambda-Physik LPX) laser fired at a pulse repetition frequency of 5 Hz. Detection of the proposed alkoxy radical products from the subsequent reaction of OH with the alcohol was attempted either as a function of time or probe laser wavelength. For the former, the probe laser was tuned to a wavelength corresponding to the maximum of the $\tilde{A}^2A_1 \leftarrow \tilde{X}^2E, \boldsymbol{\nu}_3 = 1 \leftarrow 0$ (~ 310 nm) and $\tilde{B}^2A \leftarrow \tilde{X}^2A\ \boldsymbol{\nu}_{10} = 3 \leftarrow 0$ band (~ 323 nm) transitions for methoxy and ethoxy respectively. The delay time between the photolysis and probe lasers was increased so the temporal evolution of the alkoxy radicals could be obtained. In the latter case, the time delay between the photolysis and probe lasers was fixed (between ~ 140 – 200 μs) and the wavelength of the probe laser was scanned around the transition wavelength for the relevant alkoxy radical. In both cases, any off resonance fluorescence from the alkoxy radicals was collected via a PMT situated perpendicular to the jet and laser beams, fitted with a Perspex or wide bandpass filter (Thorlabs 400 ± 40 nm). The signal

was integrated using an oscilloscope (LeCroy Waverunner-2) and transferred to a PC for analysis. These experiments were performed at 88 ± 5 K with a total gas density of (3.5 ± 0.5) × 10^{16} molecule cm^{-3}, and at 91 ± 4 K with a total gas density of (1.1 ± 0.1) × 10^{17} molecule $cm^{-3.}$ Typical OH and alcohol concentrations ranged from around 1 × 10^{12} - 2.5 × 10^{12} molecule cm^{-3} and 1.9 × 10^{14} - 2.1 × 10^{15} molecule cm^{-3}, respectively.

3.4.2 Results and discussion – Pulsed Laval nozzle apparatus

Using the alkyl nitrite precursors, LIF spectra were obtained for methoxy and ethoxy radicals and are shown in Figures 3.17 and 3.18 respectively. Good agreement was seen with the literature with regards to the maximum line positions of the LIF spectra for methoxy and ethoxy radicals , as shown in Figure 3. 19 and Figure 3. 20 respectively.[54,60]

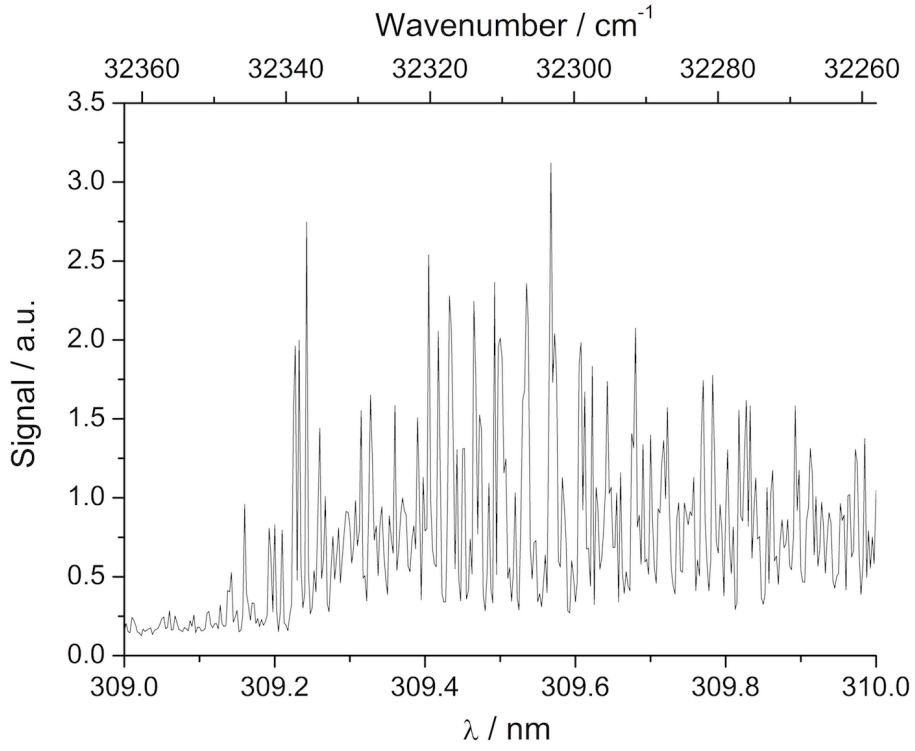

Figure 3. 17: Laser excitation spectrum of the methoxy radical obtained from 248 nm photolysis of methyl nitrite, corresponding to the $\tilde{A}^2A_1 \leftarrow \tilde{X}^2E, \nu_3 = 1 \leftarrow 0$ band. Experimental details were as follows. Delay time between photolysis and probe lasers; 30 µs. Photolysis laser energy; 303 mJ/pulse. Concentration of methyl nitrite; 1.2 × 10^{13} molecule cm^{-3}, yielding methoxy radical concentration of ~ 2.2 × 10^{12} molecule cm^{-3} (using cross section by Sander *et al.*,[56] see Appendix D). Jet conditions; 88 ± 5 K, (3.5 ± 0.5)× 10^{16} molecule cm^{-3}. Scan recorded at increments of 0.005 nm with 6 shots per point. Fluorescence signal normalised for probe laser power, and collected through a 400 ± 40 nm filter (Thor labs).

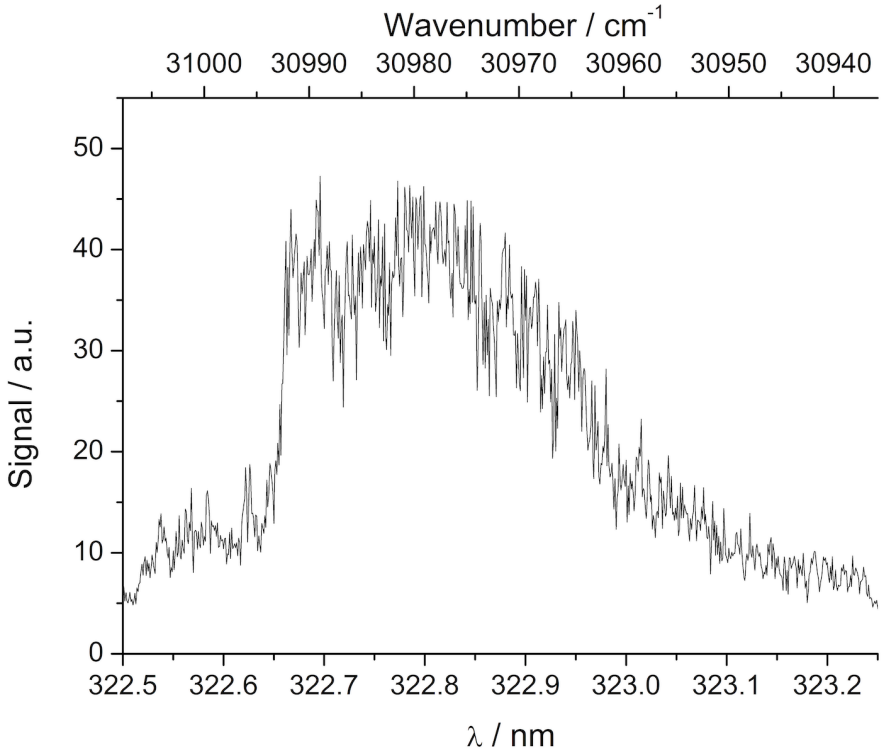

Figure 3. 18: Laser excitation spectrum of the ethoxy radical obtained from 248 nm photolysis of ethyl nitrite, corresponding to the $B^2A' \leftarrow X^2A''$ $\nu_{10} = 3 \leftarrow 0$ band. Experimental details were as follows. Delay time between photolysis and probe lasers; 30 μs. Photolysis laser energy; 327 mJ/pulse. Concentration of ethyl nitrite; 8.3×10^{12} molecule cm^{-3}, yielding ethoxy radical cocentration of ~ 2.3×10^{12} molecule cm^{-3} (using cross section by Mariq and Wallington,[57] see Appendix D) Jet conditions; 88 ± 5 K, (3.5 ± 0.5)× 10^{16} molecule cm^{-3}. Scan recorded at increments of 0.002 nm with 6 shots per point. Flurorescence signal normalised for probe laser power, and collected through a 400 ± 40 nm filter (Thor labs).

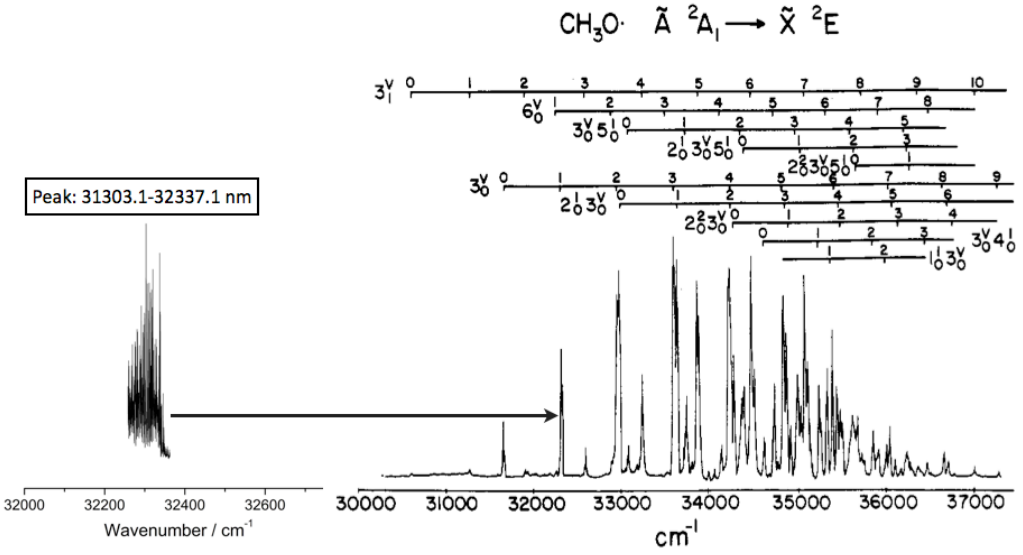

Figure 3. 19: Laser excitation spectrum of the methoxy radical obtained from 248 nm photolysis of methyl nitrite from this work (left), corresponding to the $\tilde{A}^2A_1 \leftarrow \tilde{X}^2E, \nu 3 = 1 \leftarrow 0$ band alongside the ethoxy radical laser excitation spectrum reproduced from Foster *et al*. (jet rotational temperature 3-25 K).[55]

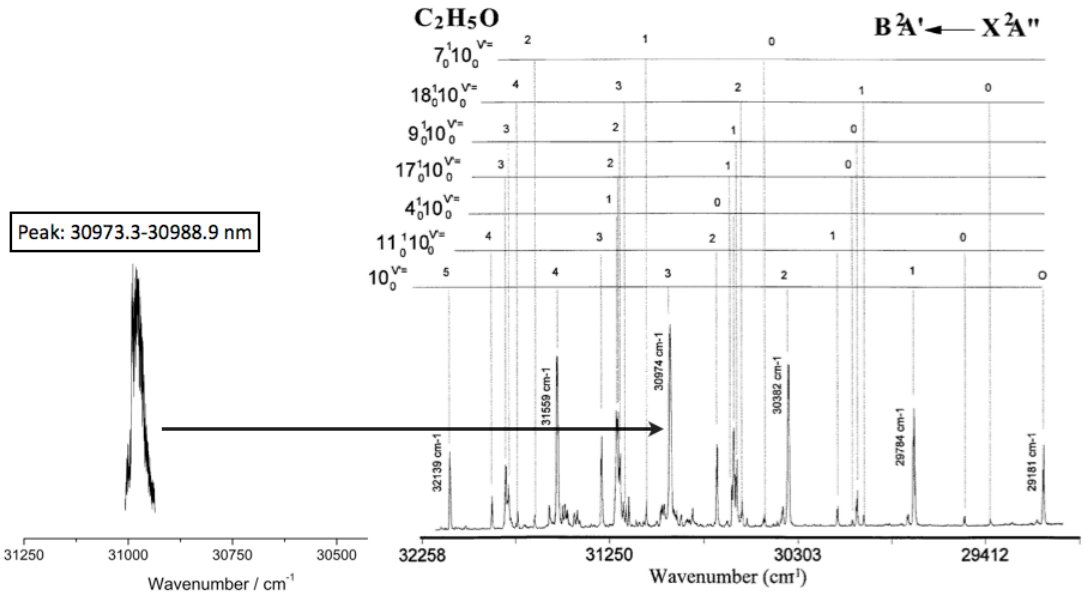

Figure 3. 20: Laser excitation spectrum of the ethoxy radical obtained from 248 nm photolysis of ethyl nitrite from this work (left), correseponding to the $B^2A' \leftarrow X^2A''$ $\nu_{10} = 3 \leftarrow 0$ band alongside the ethoxy radical laser excitation spectrum reproduced from Zhu *et al.* (cold jet expansion).[54]

The detection of the ethoxy radical was first attempted via time dependent traces over at the maximum transition wavelength identified using the alkoxy radical precursor. Growth in the signal was not seen with time nor was any signal observed on the oscilloscope, and so LIF scans were performed at long laser delay times over the wavelength range used to identify the maximum in the LIF spectra from the alkoxy radical precursors.

A possible secondary reaction which could influence the ability to observe ethoxy radical product from the OH + ethanol reaction is the reaction of the alkoxy radical with O_2, which is introduced into the jet through the ozone cylinder (there is ~ 2 % conversion from oxygen to ozone by the corona discharge of oxygen). The rate coefficient for this reaction has not previously been studied at low temperatures, however the room temperature rate coefficient reported by Gutman *et al.* is 7.97×10^{-15} molecule^{-1} cm^3 s^{-1}.[61] To investigate whether this reaction may affect the lifetime of ethoxy radicals in the Laval instrument, and hence reduce the reactivity of ethoxy with oxygen, the rate coefficient of this reaction was measured at 88 ± 5 K and (3.5 ± 0.5) × 10^{16} molecule cm^{-3}, using ethyl nitrite as a photolytic precursor of ethoxy radicals. The pseduo first order rate coefficients obtained from this reaction as a function of oxygen concentration as shown in Figure 3. 21.

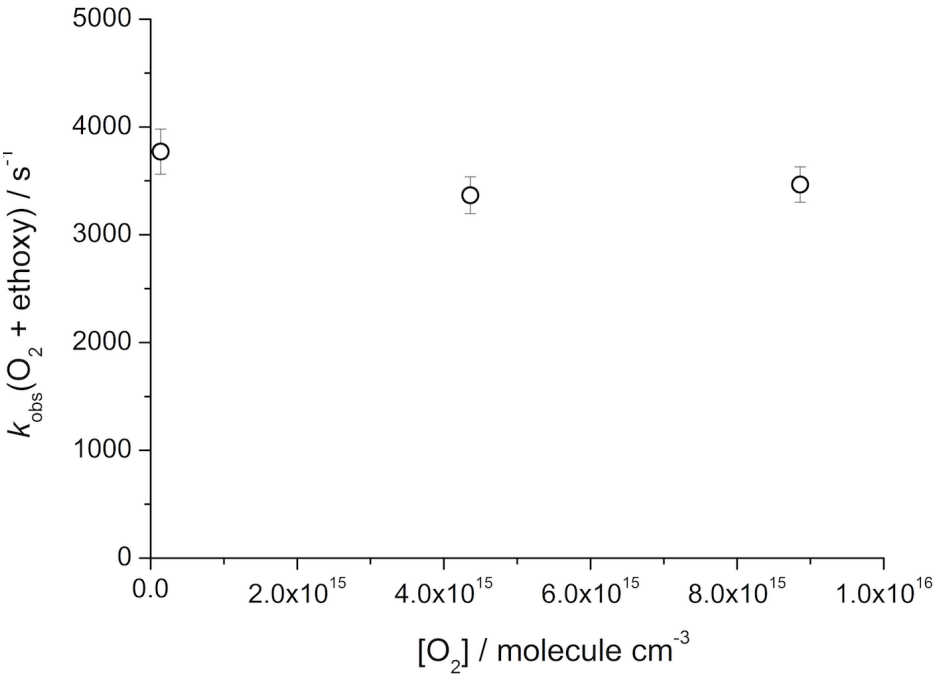

Figure 3. 21: Bimolecular plot obtained for the reaction of ethoxy radicals with oxygen at 88 ± 5 K and (3.5 ± 0.5) × 10^{16} molecule cm^{-3}, using N_2 bath gas. Ethyl nitrite concentration = 7.8 × 10^{12} molecule cm^{-3}, yielding an ethoxy radical concentration of ~ 1.9 × 10^{12} molecule cm^{-3} , with a given photolysis laser energy of 291 mJ/pulse. The flat gradient of the bimolecular plot for ethoxy + oxygen indicates that under our experimental conditions, this reaction will not act as a significant loss process for ethoxy radicals, and thus will not influence our ability to detect ethoxy radicals from OH + alcohol reactions.

As it can be observed from the apparent independence of the decay rate of ethoxy radicals on oxygen concentration in Figure 3. 21, the ethoxy radical concentration is not reduced in the presence of oxygen on the timescale of the Laval experiment, and so this reaction is not expected to be a significant loss channel for ethoxy radicals produced in the OH + ethanol reaction.

The methoxy radical was previously detected by Shannon *et al.* from the reaction of OH with methanol at 82 K using this apparatus, via the $\tilde{A}^2A_1 \leftarrow \tilde{X}^2E, \nu_3 = 3 \leftarrow 0$ transition at ~298 nm.[32] To optimise the experimental setup for the detection of alkoxy radical product species, methoxy radical detection following the reaction of OH with methanol was attempted using the $\tilde{A}^2A_1 \leftarrow \tilde{X}^2E, \nu_3 = 1 \leftarrow 0$ transition at ~ 310 nm. Although it must be noted that the same band was not used, the same electronic transition was probed, and literature spectra demonstrate that these bands have comparable intensity.[55] As for the ethoxy radical, the methoxy radical was unable to be directly detected by LIF. The only experimental evidence for the production of both alkoxy radicals was the presence of a chemiluminecsence-like signal with a lifetime of 2 μs at emission wavelengths between 360-440 nm. In a further attempt to detect the methoxy radical product, a series of experiments were then performed on a flowtube apparatus coupled with LIF and mass

spectrometry, in collaboration with Professor J. Plane and Dr J.C. Gomez Martin. Using this apparatus, the temperature of the flowtube could be gradually cooled from room temperature down to 140 K. A brief experimental outline is given below for this apparatus prior to presenting results from this study.

3.4.3 Experimental procedure - Cryogenically cooled flowtube apparatus

Experiments were performed using a cryogenically cooled flowtube coupled to a 6-way cross PLP-LIF cell as shown in Figure 3. 22. This experimental setup was also employed for the measurements of the OH + methanol rate coefficients performed by Dr J.C. Gomez Martin as part of a joint publication, and as shown in Figure 3. 10.[40]

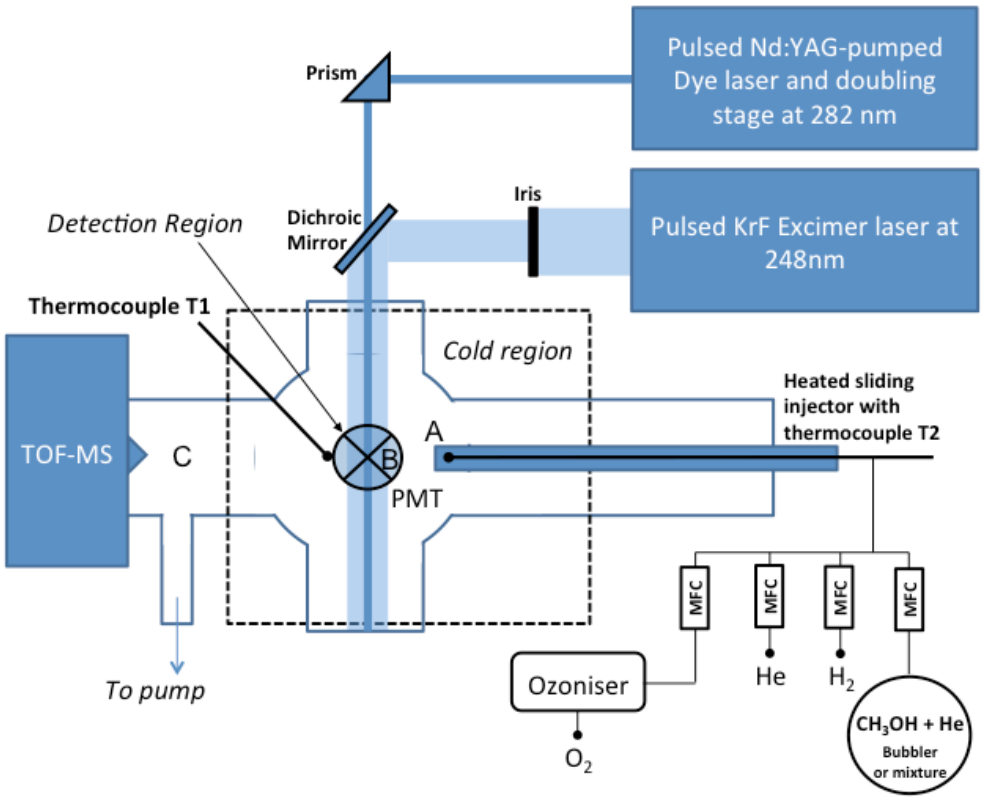

Figure 3. 22: Low temperature flowtube coupled with 6-way cross photolysis cell. The photolysis and probe lasers for laser induced fluorescence detection are collinearly aligned through the 6-way cross cell, perpendicular to the axis of gas flow. A indicates the injection point of the gas mixture into the photolysis cell. B indicates the reaction zone. C indicates the region where the methanol concentration is sampled by the TOF-MS. Diagram reproduced with permission from Dr Gomez Martin.[40]

The apparatus, which was insulated using neoprene, was cooled by liquid nitrogen that was circulated around copper tubing that surrounded the photolysis cell and a portion of the flowtube upstream of the photolysis cell. The temperature was controlled by a thermocouple positioned at the 6-way cross end of the flowtube providing feedback to a temperature controlled solenoid valve on the liquid nitrogen dewar. The gas was delivered by a sliding injector which was heated by a 20 W wire to avoid condensation of methanol. The sliding injector was positioned 3 cm upstream of the OH detection region in the photolysis cell to allow sufficient time for the gas mixture, which was warmed from the heating wire, to cool.

One of the biggest challenges in performing low temperature chemical kinetics is the potential loss of reactants to the cold walls of the reaction cell. To characterise the loss of methanol to the walls, an electron impact mass spectrometer (Kore Ltd.) positioned 20 cm downstream of the reaction chamber (and out of the cooled region) was utilised. Methanol was then monitored throughout the experiments by its fragmentation peaks at m/z 15,29 and 30.

OH was generated by the flash photolysis of ozone in the presence of H_2 using a 248 nm excimer laser (Lambda-Physik Complex 102) operating at 10 Hz. He bath gas (99.9999 %, BOC), ozone (generated from the electrical discharge of O_2 (99.995 % BOC)), methanol (≥ 99.9 % Sigma-Aldrich, seeded in He bath gas via a bubbler) and H_2 (99.9999 %, BOC) were delivered to a mixing manifold by a set of calibrated mass flow controllers (MKS). The mixed gas was then delivered to the sliding injector at a total flow rate of ~ 250 sccm yielding a reactor pressure of 0.5 - 3 Torr. Methoxy detection was attempted by LIF excitation of the $\tilde{A}^2A_1 \leftarrow \tilde{X}^2E$ band at ~310 nm by the frequency doubled output of an Nd:YAG pumped dye laser (Continuum Surelite II, Lambda Physik Cobra Stretch with KDP doubling crystal). The signal was detected by a PMT (Thorn EMI, B-216F) through a 400 ± 40 nm interference filter (Thorlabs) and visualised by an oscilloscope (LeCroy Waverunner LT 342) before being transferred to a PC for analysis.

Three back-to-back experiments were performed in the flowtube apparatus to attempt to elucidate the emission resulting from methoxy produced from the OH + methanol reaction. The three traces resulting from these experiments were obtained under the following conditions:

(1) **He/O_3:** To obtain the background signal from the excimer and probe lasers.

(2) **He/O_3/CH_3OH:** $O(^1D)$ is produced from ozone photolysis at 248 nm (P3.2). $O(^1D)$ then reacts with methanol (R3.8), which yields the methoxy radical with a branching ratio of ~ 0.82 reported by Matsumi *et al.*[62] This ensured that the probe laser was aligned to a wavelength coincident with the methoxy radical excitation spectrum.

$$O_3 \xrightarrow{248\,nm} O(^1D) + O_2 \qquad \text{P3.2}$$

$$O(^1D) + CH_3OH \longrightarrow OH + CH_3O \qquad \text{R3.8a}$$

$$O(^1D) + CH_3OH \longrightarrow H + HOCH_2O \qquad \text{R3.8b}$$

(3) **He/O_3/CH_3OH/H_2:** The $O(^1D)$ generated via O_3 photolysis was intercepted by H_2 yielding OH, which could then react with methanol.

$$O_3 \xrightarrow{248\,nm} O(^1D) + O_2 \qquad \text{P3.2}$$

$$O(^1D) + H_2 \longrightarrow OH\ (v \geq 0) + H \qquad \text{R3.6}$$

$$OH\ (v \geq 0) + M \longrightarrow OH\ (v = 0) + M \qquad \text{R3.7}$$

$$OH + CH_3OH \longrightarrow products \qquad \text{R3.2}$$

$$OH + CH_3OH \longrightarrow CH_2OH + H_2O \qquad \text{R3.2a}$$

$$OH + CH_3OH \longrightarrow CH_3O + H_2O \qquad \text{R3.2b}$$

The concentrations of the reactants used in these experiments were as follows; [O_3] ~ 2 × 10^{14} molecule cm^{-3}, [methanol] ~ 1 × 10^{15} molecule cm^{-3} and [H_2] ~ 1 × 10^{16} molecule cm^{-3}. Prior to analysis, trace (1) was subtracted from traces (2) and (3) to remove the background signal due to the photolysis laser. Subsequent subtraction of trace (2) from trace (3) yielded the methoxy signal from the reaction of OH + methanol.

The back-to-back experiments were performed at a range of temperatures between 223 and 143 K. Experiments were not conducted below 143 K owing to substantial wall loss effects.

3.4.4 Results and discussion - Cryogenically cooled flowtube apparatus

At temperatures above 180 K, there was no overall methoxy radical signal from the OH + methanol reaction although the methoxy radical was readily observed from experiment (2) when the probe laser was fired.

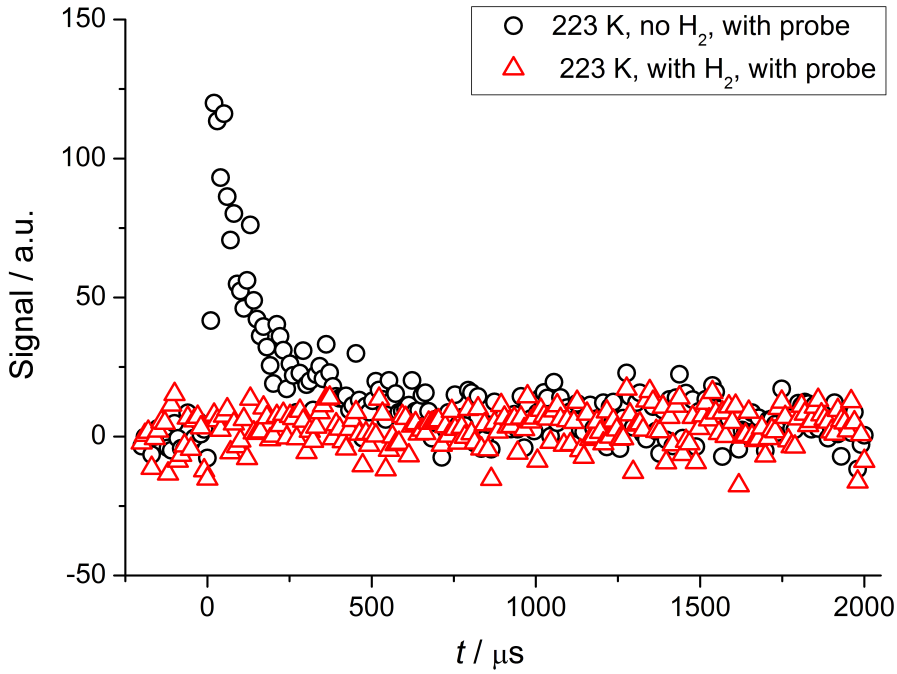

Figure 3. 23: Signal as a function of time at 223 K when the probe laser was fired in the absence (open black circles) and presence (open red triangles) of hydrogen, corresponding to the experimental conditions of traces (2) and (3) respectively. The background signal resulting from the photolysis and probe lasers has been subtracted from both traces.

Below 180 K, the LIF signal was overwhelmed by a much larger signal (emission at wavelengths between 360-440 nm), which was present even without the probe laser firing, this signal was also observable in the Laval setup. The lifetime of this signal was similar to the fluorescence lifetime of methoxy (~ 2 μs) and so would obscure any signal resulting from methoxy radical fluorescence. At 163 K, the signal from (2) was larger than that observed under the conditions of experiment (3), both without the probe laser. Below 163 K, the signal observed when H_2 was added to the system was larger, as shown in Figure 3. 24, both in the absence of the probe laser.

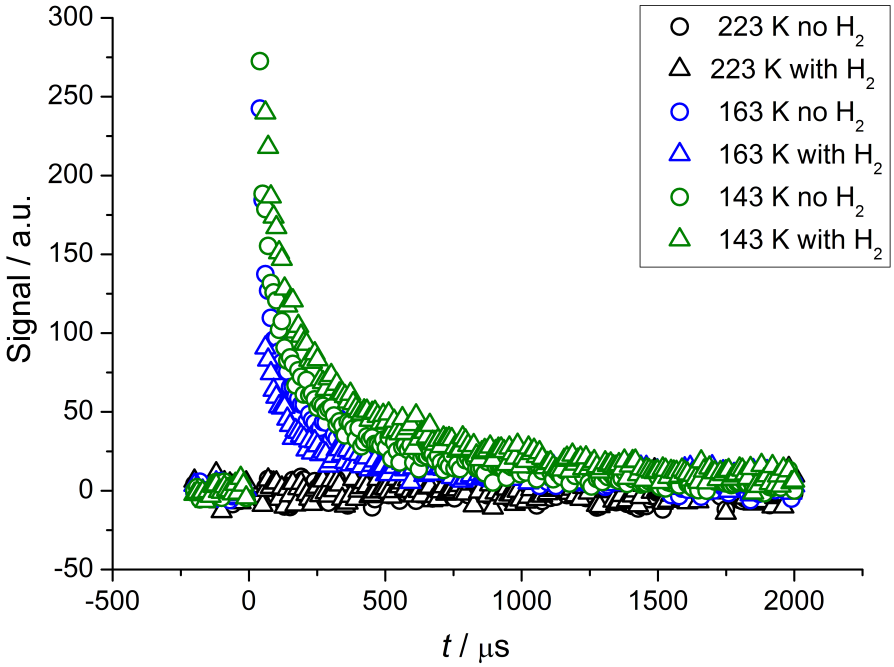

Figure 3. 24: Chemiluminescence signal as a function of time resulting from the OH + methanol reaction, in the presence and absence of hydrogen (traces 3 and 2), as a function of temperature. For 163 K and 223 K, it can be seen that the signal in the absence of hydrogen is larger than in the presence of hydrogen – indicating that the OH + methanol is not contributing to the chemiluminescence signal. However, at 143 K, the signal in the presence of hydrogen is larger than without indicating the formation of methoxy from OH + methanol.

It is proposed that this signal observed at low temperatures is chemiluminescence from internally excited formaldehyde, which is anticipated to be produced by the reactions of methoxy radicals with H atoms (present from the reaction of H_2 with $O(^1D)$ and also with OH. The presence of the signal in the absence of the probe laser gives support to the signal being chemiluminescenct in nature. A chemilumiscent signal in the visible/ UV wavelength would require the formaldehyde to be produced in an electronically excited state, which as shown below, would be accessible from the energetics of the proposed reactions.

$CH_3O + H \longrightarrow CH_2O + H_2$ ($\Delta H°298 = -341.7$ kJ mol^{-1}) R3.9

$CH_3O + OH \longrightarrow CH_2O + H_2O$ ($\Delta H°298 = -402.0$ kJ mol^{-1}) R3.10

The $^1A''$ excited electronic state lies 337.3 kJ mol^{-1} above the $^1A_1$ ground state of formaldehyde and therefore would be made accessible by the exothermicity of either of the above reactions. However, this would require non-statistical partitioning of the energy released from the exothermic reactions into the electronic transition of formaldehyde. The transition $\tilde{A}^1A'' \rightarrow \tilde{X}^2A_1$ results in the well-characterised 350 nm band system of formaldehyde, and is a plausible explanation for the observed signal.[63-65]

The onset of the signal is coincident with the apparent low temperature turnaround in the rate coefficient for OH + methanol and the magnitude of the signal increases with decreasing temperature. The branching of OH + methanol to the methoxy radical also increases with decreasing temperature, which corroborates that this signal is a proxy for the production of methoxy.[32] For this mechanism to be viable there are a few further conditions that need to be satisfied, and these are outlined below. First, the reactions for the formation of formaldehyde must be sufficiently fast so that signal could be observed within the experimental timeframe. Room temperature measurements in the literature for reactions R3.9 and R3.10 report rate coefficients are 3.3×10^{-11} and 3×10^{-11} molecule^{-1} cm^3 s^{-1}, respectively.[66,67] Given the initial O(^{1}D) concentration of ~ 3×10^{13} molecule cm^{-3} (from the quantum yield and cross section of ozone photolysis at 248 nm, the laser energy, and the initial ozone concentration), $k_{3.9}$'~ $k_{3.10}$' is around 1000 s^{-1}, which is within the timescale of the flowtube experiment. Another consideration is that CH_2OH (a possible product from OH + methanol) may also react rapidly with OH to form formaldehyde with sufficient exothermicity (370.3 kJ mol^{-1}) that it may occupy the ^{1}A'' state. However, whilst this reaction is fast (4×10^{-11} molecule^{-1} cm^3 s^{-1}),[68] it is not competitive with the reaction of CH_2OH with O_2,[69] which is much less exothermic (81.7 kJ mol^{-1}) and therefore would not produce formaldehyde in the ^{1}A'' state.

Numerical modelling has been undertaken by Dr J.C. Gomez Martin using the energetics above to assess the feasibility of the aforementioned scheme. A model including the rate coefficients of the reactions listed in Table 3. 3, the excited state lifetime of CH_2O ^{1}A'' and the branching ratios for OH + methanol calculated by Shannon *et al.*, was used to simulate the integrated chemiluminscence signal in the presence of hydrogen and the absence of the probe laser.[32] Experimental data for these conditions are shown below in Figure 3. 25.[32] The majority of the rate coefficients for the reactions utilised by Dr Gomez Martin (and listed in Table 3. 3) have not been studied below room temperature, and so this model is semi-quantative. Except for R3.2a and R3.2b, the reaction rate coefficients employed in the model are room temperature values and where necessary, branching ratios. In the case of R3.2a and R3.2b, the rate coefficients utilised were those reported in a joint publication with Dr Gomez Martin measured using a cryogenically cooled flowtube apparatus.[40] The temperature dependent branching ratios for the OH + methanol reaction (R3.2a and R3.2b) were obtained from the master equation calculations by Shannon *et al.*[32]

Table 3. 3: Reactions included in the numerical model constructed and employed by Dr J.C. Gomez Martin to model the observed chemiluminescence.

Reaction	$\Delta H°_{298}$/ kJ mol^{-1}	$k_{(298\ K)}$ / molecule^{-1} cm^3 s^{-1}		
$O_3+h\nu \rightarrow O(^1D)+O_2$		1×10^{20} (s^{-1})	Matsumi *et al.*[70]	P3.2
$OH+CH_3OH \rightarrow CH_2OH+H_2O$	-86.0	N/A	This work.[40]*	R3.2a
$OH+CH_3OH \rightarrow CH_3O+H_2O$	-54.3	N/A	This work.[40]*	R3.2b
$O(^1D)+H_2 \rightarrow OH(v>0)+H$	-183.2	1.1×10^{-10}	Atkinson *et al.*[71]	R3.6
$OH(v>0)+M \rightarrow OH(v=0)+M$		M= CH_3OH: 3.0×10^{-11}	Arbitrarily high[‡]	R3.7
$O(^1D)+CH_3OH \rightarrow OH+CH_3O$	-177.2	5.1×10^{-10} (ϕ= 0.82)	Matsumi *et al.*[62]	R3.8a
$O(^1D)+CH_3OH \rightarrow H+HOCH_2O$	-196.7	5.1×10^{-10} (ϕ= 0.18)	Matsumi *et al.*[62]	R3.8b
$CH_3O+H \rightarrow CH_2O+H_2$	-341.7	3.3×10^{-11}	Hoyermann *et al.*, Tsang and Hampson.[66,67]	R3.9
$CH_3O+OH \rightarrow CH_2O+H_2O$	-402.0	3.0×10^{-11}	Tsang and Hampson.[67]	R3.10
$O(^1D)+O_2 \rightarrow O(^3P)+O_2$		4.0×10^{-11}	Atkinson *et al.*[71]	R3.11
$CH_2OH+O_2 \rightarrow CH_2O+HO_2$	-81.7	1.2×10^{-12}	Radford[69]	R3.12
$CH_2OH+OH \rightarrow CH_2O+H_2O$	-370.3	4×10^{-11}	Tsang *et al.*[68]	R3.13
$CH_3O \rightarrow CH_2O + H$	-402.0	1×10^{7} (s^{-1})	Tsang *et al.*[68#]	R3.14

*Branching ratio (ϕ) obtained from the master equation calculations by Shannon *et al.*[32]
[#]Estimated given the exothermicity of the R3.8a. [‡]Arbitrarily high value as chemiluminescence is not sensitive to this parameter and relaxation is fast on timescale of reaction.

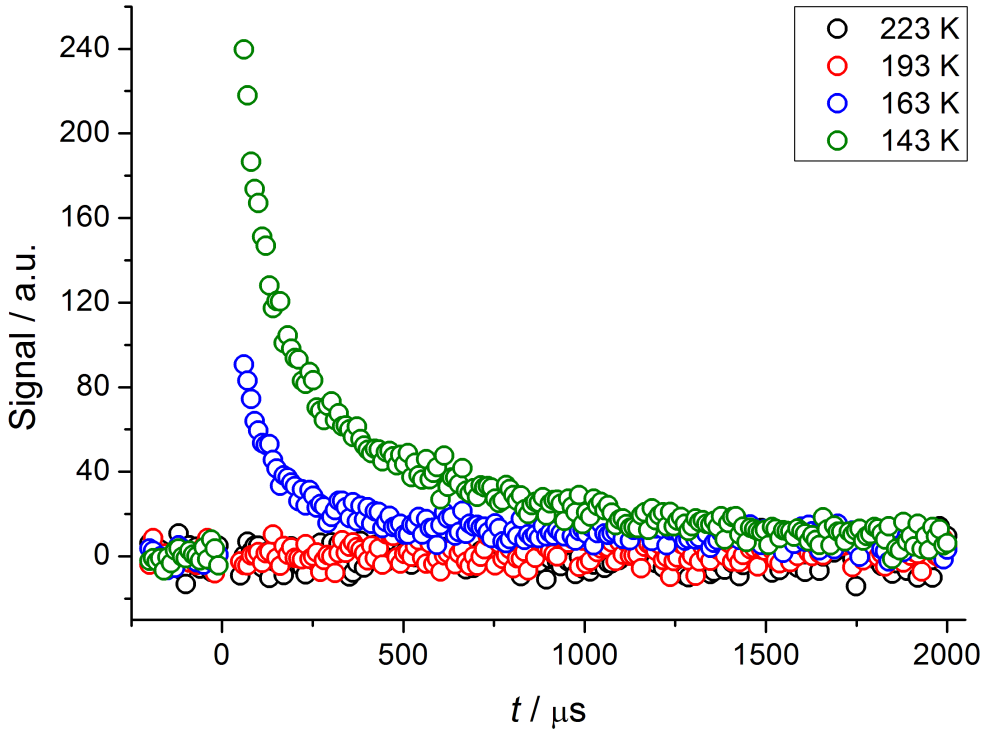

Figure 3. 25: Chemiluminescence signal as a function of time resulting from the OH + methanol reaction, in the presence hydrogen without the probe laser firing, as a function of temperature.

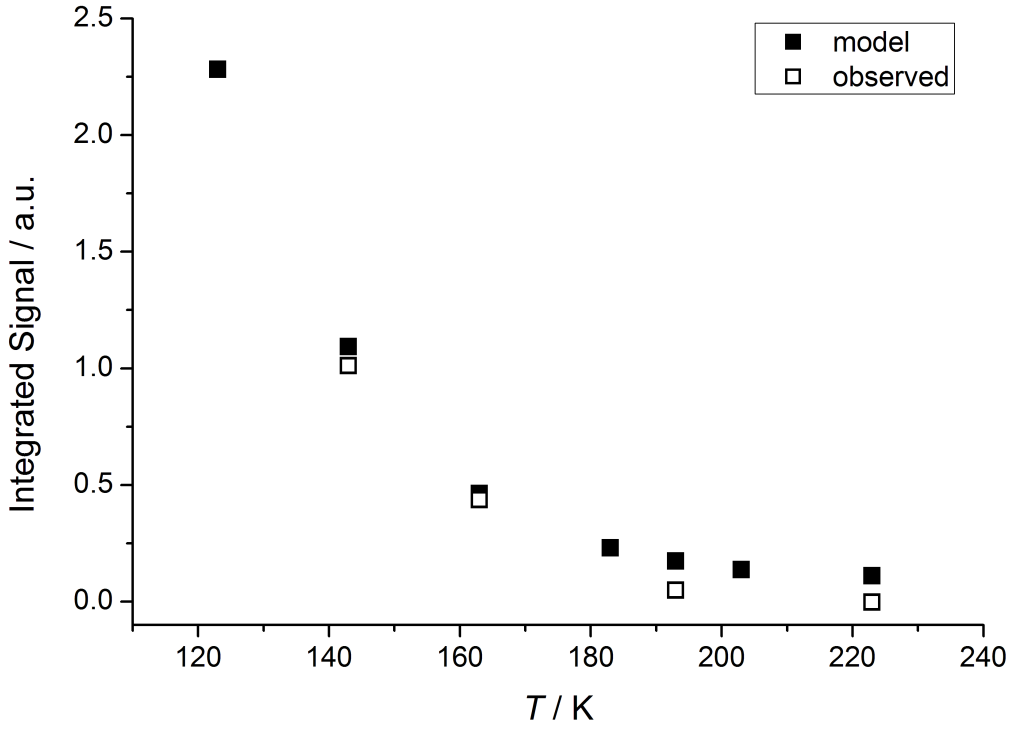

Figure 3. 26: Integrated signal obtained from the numerical model compared with the integrated signal obtained experimentally, as shown in Figure 3. 25. Modelled signal is normalised by a constant factor to aid comparison with experimental data. Figure reproduced with permission from Dr Gomez Martin.[40]

As shown in Figure 3. 26, the model shows good agreement with the observed increase in intensity as the temperature is lowered. This indicates that the model accounting for the apparent chemiluminescenct signal is viable, and therefore the chemiluminescenct signal may be interpreted as a proxy for the methoxy radical formation in our experimental setup. Kinetic data regarding the formation of electronically excited formaldehyde unfortunately cannot be obtained from these chemiluminescence traces owing to overloading of the PMT at early times from excimer laser scatter, leading to incorrect temporal behaviour.

Reactions R3.9 and R3.12 could be avoided with an alternative OH precursor, for example, $(CH_3)_3COOH$, which is more commonly used to produce OH in our experiments. However, due to limited sensitivity to alkoxy radicals in our system (OH, via excitation at 308 nm, is around a factor of 300 easier to detect than methoxy radicals, see Appendix D) the use of ozone as an OH precursor has been previously shown by Shannon *et al.* to be a necessity in these experiments as it can produce a much higher concentration of OH, and subsequently a higher concentration of the alkoxy products.[32,52]

To reduce the loss of methoxy radicals from secondary chemistry, specifically reaction R3.9, OH could instead be produced using ozone/H_2O, which would remove H atoms from the system.

$$O_3 + h\nu \rightarrow O(^1D) + O_2 \qquad \text{P3.2}$$

$$O(^1D) + H_2O \rightarrow 2OH \qquad \text{R3.15}$$

However this is reliant of sufficient water vapour being delivered to the jet without significant freezing out. Whilst LIF allows sensitive detection on a zero background, it may be possible to utilize mass spectrometry to directly detect the products for this system. For example, it may be possible to couple a cryogenically cooled flowtube system with a multiplexed photoionization mass spectrometer or iPEPICO (imaging photoion photoelectron coincidence spectroscopy), and confirm the products of the reaction both by mass spectrometry and photoionization spectra using synchrotron radiation as the ionization source.[72-74]

3.5 Interstellar impact of OH + alcohol reactions

The potential impact of OH + alcohol reactions has been assessed through astrochemical modelling in collaboration with Dr Kinsuk Acharyya and Professor Eric Herbst at the University of Virginia.[41] Acharyya and Herbst constructed a model encompassing both gas phase and gas-grain processes, comprising reactions from the KIDA database with recommended and valid status, and those listed by Garrod *et al.*[75] In the gas phase 8620 reactions were included involving 670 species. The temperature dependence of these reactions was approximated using a modified Arrhenius expression where α, β and γ are parameters.

$$k(T) = \alpha \left(\frac{T}{300}\right)^{\beta} exp\left(-\frac{\gamma}{T}\right) \quad \text{E3.9}$$

Ion-neutral reactions were treated in one of two ways depending on whether the neutral reactant was considered polar or non-polar. The difference between the former and the latter treatment is as to whether the long-range capture forces are non-central (former) or central (latter).

For the non-polar case, a Langevin value of the rate coefficient (k_L) was obtained using E3.10, where α is the dipole polarisability and μ is the reduced mass of the reactants.

$$k_L = 2\pi\, exp\left(\frac{\alpha}{\mu}\right)^{0.5} \quad \text{E3.10}$$

In the case of polar molecules, the Su- Chesnavich approach was utilised.[76] Firstly, the value of χ was calculated using the dipole moment (μ_D) as shown in E3.11, where α is the dipole polarisability and K_B is the Boltzmann constant.

$$x = \frac{\mu_D}{(2\alpha K_B T)^{0.5}} \quad \text{E3.11}$$

If the value of χ was determined to be less than 2, then E3.12 was utilised, and if χ was determined to be equal or greater than 2, E3.13 was used.

$$\frac{k_D}{k_L} = \frac{(x+0.5090)^2}{10.5026+0.9754} \quad \text{E3.12}$$

$$\frac{k_D}{k_L} = 0.4767x + 0.6200 \quad \text{E3.13}$$

The gas phase reaction types included in the model are shown alongside a brief description in Table 3. 4.

Table 3. 4: Gas phase reactions types included in the model constructed by Dr Kinsuk Acharyya and Professor Eric Herbst. Table taken from the resultant joint publication by Acharyya *et al*.[41]

Reaction type	Description
Direct CR process	Dissociation or ionization of species due to collision with cosmic rays
CR induced photo processes	Dissociation or ionization of species due to secondary UV photons
Photo processes	Dissociation or ionization of species due to external interstellar UV field
Bimolecular reactions	Including neutral-neutral, ion-neutral, ionic, and associative ionization reactions
Charge exchange reactions	Reaction between two oppositely charged particles
Radiative association	Association reaction between two species stabilised by photon emission.
Associative detachment	Association of a neutral species and an anion resulting in the ejection of an electron
Dissociative recombination	Recombination of a positive ion with an electron resulting in the dissociation of the parent neutral
Radiative attachment	Emission of a photon following the attachment of an electron to a neutral radical

Surface reactions were also included in the model, these types of reactions are beyond the scope of this thesis and so only a brief outline of their treatment is given. Laboratory studies of astrochemically relevant reactions on the surface have been shown to operate only via the Langmuir-Hinshelwood mechanism, whereby the gas phase species must both be adsorbed onto the surface before reaction can occur. Very few laboratory studies have found evidence as of yet for the Eley-Rideal mechanism - where only one species is adsorbed onto the surface and reacts with a gas-phase species. As such, only the Langmuir-Hinshelwood case is accounted for in the model.

For a surface reaction between species *j* and *k*, the rate of adsorption of the gas phase species onto the grain surface is calculated using E3.14

$$r_{ad(j)} = S_j \sigma v_j [j] \quad \text{E3.14}$$

where S_j is the sticking probability (assumed to be 0.5 or 1), σ is the cross section of the grain (in cm^2), v_j is the velocity of the adsorbing gas phase species, and [*j*] is concentration of *j* (cm^{-3}).

To participate in a reaction, the adsorbed species must diffuse along the surface to encounter a co-reagent. The rate of diffusion is given by E3.15

$$r_{diff} = \frac{v_0 \exp\left(\frac{-E_b}{T_d}\right)}{N_s} \quad \text{E3.15}$$

where v_0 is the attempt frequency for the adsorbed species (assumed to be on the order of 10^{12} s^{-1}) , E_b is the energy barrier between different adsorption sites, T_d is the temperature of the grain and N_s is the total number of sites.

Finally, the bimolecular reaction between species *j* and *k* is calculated by E3.16

$$k_{jk} = \kappa_{jk}\left(r_{diff,j} + r_{diff,k}\right) n_j n_k [grain] \quad \text{E3.16}$$

where κ_{jk} is the probability of reaction to occur between species *j* and *k* upon an encounter, n_j and n_k are the number of species of type *j* and *k* per grain, and [*grain*] is the number of grains per volume.

Recent experimental work has found evidence for tunnelling through the barrier to diffusion along grain surfaces for species as large as oxygen atoms.[77,78] However, the model employed in the current work does not account for this type of behaviour. A total of 2764 surface reactions between 247 species were included in the model.

The initial gas phase elemental abundances were representative of cold clouds and H_2, all species were in their atomic components. The standard total hydrogen density (n_H), which is the sum of the concentrations of atomic hydrogen and twice the concentration of molecular hydrogen, was set to a value of 2×10^4 cm^{-3}. The model as operated in pseudo time dependence mode, whereby the physical parameters (such as temperature, the cosmic ray ionisation rate and sticking coefficients) were kept the same throughout the model and the temporal evolution of the species through is monitored.

The model was run at three temperatures, 10, 50 and 100 K. The OH + propan-2-ol reaction was not included in the model as there are no confirmed interstellar detections of propanol as of yet. The rate coefficients utilised in the model for the OH + methanol reaction were those from the MESMER fit by Shannon *et al.*[32] For the OH + ethanol reaction, the

experimentally obtained values at 56 K and 86 K were utilised for 50 and 100 K respectively, however it must be noted that these values will be an upper limit to the true values as they contain a contribution from the pressure dependence channel. Therefore, these values will subject to error and to obtain more accurate values, full master equation analysis of this reaction should be performed. The values utilised in the model are summarised in Table 3. 5.

Table 3. 5: Rate coefficients utilised in the model constructed by Dr Kinsuk Acharyya and Professor Eric Herbst.[41]

Reaction	Rate coefficient utilised / 10^{-10} molecule^{-1} cm^3 s^{-1}		
	10 K	50 K	100 K
OH + methanol	3.0	0.49	0.38
OH + ethanol	0.6	0.6	0.5

The products of the reactions were assumed to be the methoxy radical or the ethoxy radical and water vapour (R3.2b and R3.3c).

The model results show that the OH + ethanol reaction has little impact on the hydroxyl radical and ethanol abundances and is unlikely to be a significant loss channel for these species in interstellar environments.

The OH + methanol has a higher impact. The maximum enhancement in methanol loss when the OH + methanol reaction is included in the model is at 10 K and 5×10^5 years, where the methanol concentration is reduced by 20 %. This loss is decreased at 50 and 100 K, corresponding to the slower rate coefficient for the OH + methanol reaction at higher temperatures. At 10 K, the maximum enhancement of H_2O when the alcohol reactions are included is by 25 %, which occurs at 5×10^6 years, as shown in Figure 3. 27.

At 10 K and 10^6 years, the concentration of the methoxy radical is twice as large when the OH + methanol reaction is included in the model, as shown in Figure 3. 28. At 50 K, the maximum enhancement in the methoxy radical concentration is 50 % (at 2×10^6 years) and at 100 K, the methoxy radical concentration is enhanced only by 2 %.

There were no loss routes of the alkoxy radical products included in the model and as such the methoxy radical concentration was overestimated by at least a factor of 30 at 10 K compared to astrochemical observations. Potential loss routes of alkoxy radicals relevant to cold astrochemical environments should therefore be investigated to aid future modelling work.

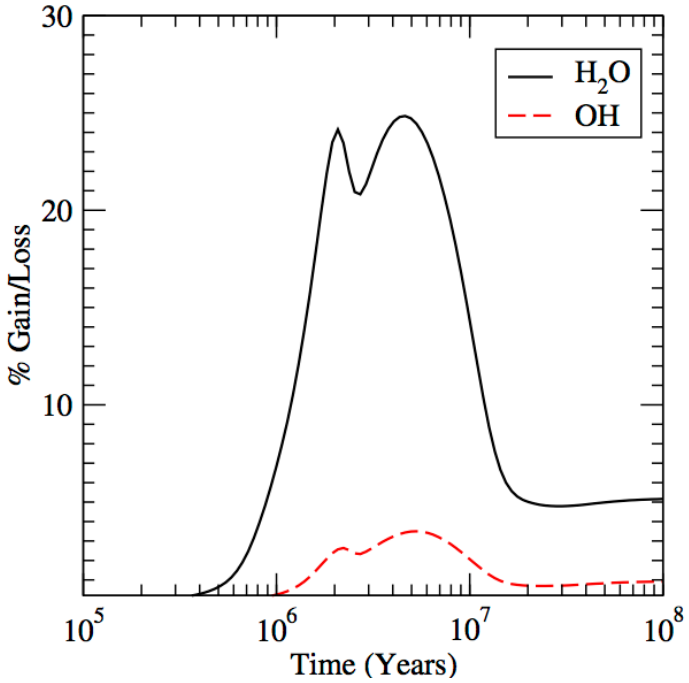

Figure 3. 27: Temporal percentage gains or losses of water vapour (black line), and the hydroxyl radical (red dashed line) on the inclusion of the OH + alcohol reactions compared to without. Reproduced from Acharyya *et al.*[41]

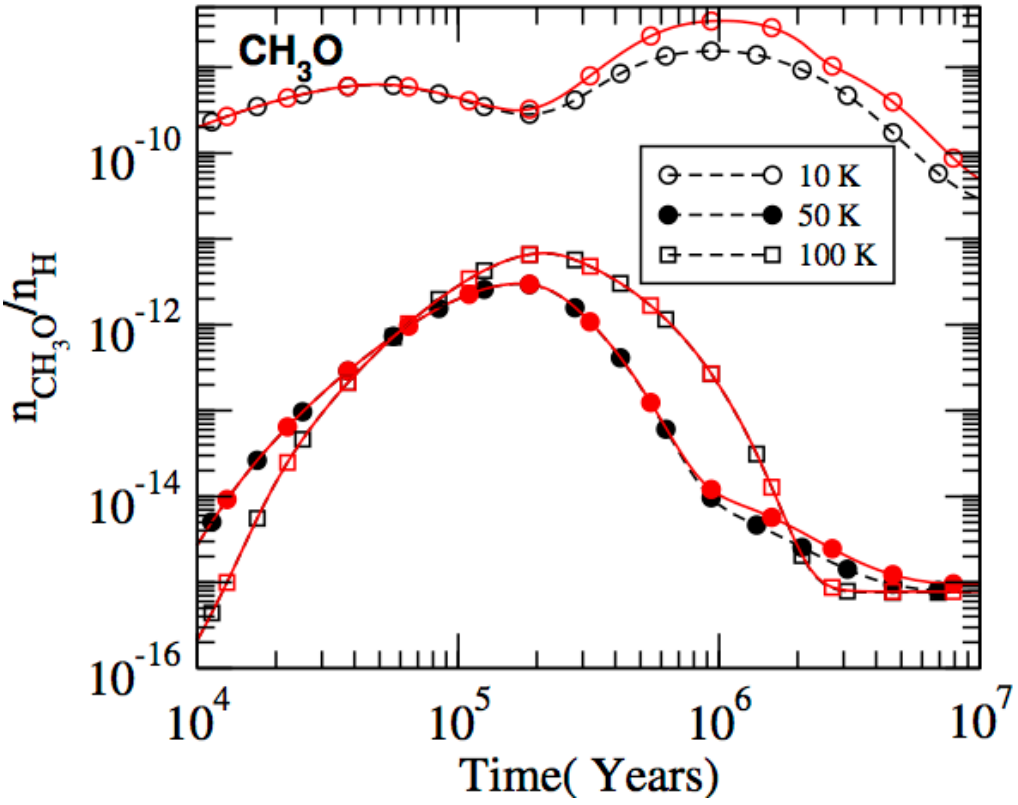

Figure 3. 28: Temporal methoxy radical concentration with respect to hydrogen as a function of temperature, with (red symbols and lines) and without (black symbols and lines) the OH + methanol reaction included in the literature. Reproduced from Acharyya *et al.*[41]

3.6 Summary

This chapter has covered the work undertaken on the low temperature kinetics of OH + alcohol reactions. Prior to this work, only one study had been performed on the reaction kinetics of OH with methanol below 200 K. The work by Shannon *et al.*, also performed in this laboratory, demonstrated a dramatic negative temperature dependence of the rate coefficient below 200 K with measurements of the rate coefficient at 65 K.[32] However, there was significantly uncertainty about the turnaround in the rate coefficient from the apparent Arrhenius-type high temperature behaviour and the low temperature kinetic behaviour. The current work has built upon the work by Shannon *et al.* through kinetic measurements of the OH + methanol rate coefficient at both higher (138-148 K) and lower (54 K) temperatures than measured in the previous work.[40] The experimentally obtained rate coefficients support the work of Shannon *et al.*[40] Further experimental rate coefficients have been obtained by Dr Gomez Martin as part of a collaboration, using a cryogenically cooled flow tube apparatus.[40] The results obtained by Dr Gomez Martin overlap with data by Dillon *et al.*, and also with the 138-148 K data reported in this thesis.[4,40]

The reaction kinetics of OH with ethanol and with propan-2-ol have been studied below 200 K for the first time. [42] Similar behaviour is observed for the low temperature kinetics as for the OH + methanol reaction. A common mechanism operating in these reactions has been identified, involving the formation of a weakly bound complex prior to the overall barrier to hydrogen abstraction. The extended lifetime of this complex at decreasing temperatures enhances the probability of transmission through the barrier by quantum tunnelling. For the longer chain alcohols, a pressure-dependent channel is also observed which corresponds to the collisional stabilisation of the weakly bound complex in to the pre-barrier well. Study of the pressure dependence of the rate coefficients and fitting the data with an extended Lindemann-Hinshelwood expression has enabled the low pressure limiting rate coefficients for the OH + ethanol and propan-2-ol reactions to be obtained. These pressure independent rate coefficients, corresponding to the bimolecular H-abstraction reaction, are around a factor of 8 greater at 89 K than at room temperature for both systems. The turnaround in the pressure-independent component of the rate coefficient is less dramatic for these systems than the OH + methanol reaction. This is expected as the barrier heights for hydrogen abstraction decrease with increasing carbon chain length, as demonstrated by the calculations by Galano *et al.*, and

shown in Figures 3.1-3.3.[37] The effect therefore is two-fold: At temperatures above 200 K, the decrease in the rate coefficient with decreasing temperature becomes less steep, and at lower temperatures where tunnelling may contribute significantly to the rate coefficient, the barrier heights are lowered and so the probability of tunnelling is increased at a higher temperature.

Product detection via laser induced fluorescence spectroscopy has been attempted for the methanol and ethanol reactions. Whilst direct detection of methoxy and ethoxy radicals was unsuccessful, a chemiluminescenct signal was observed at temperatures coincident with and below where the OH + methanol reaction rate coefficient is observed to increase, and where the methoxy radical becomes the dominant reaction product. A simple chemical model constructed by Dr Gomez Martin rationalises the temperature dependent signal of the chemiluminescence by secondary reactions of the methoxy radical products. In the case of the OH + ethanol reaction, a similar chemiluminescent signal was observed in the pulsed Laval apparatus, but further investigation was not carried out. The difficulty in detecting the products of these reactions indicates the need for alternative detection methods to be coupled to the Laval apparatus, and also for high level rate theory calculations to be performed on these systems.

Methanol, ethanol and OH have been detected in appreciable concentrations in various interstellar environments where temperatures can reach as low as 10 K.[10-18,22-26,28] Despite this, the gas phase reactions between OH and alcohols have thus far been neglected or severely underestimated in interstellar networks due to extrapolation of Arrhenius data from room temperature measurements, which neglects the role of the complex. These low temperature interstellar environments are typically very low pressure (10^2-10^4 molecule cm^{-3}) and so only the bimolecular, pressure-independent tunnelling reaction would be viable.[24] From the pressure dependence measurements in this work and by Shannon, the pressure-independent bimolecular rate coefficients at low temperatures for this class of reactions are obtained for the first time. These values are of interest to the astrochemical modelling community. A collaboration with the Herbst group (U.Virginia) using our measurements in an interstellar chemical model has been undertaken to assess the potential impact of these reactions.[41] It was demonstrated that the OH + methanol reaction has a notable impact on interstellar methoxy radical abundances, and at 10 K and 10^6 years the methoxy radical is enhanced by a factor of two when the reaction is included

in the model. However, the methoxy radical concentration determined by the model is at least a factor of thirty greater than observations, suggesting unknown low temperature loss channels of the methoxy radical that should further be investigated.

3.7 References

1 Beale, R., Liss, P. S. & Nightingale, P. D. First oceanic measurements of ethanol and propanol. *Geophysical Research Letters* **37**, L24607 (2010).

2 Legreid, G. *et al.* Measurements of OVOCs and NMHCs in a Swiss Highway Tunnel for Estimation of Road Transport Emissions. *Environ Sci Technol* **41**, 7060-7066 (2007).

3 Wu, H., Mu, Y., Zhang, X. & Jiang, G. Relative Rate Constants for the Reactions of Hydroxyl Radicals and Chlorine Atoms with a Series of Aliphatic Alcohols. *Int. J. Chem. Kinet.* **35**, 81-87 (2003).

4 Dillon, T. J., Holscher, D., Sivakumaran, V., Horowitz, A. & Crowley, J. N. Kinetics of the Reactions of HO with Methanol (210-351 K) and with Ethanol (216-368 K). *Phys. Chem. Chem. Phys.* **7**, 349-355 (2005).

5 Jimenez, E., Gilles, M. K. & Ravishankara, A. R. Kinetics of the Reactions of the Hydroxyl Radical with CH_3OH and C_2H_5OH between 235 and 360 K. *J. Photoch. Photobio. A* **157**, 237-245 (2003).

6 Dunlop, J. R. & Tully, F. P. Catalytic Dehydration of Alcohols by Hydroxyl: 2-Propanol; An Intermediate Case. *J. Phys. Chem.* **97**, 6457-6464 (1993).

7 Wallington, T. J. & Kurylo, M. J. The Gas-Phase Reactions of Hydroxyl Radicals with a Series of Aliphatic-Alcohols over the Temperature-Range 240-440-K. *Int. J. Chem. Kinet.* **19**, 1015-1023 (1987).

8 Carr, S. A., Blitz, M. A. & Seakins, P. W. Site-Specific Rate Coefficients for Reaction of OH with Ethanol from 298 to 900 K. *J. Phys. Chem. A* **115**, 3335-3345 (2011).

9 Heard, D. E. in *Encyclopedia of Atmospheric Sciences* (ed R. Holton Editor-in-Chief: James) 2185-2193 (Academic Press, 2003).

10 Ball, J. A., Gottlieb, C. A., Lilley, A. & Radford, H. Detection of methyl alcohol in sagittarius. *The Astrophysical Journal* **162**, L203 (1970).

11 Garrod, R., Park, I. H., Caselli, P. & Herbst, E. Are gas-phase models of interstellar chemistry tenable? The case of methanol. *Faraday Discussions* **133**, 51-62 (2006).

12 Jørgensen, J. K., Schöier, F. L. & van Dishoeck, E. F. H_2CO and CH_3OH abundances in the envelopes around low-mass protostars. *A&A* **437**, 501-515 (2005).

13 van der Tak, F., van Dishoeck, E. & Caselli, P. Abundance profiles of CH_3OH and H_2CO toward massive young stars as tests of gas-grain chemical models. *Astronomy and Astrophysics* **361**, 327-339 (2000).

14 Friberg, P., Hjalmarson, A., Madden, S. & Irvine, W. M. Methanol in dark clouds. *Astronomy and Astrophysics* **195**, 281-289 (1988).

15 Smith, I. W., Herbst, E. & Chang, Q. Rapid neutral–neutral reactions at low temperatures: a new network and first results for TMC1.

Monthly Notices of the Royal Astronomical Society **350**, 323-330 (2004).

16 Turner, B. E. The Physics and Chemistry of Small Translucent Molecular Clouds. XI. Methanol. *The Astrophysical Journal* **501**, 731 (1998).

17 Maret, S. *et al.* CH_3OH abundance in low mass protostars. *A&A* **442**, 527-538 (2005).

18 Menten, K., Walmsley, C., Henkel, C. & Wilson, T. Methanol in the Orion region. I-Millimeter-wave observations. II-The 25 GHz masers revisited. *Astronomy and Astrophysics* **198**, 253-273 (1988).

19 Charnley, S., Kress, M., Tielens, A. & Millar, T. Interstellar alcohols. *The Astrophysical Journal* **448**, 232-239 (1995).

20 Hidaka, H., Watanabe, N., Shiraki, T., Nagaoka, A. & Kouchi, A. Conversion of H_2CO to CH_3OH by reactions of cold atomic hydrogen on ice surfaces below 20 K. *The Astrophysical Journal* **614**, 1124 (2004).

21 Watanabe, N. & Kouchi, A. Efficient formation of formaldehyde and methanol by the addition of hydrogen atoms to CO in H_2O-CO ice at 10 K. *The Astrophysical Journal Letters* **571**, L173 (2002).

22 Thi, W.-F., van Zadelhoff, G.-J. & van Dishoeck, E. F. Organic Molecules in Protoplanetary Disks Around T Tauri and Herbig Ae Stars. *Astron. Astrophys.* **425**, 955-972 (2004).

23 Ohishi, M. in *Molecules in Astrophysics : Probes and Processes. Proceedings of the 178th Symposium of the International Astronomical Union, held in Leiden, The Netherlands, July 1-5, 1996.* (ed E. F. van Dishoeck) (Kluwer Academic Publishers, 1996).

24 van Dishoeck, E. F., Blake, G. A., Draine, B. T. & Lunine, J. I. in *Protostars and planets* Vol. III (A93-42937 17-90) 163-241 (1993).

25 Millar, T. J., Macdonald, G. H. & Habing, R. J. The Detection of Hot Ethanol in G34.3+0.15. *Mon Not R Astron Soc* **273**, 25-29 (1995).

26 Smith, I. W. M., Sage, A. M., Donahue, N. M., Herbst, E. & Quan, D. The Temperature-Dependence of Rapid Low Temperature Reactions: Experiment, Understanding and Prediction. *Faraday Discuss.* **133**, 137-156 (2006).

27 Schriver, A., Schriver-Mazzuoli, L., Ehrenfreund, P. & d'Hendecourt, L. One possible origin of ethanol in interstellar medium: Photochemistry of mixed CO_2–C_2H_6 films at 11K. A FTIR study. *Chemical physics* **334**, 128-137 (2007).

28 Robinson, B. J. & McGee, R. X. OH Molecules in the Interestellar Medium. *Ann. Rev. Astron. Astr.* **5**, 183-212 (1967).

29 Shannon, R. J., Taylor, S., Goddard, A., Blitz, M. A. & Heard, D. E. Observation of a Large Negative Temperature Dependence for Rate Coefficients of Reactions of OH with Oxygenated Volatile Organic Compounds Studied at 86-112 K. *Phys. Chem. Chem. Phys.* **12**, 13511-13514 (2010).

30 Shannon, R. J., Caravan, R. L., Blitz, M. & Heard, D. E. A combined experimental and theoretical study of reactions between the hydroxyl radical and oxygenated hydrocarbons relevant to astrochemical environments. *Phys. Chem. Chem. Phys.* **16**, 3466-3478 (2014).

31 Tizniti, M. *et al.* The Rate of the F + H_2 Reaction at Very Low Temperatures. *Nature Chem.* **6**, 141-145 (2014).

32 Shannon, R. J., Blitz, M. A., Goddard, A. & Heard, D. E. Accelerated Chemistry in the Reaction between the Hydroxyl Radical and Methanol at Interstellar Temperatures Facilitated by Tunnelling. *Nature Chem.* **5**, 745-749 (2013).

33 Carr, S. A. *et al.* OH yields from the $CH_3CO + O_2$ reaction using an internal standard. *Chemical Physics Letters* **445**, 108-112 (2007).

34 Hess, W. P. & Tully, F. P. Hydrogen-atom abstraction from methanol by hydroxyl radical. *The Journal of Physical Chemistry* **93**, 1944-1947 (1989).

35 Meier, U., Grotheer, H. H. & Just, T. Temperature dependence and branching ratio of the CH_3OH+ OH reaction. *Chemical physics letters* **106**, 97-101 (1984).

36 Xu, S. & Lin, M. C. Theoretical Study on the Kinetics for OH Reactions with CH_3OH and C_2H_5OH. *P. Combust. Inst.* **31**, 159-166 (2007).

37 Galano, A., Alvarez-Idaboy, J. R., Bravo-Pérez, G. & Ruiz-Santoyo, M. E. Gas Phase Reactions of C1–C4 Alcohols with the OH Radical: A Quantum Mechanical Approach. *Phys. Chem. Chem. Phys.* **4**, 4648-4662 (2002).

38 Sivaramakrishnan, R. *et al.* Rate Constants for the Thermal Decomposition of Ethanol and Its Bimolecular Reactions with OH and D: Reflected Shock Tube and Theoretical Studies. *J. Phys. Chem. A* **114**, 9425-9439 (2010).

39 Zheng, J. & Truhlar, D. G. Multi-Path Variational Transition State Theory for Chemical Reaction Rates of Complex Polyatomic Species: Ethanol+ OH Reactions. *Faraday Discuss.* **157**, 59-88 (2012).

40 Gomez Martin, J. C., Caravan, R. L., Blitz, M. A., Heard, D. E. & Plane, J. M. C. Low Temperature Kinetics of the CH_3OH + OH Reaction. *J. Phys. Chem. A* **118**, 2693-2701 (2014).

41 Acharyya, K. *et al.* The Importance of OH Radical-Neutral Low Temperature Tunneling Reations in Interstellar Clouds Using a New Model. *Molecular Physics* **Accepted** (2015).

42 Caravan, R. L., Shannon, R., Lewis, T., Blitz, M. A. & Heard, D. E. Measurements of Rate Coefficients for Reactions of OH with Ethanol and Propan-2-ol at Very Low Temperatures. *The Journal of Physical Chemistry A* (2014).

43 Hess, W. P. & Tully, F. P. Catalytic Conversion of Alcohols to Alkenes by OH. *Chem. Phys. Lett.* **152**, 183-189 (1988).

44 Nelson, L. *et al.* Absolute and Relative Rate Constants for the Reactions of Hydroxyl Radicals and Chlorine Atoms with a Series of Aliphatic Alcohols and Ethers at 298 K. *Int. J. Chem. Kinet.* **22**, 1111-1126 (1990).

45 Romero, M. T. B. *et al.* OH Formation from the $C_2H_5CO+ O_2$ Reaction: An Experimental Marker for the Propionyl Radical. *Chem. Phys. Lett.* **408**, 232-236 (2005).

46 Jaffer, D. H. & Smith, I. W. M. Time-Resolved Measurements on the Relaxation of OH(v= 1) by NO, NO_2 and O_2. *Faraday Discuss.* **67**, 212-220 (1979).

47 Quack, M. & Troe, J. Complex Formation in Reactive and Inelastic Scattering: Statistical Adiabatic Channel Model of Unimolecular

Processes III. *Berichte der Bunsengesellschaft für physikalische Chemie* **79**, 170-183 (1975).

48 Greenwald, E. E., North, S. W., Georgievskii, Y. & Klippenstein, S. J. A Two Transition State Model for Radical−Molecule Reactions: A Case Study of the Addition of OH to C_2H_4. *J. Phys. Chem. A* **109**, 6031-6044 (2005).

49 Greenwald, E. E., North, S. W., Georgievskii, Y. & Klippenstein, S. J. A Two Transition State Model for Radical−Molecule Reactions: Applications to Isomeric Branching in the OH−Isoprene Reaction. *J. Phys. Chem. A* **111**, 5582-5592 (2007).

50 Bell, R. P. *The Tunnel Effect in Chemistry*. (Chapman and Hall, 1980).

51 Carpenter, B. K. Heavy-Atom Tunneling as the Dominant Pathway in a Solution-Phase Reaction? Bond Shift in Antiaromatic Annulenes. *J. Am. Chem. Soc.* **105**, 1700-1701 (1983).

52 Shannon, R. J. *Experimental and computational studies of hydroxyl radical kinetics at very low temperatures* PhD thesis, University of Leeds, (2012).

53 Taylor, W. D. *et al.* Atmospheric photodissociation lifetimes for nitromethane, methyl nitrite, and methyl nitrate. *International Journal of Chemical Kinetics* **12**, 231-240 (1980).

54 Zhu, X., Kamal, M., M. & Misra, P. Laser-induced excitation and dispersed fluorescence spectra of the ethoxy radical. *Pure and Applied Optics: Journal of the European Optical Society Part A* **5**, 1021 (1996).

55 Foster, S. C. *et al.* Free jet-cooled laser-induced fluorescence spectrum of methoxy. 1. Vibronic analysis of the~ A and~ X states. *The Journal of Physical Chemistry* **92**, 5914-5921 (1988).

56 Sander, S. *et al.* Chemical Kinetics and Photochemical Data for use in Atmospheric Studies–Evaluation Number 17, JPL Publication 10–6. (JPL, 2011).

57 Maricq, M. M. & Wallington, T. J. Absolute UV cross sections of methyl and ethyl peroxy radicals. *The Journal of Physical Chemistry* **96**, 986-992 (1992).

58 Molina, L. & Molina, M. Absolute absorption cross sections of ozone in the 185 to 350 nm wavelength range. *Journal of Geophysical Research: Atmospheres (1984–2012)* **91**, 14501-14508 (1986).

59 Baasandorj, M., Papanastasiou, D. K., Talukdar, R. K., Hasson, A. S. & Burkholder, J. B. $(CH_3)_3COOH$ (tert-butyl hydroperoxide): OH reaction rate coefficients between 206 and 375 K and the OH photolysis quantum yield at 248 nm. *Physical Chemistry Chemical Physics* **12**, 12101-12111 (2010).

60 Inoue, G., Akimoto, H. & Okuda, M. Laser-induced fluorescence spectra of CH_3O. *Chemical Physics Letters* **63**, 213-216 (1979).

61 Gutman, D., Sanders, N. & Butler, J. E. Kinetics of the reactions of methoxy and ethoxy radicals with oxygen. *The Journal of Physical Chemistry* **86**, 66-70 (1982).

62 Matsumi, Y., Inagaki, Y. & Kawasaki, M. Isotopic Branching Ratios and Translational Energy Release of H and D Atoms in the Reaction of $O(^1D)$ with CH_3OD and CD_3OH. *The Journal of Physical Chemistry* **98**, 3777-3781 (1994).

63 Job, V., Sethuraman, V. & Innes, K. The 3500 Å $^1A_2$-$\tilde{X}^1A_1$ transition of formaldehyde-h_2, d_2, and hd: Vibrational and rotational analyses. *Journal of Molecular Spectroscopy* **30**, 365-426 (1969).

64 Sheinson, R. S. & Williams, F. W. Chemiluminescence spectra from cool and blue flames: Electronically excited formaldehyde. *Combustion and Flame* **21**, 221-230 (1973).

65 Henderson, J. & Muramoto, M. 3546 Å System of Formaldehyde. *The Journal of Chemical Physics* **43**, 1215-1219 (1965).

66 Hoyermann, K., Loftfield, N. S., Sievert, R. & Wagner, H. G. Mechanisms and rates of the reactions of CH_3O and CH_2OH radicals with H atoms. *Symposium (International) on Combustion* **18**, 831-842 (1981).

67 Tsang, W. & Hampson, R. Chemical kinetic data base for combustion chemistry. Part I. Methane and related compounds. *Journal of Physical and Chemical Reference Data* **15**, 1087-1279 (1986).

68 Tsang, W. Chemical kinetic data base for combustion chemistry. Part 2. Methanol. *Journal of Physical and Chemical Reference Data* **16**, 471-508 (1987).

69 Radford, H. The fast reaction of CH_2OH with O_2. *Chemical physics letters* **71**, 195-197 (1980).

70 Matsumi, Y. *et al.* Quantum yields for production of $O(^1D)$ in the ultraviolet photolysis of ozone: Recommendation based on evaluation of laboratory data. *Journal of Geophysical Research: Atmospheres (1984–2012)* **107**, 1.1-1.12 (2002).

71 Atkinson, R. *et al.* Evaluated kinetic and photochemical data for atmospheric chemistry: supplement VI. IUPAC subcommittee on gas kinetic data evaluation for atmospheric chemistry. *Journal of Physical and Chemical Reference Data* **26**, 1329-1499 (1997).

72 Bodi, A., Hemberger, P., Osborn, D. L. & Sztáray, B. I. Mass-Resolved Isomer-Selective Chemical Analysis with Imaging Photoelectron Photoion Coincidence Spectroscopy. *The Journal of Physical Chemistry Letters* **4**, 2948-2952 (2013).

73 Osborn, D. L. *et al.* The multiplexed chemical kinetic photoionization mass spectrometer: A new approach to isomer-resolved chemical kinetics. *Review of Scientific Instruments* **79**, 104103 (2008).

74 Taatjes, C. A. *et al.* “Imaging” combustion chemistry via multiplexed synchrotron-photoionization mass spectrometry. *Physical Chemistry Chemical Physics* **10**, 20-34 (2008).

75 Garrod, R. T., Weaver, S. L. W. & Herbst, E. Complex chemistry in star-forming regions: an expanded gas-grain warm-up chemical model. *The Astrophysical Journal* **682**, 283 (2008).

76 Su, T. & Chesnavich, W. J. Parametrization of the ion–polar molecule collision rate constant by trajectory calculations. *The Journal of Chemical Physics* **76**, 5183-5185 (1982).

77 Minissale, M. *et al.* Quantum tunneling of oxygen atoms on very cold surfaces. *Physical review letters* **111**, 053201 (2013).

78 Congiu, E. *et al.* Efficient diffusive mechanisms of O atoms at very low temperatures on surfaces of astrophysical interest. *Faraday Discussions* **168**, 151-166 (2014).

Chapter 4. The low temperature reaction kinetics of OH with acetone and dimethyl ether: Experimental studies and master equation calculations.

4.1 Background and previous work on the reactions of OH with acetone and dimethyl ether

The reaction of OH with acetone has been extensively studied at ambient and high temperatures owing to its importance to the Earth's atmosphere. Acetone is emitted into the atmosphere via anthropogenic sources such as solvent usage[1] and biomass burning[2] and a recent field campaign has demonstrated that abundance levels in an urban environment can range from 0.37-6.7 ppb.[3] Dimethyl ether (DME) is currently used as a fuel additive and is being investigated as a potential substitute to diesel.[4] In both atmospheric and combustion environments the reaction of these oxygenated volatile organic compounds (oVOCs) with OH is important. The daytime sink of many oVOCs, such as acetone and DME, is reaction with the hydroxyl radical, OH, and the initial propagation step in DME combustion is its reaction with OH.[4,5]

The rate coefficient for the reaction of OH with acetone ($k_{4.1}$), which has largely been studied via PLP-LIF of OH, was found to exhibit Arrhenius-type behaviour at higher temperatures consistent with hydrogen abstraction from acetone by OH over a barrier. No pressure dependence of this reaction, which would indicate an association mechanism, has previously been observed.[6,7] However, approaching room temperature there is notable deviation from Arrhenius behaviour and at lower temperatures, the rate coefficient appears to exhibit a slightly negative temperature dependence.

The reaction of OH with acetone has two possible product channels, as shown in Figure 4. 1.

$$OH + CH_3C(O)CH_3 \xrightarrow{k_{4.1}} Products \qquad \text{R4.1}$$

$$OH + CH_3C(O)CH_3 \rightarrow H_2O + CH_2C(O)CH_3 \qquad \text{R4.1a}$$

$$OH + CH_3C(O)CH_3 \rightarrow CH_3 + CH_3C(O)OH \qquad \text{R4.1b}$$

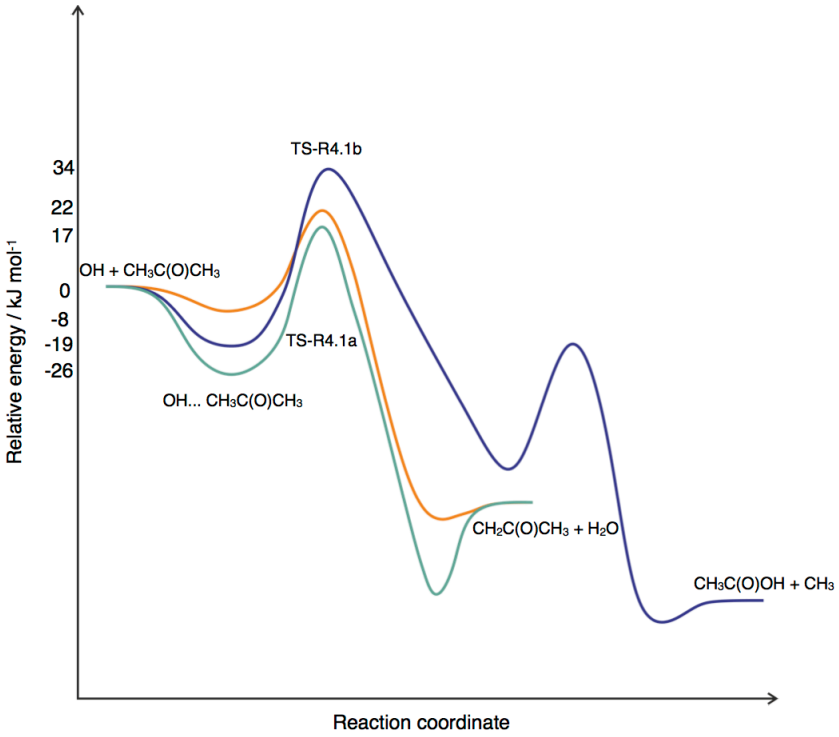

Figure 4. 1: To-scale potential energy surface for the reaction of OH with acetone, based on calculations by Henon *et al.*[8]

Initial experiments by Wollenhaupt *et al.* at room temperature indicated that the route to form acetic acid and methyl radicals may be significant – with a branching fraction of up to 50 %.[6] However, subsequent experimental and theoretical work by authors such as Vandenberk *et al.,* Gierczak *et al.*, and Talkukdar *et al.* has demonstrated that this channel is negligible (less than 1 %) and the dominant channel is the formation of acetonyl and water.[9-11]

The reaction of OH with DME, R4.2, has been studied from combustion temperatures down to ~ 200 K. At ambient and high temperatures, the mechanism is expected to be purely abstractive, leading to the formation of methoxy methyl and water as shown in Figure 4. 2, and Carr *et al.* found no direct evidence of collisional stabilization of the weakly bound OH-DME pre-reactive complex.[4] This was corroborated by studies of OH reactions with various deuterated analogues of DME also performed by Carr *et al.*.[4] Below room temperature, there appears to be some deviation from Arrhenius type behaviour.[4,12,13]

$$OH + CH_3OCH_3 \xrightarrow{k_{4.2}} Products \qquad \text{R4.2}$$

$$OH + CH_3OCH_3 \rightarrow H_2O + CH_2OCH_3 \qquad \text{R4.2a}$$

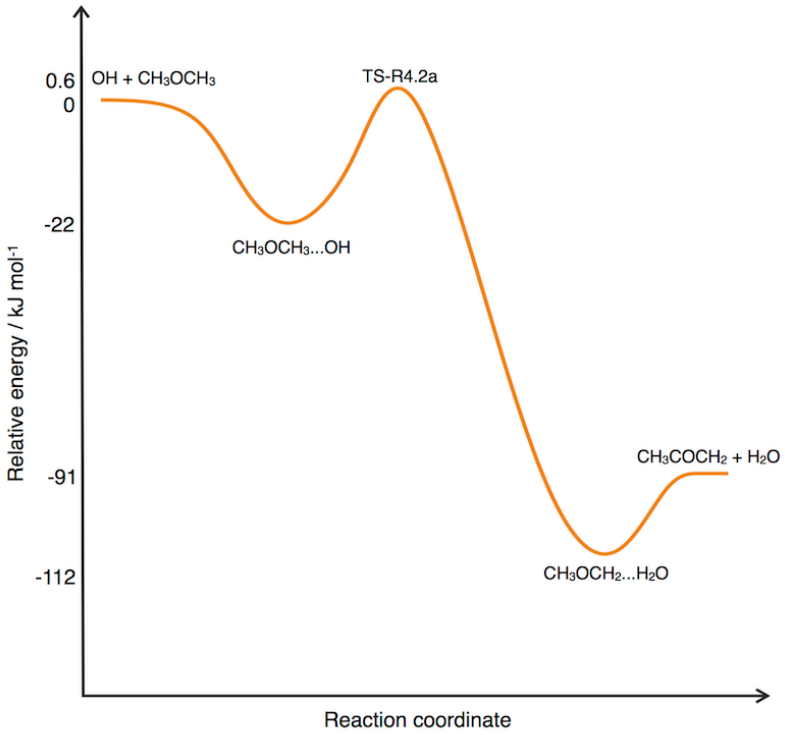

Figure 4. 2: To-scale potential energy surface for the reaction of OH with dimethyl ether, based on calculations by Carr *et al.*[4]

The reaction between these species is also relevant to cold interstellar environments, for example, DME, acetone and OH have all been detected in the Sagittarius molecular cloud, where temperatures reach as low as 40 K. [14-16] As such, the reaction between OH and acetone has been studied in this laboratory at 62- 93 K by Taylor *et al.* and Shannon *et al.* and the reaction of OH + DME has been studied by Shannon *et al.* at 93-112 K, both using the pulsed Laval nozzle apparatus utilised in this work in tandem with PLP-LIF of OH.[17-19]

Prior to the low temperature work by Shannon *et al.* and Taylor *et al.*, it had been noted that towards 200 K, the rate coefficient for OH + acetone tended towards a temperature-independent value of ~ 1 × 10^{-13} molecule^{-1} cm^3 s^{-1}.[17-21] Two mechanisms were proposed to account for this behaviour in the literature. Following theoretical work, Caralp *et al.* concluded that the deviation from typical Arrhenius behaviour at low temperatures could be accounted for by the quantum tunnelling mechanism.[20] The occurrence of tunnelling is often manifested in deviation from Arrhenius behaviour, where the low temperature rate coefficients are not as small as expected.[22,23] Tunnelling has recently been shown to be an important contribution to the enhanced rate coefficients at low temperatures for several hydrogen abstraction reactions and so this mechanism is plausible.[24,25] Wallington and Kurylo suggested that the turnaround is perhaps due to the collisional

stabilisation of the weakly bound complex between OH and acetone into the pre-barrier well.[21] Analogous mechanisms could be expected to be operating for OH + DME, due to the similarity of the potential energy surfaces.

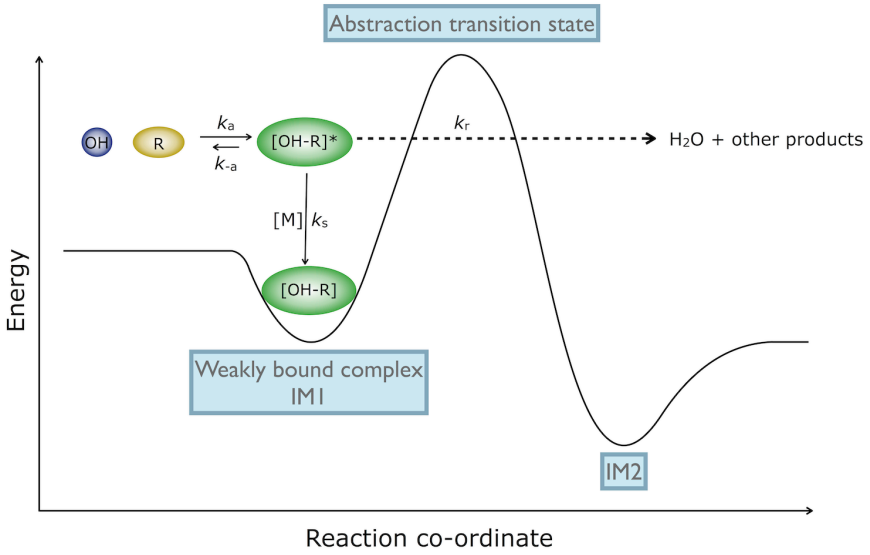

Figure 4. 3: Simplified PES for the OH + oVOC reactions, where IM1 denotes the pre-barrier complex between the reactant species, and IM2 denotes the post-barrier complex between the products.

At low temperatures two mechanisms are possible. The simplified potential energy surfaces for both OH + acetone and OH + DME, based on calculations in the literature, as shown in Figure 4. 3, feature a weak well (~18-29 kJ mol^{-1}) followed by a significant barrier to hydrogen abstraction. The OH and co-reactant can form a weakly bound complex (via a barrierless association reaction), which at higher temperatures will quickly dissociate. As the temperature is lowered, the internal energy of the complex is also lowered, and so redissociation is slower and consequently the complex lifetime is enhanced. The complex then has three possible fates – stabilization into the weak pre-barrier well via collisions with the bath gas, redissociation back to reactants, or reaction via quantum tunnelling through the barrier to hydrogen abstraction. At low temperatures the bimolecular reaction channel, which is pressure-independent, is only able to occur via the latter mechanism as the internal energy of the reactants is insufficient to transcend the barrier to reaction. Thus if reaction occurs, it must do so by quantum mechanical tunnelling through the barrier.

The collisional stabilisation mechanism as well as the tunnelling mechanism is likely to be enhanced as low temperatures. The complex, which will be longer lived at low temperatures, has less internal energy and so fewer collisions will be required to stabilise it into the pre-barrier well, and the high pressure limiting rate coefficient will be achieved at a lower pressure. Thus,

to understand which mechanism operating at low temperatures, the pressure dependence of the rate coefficient, as well as the temperature dependence needs to be examined.

The non-Arrhenius behaviour observed previously for OH + acetone was found to be exacerbated at lower temperatures in investigations by Shannon *et al.* and Taylor *et al.*, and this reaction was observed to exhibit a large inverse temperature dependence below 200 K, with $k_{86\ K/298\ K}$ ~ 334.[17] A less dramatic enhancement was observed by Shannon *et al.* on the OH + DME reaction with $k_{93\ K/298\ K}$ ~ 3.[17]

Despite the extensive study of these reactions, there are no experimental data in the range 93 to 202 K, and prior to the work of Shannon, first published alongside this work, no pressure dependent studies at low temperatures.[19,26] Therefore, both the shape of the turnaround from the high temperature to the low temperature regime of the bimolecular rate coefficients and the mechanisms operating at 200 K and below are not well understood.

This present study has built upon the existing experimental work by measurements of the rate coefficient for the OH + acetone reaction from 133-146 K using both deuterated (R4.3) and non-deuterated (R4.1) analogues of OH and acetone to attempt to assess the contribution of the two channels to the overall rate coefficient, and by measurements of the OH + DME (R4.2) rate coefficient at 133 and 138 K.

$$OD + CD_3C(O)CD_3 \xrightarrow{k_{4.3}} Products \qquad \text{R4.3}$$

$$OH + CD_3C(O)CD_3 \rightarrow D_2O + CD_2C(O)CD_3 \qquad \text{R4.3a}$$

This work has been published alongside further work by Shannon on these reactions including low temperature pressure dependence studies and master equation work.[26] The work by Shannon as part of the joint publication will be discussed in the context of the work carried out as part of this thesis.[26]

4.2 Experimental procedure

The experiments were carried out as described in Chapter 2 and so only a brief outline will be given below.

For the OH + acetone (and OD + acetone-d6) reaction, acetone(acetone-d6) was also used as an OH(OD) precursor. Carr *et al.* demonstrated that photolysis of acetone at 248 nm leads to acetyl radical formation with a

quantum yield of 0.9.[27] In the presence of sufficient oxygen, the acetyl is titrated to a lactone molecule and OH.[28]

$$CH_3C(O)CH_3 + h\nu \rightarrow CH_3CO + CH_3 \qquad \phi_{248\,nm} = 0.9 \qquad \text{P4.1}$$

$$CH_3CO + O_2 \rightarrow OH + \alpha - lactone \qquad \text{R4.4}$$

Shannon *et al.* have seen evidence that in the case of OH + NH_3 at very low temperatures, the *t*-BuOOH hydroxyl radical precursor was found to form a complex to the NH_3 co-reagent which itself was reactive with OH.[19] For the OH + acetone study, both acetyl and *t*-BuOOH were used as OH precursors in comparative experiments to ensure that no secondary chemistry between the OH precursor and the co-reagent was occurring.

$$(CH_3)_3COOH + h\nu \rightarrow OH, OH^* + co - products \qquad \text{P4.2}$$

$$OH^* + M \xrightarrow{k_{rel}} OH + M \qquad \text{R4.5}$$

The vapour pressure of acetone, DME or acetone-d6, was admitted to an empty cylinder and diluted with nitrogen (BOC, OFN) then left to mix overnight. Nitrogen bath gas (BOC, OFN), the acetone (VWR > 99.9 %), DME (Aldrich > 99.9 %) or acetone-d6 (Eur-isotop > 99.8 %) / nitrogen (BOC, OFN) mixture and either oxygen (BOC 99.999 %) or *t*-BuOOH (Aldrich, 70 % wt. in H_2O,) were flowed through a set of calibrated mass flow controllers (MKS, Mass-Flo). The gas was mixed in a 2 L stainless steel ballast tank prior to delivery to the Laval nozzle reservoir via two pulsed solenoid valves (Parker, series 9) operating at a pulse repetition frequency of 5 Hz with ~ 10-20 ms pulses (depending on the desired jet density). A 248 nm excimer laser (Lambda-Physik LPX) with a pulse repetition frequency of 5 Hz aligned collinearly to the jet was used to photolyse the OH (or OD) precursor.

The relative population of OH (or OD) radicals was probed using LIF via a Nd:YAG (Litron LPY 664-10) pumped dye laser (Sirah Gmbh Cobra stretch) tuned to be resonant with an OH (or OD) $A^2\Sigma^+ \leftarrow X^2\Pi_i$ (1,0) at ~ 282 nm (or ~ 287 nm). The off-resonant fluorescence from the excited OH (or OD) was collected by a PMT (Thorn EMI 9813QB) fitted with an interference filter (Barr associates, λ_{max} =308.5 nm, 5nm FWHM) .The temporal evolution of OH (OD) was obtained by increasing the delay time between the photolysis and probe lasers and traces were acquired which were found to be exponential in nature. For pseudo first order conditions [ROH]>>[OH] the temporal evolution of OH is given by E4.1(see Appendix C for derivation).

$$[OH]_t = \left(\frac{k_{rel}}{k_{obs-}k_{rel}}\right)[OH^*]_0\left(e^{-k'_{rel}t} - e^{-k_{obs}t}\right)+[OH]_0 e^{-k_{obs}t} \quad \text{E4.1}$$

where k_{obs} is the pseudo first order rate coefficient , *OH** is an initially rotationally excited hydroxyl radical, formed in v″= 0 from photolysis of the precursor, and k'_{rel} is the pseudo first order rate coefficient for rotational relaxation of the rotationally excited hydroxyl radical into the laser-probed level, OH.

By varying the acetone , DME or acetone-d6 concentration, pseudo first order decay traces were obtained at a range of co-reagent concentrations. The bimolecular rate coefficient was determined from the gradient of a plot of pseudo first order rate coefficient versus co-reagent concentration.

$$k_{obs} = k_{4.1}[acetone] + k_{loss} \quad \text{E4.2}$$

$$k_{obs} = k_{4.2}[DME] + k_{loss} \quad \text{E4.3}$$

$$k_{obs} = k_{4.3}[acetone - d6] + k_{loss} \quad \text{E4.4}$$

k_{loss} is the rate coefficient for the loss of OH out of the detection region via diffusion and reaction with the precursor.

4.3 Computational methods

Ab initio and master equation calculations were carried out by Dr Robin Shannon (University of Leeds) as part of this work and the results of these calculations are used to aid interpretation of the experimental data. A brief outline of the theoretical methods employed by Dr Shannon for these calculations is given below.

Statistical rate theory calculations were performed using the master equation solver software, MESMER – further details regarding this are in Chapter 1.[29] RRKM (Rice-Ramsperger-Kassel-Marcus) theory was used to model the transfer of the population of isoenergetic grains between isomers, and an exponential down model was used for collisional energy transfer. A bimolecular source term was added into MESMER, where the barrierless association of OH and the co-reagent was modelled using the inverse Laplace transform of the high pressure limiting rate coefficient (see Appendix A). For both the DME and acetone systems, a grain size of 50 cm^{-1} was utilised, except below 60 K, where convergence was only achieved with a smaller grain size of 10 cm^{-1}. Given the role of tunnelling observed for H-transfer reactions at low temperatures previously, tunnelling was accounted for by two methods : Using an Eckart potential and the imaginary frequency

of the barrier via the method of Miller, and also using the semi-classical WKB (Wentzel-Kramers-Brillouin) method. For the latter, an IRC (intrinsic reaction coordinate) calculation was performed at the MBW1K/6-31+G(2d,2p) level using Gaussian 03.[30-32]

Due to the availability of potential energy surfaces in the literature, a new surface was not calculated for the reaction of OH + acetone. The surface of Caralp *et al.*, based on calculations of Henon *et al.* at the MP2/6-31G**//CCSD/6-31G** level was employed.[8,20] In the case of OH + DME, Dr Shannon had recently calculated a potential surface at the FCC/CBS//CCSD/AVDZ level of theory as part of a publication by Carr *et al.*, and so this was utilised for the current work.[4] More than one transition state was reported for H-abstraction in both reactions. For the DME reaction, these were found to be conformers of one another – linked by a hindered internal rotation. Given the low temperature focus of the present work, only the lowest energy transition state was considered for each system.

Further approximations were made to simplify the master equation calculations First, IM2 was treated as a sink (see Figure 4. 3), and so the final reaction out to bimolecular reactions was not included in the calculations. And secondly, the final step from IM1 to IM2 (see Figure 4. 3) was treated as irreversible. To better represent the low frequency vibrations obtained from the initial *ab initio* calculations, they were treated as hindered rotors, with hindered rotor calculations performed in Gaussian 03 at the MBW1K/6-31+G(2d,2p) level.[30]

The experimental data from both this, and previous higher temperature studies, were used in a Levenberg Marquardt fitting routine within MESMER. Due to the highly coupled nature of the well-depth of IM1 and the value of $<\Delta E_{down}>$ it was necessary to fix one of these parameters, and so for both the reaction of OH with acetone and with DME, $<\Delta E_{down}>$ was fixed at 300 cm^{-1}.

4.4 Results and discussion

Examples of the temporal evolution of the OH LIF signal following 248 nm photolysis of *t*-BuOOH, in the presence of acetone and DME are shown in Figure 4. 4 and Figure 4. 5, respectively, together with the non-linear least squares fits of E4.1 to the data which yielded k_{obs}. Experiments were conducted over a range of co-reagent concentrations and Figure 4. 6 and Figure 4. 7 are examples of the variation of k_{obs} with [co-reagent], from which

the bimolecular rate coefficients are obtained. The rate coefficients obtained in this study, alongside rate coefficients obtained as part of a joint publication with Dr Robin Shannon using this apparatus,[26] and also those previously obtained by Shannon *et al.* are summarized in Table 4. 1 and the temperature dependence of the rate coefficients for OH + acetone and OH + DME are shown in Figure 4. 8 and Figure 4. 9 respectively. Rate coefficients were measured experimentally between 63 K and 148 K and total gas densities spanning 3.2×10^{16} - 2.6×10^{17} molecule cm^{-3}.

Table 4. 1: Measured rate coefficients of the reactions of OH with acetone and DME and OD + acetone-d6 obtained in this study, together with previous work presented by Shannon *et al.* using this apparatus, shown alongside with the temperatures and total gas densities of the flows generated by the pulsed Laval nozzle utilised in the measurements. Errors have been calculated by propagation of the 95 % confidence limits in the bimolecular rate coefficients with the errors in the expansion densities.

T/K	[M] / 10^{16} molecule cm^{-3}	OH/OD precursor for $k_{4.1}$	$k_{4.1}$ / 10^{-11} molecule^{-1} cm^3 s^{-1}	$k_{4.3}$ / 10^{-11} molecule^{-1} cm^3 s^{-1}	$k_{4.2}$ / 10^{-11} molecule^{-1} cm^3 s^{-1}
63 ± 2	3.4 ± 0.3	-	-	-	1.7 ± 0.1 [a]
79 ± 3	17 ± 2	Acetyl/O_2	10 ± 1 [a]	-	1.9 ± 0.2 [a]
82 ± 4	3.2 ± 0.6	Acetyl/O_2	3.7 ± 0.4 [a]	-	-
82 ± 4	5.1 ± 0.5	Acetyl/O_2	5.9 ± 0.6 [a]	-	-
83 ± 3	6.1 ± 0.5	-	-	-	0.8 ± 0.1 [b]
86 ± 3	6.5 ± 0.6	Acetyl/O_2	5.6 ± 0.6 [b]	-	-
83 ± 3	8.9 ± 0.6	Acetyl/O_2	7.6 ± 0.8 [a]	-	0.9 ± 0.1 [a]
81 ± 4	13 ± 2	Acetyl/O_2	8.9 ± 0.9 [a]	-	1.6 ± 0.3 [a]
93 ± 4	6.5 ± 0.5	Acetyl/O_2	5.6 ± 0.8 [a]	-	0.77 ± 0.04 [b]
93 ± 4	6.5 ± 0.5	*d*-Acetyl/O_2	-	6.8 ± 0.7 [a]	-
112 ± 9	6 ± 1	Acetyl/O_2	0.5 ± 0.1 [b]	-	-
110 ± 8	9 ± 1	-	-	-	0.4 ± 0.1 [a]
138 ± 9	8 ± 1	*t*-BuOOH	0.13 ± 0.09	-	0.31 ± 0.05
133 ± 10	13 ± 3	*t*-BuOOH	0.28 ± 0.06	-	0.30 ± 0.04
148 ± 15	10 ± 1	*t*-BuOOH	0.16 ± 0.08	-	-
143 ± 15	18 ± 2	*t*-BuOOH	0.2 ± 0.1	-	-
146 ± 15	26 ± 4	*t*-BuOOH	0.35 ± 0.07	-	-
146 ± 15	26 ± 4	Acetyl/O_2	0.3 ± 0.1	-	-
146 ± 15	26 ± 4	*d*-Acetyl/O_2	-	0.16 ± 0.05	-

[a] Data obtained by Shannon as part of this study and published in co-authored paper.[26]
[b] Data obtained previously by Shannon *et al.*.[17]

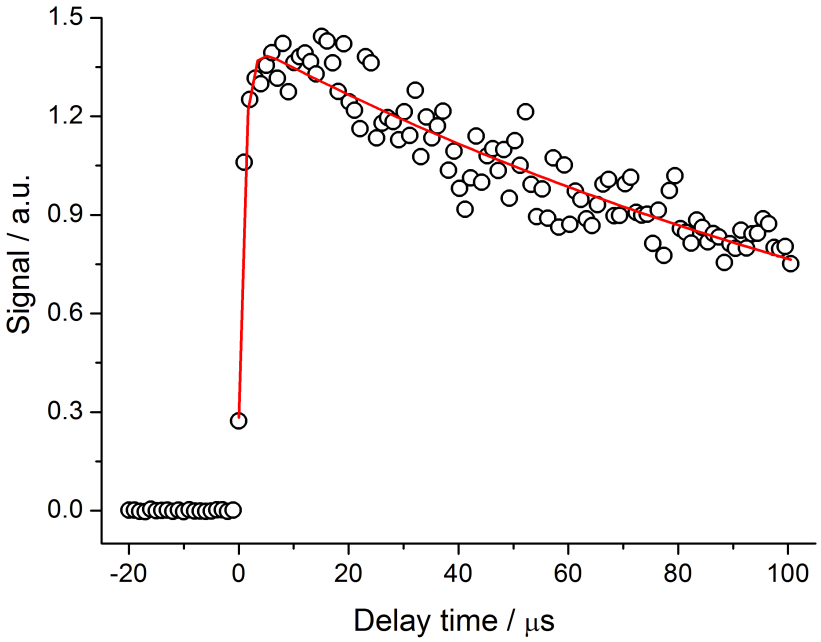

Figure 4. 4: Pseudo first order LIF trace of OH together with the non linear least squares fit of E4.1 to the data from the 248 nm photolysis of $(CH_3)_3COOH$ in the absence of a co-reagent at 146 ± 15 K and a total gas density of (2.6 ± 0.4) × 10^{17} molecule cm-^{3} using N_2 bath gas. The least squares fit of E4.1 to the data yields a pseudo first order rate coefficient of 6269 ± 258 s^{-1}.

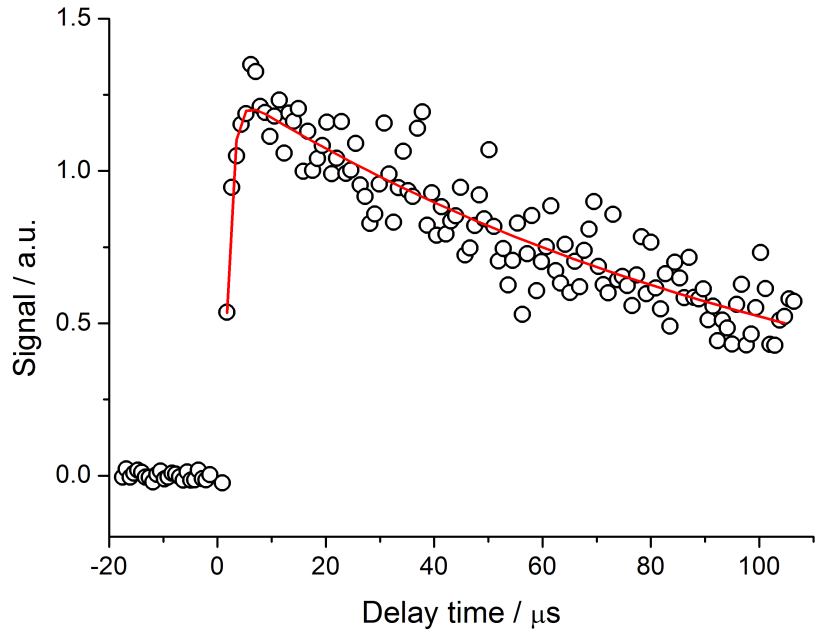

Figure 4. 5: Pseudo first order LIF trace of OH together with the non linear least squares fit of E4.1 to the data from the 248 nm photolysis of $(CH_3)_3COOH$ in the presence of DME (1.48 × 10^{15} molecule cm^{-3}) at 133 ± 10 K and a total gas density of (1.3 ± 0.3) × 10^{17} molecule cm^{-3} using N_2 bath gas. The least squares fit of E4.1 to the data yields a pseudo first order rate coefficient of 9001 ± 401 s^{-1}.

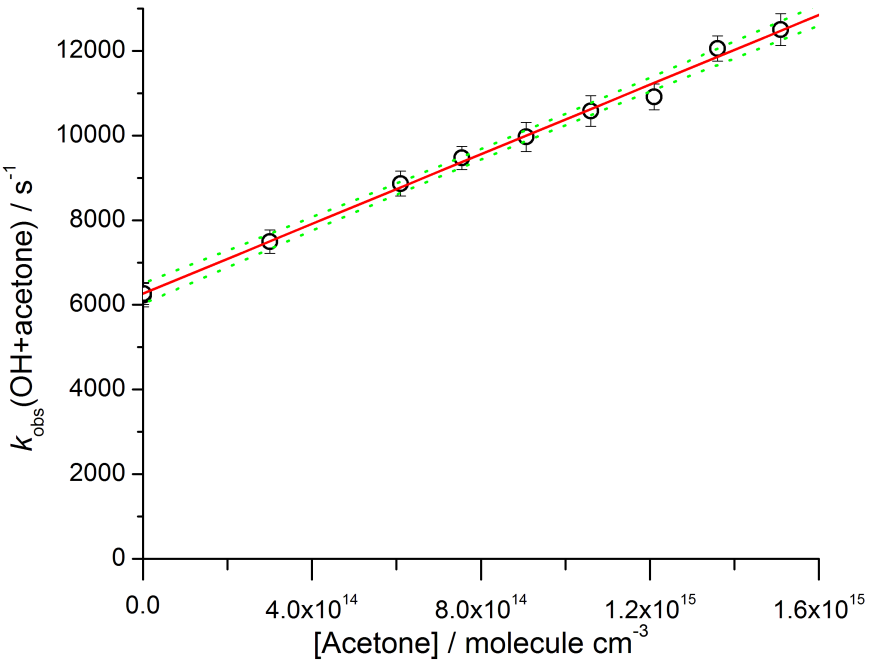

Figure 4. 6: Variation of k_{obs} with acetone concentration obtained at 146 ± 15 K and a total gas density of (2.6 ± 0.4) × 10^{17} molecule cm^{-3} using N_2 bath gas, together with a weighted linear least squares fit of E4.2 to the data, the gradient of which yields the bimolecular rate coefficient, $k_{4.1}$= (3.5 ± 0.7) × 10^{-12} $molecule^{-1}$ cm^3 s^{-1} .The green dashed lines represent the upper and lower 95 % confidence limits. The overall error in the bimolecular rate coefficient is the 95% confidence limits propagated with the error in the determination of the total density from the impact pressure measurements.

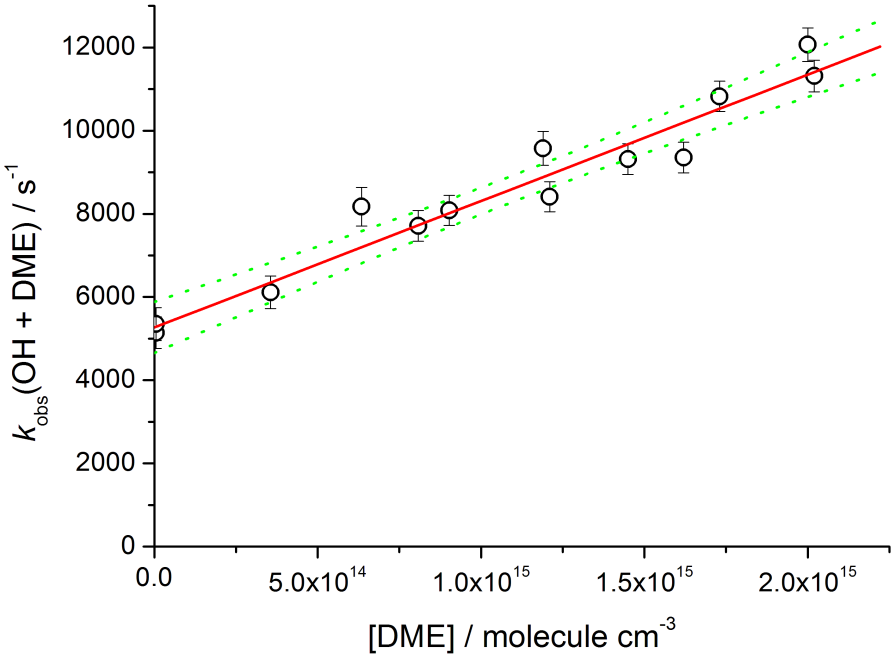

Figure 4. 7: Variation of k_{obs} with DME concentration obtained 133 ± 10 K and a total gas density of (1.3 ± 0.3) × 10^{17} molecule cm^{-3} using N_2 bath gas, together with a weighted linear least squares fit of E4.3 to the data, the gradient of which yields the bimolecular rate coefficient, $k_{4.2}$= (2.8 ± 0.6) × 10^{-12} $molecule^{-1}$ cm^3 s^{-1}. The green dashed lines represent the upper and lower 95 % confidence limits. The overall error in the bimolecular rate coefficient is the 95% confidence limits propagated with the error in the determination of the total density from the impact pressure measurements.

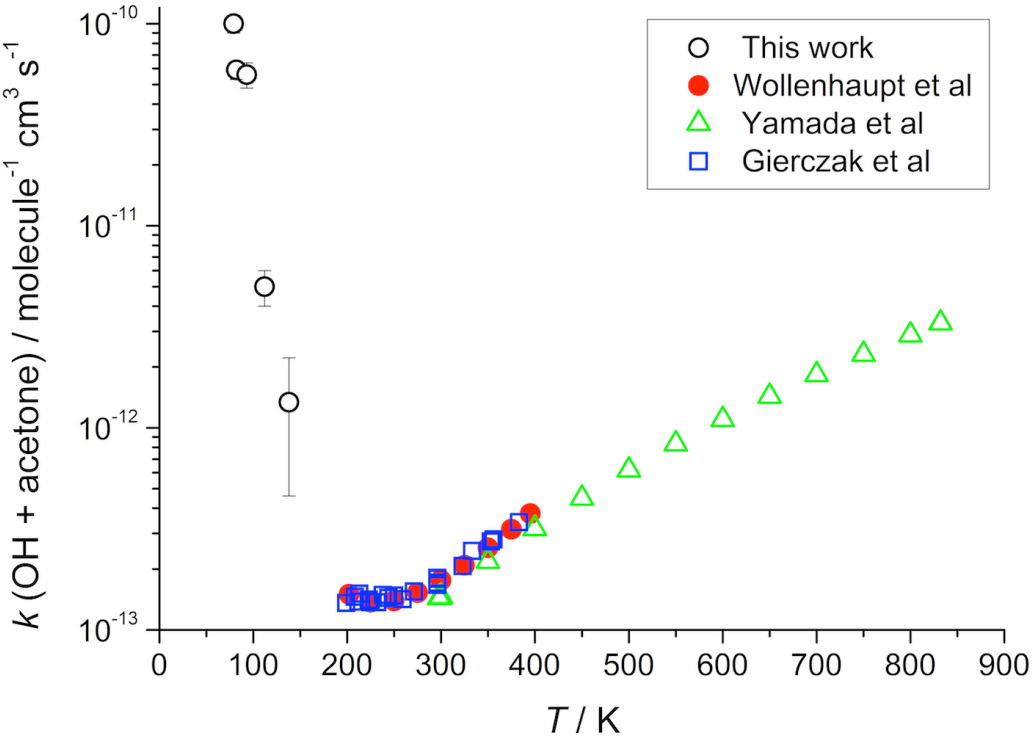

Figure 4. 8: Temperature dependence of $k_{4.1}$, the OH + acetone rate coefficient from this work and other studies.[6,10,26,33]

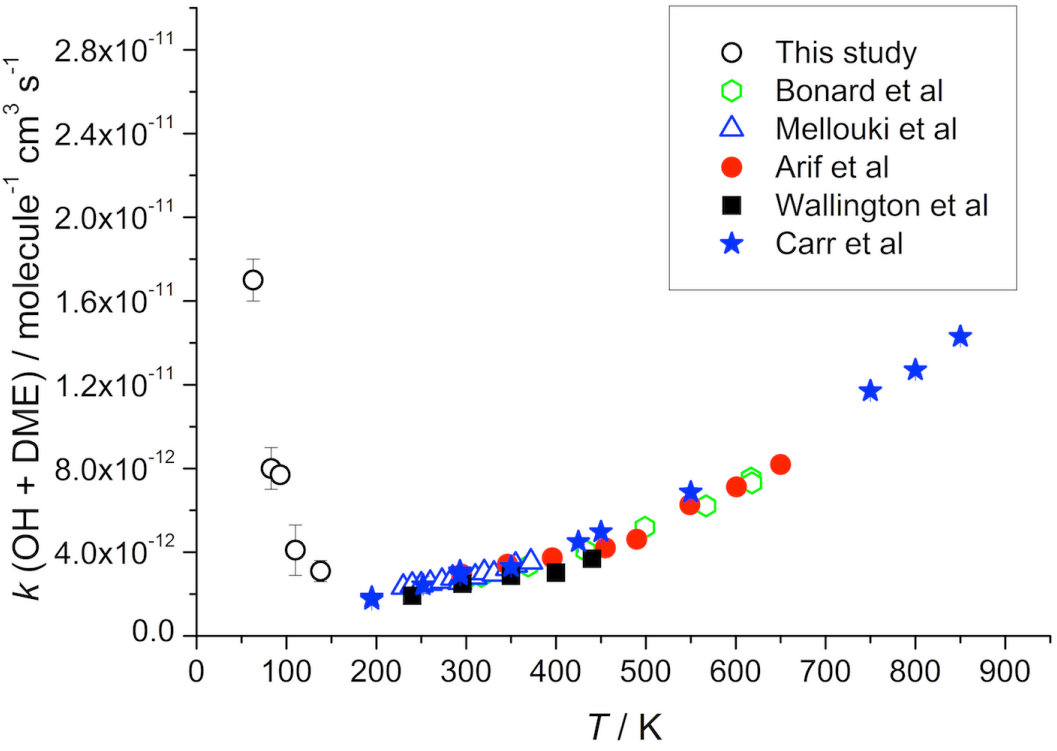

Figure 4. 9: Temperature dependence of $k_{4.2}$, the OH + DME rate coefficient from this work and other studies.[4,12,13,26,34,35]

The rate coefficients measured in this work for both reactions show a clear negative temperature dependence below 200 K, in concurrence with the previous measurements reported by Shannon *et al.* over a smaller temperature range and at a single pressure.[17] Two mechanisms have been considered to rationalize the significant turnaround in both rate coefficients below 200 K.

As for the reactions of OH with alcohols discussed in Chapter 3, the PES of OH + acetone and DME also feature a weakly bound complex prior to the overall barrier to reaction (Figure 4. 3) with binding energies of ~ 6.1-16.7 and 29.4 kJ mol^{-1} respectively.[4,8,9,26,33] Wallington and Kurylo attributed the non-Arrhenius behaviour for the OH + acetone rate coefficient below room temperature to be indicative of the third-body stabilization of the OH-acetone complex into the pre-barrier well. [21] As discussed in Chapter 3, this mechanism would manifest itself experimentally by the linear dependence of the rate coefficient on pressure. However, no previous measurements have explored the pressure dependence of the rate coefficient in the non-Arrhenius temperature regime. The second mechanism, as suggested by Caralp *et al.*, attributes the turnaround to quantum tunnelling through the barrier to H-abstraction.[20] Experimentally, the presence of this channel in the non-Arrhenius temperature regime can be explored by studies, detection directly or indirectly of the products of the reaction, or by evidence of a non-zero intercept in a plot of rate coefficient versus pressure. No such previous investigations have been reported.

Rate coefficients for OH + acetone were measured over 5 densities from 79-83 K and over 5 densities from 133 to 148 K. At both temperatures, from the dependence of the rate coefficient on density it is evident that the collisional stabilization mechanism proposed by Wallington and Kurylo is operating as shown in Figure 4. 10.[21]

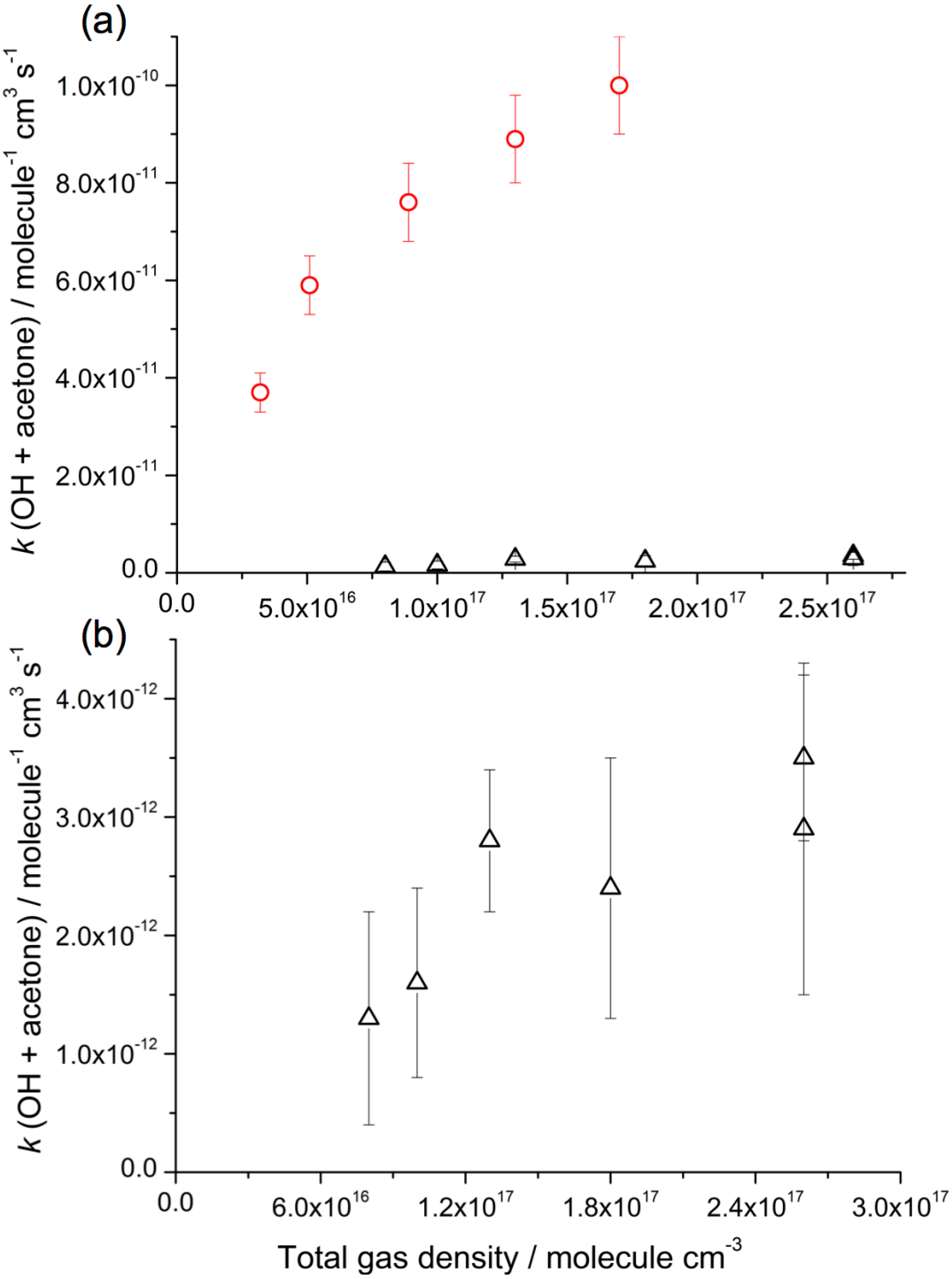

Figure 4. 10: (a) Pressure dependence of $k_{4.1}$, the OH + acetone rate coefficient at ~ 80 K (N_2 bath gas, red open circles) and 133-148 K (N_2 bath gas, black open triangles). The error bars are the result of propagation of the 95 % confidence limits in the bimolecular rate coefficients with the errors in the expansion densities. (b) Enlarged segment showing the pressure dependence of the rate coefficient of the 133-148 K (N_2 bath gas, black open triangles) data.

At the lower temperature and higher total gas densities, the rate coefficient appears to plateau with increasing pressure, indicating that the rate coefficient is approaching the high pressure limit. At 133-148 K, the rate coefficient appears to be less dependent on pressure – however, it must be noted that these rate coefficients have large errors associated with them due to the rate coefficients approaching the detection limit for the Laval apparatus (around 1 x 10^{-12} molecule^{-1} cm^3 s^{-1}, see Chapter 2 for further explanation). The kinetic time available from the jet produced by the 133-148 K nozzle (~ 100 us) was significantly shorter than for the 80 K nozzle (~ 250 us), and to maintain the stable expansion it is not possible to compensate for this by adding higher concentrations of the co-reagent (see Chapter 2) and so it is more challenging to measure lower rate coefficients. It was also not possible to obtain a rate coefficient at a lower density as the rate coefficient was too slow to measure in the kinetic time available. Nevertheless, the 133-148 K data indicate that the complex lifetime is reduced compared to at 80 K so that collisional stabilization less able to compete with the redissociation of the complex. There is a modest increase in the rate coefficient with pressure, which indicates that there is some stabilization of the complex into the well, however, there may also be some contribution from a pressure independent channel, such as tunnelling through the H-abstraction barrier.

The observed dependence on pressure at 80 K does not preclude some minor contribution of the tunnelling mechanism to the overall rate coefficient. The probability of tunnelling is inversely proportional to the mass of the tunnelling atom (see Chapter 1) and if tunnelling were occurring in this reaction, the rate coefficient would be expected to decrease if the abstracted hydrogen atom were replaced by a deuterium atom. To assess the potential contribution of the bimolecular channel, rate coefficients for the reaction of OD with acetone-d6 (R4.3) were measured at 93 and 146 K.

$$OD + CD_3C(O)CD_3 \xrightarrow{k_{4.3}} Products \qquad \text{R4.3}$$

This reaction was chosen in preference of the reaction of OH with acetone-d6 as acetone-d6 acts as the reagent and additionally, an OD source following 248 nm photolysis in the presence of O_2.

An example of a pseudo first order decay trace of OD in the presence of acetone-d6 is shown in Figure 4. 11 and the resultant bimolecular plot is shown in Figure 4. 12.

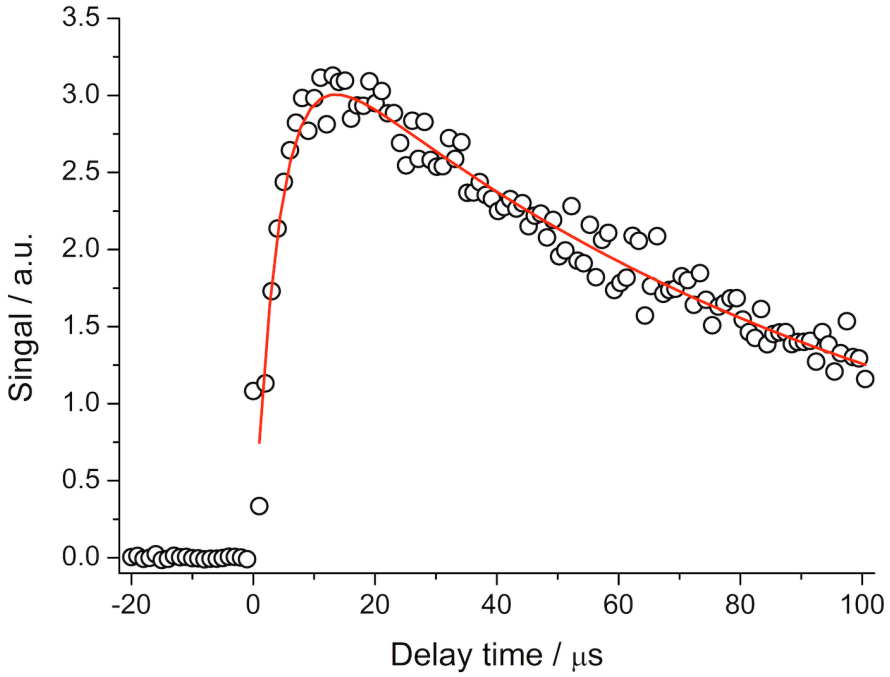

Figure 4. 11: Pseudo first order LIF trace of OD together with the non linear least squares fit of E4.1 to the data from the 248 nm photolysis of $CD_3C(O)CD_3$ (1.52×10^{15} molecule cm^{-3}) in the presence of oxygen at 145 ± 15 K and a total gas density of (2.6 ± 0.4) × 10^{17} molecule cm^{-3} using N_2 bath gas. The least squares fit of E4.1 to the data yields a pseudo first order rate coefficient of 10577 ± 277 s^{-1}.

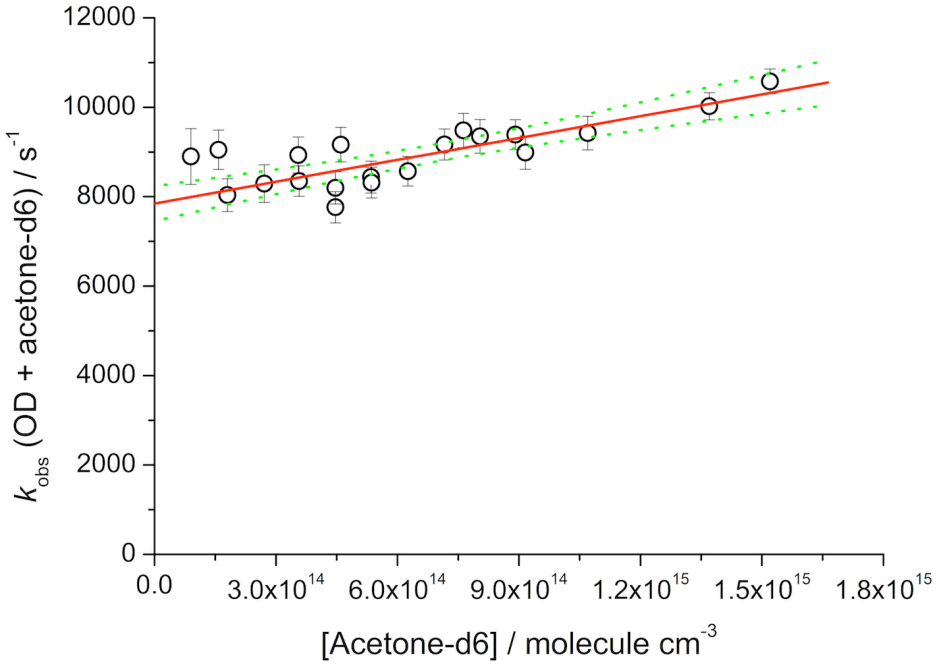

Figure 4. 12: Variation of k_{obs} with acetone-d6 concentration obtained at 146 ± 15 K and a total gas density of (2.6 ± 0.4) × 10^{17} molecule cm^{-3} using N_2 bath gas, together with a weighted linear least squares fit of E4.3 to the data, the gradient of which yields the bimolecular rate coefficient, $k_{4.3}$= (1.6 ± 0.5) × 10^{-12} molecule^{-1} cm^3 s^{-1} .The green dashed lines represent the upper and lower 95 % confidence limits. The overall error in the bimolecular rate coefficient is the 95% confidence limits propagated with the error in the determination of the total density from the impact pressure measurements.

If there was a significant contribution from tunnelling, then the rate coefficient of $k_{4.3}$ would be notably reduced compared to $k_{4.1}$, as the probability tunnelling is dependent on mass, with the probability decreasing for higher mass particles.[22,23] However, the rate coefficients obtained for $k_{4.3}$ are supportive of the pressure dependence data and indicate that tunnelling does not play a large role between 93-146 K in the OH + acetone reaction. At 93 K, the measured rate coefficients for the deuterated and undeuterated systems are found to be within error of each other. At 146 K, $k_{4.1}$ is around a factor of two slower than $k_{4.3}$, however these rate coefficients are subject to much larger uncertainties than at 93 K owing to the rate coefficients being almost the limit of what can be measured in the limited time window of the pulsed Laval nozzle apparatus.

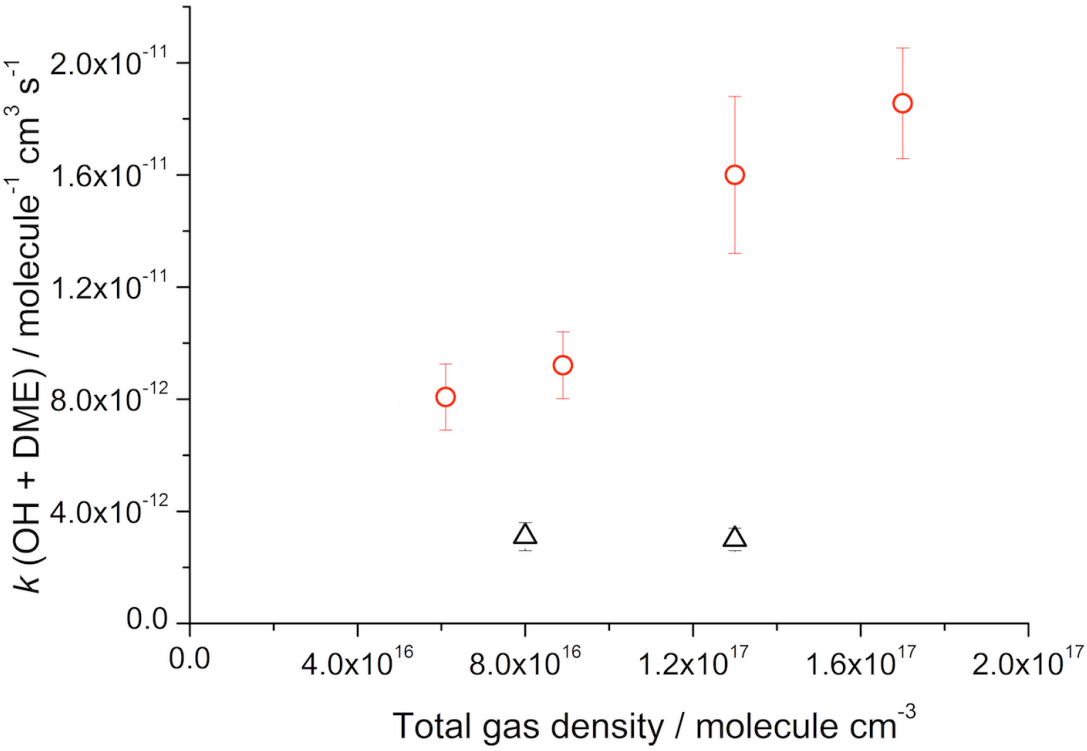

Figure 4. 13: Pressure dependence of $k_{4.2}$, the OH + DME rate coefficient at 79-83 K (N_2 bath gas, red open circles) and 133-138 K (N_2 bath gas, black open triangles).

For the reaction of OH with DME, rate coefficients were measured at four densities between 79 – 83 K and at two densities between 133-138 K. At the lower temperature, the rate coefficient demonstrates an approximately linear dependence on pressure indicating the role of collisional stabilization. As seen for the reaction of OH with acetone, at the higher temperature the rate coefficient for OH + DME appears to be much less dependent on pressure, however only 2 data points are available and so few conclusions

can be drawn from this. The presence of the intercept of the 79-83 K pressure dependence plot of Figure 4. 13 indicates that the zero pressure rate coefficient may be non-zero and so there may be a contribution from the tunnelling channel.

To provide evidence for the contribution from the bimolecular channel, the products of the OH + DME reaction can be probed indirectly by monitoring of OH LIF signal following addition of oxygen.

$$OH + CH_3OCH_3 \rightarrow H_2O + CH_3OCH_2 \quad \text{R4.2a}$$

$$O_2 + CH_3OCH_2 \rightarrow CH_3OCH_2OO^* \quad \text{R4.6}$$

$$M + CH_3OCH_2OO^* \rightarrow CH_3OCH_2OO + M \quad \text{R4.7}$$

$$CH_3OCH_2OO^* \rightarrow OH + 2H_2CO \quad \text{R4.8}$$

OH regeneration has been observed in many hydroxyl radical reactions in the presence of O_2 and is of relevance to both atmospheric and combustion environments.[36-38] Provided that the experiments are performed in the presence of significant oxygen so that $k_{4.2}$ is the rate determining step, then the absolute OH yield (α) can de determined by the ratio of $k_{4.6}$ in the presence and absence of oxygen.

$$k_{obs} = k_{4.2}[CH_3OCH_3] + k_{loss} \quad \text{E4.4}$$

$$k_{obs}(O_2) = (k_{4.2}[CH_3OCH_3] + k_{loss})\,(1 - \alpha) \quad \text{E4.5}$$

$$\propto = 1 - \left(\frac{k_{obs}(O_2)}{k_{obs}}\right) \quad \text{E4.6}$$

Experiments by Shannon were carried out on this reaction at 93 K and O_2 as 20 % of the total density.

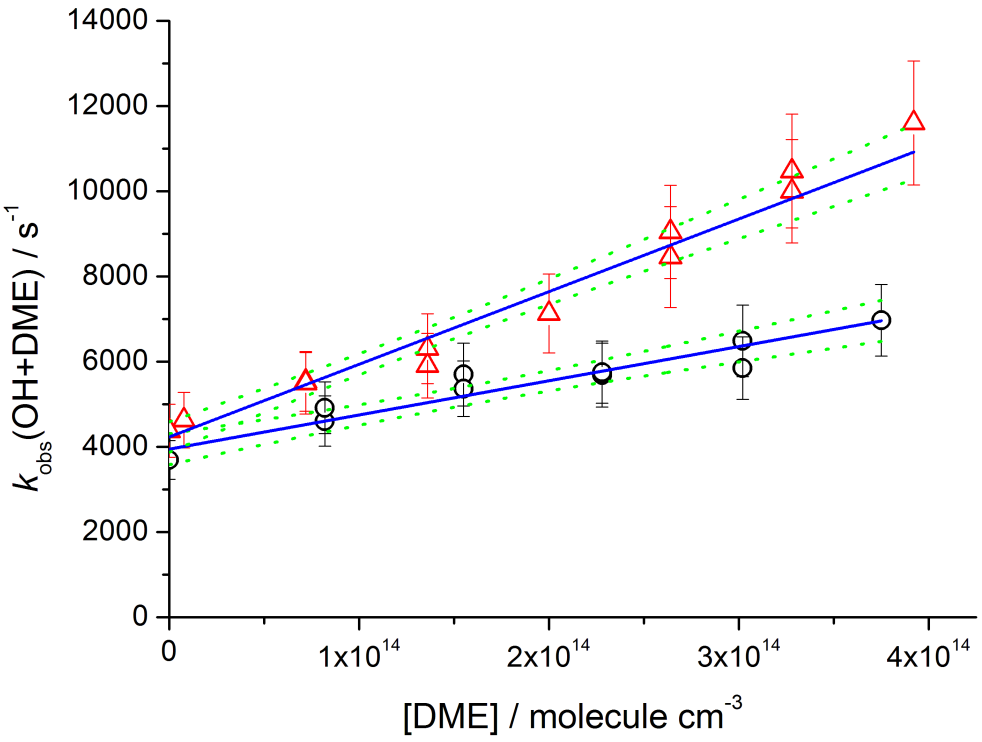

Figure 4. 14:Bimolecular plot showing the variation of pseudo first order rate coefficients for the reaction of OH with DME in the absence (red triangles) and presence (black circles) of 3.5×10^{15} molecule cm^{-3} oxygen. Data obtained by, and reproduced with permission of Dr Robin Shannon. The blue full lines are the weighted fit to the data of E4.3, and the green dashed lines represent the upper and lower 95 % confidence limits. The overall error in the bimolecular rate coefficient is the 95% confidence limits propagated with the error in the determination of the total density from the impact pressure measurements.

Examination of Figure 4. 14 shows that in the presence of oxygen, $k_{4.2}$ is notably reduced, providing clear evidence that OH recycling, and therefore, the bimolecular channel of $k_{4.2}$ is operating at 93 K. Using the rate coefficients obtained from the bimolecular plots in Figure 4. 14, α, the OH yield is calculated as 0.53 . This corresponds to the branching ratio of R4.2 to the bimolecular channel of around 53 %. However, there is likely to be some loss of $CH_3OCH_2O_2$* via third body stabilization, and so the branching ratio obtained from the OH yield is only a lower limit. Using the lower limit of 0.53, the zero-pressure limiting rate coefficient can be obtained by multiplication of this value by $k_{4.2(no\ O2)}$. This value is shown later in Figure 4. 18 along with the direct pressure dependence measurements of the rate coefficient. It can be seen that this lower limiting value fits the trend of the experimental data well and is consistent with a significant contribution from quantum mechanical tunnelling.

Master equation calculations performed by Shannon on these systems were used to further interpret the experimental data and explore the temperature and pressure dependencies further. For the OH + acetone reaction, the

experimental data obtained in this work, and additional rate coefficients in the literature by Yamada *et al.* and Gierczak *et al.* from 200-800 K (13 data points in total with no more than 100 K between each) were used to fit the values for the barrier height, the well depth of the pre-reaction complex.[10,33] Good agreement for the barrier height is obtained between previous calculations performed at the CBS-QB3 and CCSD(T)/6-311G levels of theory and this work once the hindered rotor model was used to describe vibrational motions.[8,20,33] The well depth was required to be much deeper than values reported in the literature from *ab initio* calculations to fit to the experimental temperature dependence data, whether a hindered rotor or harmonic oscillator model was used to describe the vibrational modes. It is expected that if a more rigorous method was used to describe, in particular, the low frequency bending modes of the pre-barrier complex, then this would correct the density of states so that the retrieved well depth was closer to the *ab initio* obtained values.[26]

The values used by Shannon for the calculations are given alongside those used for the OH + DME work in Table 4. 2.

Table 4. 2: Theoretical parameters used for master equation fitting for both reactions.

	OH + acetone			*OH + DME*
Parameter	Harmonic oscillator	Hindered rotor	Literature values range[8,9,33]	Carr *et al.* values[4]
Barrier height / kJ mol^{-1}	3.6	13.0	6.1-16.7	0.6
Well depth / kJ mol^{-1}	-38.1	-29.4	-22.2-18.4	-22.0 (-29.8)
Imaginary frequency of tunnelling mode / cm^{-1}	541	1116	1107 - 1293	1697
A factor for barrierless formation of the complex / $molecule^{-1}$ cm^3 s^{-1}	2.1×10^{-10}	1.9×10^{-10}	N/A	5.0×10^{-10}

*Value in brackets is the lowered well depth required to fit the low temperature experimental data in this work.

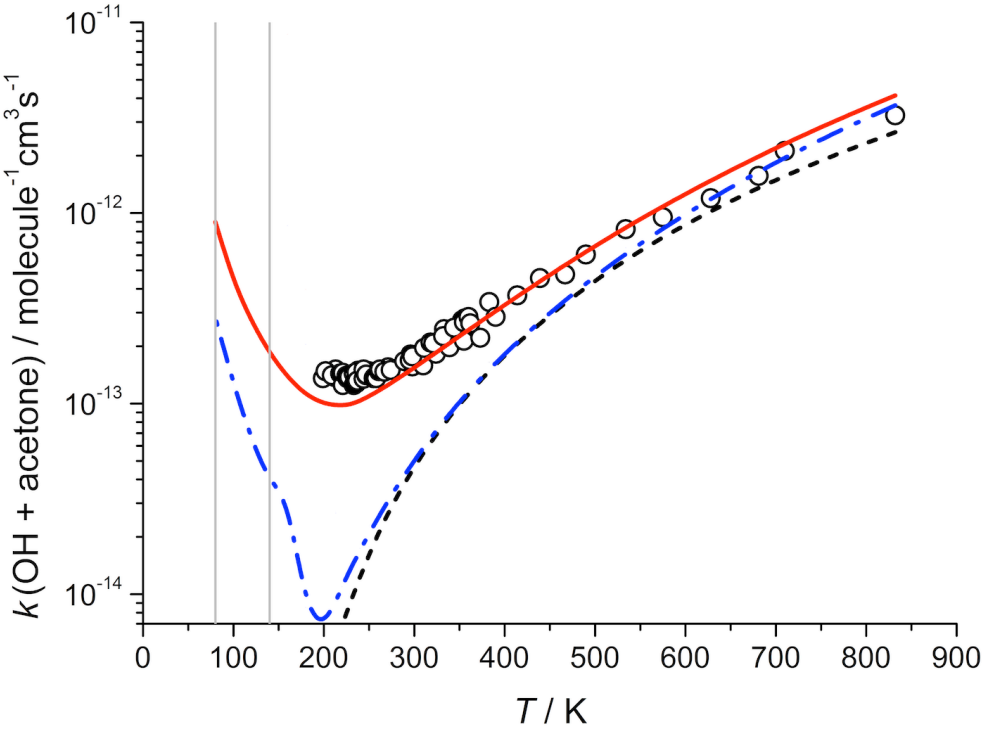

Figure 4. 15: Fitted temperature dependence for the rate coefficient for OH + acetone at zero pressure obtained from master equation calculations with hindered rotor treatment by Dr Robin Shannon using three different tunnelling treatments. Red solid line; Eckart method. Blue dot-dash line; WKB method. Black dash line; no tunnelling correction. The grey vertical lines are positioned at 80 K and 140 K to aid comparison with the experimentally obtained rate coefficients obtained at a range of pressures, and given in Error! Reference source not found..

Using the values obtained from fitting the experimental temperature dependence data, the zero-pressure rate coefficients were calculated using two models for tunnelling; Eckart and WKB. Good agreement across the temperature range between the experimental data the and theoretical calculations is achieved using the Eckart model with a fitted imaginary frequency of 1116 cm^{-1}(Figure 4. 15). The WKB tunnelling model significantly underestimates the rate coefficients across the whole temperature range, in particular below 350 K. Only the experimental data above 200 K is shown in Figure 4. 15, owing to the low temperature rate coefficients obtained in this work being in the fall off regime, and the values shown being in the low pressure limit.

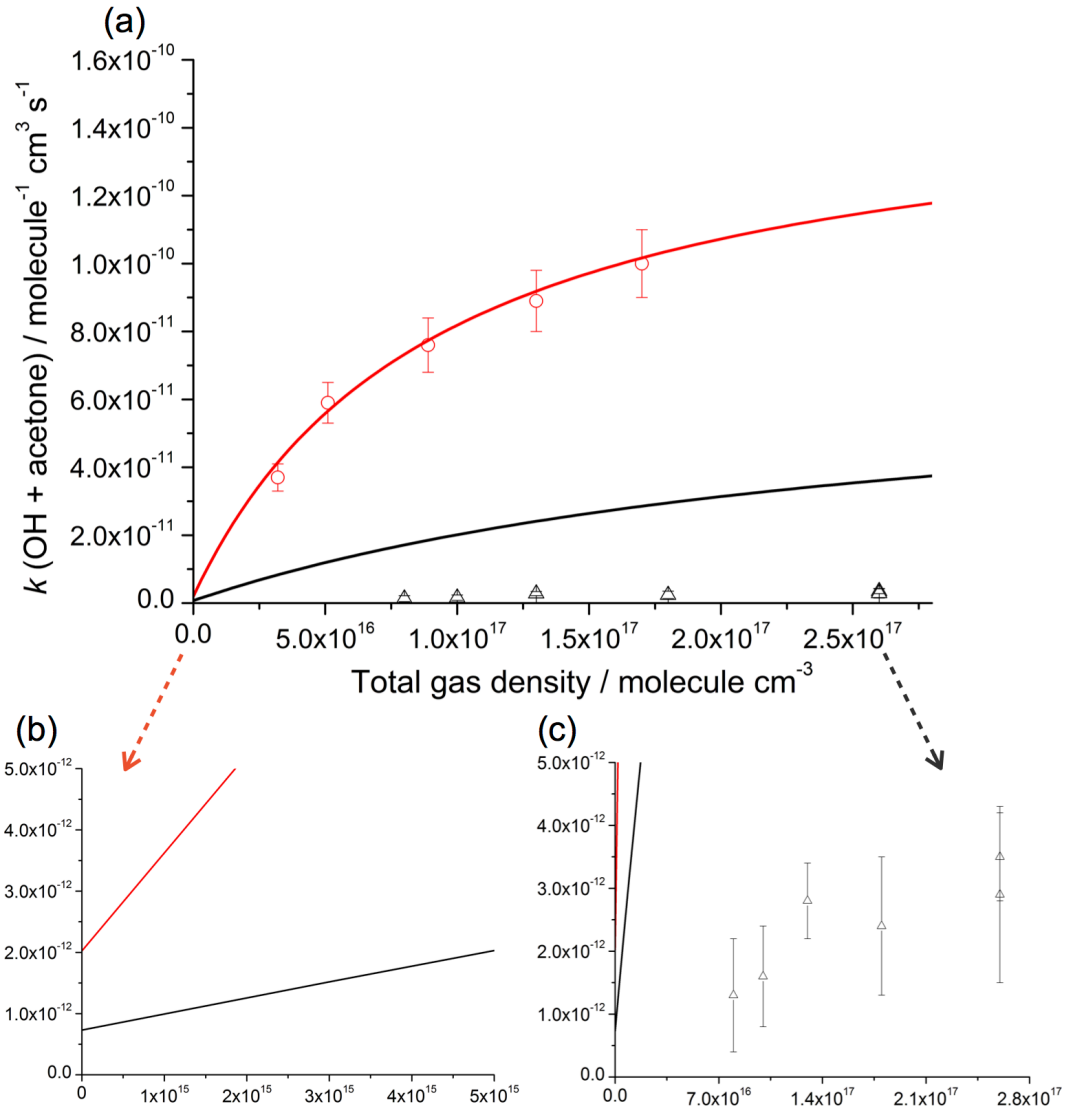

Figure 4. 16: (a) Pressure dependence of the OH + acetone rate coefficient at ~ 80 K (red open circles) and ~ 140 K (black open triangles) together with the master equation fits to the data at 80 K (red line) and 140 K (black line). The errors bars are the result of propagation of the 95 % confidence limits in the bimolecular rate coefficients with the errors in the expansion densities . (b) Enlarged section showing the MESMER calculated zero-pressure rate coefficients, which is the contribution of the bimolecular channel to the overall rate coefficients, which are calculated to be non-zero for both 80 K (red line) and 140 K (black line).(c) Enlarged section showing the experimentally obtained pressure dependence of the rate coefficient, which is over predicted by the MESMER calculations.

Figure 4. 16 shows the master equation fits to the 80 K (red line) and 140 K (black line) pressure dependence data. At 80 K, the pressure dependence is well modelled by the master equation calculations, and inspection of the intercept (Figure 4. 16 (b)) shows a small but significant contribution from tunnelling (k = 2 × 10^{-12} molecule^{-1} cm^3 s^{-1}). The tunnelling only rate coefficient at 80 K, obtained from this intercept, is around 12 times faster than the reported bimolecular room temperature value and so this reaction may operate in low temperature, low density interstellar environments.

At 140 K, the rate coefficient across the whole pressure range is significantly overestimated as shown in Figure 4. 16, parts (a) and (c). Whilst the experimental data have large errors associated with them, the master equation obtained values are not within the experimental errors. It is suggested that this discrepancy could be due to the incorrect energy dependence of the density of states of the pre-reaction complex owing to insufficiently rigorous treatment of the low frequency vibrational modes, and consequently having to lower the well depth significantly.[26] Alternatively, and more speculatively, this could be due to non-statistical behaviour at 140 K, where the complex is insufficiently long lived so that the ergodic assumption does not hold and internal vibrational relaxation cannot occur. The ergodicity assumption is key to statistical rate theory calculations, for example master equation methods, and so there would be deviation between experimentally and theoretically obtained rate coefficients.

Master equation calculations across a large temperature range had been performed by Carr *et al.* on the reaction of OH + DME and so the optimized values from their work was used by Shannon in this study, with the exception of the well depth which had to be reduced by ~ 8 kJ mol^{-1} to replicate the low temperature experimental values. The optimized values obtained by Carr *et al.*, along with the modified well depth used in this work, are given in Table 4. 2.[4]

As can be observed from Figure 4. 17, the temperature dependence of the rate coefficient for OH + DME, $k_{4.2}$, is well replicated by the master equation calculations, and the theoretically obtained zero pressure value at 91 K and the value obtained experimentally by the OH recycling experiment are within a factor of two. The smaller upturn in the rate coefficient for the OH + DME reaction in comparison to the OH + acetone rate coefficient at low temperatures may be rationalised by the relative lifetimes of the pre-barrier complexes. Acetone is a larger molecules than DME, and therefore, the density of states in the OH-acetone complex compared to reactants is larger than for the DME case.[39] Therefore, formation of the OH-acetone complex will have a longer lifetime, and so collisional stabilisation and tunnelling have a higher probability of occurring – enhancing the rate coefficient by a greater degree.

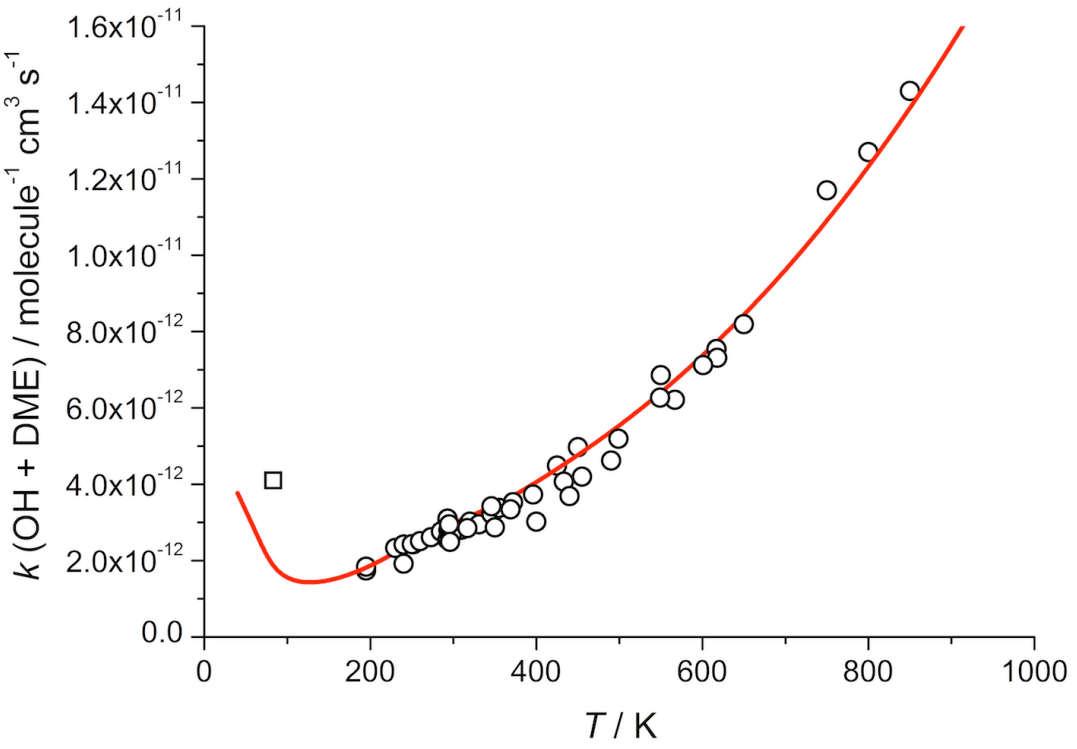

Figure 4. 17: Temperature dependence of the OH + DME rate coefficient, $k_{4.2}$, at zero pressure (red line) plotted alongside the experimental data from the literature (open circles). The contribution from the zero pressure channel at 93 K (open square) is estimated from the OH recycling experiment performed by Dr Robin Shannon and is plotted here to aid comparison between theory and experiment at low temperatures.

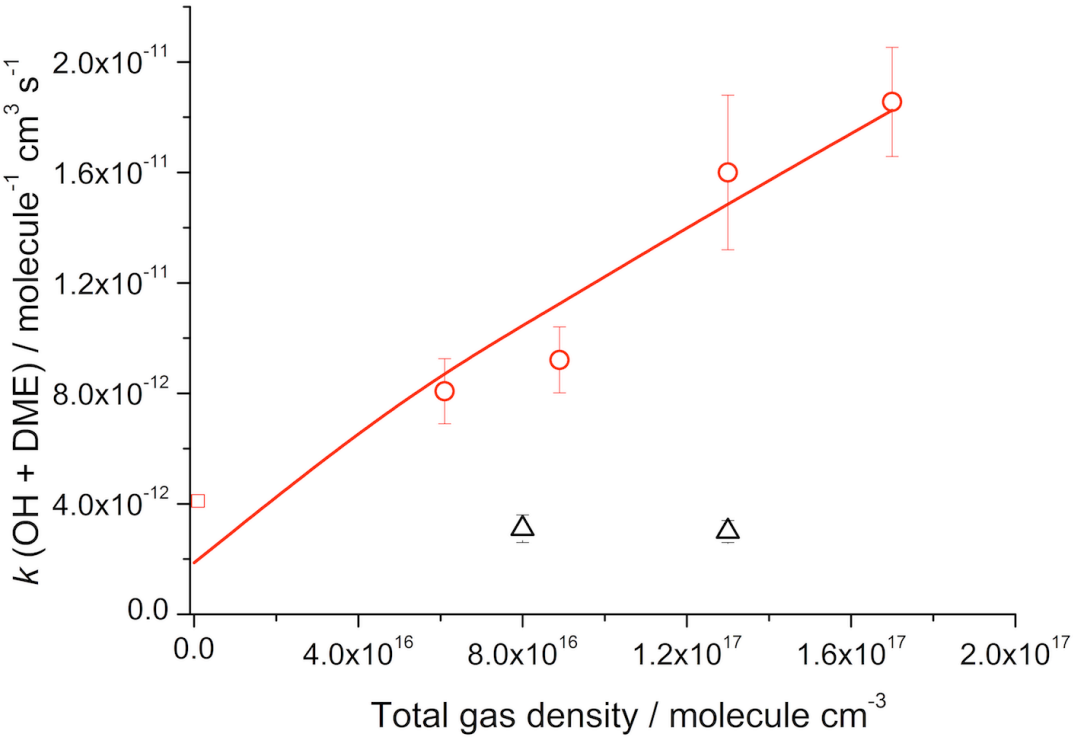

Figure 4. 18: Pressure dependence of the OH + DME rate coefficient with the master equation fit to the data (red line). Red open circles: 79-83 K N_2 bath gas. Black open triangles: 133-138 K N_2 bath gas.

The pressure dependence of the rate coefficients at 79-83 K was calculated using the fitted parameters shown in Table 4. 2, and very good agreement with the experimental values is obtained. At ~ 80 K, both the OH + acetone and OH + DME rate coefficients have contributions from the pressure independent, bimolecular channel. In the low pressures of interstellar environments, it is the bimolecular channel which would be operating, as the densities are insufficient for significant third-body stabilization to be operating. Considering only this bimolecular channel, the rate coefficients at ~80 K for OH + acetone and OH + DME are a factor of 12 and 0.6 greater respectively compared to the room temperature values. Master equation calculations demonstrate that at 10 K, the pressure independent component of the OH + acetone rate coefficient is a factor of 100 greater than at room temperature.[26] These reactions are currently not included in interstellar models despite acetone, DME and OH being detected in in a variety of interstellar environments, such as the Sagittarius molecular cloud (Sgr) where temperatures can reach as low as 40 K.[16,40] These reactions could be a potential gas-phase route to the formation of more complex organic molecules in interstellar environments– the origins of which are not currently fully understood.

4.5 Interstellar impact of the OH + acetone and OH + DME reactions

The OH + acetone and OH + DME reactions have been included in a newly constructed astrochemical model by Dr Kinsuk Acharyya and Professor Eric Herbst of the University of Virginia as part of a collaboration to explore the potential effects of H-transfer reactions on astrochemical environments. The model, which included both gas phase and gas-grain reactions, has been described fully in Chapter 3 and so only a brief outline is given here.[41]

A total of 670 gas phase reactions between 8620 gaseous species were included in the model, encompassing several reaction types such as neutral-neutral, ion-neutral, dissociative recombination and photo-induced processes, amongst others. These reactions were taken largely from the KIDA database with some omissions and additions.[42] The temperature dependence of the bimolecular neutral-neutral reactions was treated using a modified Arrhenius expression. Ion-neutral reactions were treated using either a Langevin or a Su-Chesnavich approach.[43] Reactions on the surface of grains were assumed to occur via a Langmuir-Hinshelwood mechanism.

The initial elemental abundances of the model were chosen to be representative of cold interstellar clouds, with all elements in their atomic form, except for molecular hydrogen. The model was run in a pseudo time dependence mode, whereby the physical parameters were maintained throughout the run, and the molecular abundances monitored as a function of time. The model runs were performed at temperatures of 10, 50 and 100 K. The experimentally obtained values at 79 (acetone) and 63 (DME) K were utilised for the 50 K model, the 82 and 93 K values were utilised for the 100 K model, and the 10 K values were an extrapolation of the current data set. It must be noted that these values will be an upper limit to the true values as they contain a contribution from the pressure dependence channel. Therefore, there values will subject to error and to obtain more accurate representation of the impact of these reactions, the values obtained from the master equation calculations should be utilised. The values utilised are presented in Table 4. 3.

Table 4. 3: Rate coefficients utilised in the model constructed by Dr Kinsuk Acharyya and Professor Eric Herbst.[41]

Reaction	Rate coefficient utilised / 10^{-10} molecule^{-1} cm^3 s^{-1}		
	10 K	50 K	100 K
OH + acetone	1.0	1.0	0.37
OH + DME	0.30	0.17	0.077

The model demonstrated that the reactions have a negligible impact on the acetone and DME concentrations at all temperatures, with a maximum change in DME concentration of around a factor of two between 10^5 and 10^6 years. These reactions were included in the model alongside the alcohol reactions (discussed in Chapter 3) and it was found that any effects on water and hydroxyl radical concentrations were largely dominated by the OH + methanol reaction, owing both to methanol being more abundant and the low temperature rate coefficient being significantly faster.[41]

4.6 Summary

This work has further probed the role of a pre-barrier complex in the low temperature kinetic behaviour of hydrogen abstraction reactions involving hydroxyl radicals. In collaboration with Dr Robin Shannon, the rate coefficients of two such reactions, OH + acetone and OH + DME, have been

measured below 200 K for the first time and the mechanisms investigated through pressure dependence studies and deuterated analogues.[26]

The low temperature mechanism determined for the OH + alcohol reactions reported in Chapter 3 is also observed for these reactions. A weakly bound complex between the OH and co-reactant is formed prior to the overall barrier to hydrogen abstraction. The extended lifetime of this complex at lower temperatures enhances the probability of quantum mechanical tunnelling through the reaction barrier to form molecular products, but also leads to a competitive collisional stabilisation channel. The contribution of the two channels has been investigated through pressure dependence studies and additionally, master equation calculations by Shannon using MESMER.[29] At ~140 K, the contribution of the tunnelling mechanism to the overall rate coefficient for the acetone reaction is found to be negligible, with collisional stabilisation into the pre-barrier well dominating. At ~ 80 K, the contribution is greater and master equation calculations demonstrate that at 10 K, the pressure-independent component of the rate coefficient will be ~100 times greater than the room temperature value.[26]

The rate coefficient for OH + DME was found to be less dramatically enhanced at lower temperatures, although an enhancement in the rate coefficient, now characteristic of these type of reactions, was observed. At ~140 K, there was no observable pressure dependence of the rate coefficient over the experimental range, however it should be noted that the errors in the rate coefficients at this temperature were larger owing to the difficulty in measuring relatively slow rate coefficients in a Laval apparatus. At ~ 80 K, a notable pressure dependence of the rate coefficient is observed. However master equation calculations and indirect product detection by Shannon demonstrate a significant contribution from the pressure-independent channel.

Acetone, DME and the hydroxyl radical have all been detected in astrochemical environments such as the cold Sagittarius B2 molecular cloud, and the reactions reported in this chapter may act as the initial steps to the formation of more complex species. The OH + acetone and OH + DME reactions have been included in an astrochemical model constructed by Dr Kinsuk Acharyya and Professor Eric Herbst of the University of Virginia, and the results have been published in a co-authored manuscript with the Leeds pulsed Laval nozzle group.[41] Overall the findings of the model demonstrated that the reactions had only a small effect on the fractional abundances of DME and acetone as the low temperature rate coefficients

were not sufficiently fast to compete with the production processes. However, this collaboration will hopefully provide motivation for the inclusion of a wider range of reaction types within astrochemical models, and also for the further low temperature study of H-abstraction reactions where quantum tunnelling may occur that are of potential relevance to astrochemical environments.

4.7 References

1 Lewis, A. C. *et al.* Sources and sinks of acetone, methanol, and acetaldehyde in North Atlantic air. *Atmos. Chem. Phys. Discuss.* **5**, 1285-1317 (2005).

2 Singh, H. B. *et al.* Acetone in the atmosphere: Distribution, sources, and sinks. *Journal of Geophysical Research: Atmospheres* **99**, 1805-1819 (1994).

3 Valach, A., Langford, B., Nemitz, E., MacKenzie, A. & Hewitt, C. Concentrations of selected volatile organic compounds at kerbside and background sites in central London. *Atmospheric Environment* **95**, 456-467 (2014).

4 Carr, S. A. *et al.* Experimental and Theoretical Study of the Kinetics and Mechanism of the Reaction of OH Radicals with Dimethyl Ether. *The Journal of Physical Chemistry A* **117**, 11142-11154 (2013).

5 Heard, D. E. in *Encyclopedia of Atmospheric Sciences* (ed Editor-in-Chief: James R. Holton) 2185-2193 (Academic Press, 2003).

6 Wollenhaupt, M., Carl, S. A., Horowitz, A. & Crowley, J. N. Rate Coefficients for Reaction of OH with Acetone between 202 and 395 K. *The Journal of Physical Chemistry A* **104**, 2695-2705 (2000).

7 Vasvari, G. *et al.* Reaction and complex formation between OH radical and acetone. *Physical Chemistry Chemical Physics* **3**, 551-555 (2001).

8 Henon, E., Canneaux, S., Bohr, F. & Dóbé, S. Features of the potential energy surface for the reaction of OH radical with acetone. *Physical Chemistry Chemical Physics* **5**, 333-341 (2003).

9 Vandenberk, S., Vereecken, L. & Peeters, J. The acetic acid forming channel in the acetone + OH reaction: A combined experimental and theoretical investigation. *Physical Chemistry Chemical Physics* **4**, 461-466 (2002).

10 Gierczak, T., Gilles, M. K., Bauerle, S. & Ravishankara, A. Reaction of hydroxyl radical with acetone. 1. Kinetics of the reactions of OH, OD, and ^{18}OH with acetone and acetone-d 6. *The Journal of Physical Chemistry A* **107**, 5014-5020 (2003).

11 Talukdar, R. K., Gierczak, T., McCabe, D. C. & Ravishankara, A. Reaction of hydroxyl radical with acetone. 2. Products and reaction mechanism. *The Journal of Physical Chemistry A* **107**, 5021-5032 (2003).

12 Arif, M., Dellinger, B. & Taylor, P. H. Rate coefficients of hydroxyl radical reaction with dimethyl ether and methyl tert-butyl ether over an

extended temperature range. *The Journal of Physical Chemistry A* **101**, 2436-2441 (1997).

13 Bonard, A., Daële, V., Delfau, J.-L. & Vovelle, C. Kinetics of OH radical reactions with methane in the temperature range 295-660 K and with dimethyl ether and methyl-tert-butyl ether in the temperature range 295-618 K. *The Journal of Physical Chemistry A* **106**, 4384-4389 (2002).

14 Combes, F. *et al.* Acetone in interstellar space. *Astronomy and Astrophysics* **180**, L13-L16 (1987).

15 Whiteoak, J. B. & Gardner, F. F. The Abundance Ratio $^{16}OH/^{18}OH$ in Sagittarius-A and Sagittarius-B2. *Monthly Notices of the Royal Astronomical Society* **197**, 39p (1981).

16 de Vincente, P., Martin-Pintado, J. & Wilson, T. L. A hot ring in the Sagittarius B2 molecular cloud. *Astron. Astrophys.* **320**, 957-971 (1997).

17 Shannon, R. J., Taylor, S., Goddard, A., Blitz, M. A. & Heard, D. E. Observation of a Large Negative Temperature Dependence for Rate Coefficients of Reactions of OH with Oxygenated Volatile Organic Compounds Studied at 86-112 K. *Phys. Chem. Chem. Phys.* **12**, 13511-13514 (2010).

18 Taylor, S. E. *Reaction Kinetics at Very Low Temperatures Measured Using a Pulsed Laval Nozzle System* PhD thesis, University of Leeds, (2007).

19 Shannon, R. J. *Experimental and computational studies of hydroxyl radical kinetics at very low temperatures* PhD thesis, University of Leeds, (2012).

20 Caralp, F., Forst, W., Henon, E., Bergeat, A. & Bohr, F. Tunneling in the reaction of acetone with OH. *Physical Chemistry Chemical Physics* **8**, 1072-1078 (2006).

21 Wallington, T. J. & Kurylo, M. J. Flash photolysis resonance fluorescence investigation of the gas-phase reactions of hydroxyl radicals with a series of aliphatic ketones over the temperature range 240-440 K. *The Journal of Physical Chemistry* **91**, 5050-5054 (1987).

22 Bell, R. P. *The Tunnel Effect in Chemistry*. (Chapman and Hall, 1980).

23 Pilling, M. J. & Seakins, P. W. *Reaction kinetics*. (Oxford University Press, 1995).

24 Shannon, R. J., Blitz, M. A., Goddard, A. & Heard, D. E. Accelerated Chemistry in the Reaction between the Hydroxyl Radical and Methanol at Interstellar Temperatures Facilitated by Tunnelling. *Nature Chem.* **5**, 745-749 (2013).

25 Brown, S. S., Burkholder, J. B., Talukdar, R. K. & Ravishankara, A. R. Reaction of Hydroxyl Radical with Nitric Acid: Insights into Its Mechanism. *The Journal of Physical Chemistry A* **105**, 1605-1614 (2000).

26 Shannon, R. J., Caravan, R. L., Blitz, M. & Heard, D. E. A combined experimental and theoretical study of reactions between the hydroxyl radical and oxygenated hydrocarbons relevant to astrochemical environments. *Phys. Chem. Chem. Phys.* **16**, 3466-3478 (2014).

27 Carr, S. A. *et al.* OH yields from the $CH_3CO + O_2$ reaction using an internal standard. *Chemical Physics Letters* **445**, 108-112 (2007).

28 Carr, S. A. *et al.* Experimental and Modeling Studies of the Pressure and Temperature Dependences of the Kinetics and the OH Yields in the Acetyl + O_2 Reaction. *The Journal of Physical Chemistry A* **115**, 1069-1085 (2011).

29 Glowacki, D. R., Liang, C.-H., Morley, C., Pilling, M. J. & Robertson, S. H. MESMER: an open-source master equation solver for multi-energy well reactions. *The Journal of Physical Chemistry A* **116**, 9545-9560 (2012).

30 Frisch, M. *et al.* Gaussian 03, revision c. 02; Gaussian. *Inc., Wallingford, CT* **4** (2004).

31 Miller, W. H. Tunneling corrections to unimolecular rate constants, with application to formaldehyde. *Journal of the American Chemical Society* **101**, 6810-6814 (1979).

32 Garrett, B. C. & Truhlar, D. G. Semiclassical tunneling calculations. *Journal of Physical Chemistry* **83**, 2921-2926 (1979).

33 Yamada, T., Taylor, P. H., Goumri, A. & Marshall, P. The reaction of OH with acetone and acetone-d6 from 298 to 832 K: Rate coefficients and mechanism. *Journal of Chemical Physics* **119**, 10600-10606 (2003).

34 Mellouki, A., Teton, S. & Le Bras, G. Kinetics of OH radical reactions with a series of ethers. *International Journal of Chemical Kinetics* **27**, 791-805 (1995).

35 Wallington, T. J., Liu, R., Dagaut, P. & Kurylo, M. J. The gas phase reactions of hydroxyl radicals with a series of aliphatic ethers over the temperature range 240–440 K. *International Journal of Chemical Kinetics* **20**, 41-49 (1988).

36 Glowacki, D. R. *et al.* Interception of Excited Vibrational Quantum States by O_2 in Atmospheric Association Reactions. *Science* **337**, 1066-1069 (2012).

37 Lockhart, J., Blitz, M., Heard, D., Seakins, P. & Shannon, R. Kinetic Study of the OH+ Glyoxal Reaction: Experimental Evidence and Quantification of Direct OH Recycling. *The Journal of Physical Chemistry A* **117**, 11027-11037 (2013).

38 Lockhart, J., Blitz, M. A., Heard, D. E., Seakins, P. W. & Shannon, R. J. Mechanism of the Reaction of OH with Alkynes in the Presence of Oxygen. *The Journal of Physical Chemistry A* **117**, 5407-5418 (2013).

39 Gilbert, R. G. & Smith, S. C. *Theory of unimolecular and recombination reactions*. (Blackwell Scientific, 1990).

40 van Dishoeck, E. F., Blake, G. A., Draine, B. T. & Lunine, J. I. in *Protostars and planets* Vol. III (A93-42937 17-90) 163-241 (1993).

41 Acharyya, K. *et al.* The Importance of OH Radical-Neutral Low Temperature Tunneling Reations in Interstellar Clouds Using a New Model. *Molecular Physics* **Accepted** (2015).

42 Wakelam, V. *et al.* A kinetic database for astrochemistry (KIDA). *The Astrophysical Journal Supplement Series* **199**, 21 (2012).

43 Su, T. & Chesnavich, W. J. Parametrization of the ion–polar molecule collision rate constant by trajectory calculations. *The Journal of Chemical Physics* **76**, 5183-5185 (1982).

Chapter 5. The reaction of OH with ammonia at low temperatures: Rapid bimolecular product formation via a very weakly bound complex

5.1 Background and previous work on the OH + ammonia reaction

The enhanced rate coefficients of the hydroxyl radical reactions discussed thus far in this thesis have depended on the formation of a relatively weakly bound complex between OH and its co-reactant.[1-3] A common mechanism operating below 200 K in several hydrogen abstraction reactions between OH and oxygenated volatile organic compounds has been identified. At lower temperatures (< 200 K), the complex has an extended lifetime, which enhances the probability of tunnelling through the hydrogen-abstraction barrier to form bimolecular products.[1-3] As a result, the rate coefficient for these reactions are enhanced by up to a factor of 56 between room temperature and 54 K.[2] *Ab initio* stationary point calculations for these reactions indicate that the binding energies of these complexes range from 18 to 27 kJ mol^{-1}.[3-6] Given the crucial role of the complex in the enhancement of the rate coefficients at low temperatures, how weakly bound can these complexes be for this mechanism to still be operative?

The reaction of OH with ammonia (R5.1) proceeds via a significant barrier to hydrogen abstraction, as shown in Figure 5. 1, leading to the formation of NH_2 and water (R5.1a).

$$OH + NH_3 \xrightarrow{k_{5.1}} products \qquad \text{R5.1}$$

$$OH + NH_3 \rightarrow NH_2 + H_20 \qquad \text{R5.1a}$$

Prior to this barrier there is a very weakly bound complex between the reactants with a binding energy of only 7.5 kJ mol^{-1}, according to the calculations of Monge-Palacios *et al.* at the CCSD(T)/full/aug-cc-PVTZ//CCSD(T)/FC/pVTZ level and as shown in Figure 5. 1.[7] The stationary point energies are also in reasonable agreement with those obtained by Corchado *et al.* at the QCISD(T)/MP2/aug-cc-pVDZ level of theory and by Shannon at the ROHF-UCCSD(t)/aug-cc-pVDZ//ROHF-UCCSD(t)/aug-cc-pVTZ level.[8,9]

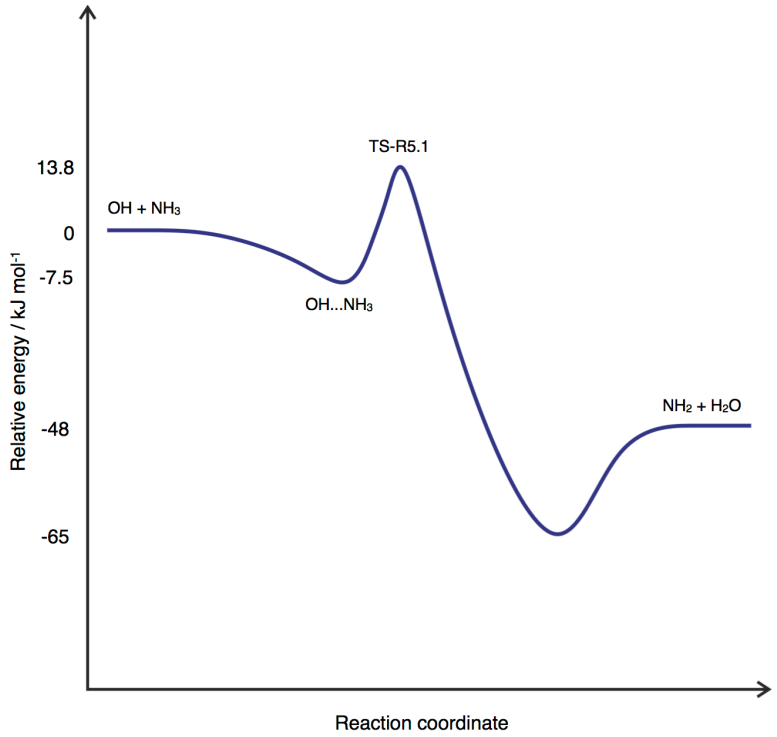

Figure 5. 1: To-scale potential energy surface for the OH + ammonia reaction based on calculations by Monge-Palacios *et al.* at the CCSD(T)/full/aug-cc-PVTZ//CCSD(T)/FC/pVTZ level of theory.[7]

The reaction of OH with ammonia is of interest to atmospheric chemistry as a source of amidogen radicals (NH_2), which are believed to have an impact on NO_x chemistry.[10,11] This reaction is also of relevance to combustion systems, as it is important for the conversion of fuel nitrogen to NO_x, and additionally, the denitrification of flue gas.[12] Several experimental studies are present in the literature, and as shown in Figure 5. 2, the rate coefficient has been shown to exhibit a positive temperature dependence and is relatively slow at room temperature (~ 1.4 $\times 10^{-13}$ molecule^{-1} cm^3 s^{-1}), corresponding to the reaction proceeding via the significant barrier to hydrogen abstraction.[10-13] At lower temperatures (down to 273 K), there is notable deviation from Arrhenius type behaviour - suggesting that tunnelling may be operative. This suggestion is supported by theoretical work by Corchado *et al.*, who demonstrated, using canonical transition state theory, that the experimentally determined rate coefficients could only be replicated when multi-dimensional tunnelling through the H-abstraction barrier was included.[8]

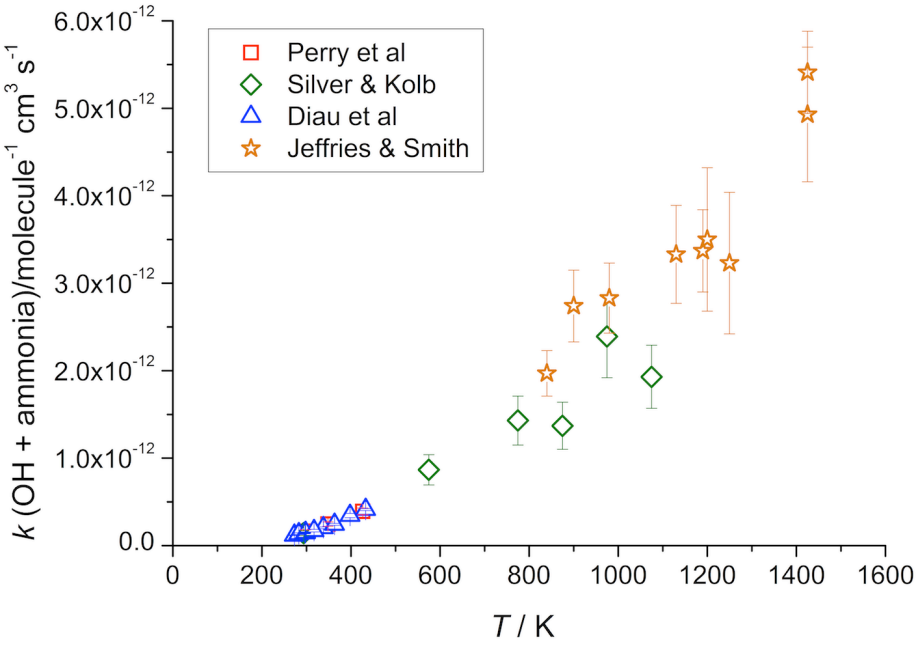

Figure 5. 2: Temperature dependence of the OH + ammonia rate coefficient as reported in the literature.[10-13]

The reaction of OH and ammonia has not previously been studied below 273 K, however it may be of importance to low temperature environments. Ammonia and the hydroxyl radical are almost ubiquitous in interstellar space, having been detected in many star forming regions, molecular clouds and hot and cold cores. Ammonia was first observed in 1968 by Cheung *et al.* in the Sagittarius B2 molecular cloud, where OH has also been detected and temperatures can reach as low as 40 K.[14,15] Additionally, both OH and ammonia have been detected towards W3(OH) (a post-star forming region), where the temperature reaches as low as 10 K with abundances relative to H_2 on the orders of 10^{-7} and 10^{-8} respectively, and also in the molecular cloud TMC-1, with column densities of ~ 10^{15} cm^{-2} for both species and a temperature of 10 K.[16-19] The reaction of ammonia with OH leads to the formation of water vapour and also NH_2 (R5.1a), a species which has also been detected in interstellar regions, and is postulated to be an important species in the production of interstellar glycine.[20,21] Interestingly, the first interstellar observation of NH_2 was in the Sagittarius B2 molecular cloud.[22]

A preliminary study of the OH + ammonia reaction was previously carried out at 79 K by Dr Robin Shannon using this apparatus.[9] However, Shannon identified a catalytic effect on the rate coefficient when using $(CH_3)_3COOH$ as the hydroxyl radical precursor.[9] Through the experimental observations and *ab initio* calculations, it was found that the $(CH_3)_3COOH$ precursor formed a complex with ammonia that reacted more rapidly with OH than the ammonia itself, and so the experimental study of the OH + ammonia rate

coefficient was limited. Preliminary *ab initio* / master equation calculations at the ROHF-UCCSD(t)/aug-cc-pVDZ//ROHF-UCCSD(t)/aug-cc-pVTZ level also by Shannon on the OH + ammonia reaction were in reasonably good agreement with the previous higher temperature experimental data.[9] When the Eckart model of tunnelling was used in combination with the calculated imaginary frequency of 1610 cm^{-1}, a notable upturn in the rate coefficient was predicted below 200 K, with a calculated rate coefficient of ~ 5 × 10^{-12} $molecule^{-1}$ cm^3 s^{-1} at 50 K.[9]

Given the ubiquity and abundance of OH and ammonia in interstellar environments, if the reaction rate coefficient is large as predicted by the master equation calculations of Shannon, this reaction could be a significant sink of both species, and also a potential source of interstellar NH_2 and water vapour which is currently not accounted for in interstellar models.[9] The first detailed study of this reaction below 273 K is reported here. The rate coefficient for the OH + ammonia reaction has been investigated at ~ 54 K and ~ 89 K in this work over a small pressure range using an alternative OH precursor to that utilised by Shannon. *Ab initio* and master equation calculations have been performed by Dr Arne Bunkan (University of Leeds / University of Oslo) and are compared with the experimental low temperature rate coefficients obtained in this work. In collaboration with Professor Eric Herbst and Dr Kinsuk Acharyya (University of Virginia), the experimental rate coefficients obtained in this work have been incorporated into a new astrochemical gas-grain model to assess the impact of the low temperature OH + ammonia reaction.

5.2 Experimental procedure

The experiments were carried out as described in detail in Chapter 2, but further details are give here.

The vapour pressure of ammonia (BOC, 99.8 %) was admitted to an evacuated cylinder and diluted with nitrogen (BOC, OFN) or argon (99.98 % , BOC). The concentration of ammonia in the cylinders was ascertained from pressure measurements. The cylinder was allowed to mix overnight before use. OH was generated chemically from the reaction of ammonia with $O(^1D)$, produced following 248 nm photolysis of ozone. Ozone was generated by the electrical discharge of O_2 (BOC 99.999 %) and was subsequently admitted to an evacuated cylinder where it was diluted with the bath gas (argon or nitrogen as before).

The ammonia, ozone and bath gas were flowed through a set of calibrated mass flow controllers into the pre-expansion reservoir via a ballast tank where the gases were allowed to mix. The gas mixture was expanded through the Laval nozzle via two pulsed solenoid valves in pulses of a fixed duration between ~10-20 ms, into the low pressure stainless steel chamber.

The rate coefficient for OH + ammonia was measured by temporal monitoring of the hydroxyl radical via PLP-LIF. The resultant jet formed from expansion through the Laval nozzle was irradiated along the jet axis by a 248 nm excimer laser, leading to the formation of $O(^1D)$ from the photolysis of ozone. The $O(^1D)$ then reacted with ammonia forming OH in vibrational states up to v=2, as demonstrated by Silvente *et al.*,[23] producing OH and NH_2 with a total branching fraction of 0.9, as demonstrated by Wang *et al.* and Shu *et al.* [24,25]

$$O_3 + h\nu(248\,nm) \rightarrow O(^1D) + O_2 \qquad \text{P5.1}$$

$$O(^1D) + NH_3 \rightarrow OH(v \geq 0) + NH_2 \qquad \phi=0.9 \qquad \text{R5.2}$$

Experiments were performed under pseudo first order conditions so that $[NH_3]$ >> [OH]. The growth and subsequent decay of OH was monitored by off-resonance LIF by probing the $A^2\Sigma^+ \leftarrow X^2\Pi_i$ (1,0) $Q_1(1.5)$ transition at ~ 282 nm. The off-resonance fluorescence was monitored by a PMT fitted with a 308 nm interference filter (Barr Associates λ_{max} = 308.5 nm, FWHM = 5 nm).

The reaction scheme for the formation and removal of OH comprises reactions P5.1, R5.1 and R5.2. For pseudo first order conditions $[NH_3]$ >> [OH] the temporal evolution of OH is given by :

$$[OH]_t = \left(\frac{k_{rel}}{k_{obs}-k_{rel}}\right)[OH^*]_0\left(e^{-k'_{rel}t} - e^{-k_{obs}t}\right) + [OH]_0 e^{-k_{obs}t} \qquad \text{E5.1}$$

and

$$k_{obs} = k_{5.1}[NH_3] + k_{loss} \qquad \text{E5.2}$$

where k_{obs} is the pseudo first order rate coefficient, k'_{rel} is the pseudo first order rate coefficient for relaxation from the rovibrationally excited states of OH formed in R5.2 into the laser probed level, OH, and k_{loss} is the rate coefficient for the loss of OH out of the detection region via diffusion and other loss processes. The derivation of E5.1 is given in Appendix C.

It is anticipated that vibrational relaxation of OH from the v>0 states produced from R5.2 may be rapid, in part due to the potential formation of an complex between OH and ammonia at low temperatures, which enhances IVR.[23] Additionally, resonance effects due to the vibrational frequencies of

OH and NH_3 being similar in magnitude (3746 and 3598 cm^{-1} respectively according to the calculations of Monge-Palacios *et al.*[7]) will also enhance VET, and resonance enhanced VET has a negative temperature dependence.[26] Furthermore, rapid VET has been observed for OH in the presence of ammonia at room temperature by Silvente *et al.,* by monitoring the vibrationally excited states of OH using LIF spectroscopy.[23]

Given the exothermicity of R5.2 (170 kJ mol^{-1} according to calculations by Wang *et al.*[24]) and that OH is formed in vibrationally excited states, it is likely that OH will also be formed in rotationally hot states. Rotational energy transfer (RET) is much more efficient with N_2 bath gas than Ar bath gas, and additionally becomes less efficient with decreasing temperature.[26,27] Therefore, at 54 K using Ar bath gas, rotational relaxation will be notably slower than at 89 K with an N_2 bath gas, and the early time growth on the OH LIF traces obtained at 54 K will be more pronounced. In the latter case where RET is on a timescale fast in comparison to the subsequent loss of OH, E5.1 can be fitted to the data. However, where RET and VET are on a comparable timescale to the loss, it is not possible to fit E5.1 to the data as the two processes are convoluted. Instead the data can be fitted with a single exponential decay expression at longer delay times (from ~ 70-100 μs onwards) to obtain the loss component (E5.3).

$$[OH]_t = [OH]_0 e^{-k_{obs}t} \qquad \text{E5.3}$$

and

$$k_{obs} = k_{5.1}[NH_3] + k_{loss} \qquad \text{E5.2}$$

5.3 Results and discussion

5.3.1 OH loss experiments

Examples of the temporal evolution of the OH LIF signal following 248 nm photolysis of ozone in the presence of ammonia are shown in Figure 5. 3 and Figure 5. 4, together with non-linear least squares fits of E5.3 and E5.1, respectively, to the data yielding k_{obs}.

Experiments were repeated for a variety of concentrations of ammonia and Figures 5 and 6 show the variation of k_{obs} with [ammonia], the gradients of which yield the bimolecular rate coefficients at 53 K and 89 K respectively.

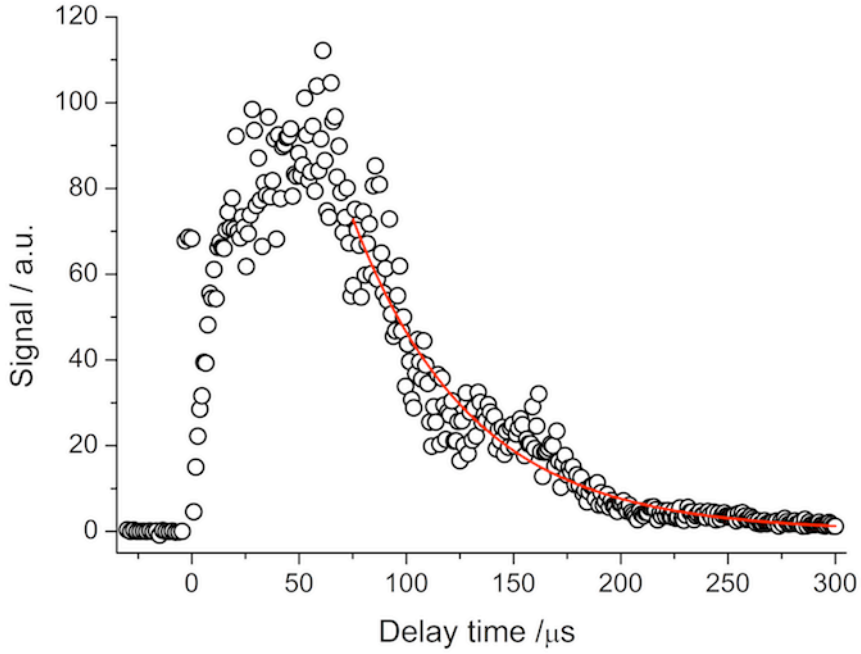

Figure 5. 3: Pseudo first order LIF trace of OH together with the non-linear least squares fit of E5.3 to the data from the 248 nm photolysis of ozone in the presence of ammonia (1.17 × 10^{15} molecule cm^{-3}) at 53 ± 9 K. The least squares fit of E5.3 to the data yields a pseudo first order rate coefficient of 18061 ± 500 s^{-1}.

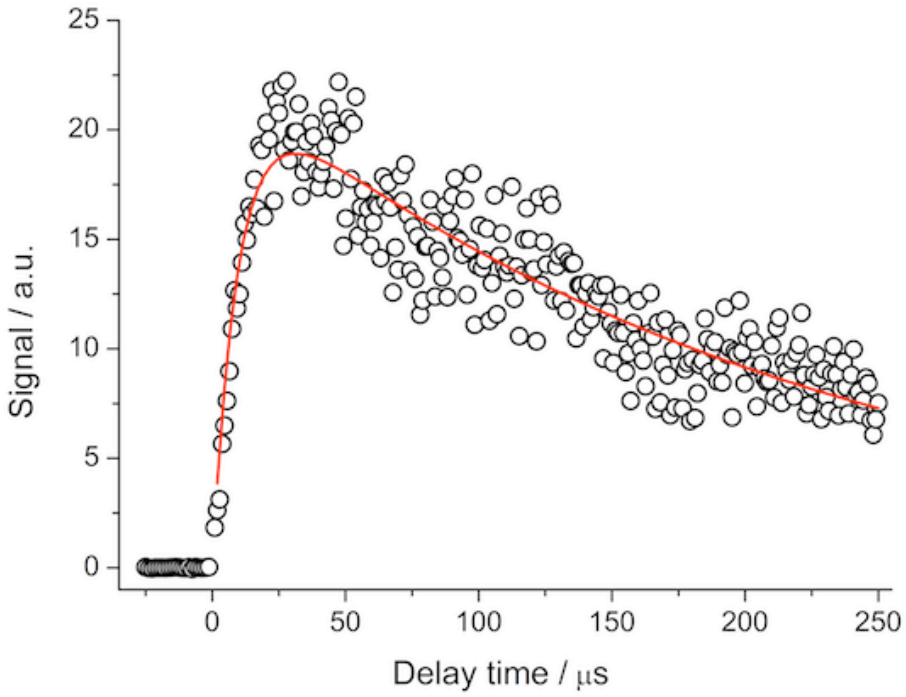

Figure 5. 4: Pseudo first order LIF trace of OH together with the non-linear least squares fit of E5.1 to the data from the 248 nm photolysis of ozone in the presence of ammonia (1.02 × 10^{15} molecule cm^{-3}) at 89 ± 4 K. The least squares fit of E5.1 to the data yields a pseudo first order rate coefficient of 4564 ± 155 s^{-1}.

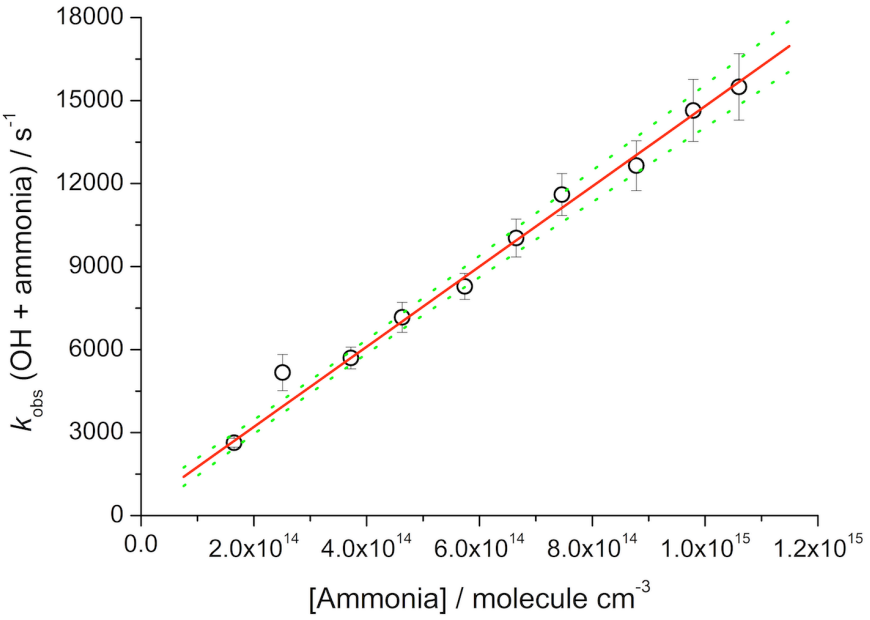

Figure 5. 5: Variation of k_{obs} with ammonia concentration obtained at 56 ± 4 K and a density of (4.4 ± 0.5) × 10^{16} molecule cm^{-3}, together with a weighted linear least squares fit of E5.2 to the data, the gradient of which yields the bimolecular rate coefficient, $k_{5.1}$ = (1.4 ± 0.2) × 10^{-11} $molecule^{-1}$ cm^3 s^{-1}. The green dashed lines represent the upper and lower 95 % confidence limits. The overall error in the bimolecular rate coefficient is the 95% confidence limits propagated with the error in the determination of the total density from the impact pressure measurements.

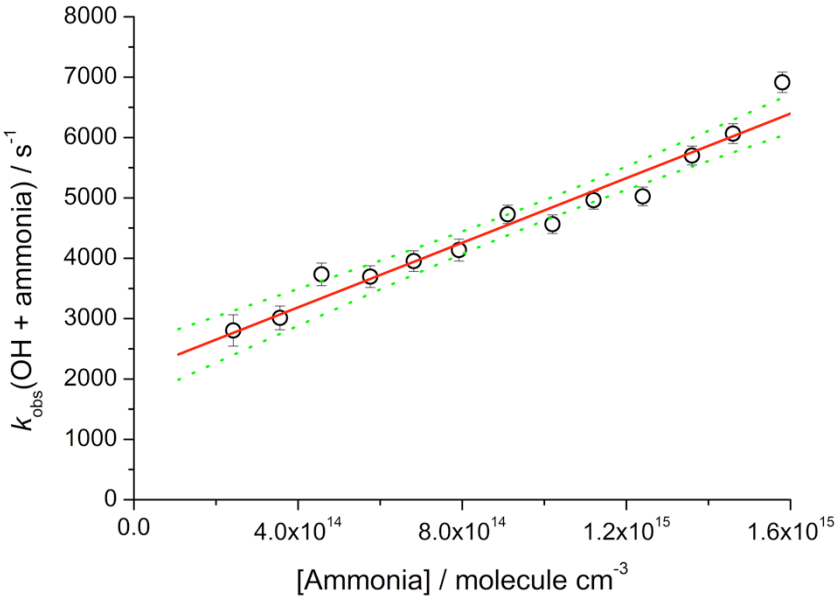

Figure 5. 6: Variation of k_{obs} with ammonia concentration obtained at 89 ± 4 K and a density of (1.1 ± 0.1) × 10^{17} molecule cm^{-3}, together with a weighted linear least squares fit of E5.2 to the data, the gradient of which yields the bimolecular rate coefficient, $k_{5.1}$= (3.6 ± 0.4) × 10^{-12} $molecule^{-1}$ cm^3 s^{-1}. The green dashed lines represent the upper and lower 95 % confidence limits. The overall error in the bimolecular rate coefficient is the 95% confidence limits propagated with the error in the determination of the total density from the impact pressure measurements.

The rate coefficients obtained in this study are summarized in Table 1, and the temperature dependence of $k_{5.1}$ is shown in Figure 5. 7.

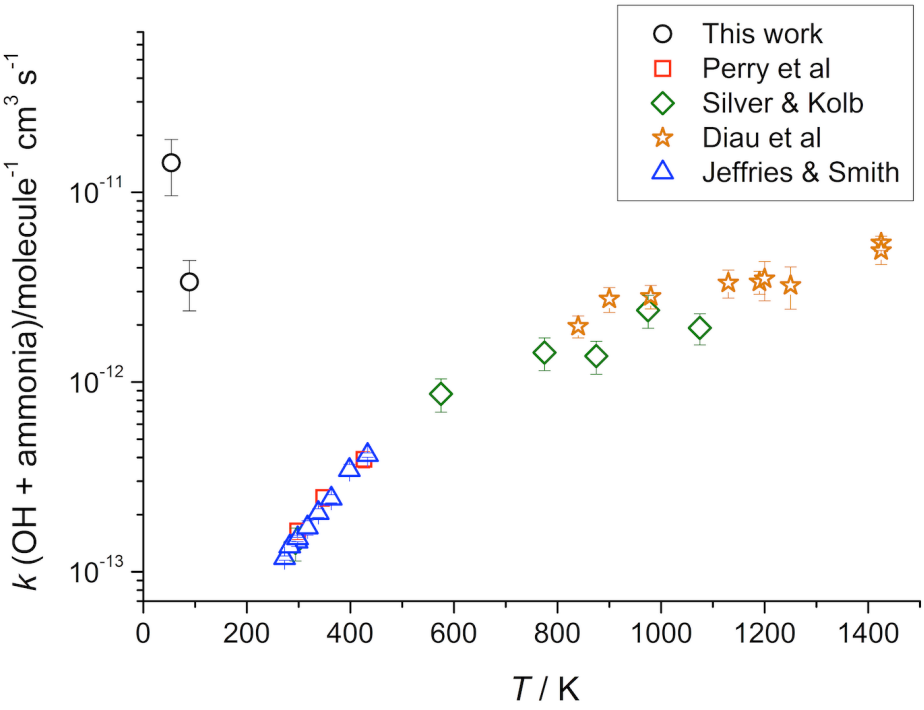

Figure 5. 7: Temperature dependence of $k_{5.1}$, the OH + ammonia rate coefficient from this work and other studies.[10-13]

Table 5. 1: Measured rate coefficients of the OH + ammonia reaction obtained in this study, together with the temperatures and total gas densities of the flows generated by the pulsed Laval nozzles. Errors have been calculated by the propagation of the 95 % confidence limits in the bimolecular rate coefficients with the errors in the expansion densities.

T / K	Bath gas (M)	[M] / 10^{16} molecule cm^{-3}	$k_{5.1}$ / 10^{-11} molecule^{-1} cm^3 s^{-1}
56 ± 4	Ar	4.4 ± 0.5	1.4 ± 0.2
54 ± 6	Ar	8.0 ± 1.4	1.3 ± 0.2
53 ± 9	Ar	15 ± 4	1.6 ± 0.4
90 ± 6	N_2	4.1 ± 0.6	0.37 ± 0.09
88 ± 4	N_2	7.4 ± 0.8	0.28 ± 0.04
89 ± 4	N_2	11 ± 1	0.36 ± 0.04

The rate coefficient for the reaction of OH with ammonia was found to be around two orders of magnitude faster at 54 K than at room temperature. At 89 K, the rate coefficient is around a factor of 25 faster than at room temperature. This dramatic turnaround in the rate coefficient has not been observed previously for a reaction with such a weakly bound complex. The

preliminary master equation work by Shannon and canonical transition state theory calculations by Corchado *et al.* indicated the significant role of tunnelling to the rate coefficient below room temperature.[8,9] The relative contributions of tunnelling and stabilisation of the complex was investigated by pressure dependence studies at both 54 K and 89 K at a total of six pressures ranging from (4-15) × 10^{16} molecule cm^{-3}. Figure 5. 8 shows the pressure dependence of the rate coefficient for OH + ammonia, obtained in this study.

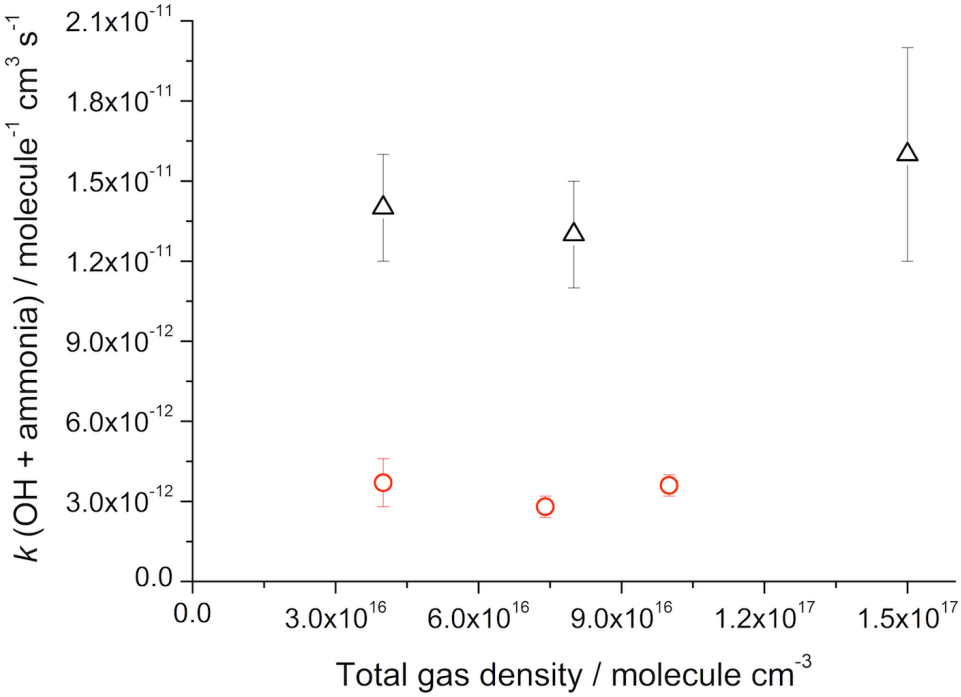

Figure 5. 8: Pressure dependence of $k_{5.1}$, the OH + ammonia rate coefficient at ~ 54 K (black open triangles) and ~ 89 K (red open circles). The error bars are the result of the propagation of the 95 % confidence limits in the bimolecular rate coefficients with the errors in the expansion densities.

There is clearly no dependence on pressure indicating that the only operative channel is the channel leading to bimolecular products. This result is consistent with the low binding energy of the complex and relatively high imaginary frequency of the H-abstraction barrier, which together would be expected to result in negligible stabilisation compared to tunnelling.

Due to the shallowness of the well, it is highly unlikely that the rate coefficient is at its high pressure limit under the experimental conditions. This has been further confirmed by measurement of the rate coefficient for OH (v=1) + NH_3 via LIF spectroscopy of OH (v=1) using the proxy method. The details of this method and results are discussed in Chapter 7.

Due to the catalytic effect of $(CH_3)_3COOH$ on the rate coefficient previously observed by Shannon, pseudo first order rate coefficients were obtained at a

range of ozone concentrations to ensure that the OH precursor was not interacting with the ammonia.[9]

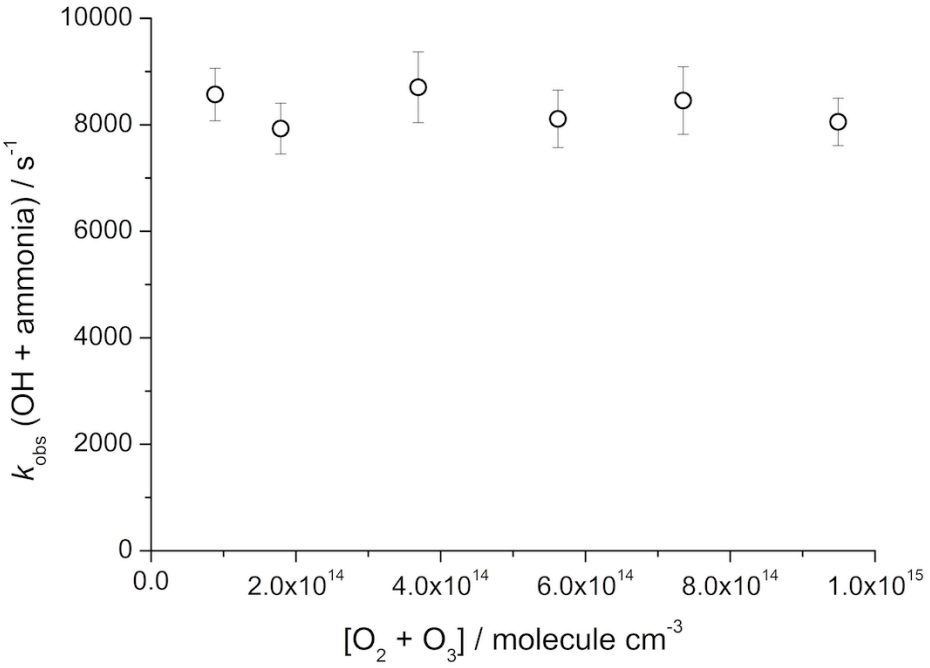

Figure 5. 9: Pseudo first order loss rate coefficients for the loss of OH in the presence of ammonia as a function of ozone (and oxygen) concentration. Pseudo first order rate coefficients obtained at 56 ± 4 K and a density of (4.4 ± 0.5) × 10^{16} molecule cm^{-3} and [ammonia] = 5.6 × 10^{14} molecule cm^{-3}.

From examination of Figure 5. 9, it can be seen that that the pseudo first order rate coefficient is independent of precursor concentration, and therefore the measured bimolecular rate coefficient is due to reaction only of OH with ammonia. Note that the bimolecular plot is presented as a function of the sum of O_2 and O_3 concentrations as the exact ozone concentration (produced from the corona discharge of O_2) was not known.

5.3.2 NH_2 detection experiments

Given that the reaction of OH + ammonia can result in only one exothermic product channel, and the potential 100 % branching ratio to products at low temperatures from the pressure independence of the rate coefficient, detection of the NH_2 product was attempted at 56 ± 4 K and a density of (4.4 ± 0.5) × 10^{16} molecule cm^{-3}.

The NH_2 radical was first observed via LIF spectroscopy by Halpern *et al.*, who characterised the fluorescence emission spectrum following excitation at 597.72 nm to the $\tilde{A}^2A_1(0,9,0)$ 3_{03} level, as shown in Figure 5. 10.[28]

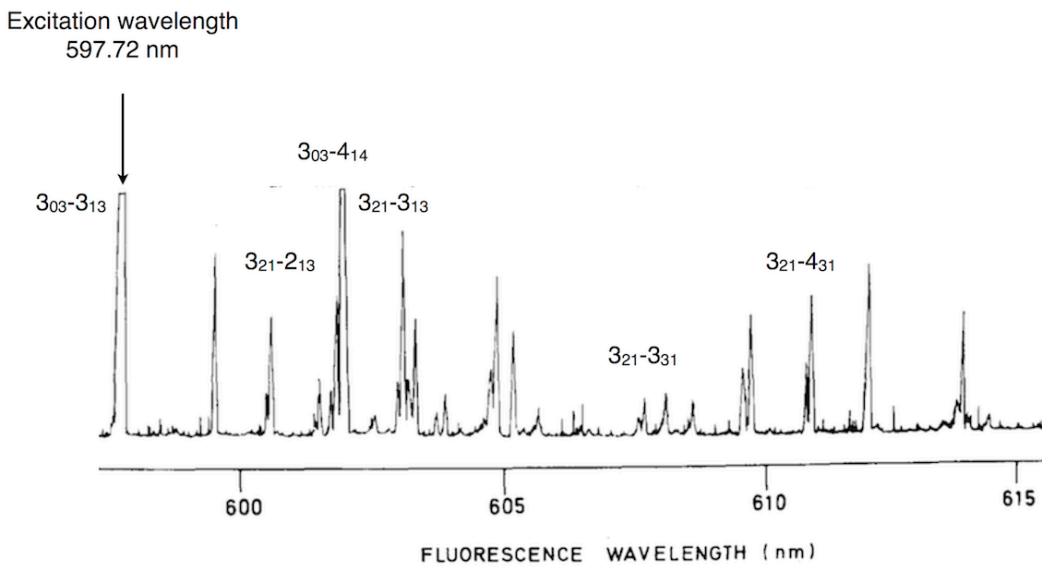

Figure 5. 10: Fluorescence emission spectra of NH_2 following laser excitation at 597.2 nm, corresponding to transitions from the $\tilde{A}^2A_1(0,9,0)$ 3_{03} level obtained by Halpern *et al.* at room temperature.[28]

The work by Halpern *et al.* indicates that NH_2 fluorescence can be observed following laser excitation at 597.72 nm.[28] However, due the limited resolution of the literature spectra, to obtain the optimum line position an NH_2 LIF spectrum was firstly generated from 193 nm photolysis of NH_3. The 193 nm excimer laser (fired at a pulse repetition rate of 5 Hz with a pulse energy of 7-8 mJ) was aligned perpendicular to the axis of the expanded gas flow and parallel to the probe laser. The probe laser (Nd:YAG pumped dye laser) was tuned to a wavelength approximately coincident with the $\tilde{A}^2A_1(0,9,0) \leftarrow \tilde{X}^2B_1$ (0,0,0) NH_2 transition.[29] The delay time between the photolysis and probe lasers was set to 7 μs and the LIF spectrum was recorded between 596.500 and 598.000 nm at increments of 0.003 nm with 2 laser shots per point. The off-resonance fluorescence was collected by a PMT fitted with a Perspex and a Thorlabs filter which transmits between 603-618 nm. Additionally, a monochromator (Applied Photophysics f/3.4 model) was mounted between the filter and the PMT to further reduce scatter. The wavelength of the monochromator was calibrated using 3 wavelengths of the dye laser, the HeNe laser and the maximum transmission from the off resonance fluorescence of OH at ~ 308 nm following 282 nm excitation. For these experiments the monochromator transmission wavelength was set to 611 nm with a slit-width of 3.3 nm, as initial tests demonstrated this yielded a favourable signal-to-noise ratio. The obtained LIF spectrum is shown in Figure 5. 11 and the maximum line position obtained was in good agreement with that reported by Halpern *et al*.[28] A wavemeter was utilised in this work to calibrate the wavelengths of the probe laser.

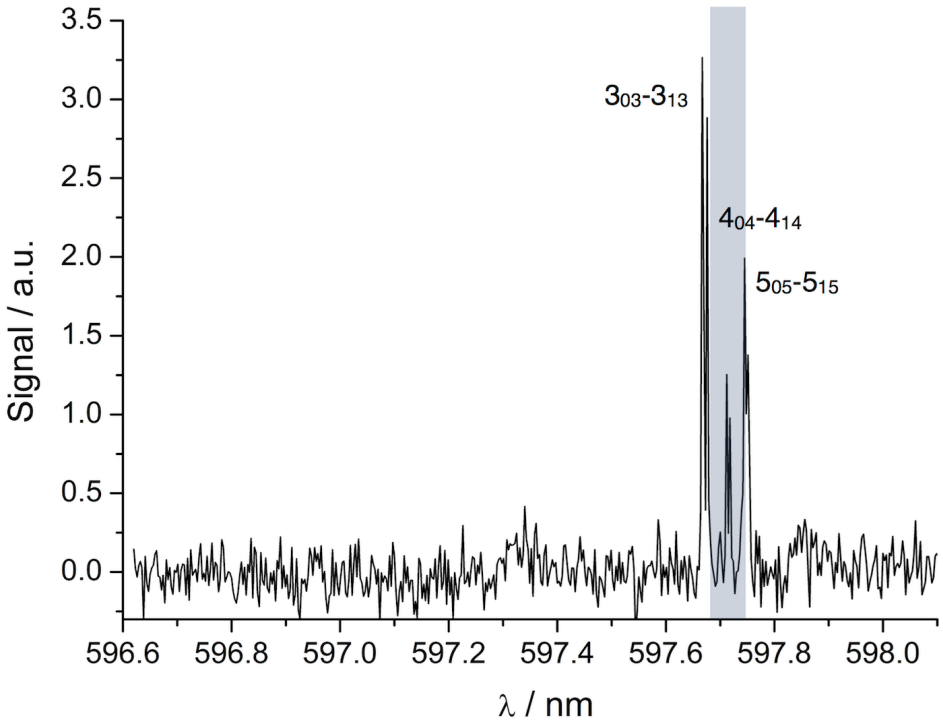

Figure 5. 11: Rotationally resolved excitation LIF spectrum of NH_2 , with points smoothed by the adjacent averaging of 5 points, formed from 193 nm photolysis of NH_3 together with the maximum line position obtained by Halpern *et al.*(grey shaded area indicating FWHM line width of the laser) .[28]

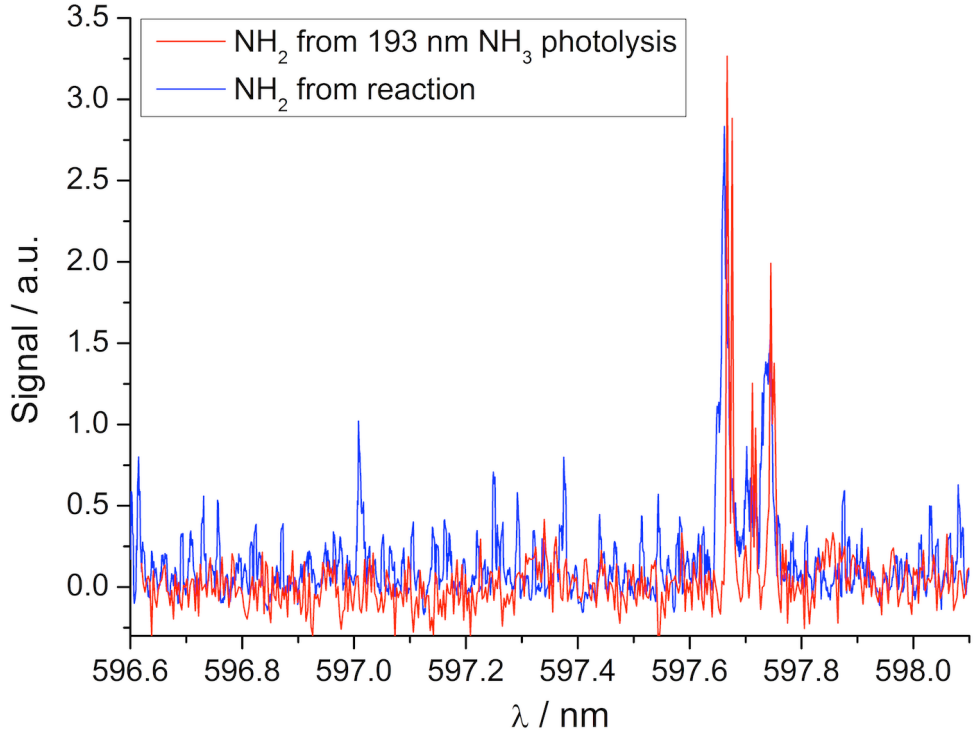

Figure 5. 12: Excitation LIF spectrum of NH_2 formed from in the reaction with points (smoothed by the adjacent averaging of 5 points to reduce noise) obtained at a probe delay time of 70 μs overlaid with the NH_2 LIF spectrum obtained by 193 nm photolysis of NH_3.

A LIF spectrum of NH_2 from E5.1a was obtained at a delay time of 70 μs and is shown in Figure 5. 12, together with the spectrum obtained from the 193 nm photolysis of NH_3 to aid comparison. The ratios of the signal heights for the three observed peaks (assigned in Figure 5. 12) are in good agreement with the values reported by Dressler and Ramsay.[30] From the observation of NH_2 via LIF at a fixed laser delay time, it is not conclusive that the observed NH_2 is from the OH + ammonia reaction. The method of generation of OH utilises the internal reaction of $O(^1D)$ + ammonia, leading to an initial formation of NH_2, with a branching fraction of 0.9 according to theoretical work by Wang *et al.* and experimental work by Shu *et al.*[24,25] To confirm the presence of the bimolecular product channel at low temperatures, NH_2 needs to be detected temporally so that the two formation pathways can be deconvoluted.

Kinetic traces of NH_2 following the production of OH in the presence of ammonia were obtained in the same way as described in section 5.2, and NH_2 was monitored by LIF via the 3_{03}-3_{13} rotational transition of the $\tilde{A}^2A_1(0,9,0) \leftarrow \tilde{X}^2B_1$ (0,0,0) vibronic band, as assigned in the wavelength scan shown in Figure 5. 12. Back to back traces were recorded of NH_2 temporal LIF profiles up to relatively short (60 μs) and relatively long (250 μs) delay times. The traces contained 150 and 250 data points respectively, each averaged 24 times. An example of the data obtained at short and long time delays at a given ammonia concentration is shown in Figure 5. 13. The former trace was used to obtain information regarding the two formation pathways for NH_2. The latter was used to obtain the loss rate coefficient for NH_2 due to reaction and diffusion out of the detection region. Due to the convoluted nature of the traces, it was necessary to fit all of the recorded traces together using global analysis. Global analysis is where the values of the parameters of the fitting equation are optimised by fitting all of the experimental data simultaneously to obtain the best fit to all of the traces included.

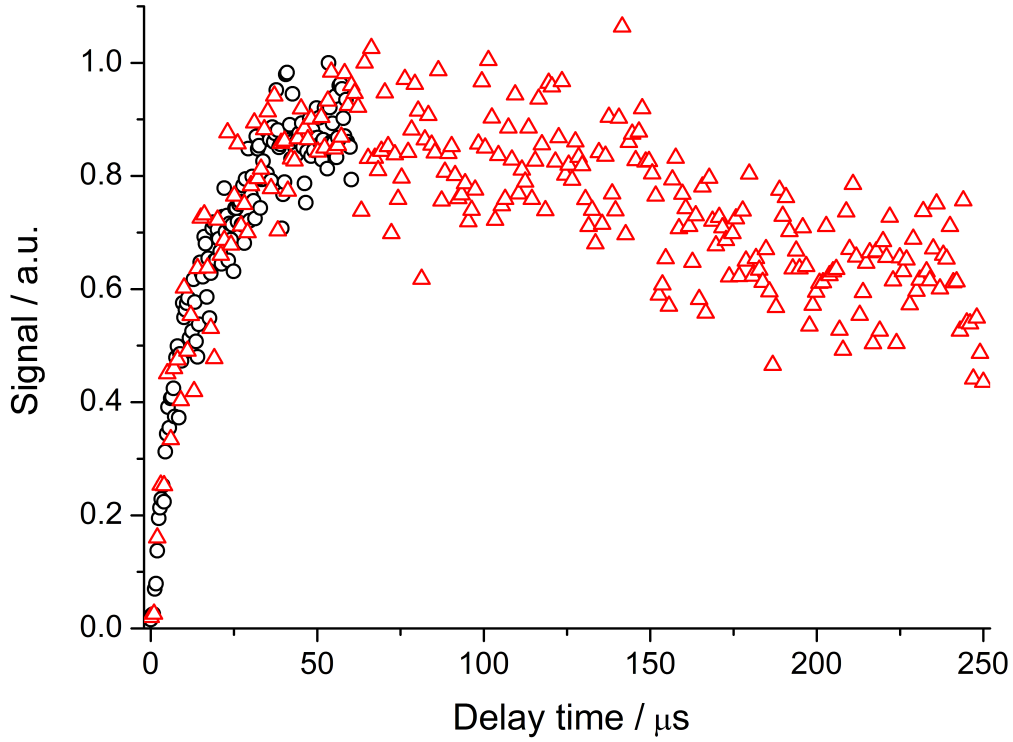

Figure 5. 13: LIF traces of NH_2 obtained at delay times out to 60 μs (black open circles) and 250 μs (red open triangles) from the 248 nm photolysis of ozone in the presence of ammonia (2.19×10^{15} molecule cm^{-3}) at 53 ± 9 K and a total gas density of (1.5 ± 0.4) × 10^{17} molecule cm^{-3}.

Twelve long time delay traces out to 250 μs were fitted globally from 76 μs onwards with a single exponential loss function (E5.4) to obtain a pseudo first order loss rate coefficient for NH_2, which was found to yield k_{loss} = 2062 ± 57 s^{-1}. This value was utilised in the global fitting of the short delay time data to obtain three parameters. The short delay time data only was used to obtain these parameters (as opposed to including the long delay time data also) as the long delay time data does not have sufficient data points at short times to describe the two growth processes.

$$[NH_2]_t = [NH_2]_0 e^{-k_{loss}t} \qquad \text{E5.4}$$

Nine short delay time NH_2 traces were fitted with E5.5 (derivation given in Appendix C).

$$[NH_2]_t = \frac{k_x[O(^1D)]_0}{k_y+k_{loss}-k_x}\left[\frac{f(k_y+k_{loss}-k_x)+k_y}{k_{loss}-k_x}\{e^{-k_x t} - e^{-k_{loss}t}\} + \{e^{(-k_y-k_{loss})t} - e^{-k_{loss}t}\}\right] \qquad \text{E5.5}$$

where $O(^1D)_0$ is the signal height from R5.2 and

$$k_x = k_{5.2}[NH_3] \quad \text{E5.6}$$

$$k_y = k_{5.1}[NH_3] \quad \text{E5.7}$$

The traces were obtained with ammonia concentrations ranging from 3.3 × 10^{14} - 2.2 × 10^{15} molecule cm^{-3}. An example of an NH_2 short delay time LIF trace fitted with E5.5 is shown in Figure 5. 14.

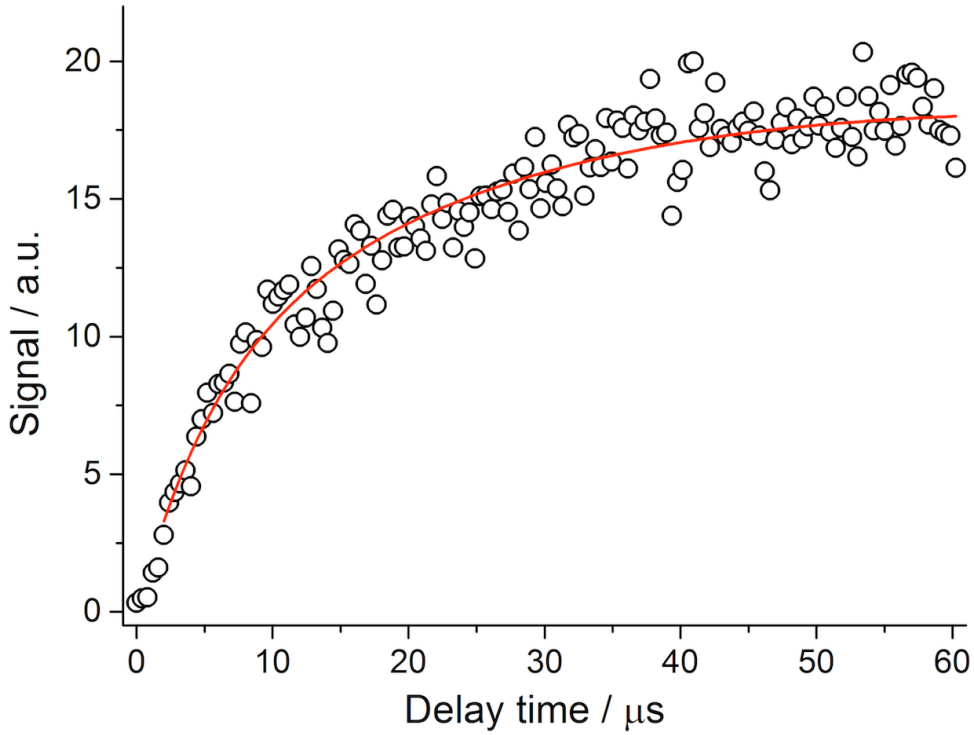

Figure 5. 14: LIF trace of NH_2 together with the non linear least squares global fit of E5.5 to the data from the 248 nm photolysis of ozone in the presence of ammonia (2.19 × 10^{15} molecule cm^{-3}) at 53 ± 9 K and a total gas density of (1.5 ± 0.4) × 10^{17} molecule cm^{-3}.

The parameters used in the fits and details regarding how they were fitted are given in Table 5. 2.

Table 5. 2: Parameters used in the global fitting of the NH_2 short delay time growth traces alongside the values obtained from the fits. Errors given are the 95 % confidence limits obtained from the fits.

Parameter	Description	Fitted/fixed	Value
$k_{5.2}$	Bimolecular rate coefficient for $O(^1D)$ + NH_3 obtained from k_x.	Fitted globally	$(8.2 \pm 2.0) \times 10^{-11}$ molecule^{-1} cm^3 s^{-1}
$k_{5.1}$	Bimolecular rate coefficient for OH + NH_3 obtained from k_y.	Fitted globally	$(1.5 \pm 0.7) \times 10^{-11}$ molecule^{-1} cm^3 s^{-1}
$O(^1D)_0$	Maximum height of signal resulting from the reaction of $O(^1D)$ with NH_3	Fitted to each trace	Various
k_{loss}	First order loss rate coefficient for NH_2	Fitted globally to the long delay time traces from 76 µs – 250 µs. Value fixed in short delay time trace fitting.	2062 s^{-1}
f	Ratio of signal heights for k_x and k_y *	Fitted globally	0.9 ± 0.2

*See E5.6 and E5.7.$O(^1D) + NH_3 \rightarrow H_2O + f.NH_2$

As NH_2 is also produced from the $O(^1D) + NH_3$ reaction, the signal height of the initial, fast growth of NH_2 can be compared with the height of the additional secondary growth to obtain a yield of NH_2 from the reaction of OH + NH_3 via this internal calibration. This acts also as a method of validating that the bimolecular channel in the OH + ammonia reaction is indeed operating. As it can be seen from Table 5. 2, the value of $k_{5.1}$ obtained from the global fitting procedure is in excellent agreement with the value of $k_{5.1}$ obtained from the independent fits to the OH LIF data. It can also be noted that $k_{5.2}$ is found to be significantly faster than $k_{5.1}$, confirming that there are indeed two growth components to the NH_2 LIF traces. The value of $k_{5.2}$ obtained from these global fits is smaller than measured by Davidson *et al.* of $(2.5 \pm 0.5) \times 10^{-10}$ molecule^{-1} cm^3 s^{-1} at 298 K.[31] However, given the exothermicity of the $O(^1D)$ + ammonia reaction (~ 170 kJ mol^{-1} according to the calculations of Wang *et al.* [24]) it could be expected that NH_2 would be formed in rotationally excited states, and given that rotational relaxation of OH in Ar bath gas at 54 K was shown to be slow (Figure 5. 3), it could be expected that the rotational relaxation of NH_2 into the LIF probed level may

also be slow. Thus, the value of $k_{5.2}$ obtained from the global fit of the NH_2 traces is likely to be convoluted with rotational relaxation of hot NH_2.

If the data at short delay times is fitted with an exponential growth-loss function such as E5.8 (where the loss is fixed at the diffusional loss rate 2062 s^{-1}), then the component of the growth owing predominantly to the $O(^1D) + NH_3$ reaction can be fitted.

$$[NH_2]_t = \left(\frac{k_x}{k_{loss-}k_x}\right)[NH_2]_{max}(e^{-k_x t} - e^{-k_{loss} t}) \qquad \text{E5.8}$$

The fit can then be simulated out to long delay times demonstrating the expected temporal signal if only this reaction (R5.2) is operating. This has been performed for the data previously shown in Figure 5. 14 and the global fit is shown alongside the simulated $O(^1D) + NH_3$ fit in Figure 5. 15.

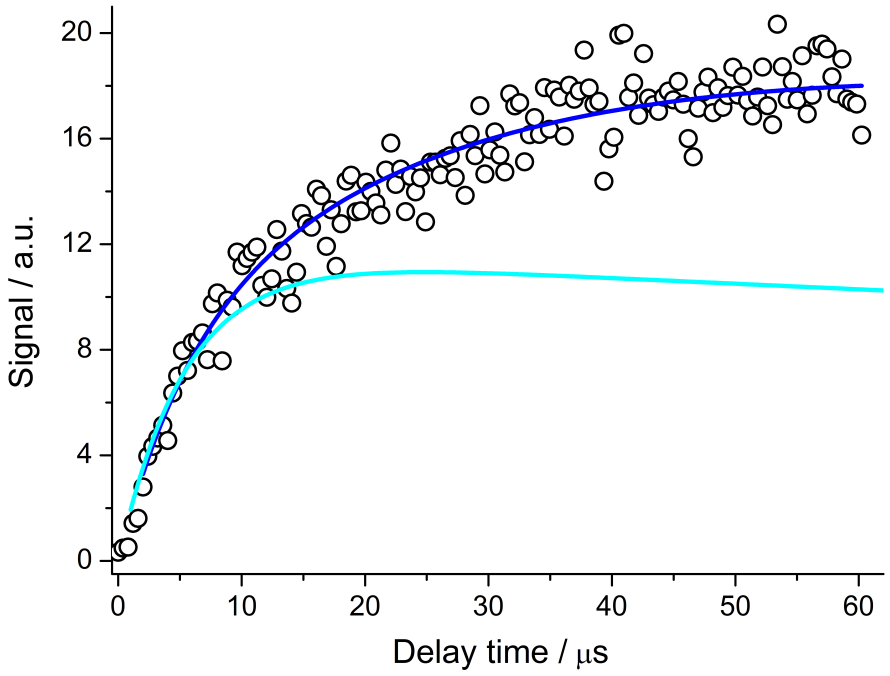

Figure 5. 15: LIF trace of NH_2 (black open circles) obtained from the 248 nm photolysis of ozone in the presence of ammonia (2.19×10^{15} molecule cm^{-3}) at 53 ± 9 K and a total gas density of (1.5 ± 0.4) × 10^{17} molecule cm^{-3}. The global fit (dark blue line) of E5.5 is shown alongside the simulated fit to the data (cyan line) of a single exponential growth process (with diffusional loss of 2062 s^{-1}) owing to only the $O(^1D) + NH_3$ reaction. The single exponential growth rate coefficient was obtained from a fit of the data out to 9 μs (183138 ± 41099 s^{-1}).

It can be seen from Figure 5. 15 that both the shape and the total signal height of the NH_2 LIF data obtained cannot be replicated by the single exponential growth trace and provides further evidence of the two processes occurring to form NH_2.

From the global fit of the NH_2 traces, a value of f = 0.9 ± 0.2 was obtained. Given the experimental and theoretically obtained branching ratio for the reference reaction, R5.2, to yield NH_2, this value of f corresponds to a yield of NH_2 from R5.1 of 0.98 ± 0.35 (error is 95 % confidence limits from the fit). This yield is consistent with the data presented in Figure 5. 8, showing the independence of the rate coefficient on pressure and thus the reaction operating purely by the bimolecular channel out to products.

The implication of this calculated branching ratio is that in very low pressure and cold environments where both OH and ammonia have been detected, such as the molecular clouds TMC-1 and Sgr-B2, the reaction will proceed at the experimentally measured rate coefficient to yield NH_2 and H_2O. The confirmed pressure independence of the rate coefficient provides further support for product formation, indicating it is necessary for this reaction to be included in interstellar models.

5.4 Comparison with *ab initio* / master equation calculations

Following the experimental work reported in this thesis, *ab initio* and master equation calculations were performed by Dr Arne Bunkan (University of Leeds / University of Oslo) to aid interpretation of the experimental data.

Stationary point calculations were performed at two levels of theory: CCSD(T)(full)/EB//CCSD(T)/aug-cc-pVTZ level and M06-2X/6-31+G(d,p). The resultant relative energies of the stationary points of the former are shown in Figure 5. 16. Contrary to previous work, intrinsic reaction co-ordinate calculations performed by Dr Bunkan demonstrated that the complex with binding energy of ~7.5 kJ mol^{-1} was not the complex on the reaction co-ordinate, and the active complex in the reaction has a binding energy of only 1.3 kJ mol^{-1}. The revised PES based on the calculations by Bunkan is shown in Figure 5. 16.

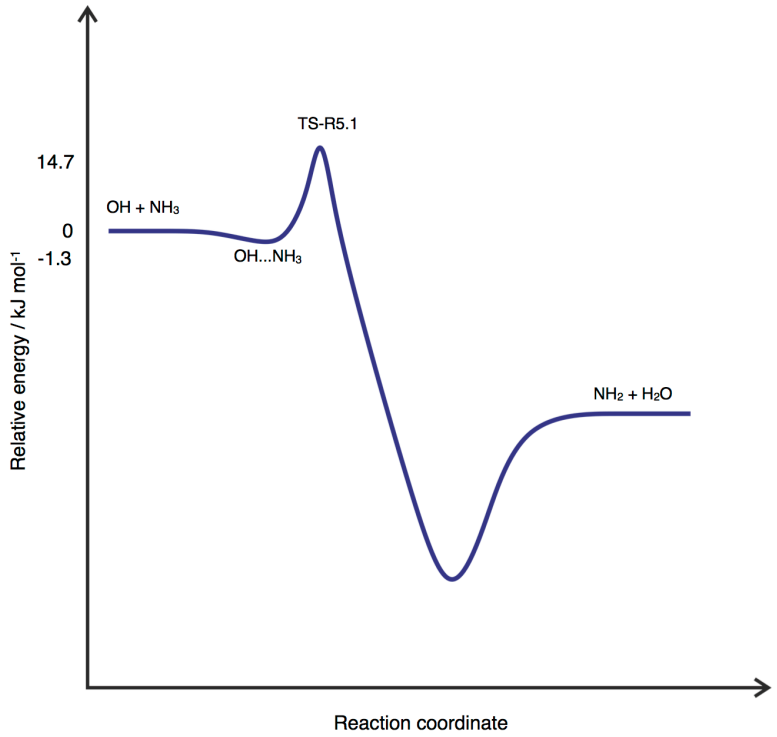

Figure 5. 16: To-scale potential energy surface for the OH + ammonia reaction based on calculations by Dr Arne Bunkan at the CCSD(T)(full)/EB//CCSD(T)/aug-cc-pVTZ level of theory.

Master equations were performed by Dr Bunkan using the software MESMER.[32] Hindered rotor calculations were performed for the low vibrational frequency torsional motion of the OH fragment in the transition state at the MP2/aug-cc-pVTZ level of theory. Tunnelling was included in the master equation calculations using an Eckart potential according to the method of Miller, with an associated imaginary frequency of 1582 cm^{-1} and a barrier height of 14.7 kJ mol^{-1}.[33] The barrierless association reaction to form the complex was treated as an inverse Laplace transform with an estimated formation rate coefficient of 5×10^{-10} $molecule^{-1}$ cm^3 s^{-1}.The calculated temperature dependence of the rate coefficient for OH + ammonia is shown alongside the experimentally obtained rate coefficients in Figure 5. 17.

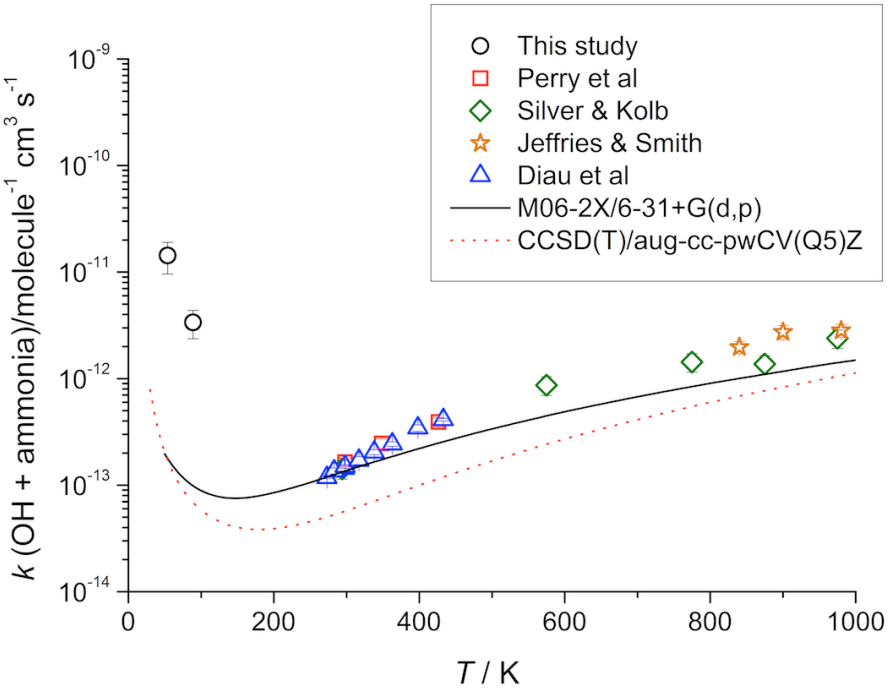

Figure 5. 17: Temperature dependence for $k_{5.1}$, the OH + ammonia rate coefficient from this work and other studies, alongside the results of the master equation calculations performed by Dr Arne Bunkan at two levels of theory.[10,11]

It can be seen that the master equation calculations capture the overall trend observed experimentally. However, the rate coefficient is consistently under-predicted across the whole temperature range which is perhaps an indication that the barrier is lower than calculated. Additionally, the theory is unable to reproduce the sharp turnaround between the decreasing rate coefficient in the Arrhenius-type regime and the rapid enhancement in the rate coefficient below 200 K. Given the statistical nature of RRKM theory master equation calculations, this result is perhaps indicative that the kinetic behaviour of the OH + ammonia reaction in this temperature range is non-statistical. To gain further insight into this and similar reactions studied in this thesis, trajectory calculations could be performed.

5.5 Interstellar impact of the OH + ammonia reaction

Through collaboration with interstellar modellers at the University of Virginia (Dr Kinsuk Acharyya and Professor Eric Herbst), the potential interstellar impact of the OH + ammonia reaction has been assessed. Further details about this model are given in Chapter 3 but a brief description is given below. A model encompassing both gas phase and grain reactions comprising around 600 species with 12,000 reactions was constructed from data available on several online databases including KIDA and OSU.[34,35]

Where experimental values are not available, the rate coefficients for neutral gas phase reactions have been calculated using the modified Arrhenius equation E5.8, where α, β and γ are parameters.

$$k(T) = \alpha \left(\frac{T}{300}\right)^{\beta} exp\left(-\frac{\gamma}{T}\right) \qquad \text{E5.8}$$

The model was operated in a pseudo time dependence mode whereby physical conditions such as the temperature and density are kept constant and the chemical evolution as a function of time is monitored. The initial chemical composition comprises only atomic species with the exception of hydrogen which is in its molecular form and typical initial abundances are representative of cold interstellar clouds. The model was run at 10, 50 and 100 K. The rate coefficient values utilised at 50 and 100 K are those obtained experimentally at 54 and 89 K respectively, whereas the value utilised at 10 K (3×10^{-10} molecule^{-1} cm^3 s^{-1}) is estimated based on the capture limit of a radical-neutral reaction, supported by the proxy method values obtained for other reactions reported in Chapter 7.

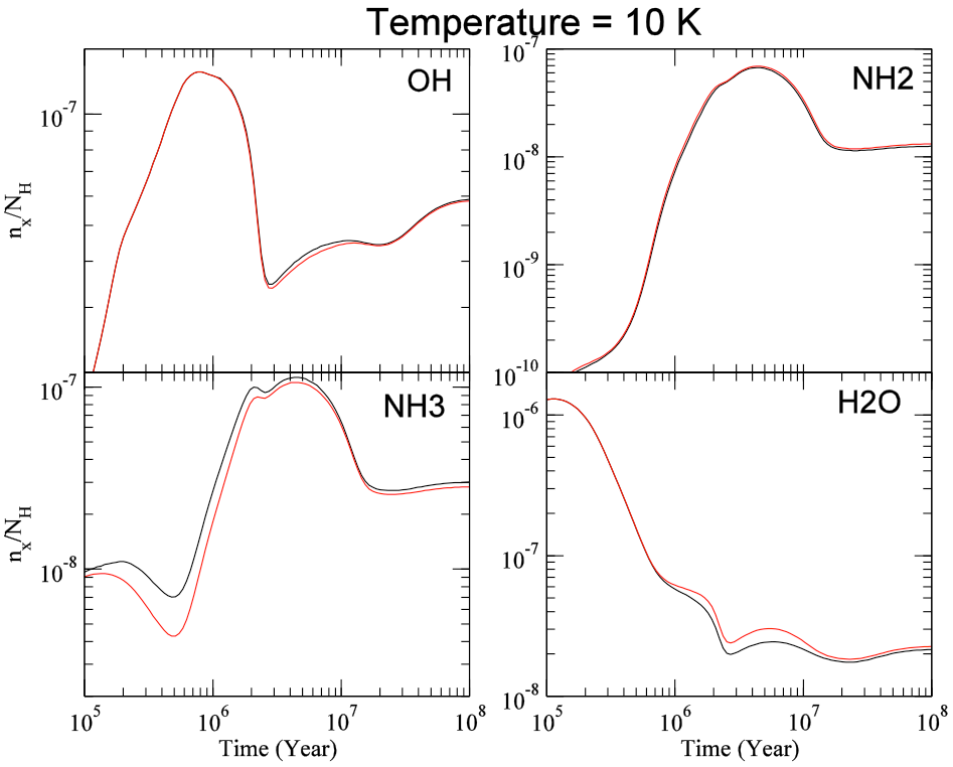

Figure 5. 18: Time dependent species profiles for OH, NH_2, NH_3 and H_2O with (red line) and without (black line) the OH + ammonia rate coefficient at 10 K, as output from the University of Virginia gas-grain model run by Dr Kinsuk Acharyya and Professor Eric Herbst.

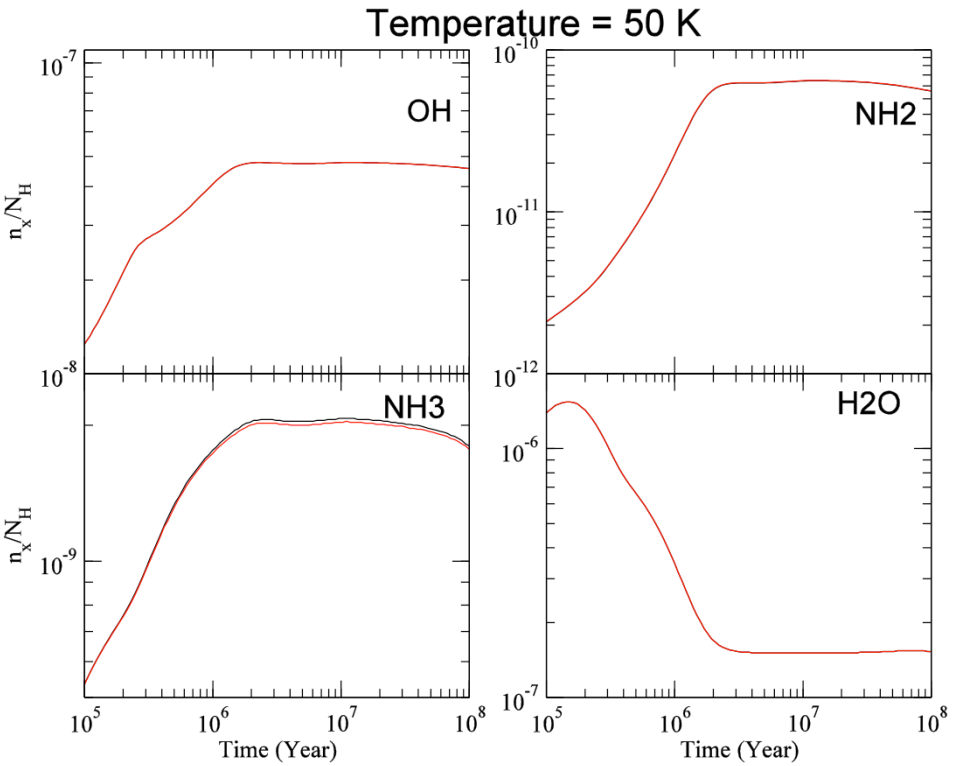

Figure 5. 19: Time dependent species profiles for OH, NH_2, NH_3 and H_2O with (red line) and without (black line) the OH + ammonia rate coefficient at 50 K, as output from the University of Virginia gas-grain model run by Dr Kinsuk Acharyya and Professor Eric Herbst.

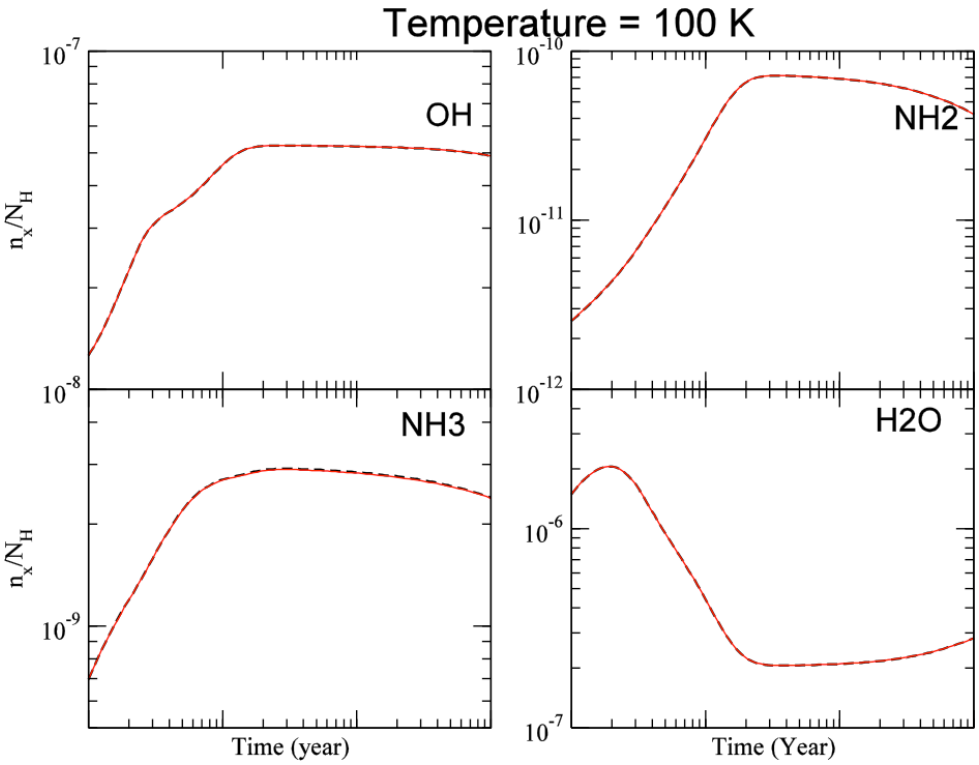

Figure 5. 20: Time dependent species profiles for OH, NH_2, NH_3 and H_2O with (red line) and without (black line) the OH + ammonia rate coefficient at 100 K, as output from the University of Virginia gas-grain model run by Dr Kinsuk Acharyya and Professor Eric Herbst.

A 100 K, including the experimentally obtained OH + ammonia rate coefficient has no apparent impact on the temporal concentrations of ammonia, OH, water or NH_2 radicals, as shown in Figure 5. 20. At 50 K, there is a very small impact (maximum ~ 7 %) on the species concentrations, which is most easily observed in the temporal profile of ammonia (Figure 5. 19). At 10 K there is a significant impact on the ammonia concentration across the whole time range, which is most prevalent between 10^5 and 10^6 years, as it can be seen in Figure 5. 18. At ~ 5×10^5 years, the ammonia concentration is reduced by around 40 % when the OH + ammonia reaction is accounted for.

The model demonstrates that the OH + ammonia reaction will have the highest impact the coldest interstellar environments. The potential impact of this reaction on the ammonia abundances as shown in Figure 5. 18 emphasises the need for this reaction to be widely incorporated into interstellar chemical models.

5.6 OH + methane – a preliminary study

Methane is one of the most important greenhouse gases with a 20 year global warming potential of 62 ± 20 (including direct and indirect effects) and its main sink in the atmosphere of Earth is reaction with OH, R5.3, which accounts for almost 90 % of its removal.[36-38] There are several origins of methane into the atmosphere including agricultural, anthropogenic and geothermal sources as well as direct emissions from natural gas extraction sites.[36-38]

The reaction of OH with methane has been subject to numerous kinetic studies due to the importance of this reaction to both atmospheric and combustion environments, and the temperature dependence of the rate coefficient is shown in Figure 5. 21 by a representative sample of studies in the literature.

$$OH + CH_4 \rightarrow CH_3 + H_2O \qquad \text{R5.3}$$

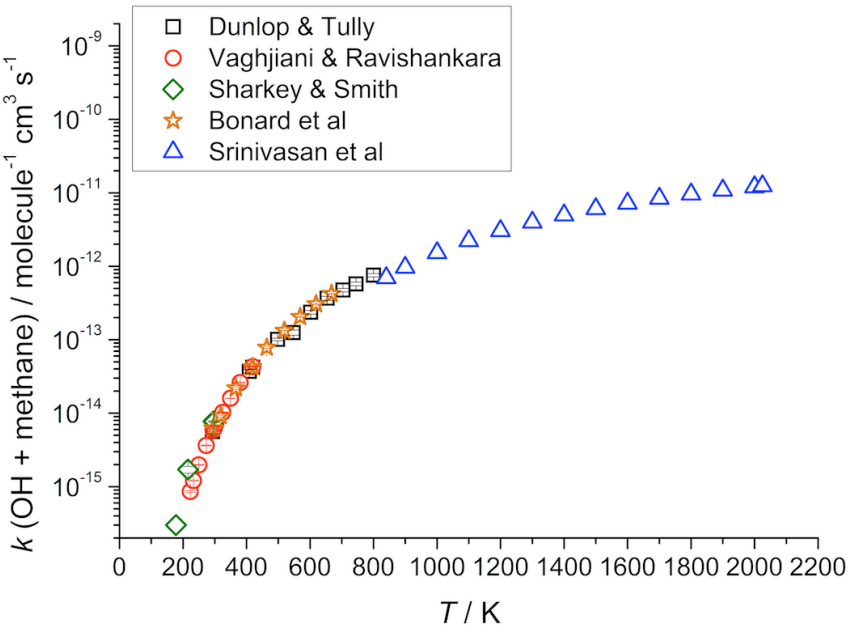

Figure 5. 21: Temperature dependence of the OH + methane rate coefficient as reported in the literature.[39-43]

Ab initio calculations of the potential energy surface for OH + methane demonstrate that the reaction proceeds via a significant barrier to hydrogen abstraction.[44,45] Raman and laser induced fluorescence spectroscopy were utilised by the group of Professor Marsha Lester at the University of Pennsylvania to identify the structure and binding energy (~ 2.5 kJ mol^{-1}) of a weakly bound pre-reaction complex between OH and methane.[46] As discussed by Smith and Ravishankara, the existing experimental data down to 173 K does not indicate the role of this complex and the reaction is instead likely to proceed directly over the barrier to reaction.[47] However, given the role of the 1.4-7.5 kJ mol^{-1} pre-reaction complex in the OH + ammonia reaction at low temperatures, it is possible that at sufficiently low temperatures, the pre-reaction complex in the reaction of OH with methane may facilitate the enhancement of the rate coefficient.

Recent *ab initio* and master equations, using the methodology described for the OH + ammonia system, by Dr Arne Bunkan (University of Leeds/ University of Oslo) propose an enhancement of the rate coefficient for the OH + methane reaction despite stationary point calculations finding a high barrier (22.5 kJ mol^{-1}) to reaction and much weaker binding energy than that obtained by the Lester group experiments (Figure 5. 22).[46]

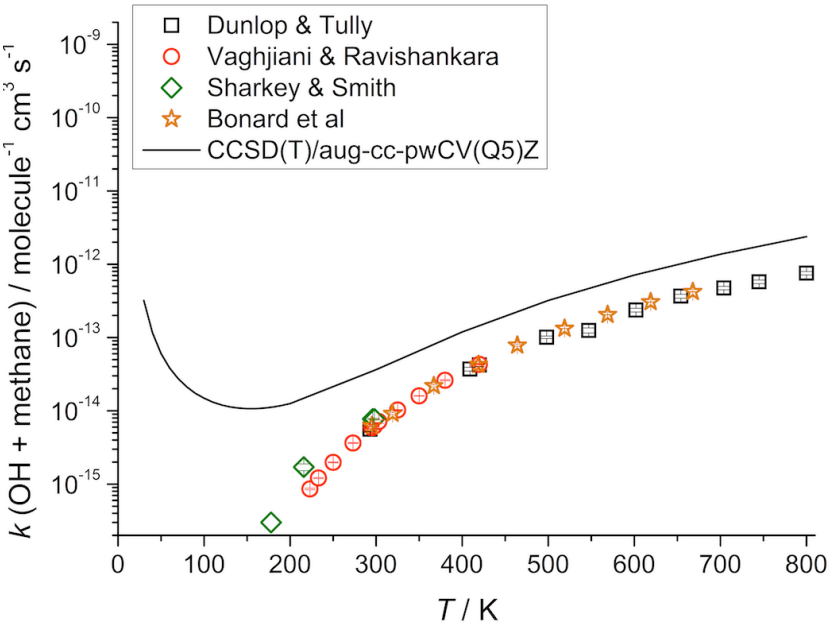

Figure 5. 22: Temperature dependence of the OH + methane rate coefficient reported in the literature alongside master equation calculation results obtained by Dr Arne Bunkan.[39,40,42,43]

The master equation calculations significantly over predict the rate coefficient over the 200-800 K range, and at room temperature the calculations over predict the rate coefficient by around a factor of 6.[40] Therefore, the calculated low temperature rate coefficients are likely to be an upper limit.

The work reported in this thesis has demonstrated that despite only a very weakly bound complex, the reaction of OH + ammonia is significantly enhanced at low temperature. To investigate this further, a preliminary experiment on the OH + methane reaction was carried out at 53 K.

The reaction was studied using two OH precursors;

$$O_3 + h\nu(248\,nm) \rightarrow O(^1D) + O_2 \qquad \text{P5.1}$$

$$O(^1D) + CH_4 \rightarrow OH(v \geq 0) + CH_3 \qquad \text{R5.4}$$

and

$$(CH_3)_3COOH + h\nu(248\,nm) \rightarrow OH, OH^* + co - products \qquad \text{R5.2}$$

$$OH^*, OH(v \geq 0) \xrightarrow{k_{rel}} OH \qquad \text{R5.5}$$

LIF monitoring of OH via the $A^2\Sigma^+ \leftarrow X^2\Pi_i$ (1,0) $Q_1(1.5)$ transition at ~ 282 nm. transition demonstrated that the $O(^1D)$ + CH_4 reaction producing OH featured a very slow growth of OH, and thus limited the time window for monitoring the OH + methane reaction. Whilst the rate coefficient for the $O(^1D)$ + CH_4 reaction is relatively fast at room temperature (1.5×10^{-10} molecule^{-1} cm^3 s^{-1} according to Vranckx *et al.*[48]), OH is formed in vibrational

states up to v=4, and therefore the slow growth of OH is due to vibrational relaxation into the ground state, which according to Hancock *et al.* is on the order of 0.5 - 5 × 10^{-12} molecule^{-1} cm^3 s^{-1} at 295 K.[49] Consequently, *t*-BuOOH was used as the OH source. The experiment was performed as detailed in section 5.2 and also Chapter 2 and so no other experimental details are given except the reagent purities which were as follows : Argon (99.98 %, BOC), Oxygen (BOC 99.999 %), Methane (100 %, BOC CP grade) and *t*-BuOOH (Aldrich, 70 % wt. in H_2O).

The bimolecular plot for the reaction of OH with methane obtained at 53 K and a total gas density of 1.5 × 10^{17} molecule cm^{-3} is shown in Figure 5. 23. Across a large range of methane concentrations, no change in the pseudo first order rate coefficient is observed (within error) and thus the rate coefficient for the reaction is below the detection limit for our apparatus, which is ~ 1 × 10^{-12} molecule^{-1} cm^3 s^{-1} under these conditions.

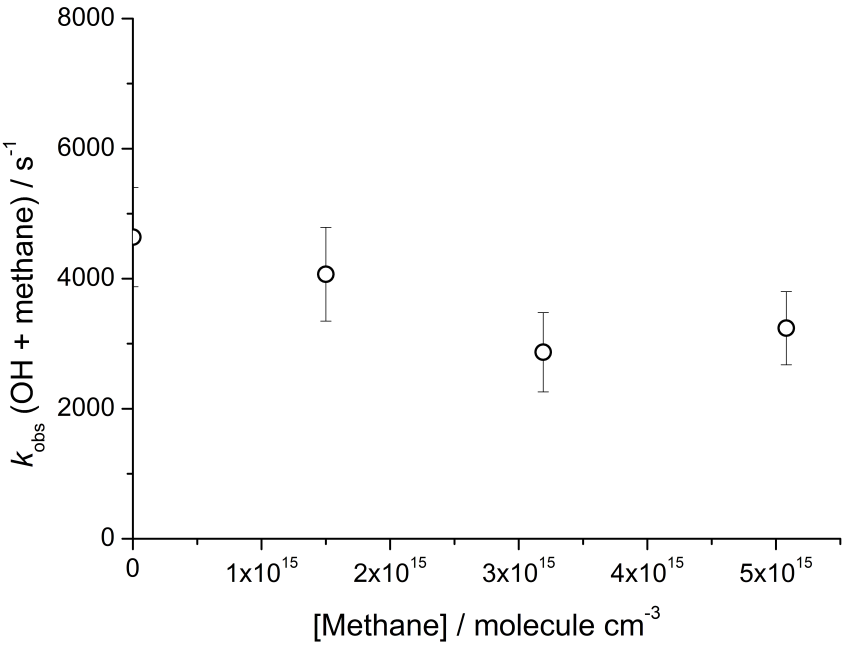

Figure 5. 23: Pseudo first order loss rate coefficients for the loss of OH in the presence of methane. Pseudo first order rate coefficients obtained at 53 ± 9 K and a density of (1.5±0.4) × 10^{17} molecule cm^{-3}.

To quantify if the very weakly bound pre-reaction complex present on the potential energy surface of OH + methane influences the rate coefficient, it will be necessary to study the reaction at much lower temperatures which are currently inaccessible with this apparatus.

5.7 Summary

The rate coefficient for the reaction of OH with ammonia has been measured at 54 and 89 K and a dramatic inverse temperature dependence has been observed. At 54 K, the rate coefficient is two orders of magnitude faster than at room temperature and the rate coefficients at both 54 and 89 K are found to be independent of pressure.

Despite the presence of only a very weakly bound pre-barrier complex, the reaction appears to be enhanced by the increased lifetime of this complex at lower temperatures. The bimolecular reaction outcompetes collisional stabilisation into the well via a quantum tunnelling mechanism so that bimolecular products are formed. The operation of this bimolecular channel has been further substantiated by direct detection of the NH_2 product as a function of time via LIF spectroscopy. The NH_2 yield from this reaction has been found to be 0.98 using $O(^1D) + NH_3$ as an internal standard.

This general mechanism has been observed both in this work, and previous work, to occur at low temperatures for reactions of OH with several oxygenated organic compounds. However, the pre-barrier complexes in these reactions are notably more strongly bound (by around 10-15 kJ mol^{-1}).

The persistence of this mechanism for H-abstraction reactions, even where the complex is very weakly bound, suggests that this mechanism is indeed general for H-abstraction reactions at low temperatures and places further emphasis on the necessity for this type of reaction to be included in interstellar networks. The abundance of OH and ammonia in cold interstellar environments where temperatures can reach as low as 10 K, means that the reaction between OH and ammonia could be occurring at a rate approaching the gas kinetic limit. Inclusion of the OH + ammonia rate coefficient obtained (and extrapolated for 10 K) in this work into a gas-grain model with representative densities and starting components leads to a 40 % decrease in ammonia concentration at ~ 5×10^5 years at 10 K. To obtain a more accurate value of the OH + ammonia rate coefficient at 10 K, and hence a better understanding of the impact of this reaction in cold molecular clouds, non-statistical theoretical calculations, for example trajectory calculations, should be performed. The impact of this reaction in low temperature interstellar environments based on the estimated 10 K rate coefficient will hopefully provide motivation for further experimental and theoretical study.

The preliminary experimental study of OH + methane performed at 54 K demonstrated that at this temperature, the very weakly bound complex (~

0.6 kJ mol^{-1}) was insufficiently long lived to facilitate tunnelling through the barrier to reaction at a bimolecular rate coefficient detectable in this experimental setup. Whilst this reaction is of interest at a fundamental level due to the extremely weakly bound nature of the pre-reaction complex, it may also be interesting from an astrochemical perspective as methane has been detected in several interstellar environments.[50-52] From the magnitude of the room temperature rate coefficient (~ 6.6 × 10^{-15} $molecule^{-1}$ cm^3 s^{-1} according to Vaghjiani and Ravishankara[40]) and the relative energies of the weakly bound complex and reaction barrier, it is perhaps inevitable that the rate coefficient for OH + methane was not significantly enhanced at 54 K to be within the detection limit of this apparatus. However, given the high imaginary frequency calculated for the barrier to reaction, it is possible that at temperatures inaccessible by this apparatus currently, the rate coefficient may be significantly enhanced. Experiments performed at lower temperatures accessible, for instance, by the continuous CRESU apparatus at Rennes, would shed light on this and provide an interesting outlook on the limitations of the mechanism observed for hydrogen transfer reactions discussed in this thesis.

5.8 References

1 Caravan, R. L., Shannon, R., Lewis, T., Blitz, M. A. & Heard, D. E. Measurements of Rate Coefficients for Reactions of OH with Ethanol and Propan-2-ol at Very Low Temperatures. *The Journal of Physical Chemistry A* (2014).

2 Gomez Martin, J. C., Caravan, R. L., Blitz, M. A., Heard, D. E. & Plane, J. M. C. Low Temperature Kinetics of the CH_3OH + OH Reaction. *J. Phys. Chem. A* **118**, 2693-2701 (2014).

3 Shannon, R. J., Caravan, R. L., Blitz, M. & Heard, D. E. A combined experimental and theoretical study of reactions between the hydroxyl radical and oxygenated hydrocarbons relevant to astrochemical environments. *Phys. Chem. Chem. Phys.* **16**, 3466-3478 (2014).

4 Galano, A., Alvarez-Idaboy, J. R., Bravo-Pérez, G. & Ruiz-Santoyo, M. E. Gas Phase Reactions of C1–C4 Alcohols with the OH Radical: A Quantum Mechanical Approach. *Phys. Chem. Chem. Phys.* **4**, 4648-4662 (2002).

5 Carr, S. A. *et al.* Experimental and Theoretical Study of the Kinetics and Mechanism of the Reaction of OH Radicals with Dimethyl Ether. *The Journal of Physical Chemistry A* **117**, 11142-11154 (2013).

6 Sivaramakrishnan, R. *et al.* Rate Constants for the Thermal Decomposition of Ethanol and Its Bimolecular Reactions with OH and D: Reflected Shock Tube and Theoretical Studies. *J. Phys. Chem. A* **114**, 9425-9439 (2010).

7 Monge-Palacios, M., Rangel, C. & Espinosa-Garcia, J. Ab initio based potential energy surface and kinetics study of the OH+ NH_3 hydrogen

abstraction reaction. *The Journal of Chemical Physics* **138**, 084305 (2013).

8 Corchado, J. C., Espinosa-Garcia, J., Hu, W.-P., Rossi, I. & Truhlar, D. G. Dual-Level Reaction-Path Dynamics (the///Approach to VTST with Semiclassical Tunneling). Application to OH+ NH_3 → H_2O+ NH_2. *The Journal of Physical Chemistry* **99**, 687-694 (1995).

9 Shannon, R. J. *Experimental and computational studies of hydroxyl radical kinetics at very low temperatures* PhD thesis, University of Leeds, (2012).

10 Perry, R., Atkinson, R. & Pitts Jr, J. Rate constants for the reactions OH+ H_2S→ H_2O+ SH and OH+ NH_3→ H_2O+ NH_2 over the temperature range 297–427 K. *The Journal of Chemical Physics* **64**, 3237-3239 (1976).

11 Diau, E. W. G., Tso, T. L. & Lee, Y. P. Kinetics of the reaction hydroxyl + ammonia in the range 273-433 K. *The Journal of Physical Chemistry* **94**, 5261-5265 (1990).

12 Jeffries, J. B. & Smith, G. P. Kinetics of the reaction hydroxyl + ammonia. *The Journal of Physical Chemistry* **90**, 487-491 (1986).

13 Silver, J. A. & Kolb, C. E. Kinetic measurements for the reaction of amidogen + nitric oxide over the temperature range 294-1215 K. *The Journal of Physical Chemistry* **86**, 3240-3246 (1982).

14 Cheung, A., Rank, D., Townes, C., Thornton, D. & Welch, W. Detection of NH_3 Molecules in the Interstellar Medium by Their Microwave Emission. *Physical Review Letters* **21**, 1701 (1968).

15 McGee, R., Gardner, F. & Robinson, B. OH observations in the directions of galactic thermal sources. *Australian Journal of Physics* **20**, 407-420 (1967).

16 Menten, K., Walmsley, C., Henkel, C. & Wilson, T. Methanol in the Orion region. I-Millimeter-wave observations. II-The 25 GHz masers revisited. *Astronomy and Astrophysics* **198**, 253-273 (1988).

17 Wilson, T., Gaume, R. & Johnston, K. Ammonia in the W3 (OH) region. *The Astrophysical Journal* **402**, 230-237 (1993).

18 Freeman, A. & Millar, T. J. Formation of complex molecules in TMC-1. *Nature* **301**, 402-404 (1983).

19 Arif, M., Dellinger, B. & Taylor, P. H. Rate coefficients of hydroxyl radical reaction with dimethyl ether and methyl tert-butyl ether over an extended temperature range. *The Journal of Physical Chemistry A* **101**, 2436-2441 (1997).

20 Robin, T. G. A Three-phase Chemical Model of Hot Cores: The Formation of Glycine. *The Astrophysical Journal* **765**, 60 (2013).

21 Sorrell, W. H. Origin of Amino Acids and Organic Sugars in Interstellar Clouds. *The Astrophysical Journal Letters* **555**, L129 (2001).

22 van Dishoeck, E. F., Jansen, D. J., Schilke, P. & Phillips, T. Detection of the interstellar NH_2 radical. *The Astrophysical Journal* **416**, L83 (1993).

23 Silvente, E., Richter, R. C. & Hynes, A. J. Kinetics of the vibrational deactivation of OH X 2 II (v= 3, 2, 1) with hydrides and reduced sulfides. *Journal of the Chemical Society, Faraday Transactions* **93**, 2821-2830 (1997).

24 Wang, L., Mebel, A. M., Yang, X. & Wang, X. Ab Initio/RRKM Study of the O (^{1}D)+ NH_3 Reaction: Prediction of Product Branching Ratios. *The Journal of Physical Chemistry A* **108**, 11644-11650 (2004).

25 Shu, J., Lin, J. J., Wang, C. C., Lee, Y. T. & Yang, X. Crossed molecular beam studies of the O (^{1}D) + NH_3 reaction. *Journal of Chemical Physics* **115**, 842-848 (2001).

26 Lambert, J. D. *Vibrational and rotational relaxation in gases*. (Clarendon Press Oxford, 1977).

27 Kliner, D. A. & Farrow, R. L. Measurements of ground-state OH rotational energy-transfer rates. *The Journal of Chemical Physics* **110**, 412-422 (1999).

28 Halpern, J., Hancock, G., Lenzi, M. & Welge, K. Laser induced fluorescence from NH_2 ($^2A_1$). State selected radiative lifetimes and collisional de−excitation rates. *The Journal of Chemical Physics* **63**, 4808-4816 (1975).

29 Ehbrecht, J., Hack, W. & Rouveirolles, P. Hydrogen Abstraction Reactions by NH_2 ($\tilde{X}^2B_1$)−Radicals from Hydrocarbons in the Gas Phase. *Berichte der Bunsengesellschaft für physikalische Chemie* **91**, 700-708 (1987).

30 Dressler, K. & Ramsay, D. The Electronic Absorption Spectra of NH_2 and ND_2. *Philosophical Transactions of the Royal Society of London. Series A, Mathematical and Physical Sciences*, 553-602 (1959).

31 Davidson, J. A. *et al.* Temperature dependence of O(^{1}D) rate constants for reactions with N_2O, H_2, CH_4, HCl, and NH_3. *The Journal of Chemical Physics* **67**, 5021-5025 (1977).

32 Glowacki, D. R., Liang, C.-H., Morley, C., Pilling, M. J. & Robertson, S. H. MESMER: an open-source master equation solver for multi-energy well reactions. *The Journal of Physical Chemistry A* **116**, 9545-9560 (2012).

33 Miller, W. H. Tunneling corrections to unimolecular rate constants, with application to formaldehyde. *Journal of the American Chemical Society* **101**, 6810-6814 (1979).

34 Wakelam, V. *et al.* A KInetic Database for Astrochemistry (KIDA). *The Astrophysical Journal Supplement Series* **199**, 21 (2012).

35 Prasad, S. & Huntress Jr, W. A model for gas phase chemistry in interstellar clouds. I-The basic model, library of chemical reactions, and chemistry among C, N, and O compounds. *The Astrophysical Journal Supplement Series* **43**, 1-35 (1980).

36 Brandt, A. *et al.* Methane Leaks from North American Natural Gas Systems. *Science* **343**, 733-735 (2014).

37 Wuebbles, D. J. & Hayhoe, K. Atmospheric methane and global change. *Earth-Science Reviews* **57**, 177-210 (2002).

38 Dlugokencky, E. J., Nisbet, E. G., Fisher, R. & Lowry, D. Global atmospheric methane: budget, changes and dangers. *Philosophical Transactions of the Royal Society of London A: Mathematical, Physical and Engineering Sciences* **369**, 2058-2072 (2011).

39 Dunlop, J. R. & Tully, F. P. A kinetic study of hydroxyl radical reactions with methane and perdeuterated methane. *The Journal of Physical Chemistry* **97**, 11148-11150 (1993).

40 Vaghjiani, G. L. & Ravishankara, A. New measurement of the rate coefficient for the reaction of OH with methane. *Nature* **350**, 406-409 (1991).

41 Srinivasan, N., Su, M.-C., Sutherland, J. & Michael, J. Reflected shock tube studies of high-temperature rate constants for OH + $CH_4 \rightarrow CH_3 + H_2O$ and $CH_3 + NO_2 \rightarrow CH_3O + NO$. *The Journal of Physical Chemistry A* **109**, 1857-1863 (2005).

42 Sharkey, P. & Smith, I. W. M. Kinetics of elementary reactions at low temperatures: rate constants for the reactions of OH with HCl (298 ≥ T/K ≥138) , CH_4 (298 ≥ *T*/K ≥178) and C_2H_6 (298 ≥ T/K ≥138). *Journal of the Chemical Society, Faraday Transactions* **89**, 631-637 (1993).

43 Bonard, A., Daële, V., Delfau, J.-L. & Vovelle, C. Kinetics of OH radical reactions with methane in the temperature range 295-660 K and with dimethyl ether and methyl-tert-butyl ether in the temperature range 295-618 K. *The Journal of Physical Chemistry A* **106**, 4384-4389 (2002).

44 Ellingson, B. A., Pu, J., Lin, H., Zhao, Y. & Truhlar, D. G. Multicoefficient Gaussian-3 Calculation of the Rate Constant for the OH + CH_4 Reaction and Its $^{12}C/^{13}C$ Kinetic Isotope Effect with Emphasis on the Effects of Coordinate System and Torsional Treatment. *The Journal of Physical Chemistry A* **111**, 11706-11717 (2007).

45 Bravo-Pérez, G., Alvarez-Idaboy, J. R., Jiménez, A. G. & Cruz-Torres, A. Quantum chemical and conventional TST calculations of rate constants for the OH + alkane reactions. *Chemical physics* **310**, 213-223 (2005).

46 Tsiouris, M., Wheeler, M. D. & Lester, M. I. Stimulated Raman and electronic excitation of CH_4–OH reactant complexes. *Chemical Physics Letters* **302**, 192-198 (1999).

47 Smith, I. W. & Ravishankara, A. Role of hydrogen-bonded intermediates in the bimolecular reactions of the hydroxyl radical. *The Journal of Physical Chemistry A* **106**, 4798-4807 (2002).

48 Vranckx, S., Peeters, J. & Carl, S. A temperature dependence kinetic study of $O(^1D) + CH_4$: overall rate coefficient and product yields. *Physical Chemistry Chemical Physics* **10**, 5714-5722 (2008).

49 Hancock, G., Morrison, M. & Saunders, M. Nascent vibrational distributions and relaxation rates of diatomic products of the reactions of $O(^1D)$ with CH_4, C_2H_6, CH_3F, CH_2F_2 and CHF_3 studied by time resolved Fourier transform infrared emission. *Journal of Photochemistry and Photobiology A: Chemistry* **176**, 191-198 (2005).

50 Fox, K. & Jennings, D. Methane detected in Orion A. *The Astrophysical Journal* **226**, L43-L47 (1978).

51 Lacy, J. *et al.* Discovery of interstellar methane-Observations of gaseous and solid CH_4 absorption toward young stars in molecular clouds. *The Astrophysical Journal* **376**, 556-560 (1991).

52 Mitchell, G. Methane in Dense Interstellar Clouds. *Astronomy and Astrophysics* **55**, 303 (1977).

Chapter 6. Radical-radical reactions at low temperatures: Kinetics of nitric oxide with alkoxy radicals.

6.1 Background and previous studies of radical-radical reactions at low temperatures

The development and first implementation of the CRESU apparatus was conducted by Bertrand Rowe and Jean-Baptiste Marquette in order to study ion-molecule reactions at low temperatures.[1,2] The technique was subsequently adapted by the group of Ian Smith to enable the kinetic studies of neutral reactions, and since then, the main focus of low temperature kinetic studies has been radical-neutral reactions.[3] Many of these reactions, such as OH + alkenes , C_2H + alkenes and C_2H + alkanes, are barrierless and so their rate coefficients exhibit a modest inverse temperature dependence.[4-13] Later studies, and also those presented in this thesis, which also concern radical-neutral reactions, have demonstrated that reactions with an overall barrier to hydrogen abstraction may be enhanced greatly at low temperatures where a weakly bound complex may be formed prior the abstraction barrier.[14-18]

There are limited studies in the literature on the kinetics of other reaction types below 200 K, for example radical-radical reactions. One of the main barriers to the kinetic study of such reactions is the necessity to produce one radical species in great excess of the other so that pseudo first order conditions are obtained. Some existing studies in the literature of these reactions at low temperatures will be briefly outlined below.

The first kinetic study of a radical-radical reaction at low temperatures was conducted by Sims and Smith on the reaction of CN with O_2 using a cryogenically cooled photolysis cell.[19] The rate coefficient was measured between 99-761 K, and a $T^{-0.5}$ dependence on the rate coefficient was observed, which was deduced to be indicative of a barrierless process.[19] The temperature range of the kinetics of this reaction was extended, initially down to 26 K in 1992, and later down to 13 K in 1994 upon the development of the CRESU apparatus for radical reactions.[3,20] A $T^{-0.63}$ dependence on the rate coefficient was concluded from these studies.[3]

The first low temperature radical-radical kinetic study whereby both radical species were produced *in situ* was on the reaction of $O(^3P)$ with OH conducted by Carty *et al.* down to 39 K.[21] The reaction of atomic oxygen in

its electronic ground state with OH at low temperatures is of interest to the astrochemical community as it is believed to be a major route to O_2 formation in the cold molecular clouds within the interstellar medium.[21,22]

$$O + OH \rightarrow H + O_2 \qquad \text{R6.1}$$

The rate coefficient was measured using a CRESU apparatus coupled with LIF detection of OH, and the O atom concentration was estimated by knowledge of O_2 absorption at 157.6 nm and the laser fluence at that wavelength. The rate coefficient was found to be independent of temperature between 142 and 39 K, indicating a barrierless process.

More recently, the kinetics of N atom reactions have been measured at low temperatures by Daranlot *et al.* within the groups of Hickson and Bergeat at the University of Bordeaux.[22-25] The reactions of N with NO, OH and CN (R6.2-R6.4) where N was produced by the microwave discharge of N_2, were studied to further understand the nitrogen cycle in the interstellar medium.

$$N + NO \rightarrow O + N_2 \qquad \text{R6.2}$$

$$N + OH \rightarrow H + NO \qquad \text{R6.3}$$

$$N + CN \rightarrow C + N_2 \qquad \text{R6.4}$$

The kinetics of N + NO was studied via LIF of NO. NO is a stable radical species and so can be added in known quantities to the gas mixture. Once the rate coefficient of this reaction had been obtained,[25] it was used to obtain the rate coefficient of N + OH via relative rate studies,[24] which in turn was then used to elucidate the N + CN rate coefficient.[23] For all of these reactions, the molecular radical reactant was monitored via LIF to obtain the rate coefficient, except in the case of the N + OH reaction, whereby the OH reactant and the NO product were simultaneously monitored via LIF using two probe lasers and two photomultiplier tubes (PMTs) for detection.

In this work, the kinetics of two radical-radical reactions (NO + methoxy and NO + ethoxy radicals) are reported below 284 K for the first time.

Alkoxy radicals are intermediates in the oxidation of hydrocarbon species, and play a role in both atmospheric and combustion chemistry.[26] Whilst the dominant reaction of atmospheric alkoxy radicals is with oxygen to generate carbonyl species, under highly polluted conditions they react with NO.[26,27] Several kinetic studies have been undertaken for the reaction of the smallest alkoxy radical, methoxy (CH_3O) with NO from 284 K upwards.[28-31]

$CH_3O + NO \rightarrow products$ R6.5

$CH_3O + NO \rightarrow CH_2O + HNO$ R6.5a

$CH_3O + NO \rightarrow CH_3ONO$ R6.5b

The reaction of the ethoxy radical (CH_3CH_2O) has been subject to fewer studies in the literature, but has been studied across the temperature range 298-403 K.[26,29,32,33]

$CH_3CH_2O + NO \rightarrow products$ R6.6

$CH_3CH_2O + NO \rightarrow CH_3CHO + HNO$ R6.6a

$CH_3CH_2O + NO \rightarrow CH_3CH_2ONO$ R6.6b

Previous work has utilised two techniques to generate alkoxy radicals: photolytic production via an alkoxy nitrite precursor (RONO), or from the reaction of the relevant alcohol with F atoms, which were generated via discharge flow. Following the generation of the alkoxy radicals using either method, the rate coefficients were subsequently measured under pseudo first order conditions where the NO co-reactant was in excess and the alkoxy radical was monitored via LIF spectroscopy.[26,28-32]

The overall rate coefficients of reactions R6.5 and R6.6 have been shown to exhibit modest negative temperature dependencies, which is consistent with the previous observations of radical-radical reaction rate coefficients.[3,19-21] In both the reactions of methoxy and of ethoxy radicals with NO, there are two competing channels. The first (R6.5a, R6.6a) is a hydrogen-abstraction disproportionation channel, yielding stable molecular products. The second (R6.5b, R6.6b) leads to the formation of the chemically activated alkoxy nitrite, which can be stabilised through collisional deactivation. The branching fraction of the two channels is pressure and temperature dependent, and for the methoxy radical reaction, this has been explored experimentally by Dobe *et al.*,[30] and through *ab initio*/RRKM calculations by Caralp *et al.*[28]

Caralp *et al.* reported that the high pressure limiting rate coefficient, (corresponding to the collisional stabilisation of the chemically activated methyl nitrite, produced from R6.5b), exhibits a negative temperature dependence, and from their experimental results deduced the following expression to describe the temperature dependence of the high pressure limiting rate coefficient:

$$k_\infty = 3.4\times10^{-11}\left(\frac{T}{298}\right)^{-0.75} \quad \text{E6.1}$$

This is in reasonable agreement with the earlier work by Frost and Smith,[29] who obtained the following expression:

$$k_{\infty} = 3.6\times10^{-11}\left(\frac{T}{298}\right)^{-0.6} \qquad \text{E6.2}$$

Frost and Smith obtained a temperature dependent expression for the low pressure limiting rate coefficient, in other words, the contribution of channel R6.5a only to the overall rate coefficient (E6.3).

$$k_{0} = 5.8\times10^{-12}\left(\frac{T}{298}\right)^{-0.6} \qquad \text{E6.3}$$

Caralp *et al.* found that at and below 350 K, the following expression for low pressure limiting rate coefficient was able to reproduce their experimental observations:

$$k_{0} = 2.5\times10^{-12}\left(\frac{T}{298}\right)^{-1.85} \qquad \text{E6.4}$$

Both the expressions of Caralp *et al.* and Frost and Smith predict negative temperature dependencies, as shown in Figure 6. 1.

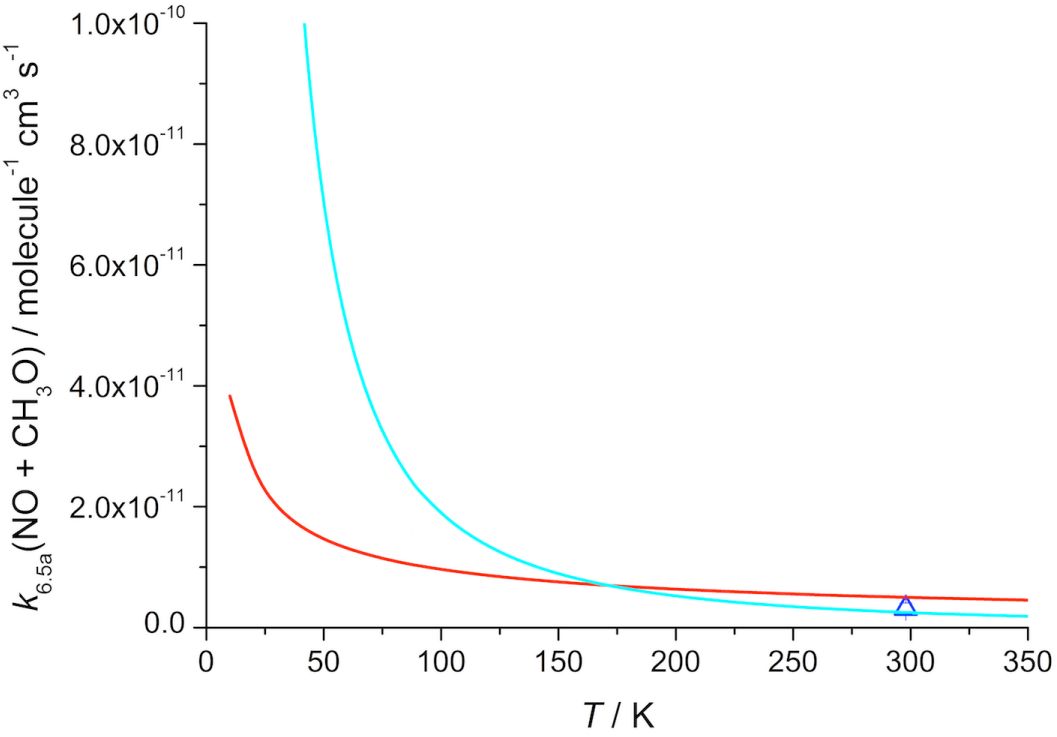

Figure 6. 1: The temperature dependence of the low pressure limiting rate coefficient for the NO + CH_3O reaction (R6.5a) in the literature up to 350 K. Blue line: extrapolation of E6.4 by Caralp *et al.*[28] Red line: extrapolation of E6.3 by Frost and Smith.[29] Open blue triangle: 298 K data point from an extended Lindemann-Hinshelwood fit of experimental data by Dobe *et al.*[30]

However, when Caralp *et al.* also included their data above 350 K, the best RRKM fit to the experimental data across the whole temperature range was obtained when abstraction via the energised adduct, CH_3ONO^*, was included alongside the direct H-abstraction mechanism, suggesting that the mechanism is more complex. A schematic outlining the potential reaction pathways is shown below in Figure 6. 2.[28] The role of direct abstraction was shown to be negligible below 350 K.

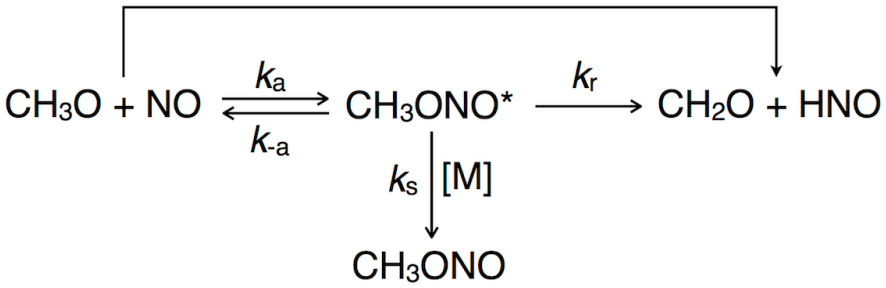

Figure 6. 2: Schematic showing the potential reaction pathways following RRKM modelling by Caralp *et al.* with the microcanonical rate coefficient labels as used for the OH + alcohols reactions (see Chapter 3).

The pressure dependence of the rate coefficient for R6.6 has been extensively investigated at room temperature by Ohmori *et al.* and by Frost and Smith, who investigated the effect of different bath gases, and the results of this are summarised in Figure 6. 3.[29,31] The work of Frost and Smith also investigated the pressure dependence over the temperature range 296-452 K using Ar and CF_4 bath gases between 3-125 Torr.[29] Work by Caralp *et al.* between 0.5-5 Torr of helium and between 248-473 K were all shown to be in the fall-off region and exhibited a clear pressure dependence.[28]

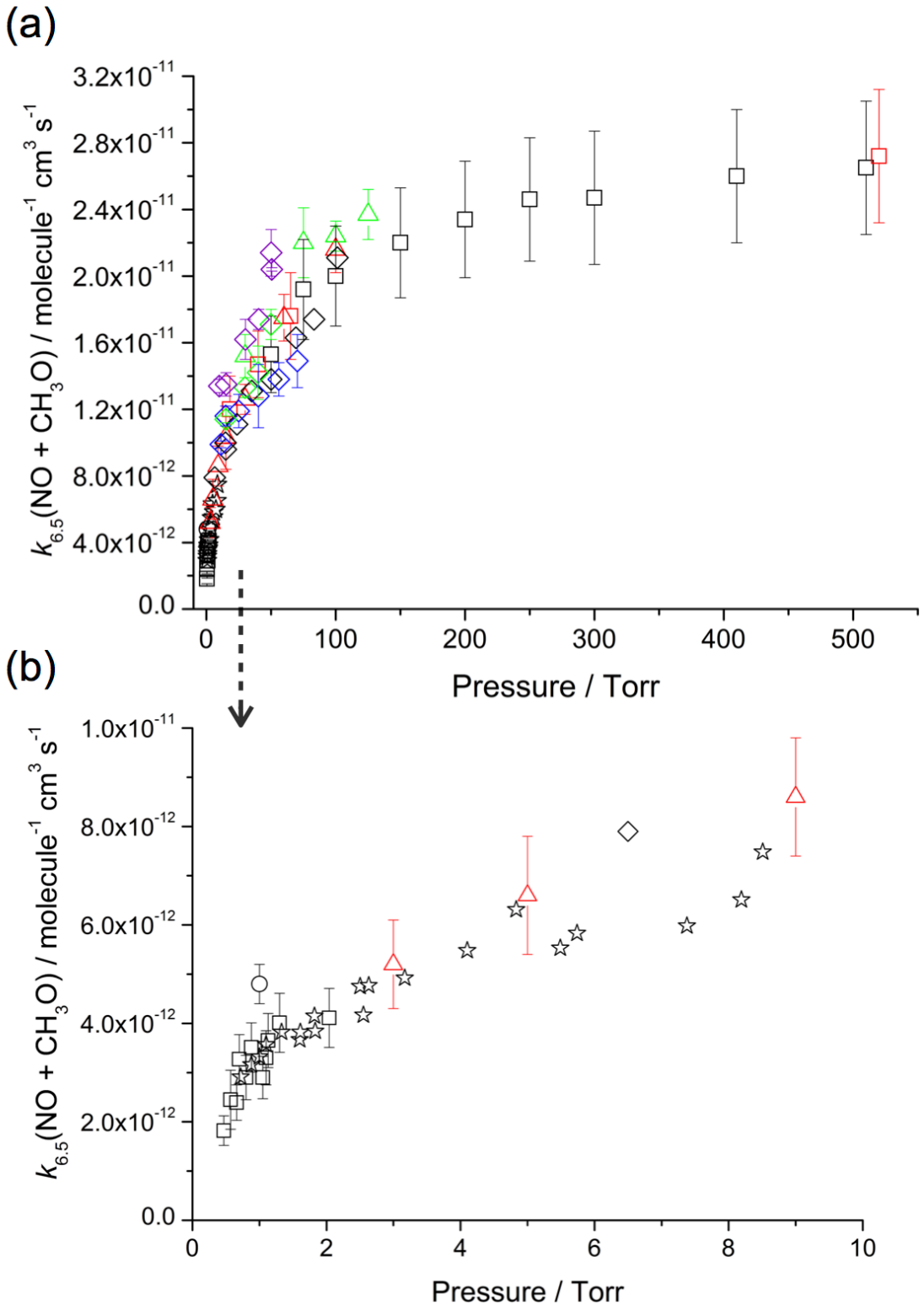

Figure 6. 3: Pressure dependence of the NO + CH_3O rate coefficient reported in the literature at 298 K (a), with inset (b) to show the low pressure work in more detail. The shape of the symbols denotes the authors. Circles: Daele *et al.*[27] Triangles: Frost and Smith.[29] Stars: Dobe *et al.*[30] Squares: Caralp *et al.*[28] Diamonds: Ohmori *et al.*[31] Colour of the symbol denotes bath gas: Black (He), red (Ar), green (CF_4), blue (N_2) and purple (SF_6).

There is some discrepancy in the literature regarding the height of the barrier to hydrogen abstraction. The *ab initio* calculations by Caralp *et al.* using the BAC-MP4 method (which were utilised in the RRKM calculations discussed above) find a submerged barrier of -8.8 kJ mol^{-1} with respect to reactants.[28] However, work by Fernandez-Ramos *et al.* at the QCISD(T)/6-311++G(d,p)//QCISD/6-311++G(d,p) reports a barrier of 18.2 kJ mol^{-1}.[34]

Recent work by Zhu *et al.* at the CASPT3(8,8)/6-31+G(3df,2p)// CASSCF(8,8)/6-311+G(d) level reports the presence of two transition states associated with H-abstraction.[35] The former is a conventional transition state with a relative energy of 25.5 kJ mol^{-1}. The second has a submerged barrier of -2.9 kJ mol^{-1} and is denoted as a roaming transition state, which is a very loose transition state with larger intermolecular distances between the two reactant species.[36-40] Examples and the intricacies of roaming-type reactions can be found in several recent reviews, notably those by Bowman and Suits.[36,37,39,40] It should also be noted that the calculated imaginary frequency of the conventional transition state associated with the H-abstraction barrier is relatively high, 1502 cm^{-1} according to the work of Caralp *et al.* and 1391 cm^{-1} from Fernandez-Ramos *et al.*[28,34] Therefore even if the barrier is positive, tunnelling may potentially contribute to the rate coefficient of the reaction, in particular at lower pressures where the methyl nitrite complex is not collisionally stabilised.

Theoretical studies in the literature are in reasonable agreement regarding the well depth associated with the formation of CH_3ONO via R6.5b, with values reported in the range 164-177 kJ mol^{-1}.[28,34,35] Potential energy surfaces based on the calculations by Caralp *et al.* and Zhu *et al.* are shown in Figure 6. 4 and Figure 6. 5 respectively.[28,35]

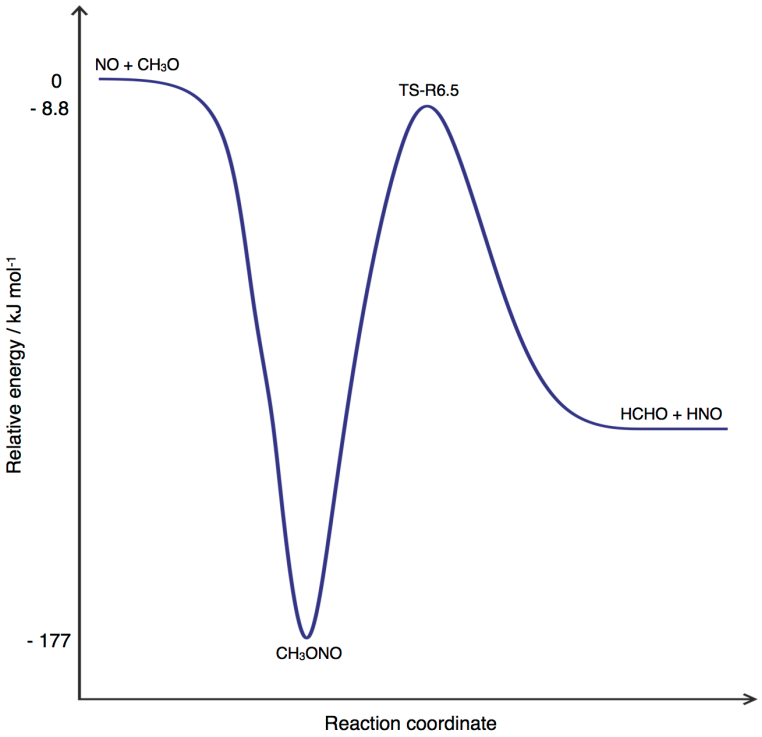

Figure 6. 4: To-scale potential energy surface for the reaction of NO with CH_3O (with relevant relative energies) based on the calculations by Caralp *et al.* at the BAC-MP4 level of theory.[28]

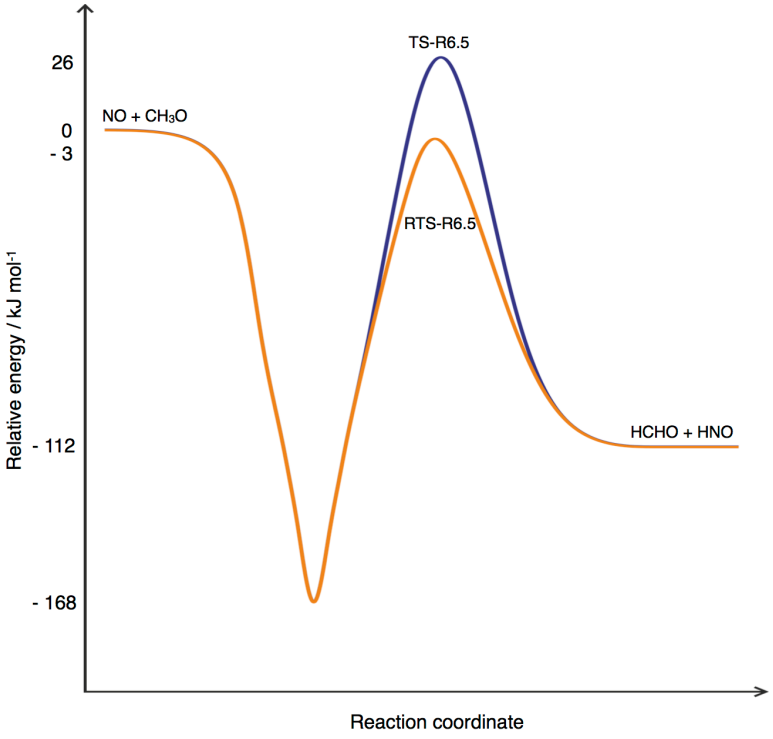

Figure 6. 5: To-scale potential energy surface for the reaction of NO with CH_3O (with relevant relative energies) based on the calculations by Zhu *et al.* at the CASPT3(8,8,)/6-31+G(3df,2p)//CASSCF(8,8)/6-311+G(d) level of theory. The orange line represents the minimum energy pathway involving the roaming transition state (RTS-R6.5) and the blue line represents the minimum energy pathway involving the conventional TS (TS-6.59).[35]

Fewer studies have been undertaken on the reaction of the ethoxy radical with NO (R6.6). To the best knowledge of the author, there have been no *ab initio* or rate theory studies, however it is assumed that the reaction pathways for higher alkoxy radicals with NO will be analogous to those found for the methoxy radical reaction.[26,29] Recent experimental work on the thermal decomposition of C_2H_5ONO by Prozument *et al.* postulated the role of a roaming mechanism following initial decomposition to NO and the ethoxy radical.[35,41] Chirped pulse rotational spectroscopy experiments performed between 1000-1800 K detected relative yields of HCHO:HNO:CH_3CO that, when resolved through kinetic analysis, indicated a significant contribution of a roaming radical channel yielding HNO and acetaldehyde. Upon decomposition of C_2H_5ONO , the NO radical subsequently 'roams' the ethoxy radical moiety via a loosely bound intermediate before abstracting a hydrogen atom yielding the molecular products.[41] Therefore, this roaming mechanism could also be operating in the bimolecular reaction of NO with the ethoxy radical (R6.6).

Experimental investigations by Fittschen *et al.* between 295-354 K found a modest negative temperature dependence on the rate coefficient of R6.6.[26] The rate coefficient obtained at 298 K in 100 Torr helium was in reasonable agreement with the value obtained by Frost and Smith in 15 and 100 Torr of argon.[29] However, the earlier work of Daele *et al.* at 0.55, 1 and 2 Torr of helium reported lower rate coefficients, and their Lindemann-Hinshelwood analysis demonstrated competition between the disproportionation channel (R6.6a) and the stabilisation of the chemically activated alkyl nitrite (R6.6b).[32] Fittschen *et al.* concluded that the rate coefficient reaches the high pressure limiting rate coefficient above 15 Torr of He between 295-354 K, and developed the following expression for the high pressure limiting rate coefficient.[26]

$$k_\infty = 2.0\times10^{-11} exp\left(\frac{600}{RT}\right) \qquad \text{E6.6}$$

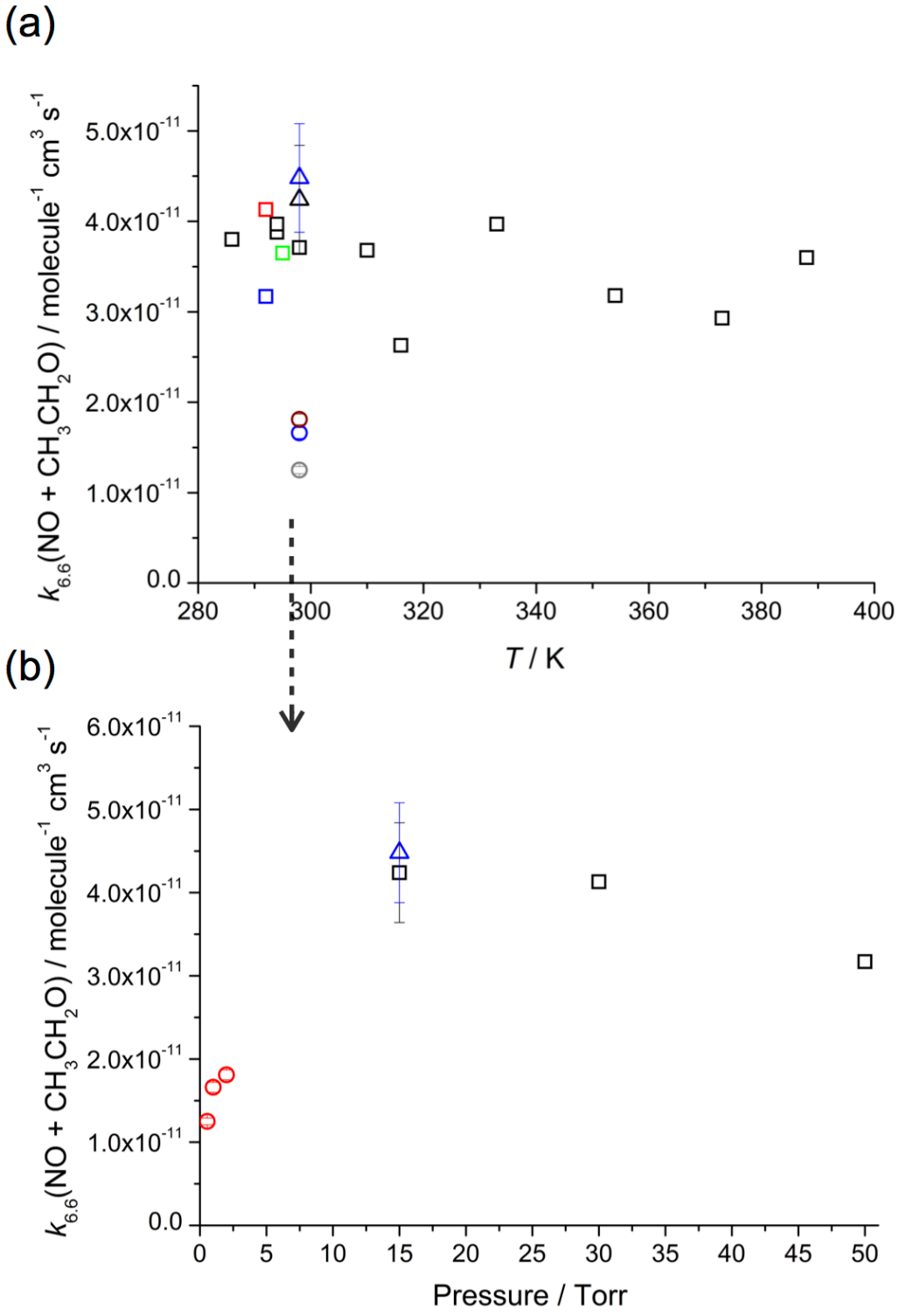

Figure 6. 6: (a) The temperature dependence of the NO + CH_3CH_2O reaction rate coefficient reported in the literature. The shape of the symbols denotes the authors. Circles: Daele *et al.*[32] Triangles: Frost and Smith.[29] Squares: Fittschen *et al.*[26] Colour of the symbol denotes bath gas: Black (He), red (Ar), green (CF_4), blue (N_2) and purple (SF_6). (b) Pressure dependence of the NO + CH_3CH_2O reaction rate coefficient reported in the literature at 298 K. Red circles: Daele *et al.*[32] (Ar bath gas). Blue triangle: Frost and Smith (N_2 bath gas).[29] Black squares: Frost and Smith (15 Torr, He bath gas) and Fittschen *et al.* (30 Torr, 50 Torr, He bath gas).[26,29]

Alkoxy radical reactions may also be of relevance to low temperature environments. As discussed in Chapter 3, Shannon *et al.* found the dominant low temperature product from the OH + methanol reaction to be the methoxy radical.[16] From the high imaginary frequency associated with the analogous abstraction site on ethanol, it is postulated that ethoxy radicals will be the major low temperature product from the OH + ethanol reaction. The methoxy radical has recently been detected for the first time in an interstellar environment in the molecular cloud Barnard-1 (B1), where temperatures can reach as low as 10 K.[42] Interestingly, both OH and methanol have been found in this molecular cloud, indicating their reaction may be a possible precursor to the methoxy radical.[42-44] An astrochemical modelling study conducted by Acharyya *et al.* to asses the impact of the OH + methanol reaction on methoxy radical formation using the low temperature rate coefficients for OH + methanol obtained by Shannon *et al.* and in this work found that at longer astrochemical times the methoxy radical concentration was overestimated compared to observation in the B1 cloud.[45] It was concluded that the methoxy radical loss processes were being underestimated.[45]

NO has also been detected within B1.[46] Given the presence of methoxy and NO within this environment, the reaction between the two species may act as a potential loss channel. As the rate coefficient has previously been reported to exhibit a pressure dependence and a complex temperature dependence, the rate coefficient of this, and the reaction of other alkoxy radicals needs to be studied under conditions relevant to cold dense molecular clouds, which can typically reach as low as 10 K. In this work, the reaction kinetics of NO with the methoxy radical and with the ethoxy radical has been studied at 89 K at three densities over the range 3.5×10^{16} to 1.1×10^{17} molecule cm^{-3}. In the case of the methoxy radical reaction, the product of R6.5a, HCHO, has been detected via LIF spectroscopy.

6.2 Experimental procedure

The apparatus and experimental procedure has been described fully in Chapter 2 of this thesis and thus only a brief outline is given here.

Methyl- and ethyl-nitrite were synthesised as outlined in the literature, but a concise outline is given below.[47] A three necked flask containing $NaNO_2$ (Sigma), distilled water and the relevant alcohol (methanol for methyl nitrite (Sigma-Aldrich ≥ 99.9 %), or ethanol for ethyl nitrite (Sigma-Aldrich, ethanol

absolute ≥ 99.8 %)) was cooled in an ice bath and stirred using a magnetic stirring plate whilst a H_2SO_4 (Fisher scientific analytical grade 98 %) /distilled water solution was added drop wise. The alkyl nitrite produced from the reaction was purged from the flask by a slow flow of nitrogen (BOC, OFN). The alkyl nitrite was passed through two traps containing NaOH (to remove H_2SO_4) and anhydrous $CaCl_2$ (to remove water) before being captured in a glass finger cooled to 195 K using a dry ice/acetone slush. The alkyl nitrite, which was pale yellow in colour, was further purified via the freeze pump thaw method. The vapour pressure of the relevant alkyl nitrite was then admitted to an evacuated cylinder via a gas manifold before being diluted to a total pressure of ~ 5000 Torr with N_2 (BOC, OFN). NO (BOC, 99.5 %) was admitted to another cylinder and diluted to a total pressure of ~ 5000 Torr with N_2. The bath gas and alkyl nitrite contained in the cylinders were allowed to mix overnight before use.

The alkyl nitrite/N_2, NO/N_2 and the N_2 bath gas (BOC, OFN) were delivered to the pre-expansion reservoir via a set of calibrated mass flow controllers (MKS instruments). All experiments were carried out under pseudo first order conditions and in addition the reagent concentration did not exceed 2 % of the total gas flow

The mixture of reagent and bath gases was expanded supersonically in pulses of a fixed width between ~ 10-20 ms through the convergent-divergent shaped Laval nozzle into a low pressure stainless steel chamber producing a thermally equilibrated, low temperature jet. The short gas pulses were achieved using two pulsed solenoid valves (Parker 9 series), which control the flow of gas from a 1 cm^3 reservoir region through the Laval nozzle.

The rate coefficients of the methoxy radical + NO and ethoxy radical + NO reactions were measured by monitoring the temporal decay of the relevant alkoxy radical via pulsed laser photolysis-laser induced fluorescence (PLP-LIF). The experiments were performed under pseudo first order conditions so that the concentration of the NO was in great excess (around a factor of 100 or more) of the alkoxy radical concentration. The alkoxy radical precursor (methyl nitrite or ethyl nitrite) was photolysed at 248 nm using an excimer laser (KrF Lambda Physik LPX 200), with typical laser energy of 280-340 mJ per pulse, along the axis of the expanded gas flow producing a uniform alkoxy radical density. The subsequent decay of the relevant alkoxy radical due to reaction and other loss processes was measured by LIF using an Nd:YAG (Litron LPY 664-10) pumped dye laser (Sirah Gmbh Cobra

stretch). The following transitions were utilised for LIF detection : the methoxy radical via the $\tilde{A}^2A_1 \leftarrow \tilde{X}^2E, \nu_3 = 1 \leftarrow 0$ transition at ~ 310 nm, and the ethoxy radical via the $\tilde{A}^2A_1 \leftarrow \tilde{X}^2A'', \nu_{10} = 3 \leftarrow 0$ transition at ~ 323 nm.[48,49] Laser excitation spectra of the methoxy and ethoxy radicals obtained via this transition following 248 nm photolysis of the alkyl nitrite precursor can be seen in Chapter 3.

The resultant fluorescence signal was collected by a PMT (Thorn EMI 9813QB) fitted with a wide band pass filter (Thor labs 400 ± 40 nm) positioned above the axis of the jet and laser beams, and was integrated and visualised on the oscilloscope (LeCroy Waverunner-2) prior to analysis using a PC .The temporal evolution of the alkoxy radicals was recorded by varying the time delay between the photolysis and probe lasers.

The concentrations of the alkoxy radical precursors were in the ranges (1.2-3.2) × 10^{13} molecule cm^{-3} and (0.53-1.3) × 10^{13} molecule cm^{-3} for the methoxy and ethoxy radical precursors, respectively. Following photolysis at 248 nm, this yielded alkoxy radicals in the ranges (2.1-5.5) × 10^{12} molecule cm^{-3} and (4.6-9.6) × 10^{12} molecule cm^{-3} of methoxy and ethoxy radicals respectively. Examples of how the concentration of methoxy and ethoxy radicals are calculated from the photolysis of the alkyl nitrite precursor at 248 nm is shown in Appendix D.

The reaction schemes for the formation and removal of the alkoxy radicals are given by:

$$CH_3ONO + h\nu \longrightarrow CH_3O + NO \qquad \text{P6.1}$$

$$CH_3O + NO \longrightarrow products \qquad \text{R6.5}$$

$$CH_3CH_2ONO + h\nu \longrightarrow CH_3CH_2O + NO \qquad \text{P6.2}$$

$$CH_3CH_2O + NO \longrightarrow products \qquad \text{R6.6}$$

For pseudo first order conditions, [NO] >> [RO] (where RO is a generic term for an alkoxy radical), the temporal evolution of the alkoxy radicals for both R6.5 and R6.6 is given by:

$$[RO]_t = [RO]_0 e^{-k_{obs}t} \qquad \text{E6.7}$$

and

$$k_{obs} = k_{6.5}[NO] + k_{loss} \qquad \text{E6.8}$$

for the reaction of NO with the methoxy radical (R6.5), and

$$k_{obs} = k_{6.6}[NO] + k_{loss} \qquad \text{E6.9}$$

for the reaction of NO with the ethoxy radical (R6.6).

k_{obs} is the pseudo first order rate coefficient and k_{loss} is the rate coefficient for the loss of the alkoxy radical out of the detection region via diffusion and reaction with the precursor.

6.3 Results and discussion

6.3.1 Alkoxy radical loss experiments

Examples of the temporal evolution of the alkoxy radical LIF signal following 248 nm photolysis of the relevant alkoxy nitrite precursor in the presence of NO are shown in Figures 7 and 8 for the methoxy and ethoxy radical reactions respectively, together with non-linear least squares fits of E6.8 and E6.9 respectively to the data, which yielded k_{obs}. The pseudo first order traces each comprise 280 points which were averaged 12 times.

The pseudo first order traces were found to contain a growth component which is indicative of the rotational relaxation (R6.7) of the photolytically produced alkoxy radical into the laser probed level, for example:

$$CH_3ONO + h\nu \longrightarrow CH_3O^* + NO \qquad \text{P6.1}$$

$$CH_3O^* + M \longrightarrow CH_3O + M \qquad \text{R6.7}$$

$$CH_3O + NO \longrightarrow products \qquad \text{R6.5}$$

As the growth component of the traces were found to be at a comparable rate to the loss component of the trace (in particular at higher alkoxy radical concentrations), it was not possible to fit the traces with a exponential growth-exponential decay trace, and so the traces were fitted with a single exponential decay expression (E6.7). However, due to the growth component, it was found that the traces were perturbed at early times and so different values for the pseudo first order rate coefficients were retrieved depending on at what delay time the fit was started from. The most extreme differences in the pseudo first order rate coefficients obtained were within 15 % of the mean value. Therefore, for these experiments, the data were fitted from time delays yielding roughly the mean value, and the error in the fit was propagated with 15 % of the returned pseudo first order rate coefficient.

Experiments were repeated for a variety of concentrations of NO and Figures 9 and 10 show the variation of k_{obs} with [NO], the gradients of which yield the bimolecular rate coefficients for the methoxy radical + NO ($k_{6.5}$) and ethoxy radical + NO reactions ($k_{6.6}$), respectively.

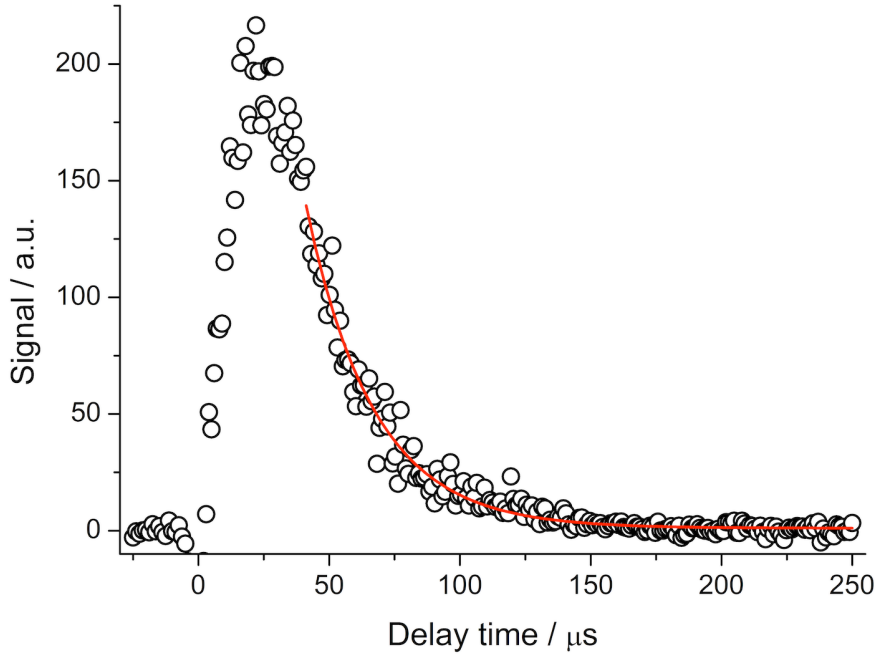

Figure 6. 7: Pseudo first order LIF profile of the methoxy radical (open circles) together with the non-linear least squares fit of E6.8 to the data (red line) from the 248 nm photolysis of methyl nitrite in the presence of NO (9.9×10^{14} molecule cm^{-3}) at 88 ± 5 K and a total density (3.5 ± 0.5) × 10^{16} molecule cm^{-3}, using N_2 bath gas. The least squares fit of E6.8 to the data yields a pseudo first order rate coefficient of 38462 ± 960 s^{-1} (± 6751 s^{-1} when propagated with 15 % of the returned k_{obs} value, see text for details).

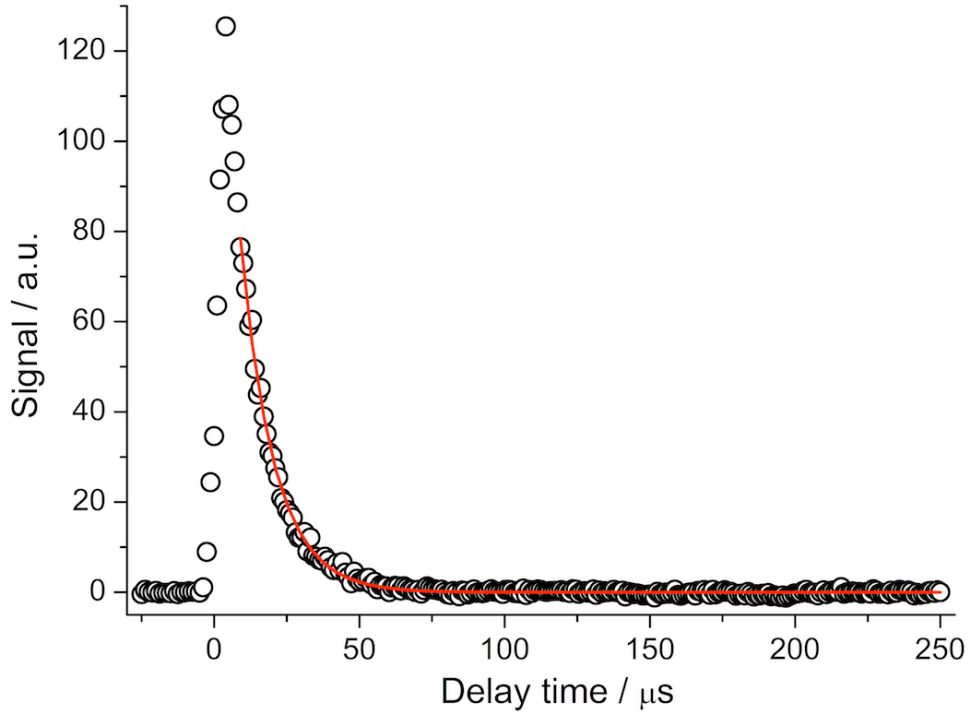

Figure 6. 8: Pseudo first order LIF profile of the ethoxy radical (open circles) together with the non-linear least squares fit of E6.9 to the data (red line) from the 248 nm photolysis of ethyl nitrite in the presence of NO (7.5×10^{14} molecule cm^{-3}) at 89 ± 3 K and a total density (6.5 ± 0.6) × 10^{16} molecule cm^{-3}, using N_2 bath gas The least squares fit of E6.9 to the data yields a pseudo first order rate coefficient of 86650 ± 744 s^{-1} (± 13741 s^{-1} when propagated with 15 % of the returned k_{obs} value, see text for details).

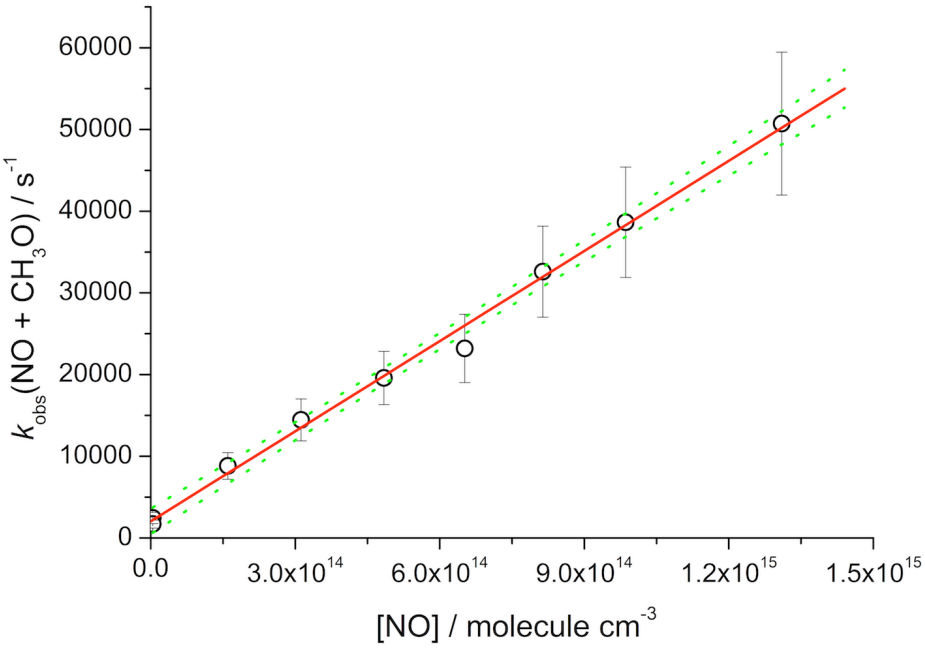

Figure 6. 9: Variation of k_{obs} with NO concentration for the reaction of NO with methoxy radicals, obtained at 88 ± 5 K and a density of (3.5 ± 0.5) × 10^{16} molecule cm^{-3} using N_2 bath gas, together with a weighted linear least squares fit of E6.7 to the data, the gradient of which yields the bimolecular rate coefficient, $k_{6.5}$= (3.5 ± 0.6) × 10^{-11} $molecule^{-1}$ cm^3 s^{-1}. The green dashed lines represent the upper and lower 95 % confidence limits. The overall error in the bimolecular rate coefficient is the 95% confidence limits propagated with the error in the determination of the total density from the impact pressure measurements.

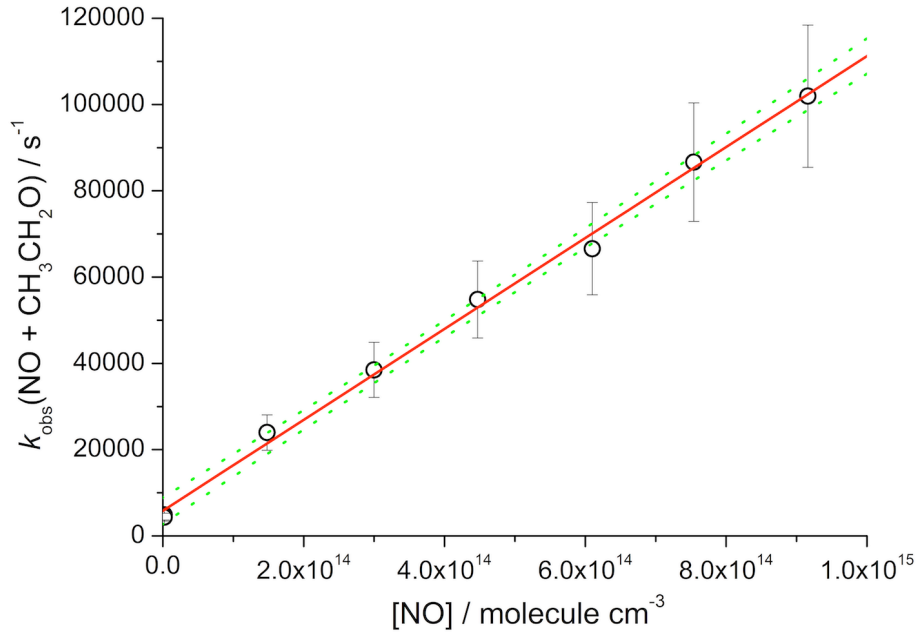

Figure 6. 10: Variation of k_{obs} with NO concentration for the reaction of NO with ethoxy radicals, obtained at 89 ± 3 K and a density of (6.5 ± 0.6) × 10^{16} molecule cm^{-3} using N_2 bath gas, together with a weighted linear least squares fit of E6.7 to the data, the gradient of which yields the bimolecular rate coefficient, $k_{6.6}$= (9.8 ± 0.9) × 10^{-11} $molecule^{-1}$ cm^3 s^{-1}. The green dashed lines represent the upper and lower 95 % confidence limits. The overall error in the bimolecular rate coefficient is the 95% confidence limits propagated with the error in the determination of the total density from the impact pressure measurements.

The bimolecular rate coefficients obtained in this work are summarised in Table 6. 1 and are notably faster than those reported in the literature at higher temperatures, which is consistent with the negative temperature dependence reported in the literature. However, given that both reactions are subject to competitive branching between stabilisation and bimolecular product formation, it is instructive to examine the pressure dependence to allow a more rigorous comparison to the literature values, and to examine the mechanisms operating at low temperatures.

Table 6. 1: Measured rate coefficients of the NO + alkoxy radical reactions obtained in this study, together with the temperatures and total gas densities of the flows generated by the pulsed Laval nozzles utilised. Errors have been calculated by propagation of the 95 % confidence limits in the bimolecular rate coefficients with the errors in the expansion densities.

T/K	Bath gas (M)	[M] / 10^{16} molecule cm^{-3}	$k_{6.5}$ / 10^{-11} molecule^{-1} cm^3 s^{-1}	$k_{6.6}$/ 10^{-11} molecule^{-1} cm^3 s^{-1}
88 ± 5	N_2	3.5 ± 0.5	3.5 ± 0.6	8.9 ± 1.7
			3.4 ± 3.0[a]	
89 ± 3	N_2	6.5 ± 0.6	4.5 ± 0.8	9.8 ± 0.9
88 ± 4	N_2	11 ± 1	5.3 ± 0.7	12 ± 2

[a] Rate coefficient obtained by the detection of HCHO products.

Both $k_{6.5}$ and $k_{6.6}$ have been studied over a small pressure range at ~ 89 K, and a modest pressure dependence was observed for both rate coefficients, as shown in Figure 6. 11. The magnitude of the NO + ethoxy reaction rate coefficients were found to be larger than those obtained for the NO + methoxy reaction across the pressure range . This is consistent with the previous experimental results, for example, at 294-298 K and 100 Torr He, Fittschen *et al.* report the NO + ethoxy radical rate coefficient as 3.9 × 10^{-11} molecule^{-1} cm^3 s^{-1}, and Caralp *et al.* report 2 × 10^{-11} molecule^{-1} cm^3 s^{-1} for the NO + methoxy radical reaction.[26,28] The experimental rate coefficients have been fitted with an extended Lindemann-Hinshelwood expression, which is given below in E6.10. The derivation of this equation was given in Chapter 3, in the context of the low temperature rate coefficients for OH + alcohol reactions.

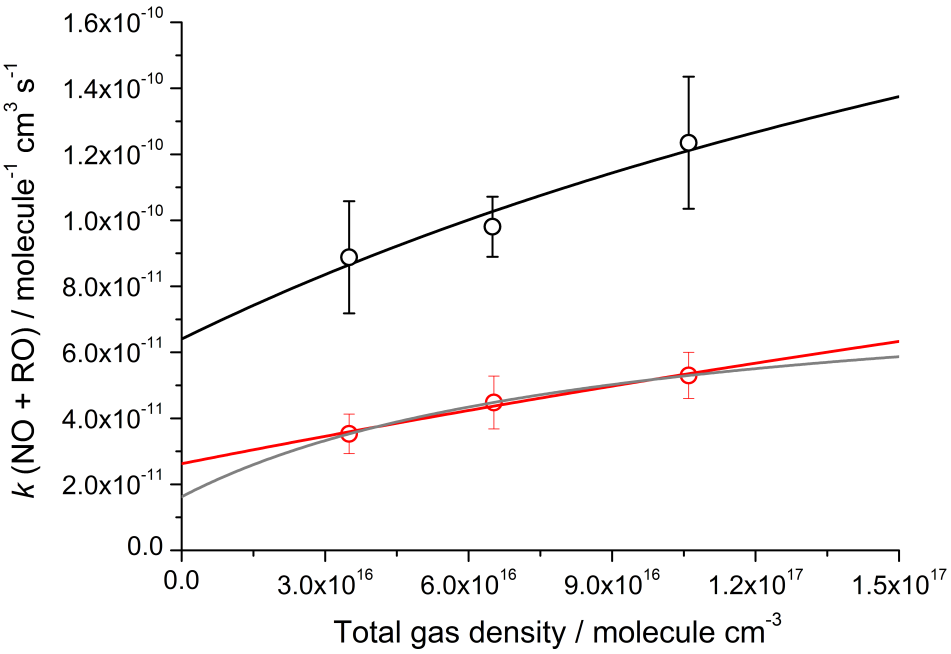

Figure 6. 11: Pressure dependence of $k_{6.5}$, the NO + methoxy radical reaction rate coefficient (red open circles) and for $k_{6.6}$, the NO + ethoxy radical reaction rate coefficient (black open circles), both measured at 89 K using N_2 bath gas. The error bars are the result of propagation of the 95 % confidence limits in the bimolecular rate coefficients with the errors in the expansion densities. The red line is the extended Lindemann-Hinshelwood fit to the NO + methoxy data using 3 × 10^{-10} molecule^{-1} cm^3 s^{-1} for k_a. The grey line is the extended Lindemann-Hinshelwood fit to the NO + methoxy data using 8.4 × 10^{-11} molecule^{-1} cm^3 s^{-1} for k_a. The black line is the extended Lindemann-Hinshelwood fit to the NO + ethoxy data using 3 × 10^{-10} molecule^{-1} cm^3 s^{-1} for k_a. See text for details.

$$k = \frac{[M]}{\frac{k_{-a}}{k_a k_s}+\frac{[M]}{k_a}+\frac{k_r}{k_a k_s}} + \frac{1}{\frac{k_{-a}}{k_a k_r}+\frac{k_s[M]}{k_a k_r}+\frac{1}{k_a}} \qquad \text{E6.10}$$

In E6.10, k_a represents the rate coefficient for formation of the complex RONO, k_{-a} is the rate coefficient for the subsequent redissociation of the complex, k_s is the rate coefficient for stabilisation of the complex into the deep well and k_r is the rate coefficient for bimolecular reaction following the initial complex formation, as illustrated in Figure 6. 2. Fitting of this equation to the experimental data as a function of [M] requires three parameters: $(k_a k_r)/(k_{-a}+k_r)$ (the low pressure limiting rate coefficient, k_0), k_r/k_s (the chemical activation ratio) and the high pressure limiting rate coefficient, k_∞, which is equal to k_a. More detail about the E6.10 is given in Chapter 3. As one of these parameters must be fixed to obtain a solution to the fit, k_a was fixed at 3.0 × 10^{-10} molecule^{-1} cm^3 s^{-1} for both reactions, as this value is in the region of the gas kinetic limit. This value was also chosen as it is a lower limit of the high pressure limiting rate coefficients for other reactions obtained in this work (see Chapter 7). In the case of the NO + methoxy radical reaction, the high pressure limiting rate coefficient obtained from

E6.1 derived by Caralp *et al.* from their experimental data was also used, yielding a value of k_a = 8.4 ×10^{-11} molecule^{-1} cm^3 s^{-1} at 89 K.[28] Whilst Fittschen *et al.* reported an expression to obtain the high pressure limiting rate coefficient as a function of temperature (E6.6) when calculated for 89 K, it was found that the value was notably less than had been measured under the conditions of these experimental studies, and so this value was not used.[26] The values of the low pressure limiting rate coefficient and the chemical activation ratio obtained from the fits for both reactions are presented in Table 6. 2.

Table 6. 2: Parameters obtained from the fit of the extended Lindemann-Hinshelwood expression (E6.10) to the experimental pressure dependent data.

System	High pressure limit k_a /molecule^{-1} cm^3 s^{-1}	Chemical activation ratio k_r/k_s /molecule cm^{-3}	Zero pressure rate coefficient $(k_a k_r)/(k_{-a}+k_r)$ /molecule^{-1} cm^3 s^{-1}
NO + CH_3O	*3.0×10^{-10}	(8.4±1.7)×10^{16}	(2.6±0.2)×10^{-11}
	#8.4×10^{-11}	(1.73±0.02)×10^{16}	(1.62±0.01)×10^{-11}
NO + CH_3CH_2O	*3.0 ×10^{-10}	(7.1±3.2)×10^{16}	(6.4±1.1)×10^{-11}

*High pressure limits estimated from approximate gas kinetic limiting rate coefficients. #Value calculated from the empirical equation from the work of Caralp *et al.*[28]

As it can be seen from Table 6. 2 and Figure 6. 11, the pressure-independent component of the rate coefficients of both R6.5 and R6.6 are significant, providing strong evidence that bimolecular product formation is occurring at low temperatures. Fitting of the data for the NO + methoxy radical reaction with the two values for k_a results in different values for the zero pressure rate coefficient. However, these values are within a factor of two of one another.

From the values obtained from the extended Lindemann-Hinshelwood fit, it is possible to examine the pressure dependence of the contributions from the bimolecular channels (R6.5a, R6.6a) leading to molecular products, and the stabilisation channels (following R6.5b and R6.6b) to the overall rate coefficient. The calculated contributions of these channels to the overall ate coefficients using the values presented in Table 6. 2 are shown below in Figure 6. 12 and Figure 6. 13 for the methoxy and ethoxy radical reactions respectively.

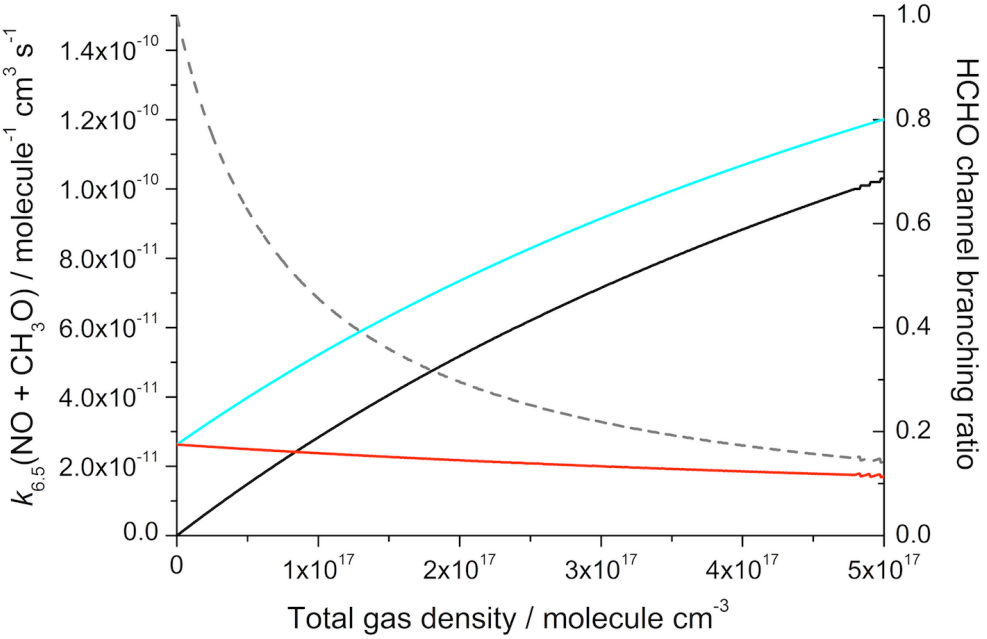

Figure 6. 12: The extended Lindemann-Hinshelwood expression (E6.10) for the NO + methoxy radical reaction, $k_{6.5}$ as a function of [M] (N_2) using the best fit parameters from fitting to experimental data (cyan line) (with k_a = 3.0 ×10^{-10} molecule^{-1} cm^3 s^{-1}). Together with the calculated contributions to $k_{6.5}$ from the pressure dependent term (black line), corresponding to collisional stabilisation of the chemically activated methyl nitrite product, and the approximately pressure independent term (red line), corresponding to bimolecular product formation, and the HCHO branching ratio (grey dashed line) as a function of total gas density.

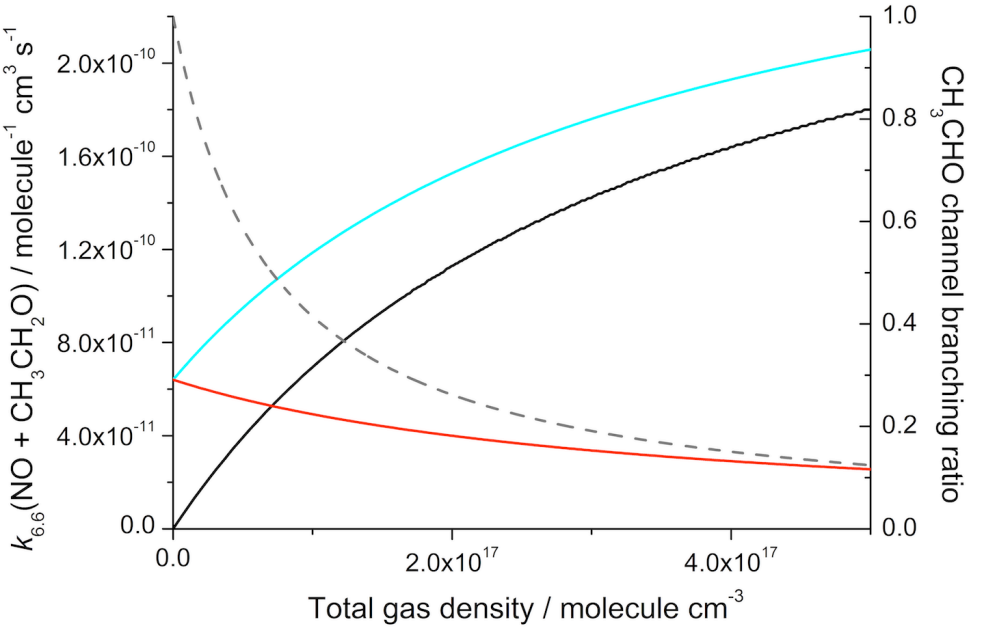

Figure 6. 13: The extended Lindemann-Hinshelwood expression (E6.10) for the NO + ethoxy radical reaction, $k_{6.6}$ as a function of [M] (N_2) using the best fit parameters from fitting to experimental data (cyan line). Together with the calculated contributions to $k_{6.6}$ from the pressure dependent term (black line), corresponding to collisional stabilisation of the chemically activated ethyl nitrite, and the approximately pressure independent term (red line), corresponding to bimolecular product formation, and the CH_3CHO branching ratio (grey dashed line) as a function of total gas density.

From the relative contribution of channels R6.5a and R6.6a to the overall rate coefficient, the total yield of bimolecular products can be calculated. The yields of the bimolecular products HCHO (for R6.5) and CH_3CHO (for R6.6) at 3.5×10^{16} molecule cm^{-3} of N_2 bath gas are approximately 0.70 and 0.67 respectively. Extrapolations of the expressions of the low pressure limiting rate coefficient for the NO + methoxy radical reaction by Frost and Smith (E6.3) and Caralp et al. (E6.4) are shown alongside the values obtained from the extended Lindemann-Hinshelwood fits to the data obtained in this study in Figure 6. 14.

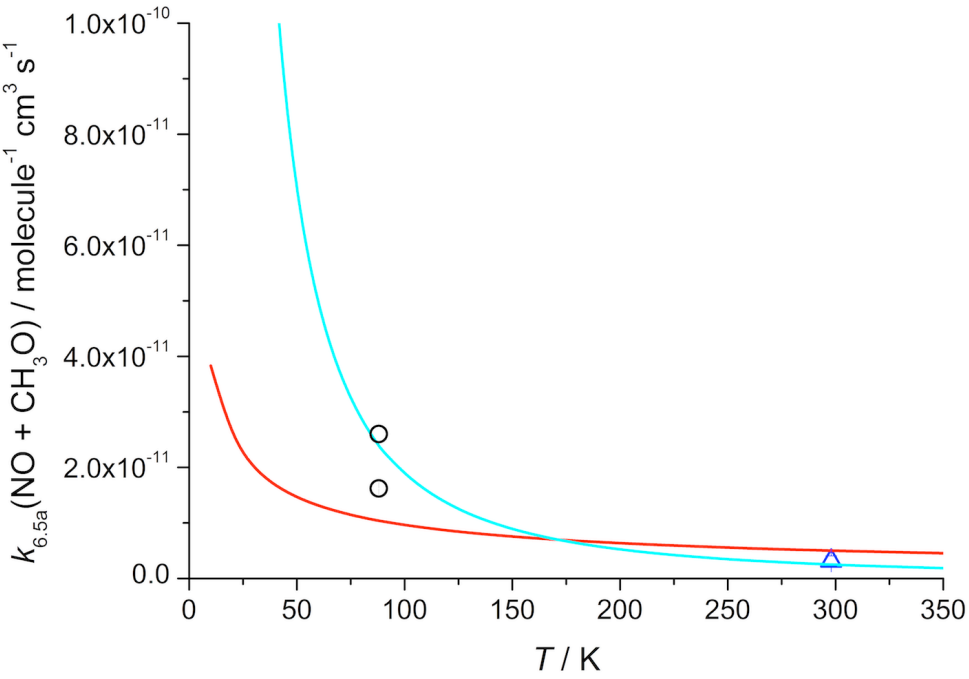

Figure 6. 14: The temperature dependence of the low pressure limiting rate coefficient for the NO + CH_3O reaction in the literature, alongside the low pressure limiting rate coefficient obtained in this study from extended Lindemann-Hinshelwood fits to the experimental data. Blue line: extrapolation of E6.4 by Caralp *et al.*[28] Red line: extrapolation of E6.3 by Frost and Smith.[29] Open blue triangle: 298 K data point from extrapolation of experimental data by Dobe *et al.*[30] Black open circles: low pressure limiting values from extrapolation of experimental data from this study . Higher value from fit with $k_a = 3.0 \times 10^{-10}$ molecule^{-1} cm^3 s^{-1}, lower value from fit with $k_a = 8.4 \times 10^{-11}$ molecule^{-1} cm^3 s^{-1}.

It can be seen from Figure 6. 14 that the low pressure limiting rate coefficients obtained in this work from the extended Lindemann-Hinshelwood expression are in reasonable agreement with the predicted values from the expressions by Caralp *et al.* and Frost and Smith.[28,29] The value obtained using $k_a = 3.0 \times 10^{-10}$ molecule^{-1} cm^3 s^{-1} is in excellent agreement with the predicted value from the temperature dependence expression by Caralp *et al.* [28] This suggests that at low temperatures the

mechanism is as expected from the higher temperature data, and the reaction is likely to proceed via a submerged barrier to bimolecular products.

For the NO + ethoxy radical reaction, there are currently no analogous low pressure limiting rate coefficient expressions or data and so it is not possible to draw a direct comparison to the literature. However, it can be seen from Figure 6. 13 that at low temperatures, the low pressure limiting rate coefficient is large ((6.4 ± 1.1) × 10^{-11} molecule^{-1} cm^3 s^{-1}) and larger than the high pressure limiting values reported in the literature.[26]

Under the experimental conditions of this study, the branching ratio to bimolecular products is significant, but product detection is desirable to confirm this. Aldehydes such as the products of R6.5 and R6.6 are detectable via laser induced fluorescence spectroscopy, although the absorption cross sections are relatively small and decrease for larger species, and acetaldehyde has an absorption cross section (4.9 × 10^{-20} cm^2 molecule^{-1} at 290 nm) than is around a factor of four weaker than that of formaldehyde (2.1 × 10^{-19} cm^2 molecule^{-1} at 353 nm). [50,51] In this work, the HCHO product of R6.5 has been temporally detected via LIF spectroscopy and a bimolecular rate coefficient obtained from its growth kinetics, as discussed below.

6.3.2 HCHO detection experiments

Formaldehyde (HCHO) has been detected as a reaction product via LIF by several studies including those performed in this laboratory, and is usually probed via the $\tilde{A}^1A_2 \leftarrow \tilde{X}^1A_1$ ($\nu_4 = 1 \leftarrow 0$) band at ~ 353 nm, which corresponds to a $n \rightarrow \pi^*$ transition in the carbonyl bond.[52-54] The UV absorption structure of this band was first identified and characterised in 1932 by Dieke and Kistiakowsky.[55,56]

According to the extended Lindemann-Hinshelwood fit to the pressure dependence data (Figure 6. 12), the branching ratio of HCHO is largest at the lowest gas density (3.5 × 10^{16} molecule cm^{-3}, 88 K). Therefore these were the conditions utilised to attempt detection of the HCHO product.

To obtain the wavelength of the strongest HCHO LIF transition at low temperatures and to ascertain that HCHO was indeed the species being probed, the wavelength of the Nd:YAG pumped dye laser was tuned to be resonant with the $\nu_4 = 1 \leftarrow 0$ vibrational band of the $\tilde{A}^1A_2 \leftarrow \tilde{X}^1A_1$ electronic transition and was set to a fixed delay time of ~ 200 μs after the photolysis laser. The probe laser was scanned over 352.500 – 354.000 nm at 0.001 nm

increments and the laser excitation spectrum recorded with two shots per point. The off-resonance fluorescence was collected by a PMT (Thorn EMI 9813QB) fitted with a wide bandpass interference filter (Thor labs 400 ± 40 nm). The spectrum was normalised for probe laser power, which was monitored by a photodiode. The concentrations of the precursors and reagents was as follows: NO = 1.4 × 10^{14} molecule cm^{-3} and methyl nitrite = 4.7 × 10^{13} molecule cm^{-3}. The resultant spectrum is shown in Figure 6. 15 and the line that was subsequently utilised for kinetics studied is labelled.

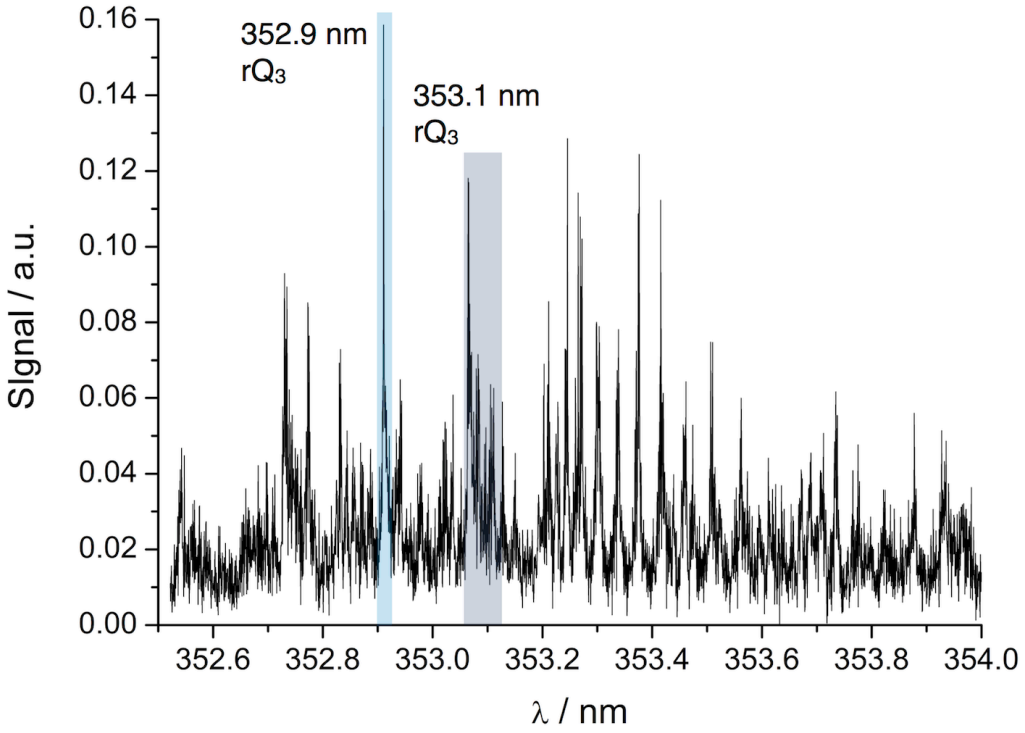

Figure 6. 15: Laser excitation spectrum of formaldehyde obtained from the reaction of NO + methoxy radicals corresponding to the 4_0^1 $\tilde{A}^1A_2 \leftarrow \tilde{X}^1A_1$ band obtained at 88 ± 5 K, N_2 = (3.5 ± 0.5) × 10^{16} molecule cm^{-3}, recorded at 0.001 nm increments with 2 shots per point. [NO] = 1.4 × 10^{14} molecule cm^{-3} and [methyl nitrite] = 4.7 × 10^{13} molecule cm^{-3}. Blue band: The rotational transition at 352.9 nm (13,3 ← 12,3 (j,k)) in the rQ_3 branch utilised for kinetics in this work. Grey band: The transition at 353.1 nm due to a combination of rotational transitions utilised previously by Gravestock *et al.* and Stone *et al.*[52,57,58] Wavelength given in air.

The vibronic band position as shown in Figure 6. 15 is in good agreement with the literature including those reported by Stone *et al*., Burket *et al.* and Gravestock *et al.* [51-53,57,59,60] Under the low temperature conditions at which this spectrum was recorded, it was found that the maximum LIF intensity in the vibronic band was at 352.9 nm, rather than at 353.1 nm which was identified previously from spectra recorded at room temperature and above.[51-53,57,58] To the authors knowledge there are no low temperature LIF

spectra of the $\nu_4 = 1 \leftarrow 0$ $\tilde{A}^1A_2 \leftarrow \tilde{X}^1A_1$ band of HCHO to directly compare with the spectrum obtained here. However, the rovibrational transition utilised by Stone *et al.* and Gravestock *et al.* for room temperature kinetic studies can also be seen in the spectrum obtained here, and is assigned alongside the band utilised in this work in Figure 6. 15.[52,53,58] Both of these transitions belong to the rQ_3 branch of the vibronic band. It should also be noted that a wavemeter was utilised to correct the wavelength of the spectrum.

To provide further evidence that the formaldehyde is indeed being formed as a product from R6.5, the pseudo first order kinetics of HCHO production were monitored at various NO concentrations. Due to the PMT overload at early reaction times from the photolysis laser, two traces were obtained for each kinetic run: (1) with both the photolysis (excimer) and probe (dye) lasers, and (2) with the photolysis laser only. This enabled the overload of the PMT from the excimer laser at early times (recorded in trace 2) to be removed from the kinetic traces, an example of trace type (2) is shown in Figure 6. 16.

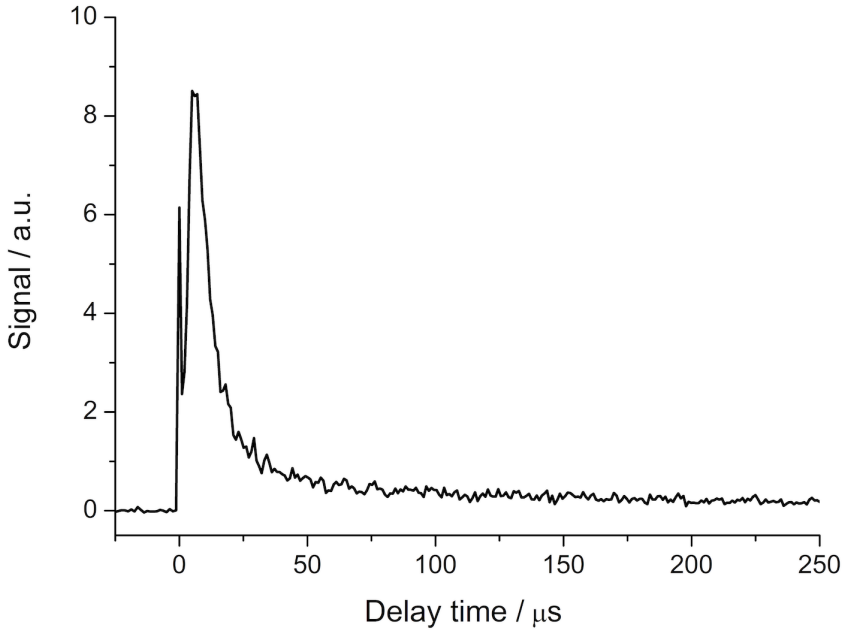

Figure 6. 16: Signal obtained in the absence of the probe laser (trace type (2)) due to the early time overload of the PMT by the excimer laser. The effect of the overload extends to ~ 75 μs, and kinetic traces were not analysed until 100 μs to avoid this effect.

As it can be observed from Figure 6. 16, the effect of the PMT overload extends out to ~ 75 μs, and even when the trace (2) is subtracted, some recovery of the PMT at short delay times is still evident (up to ~ 75 μs) and therefore the kinetic traces were only analysed from 100 μs onwards.

After the excimer-induced signal was subtracted from the two-laser trace, each resultant growth trace, purely due to HCHO LIF, was fitted with an exponential growth expression, E6.11.

$$[HCHO]_t = \left(\frac{k_{6.5}[NO]}{k_{loss} - k_{6.5}[NO]}\right)[HCHO]_m \left(e^{-k_{6.5}[NO]t} - e^{-k_{loss}t}\right) \qquad \text{E6.11}$$

where $[HCHO]_t$ is the relative formaldehyde concentration at a given laser delay time, $k_{6.5}[NO]$ is the pseudo first order rate coefficient for R6.5 at a given NO concentration, $[HCHO]_m$ is the maximum signal (relative concentration), k_{loss} is the pseudo first order loss rate coefficient for HCHO from diffusion, and t is the reaction time. This equation is adapted from the Pilling and Seakins.[61]

The k_{loss} value, corresponding to diffusion, was fixed at 1500 s^{-1} for the analysis of all traces as this was an average k_{loss} value obtained for CH_3O from the intercept of the bimolecular plot for CH_3O + NO under these conditions. The HCHO LIF traces were fitted with E6.11 from 100-250 μs. An example of a fitted HCHO trace alongside a CH_3O loss trace fitted with E6.8 from the reaction of CH_3O with NO ([NO] ~ 3.3 × 10^{11} molecule cm^{-3}) are shown in Figure 6. 17. The HCHO fit has been simulated to 0 μs using the Origin 7 software to demonstrate that the fit predicts zero HCHO at time zero. The obtained pseudo first order rate coefficients for these traces are within error of one another. HCHO traces were recorded at a range of NO concentrations and the resultant bimolecular plot of k_{obs} versus [NO] is shown in Figure 6. 18.

The bimolecular rate coefficient obtained from the HCHO kinetic traces (3.4 ± 3.0) × 10^{-11} $molecule^{-1}$ cm^3 s^{-1}) was found to be within error of the methoxy radical loss kinetics bimolecular rate coefficient at this temperature and density ((3.5 ± 0.6) × 10^{-11} $molecule^{-1}$ cm^3 s^{-1}). Whilst the error in the bimolecular rate coefficient is significantly larger than for that obtained via the CH_3O traces, it provides further evidence for the formation of formaldehyde as products from the reaction. The large error in the HCHO kinetics is in part due to the difficulty in observing formaldehyde fluorescence via LIF spectroscopy, the absorption cross section of formaldehyde at ~ 353 nm is around 900 times weaker than that of OH at ~ 282 nm.[51,62]

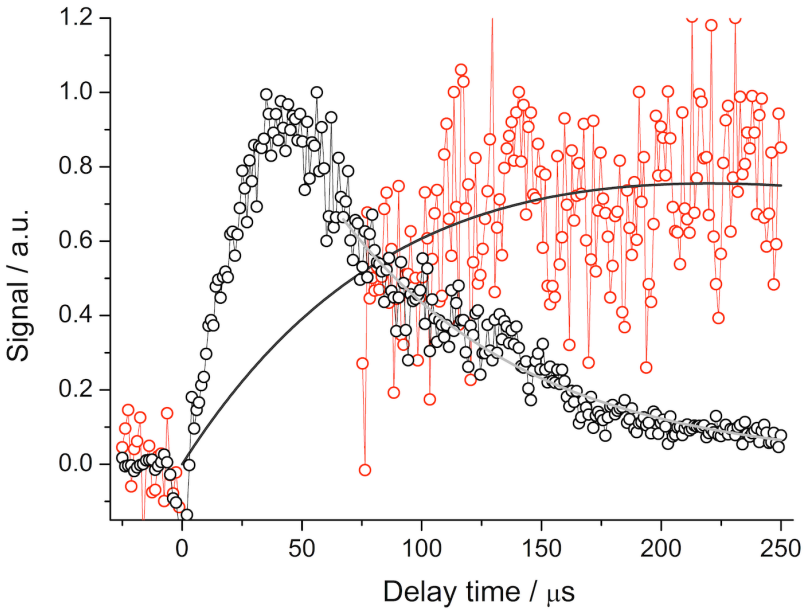

Figure 6. 17: CH_3O decay trace (black open circles) and formaldehyde growth trace (red open circles) obtained at ~ [NO] = 3.3 × 10^{11} molecule cm^{-3}. Grey line: fit of E6.8 to the CH_3O trace yielding a pseudo first order rate coefficient of 9949 ± 1981 s^{-1}. Black line: fit of E6.11 to the HCHO trace yielding a pseudo first order rate coefficient of 12663 ± 2245 s^{-1}. The HCHO trace has an early time recovery from PMT overload up to ~ 75 μs and so analysis is not started until 100 μs, but the fit is extrapolated to demonstrate the expected temporal profile.

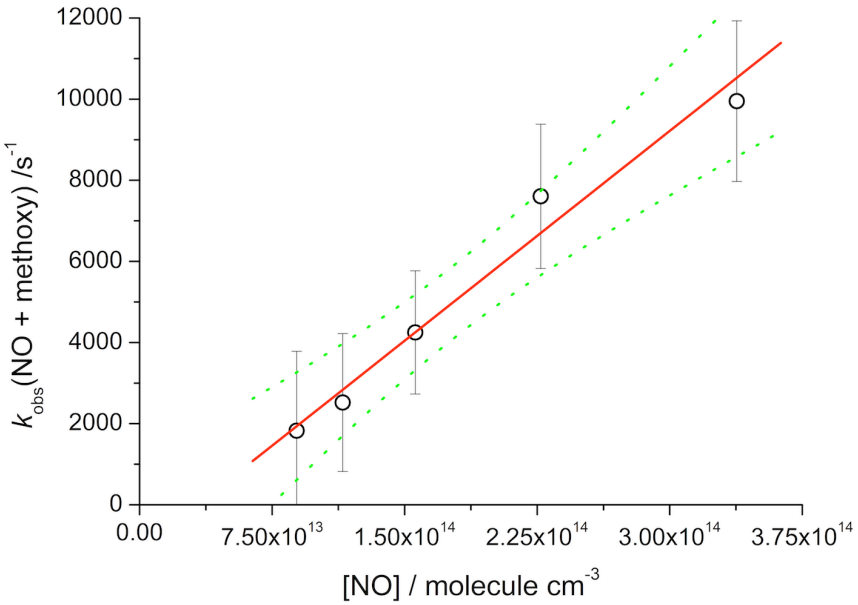

Figure 6. 18: Variation of k_{obs} with NO concentration for the reaction of NO with methoxy radicals, obtained at 88 ± 5 K and a density of (3.5 ± 0.5) × 10^{16} molecule cm^{-3} obtained via LIF spectroscopy of HCHO products. This is plotted together with a weighted linear least squares fit of E6.8 to the data, the gradient of which yields the bimolecular rate coefficient, $k_{6.5}$= (3.4 ± 3.0) × 10^{-11} molecule^{-1} cm^3 s^{-1}. A non-weighed fit to the data yields a value of $k_{6.5}$= (3.4 ± 1.0) × 10^{-11} molecule^{-1} cm^3 s^{-1}. The green dashed lines represent the upper and lower 95 % confidence limits. The overall error in the bimolecular rate coefficient is the 95% confidence limits propagated with the error in the determination of the total density from the impact pressure measurements.

The yield of HCHO from R6.5 has not been experimentally determined in this work owing to the lack of well characterised reactions at low temperatures with a known yield of HCHO as an internal standard. Whilst HCHO could be added to the Laval nozzle apparatus at a known concentration and the LIF signal height utilised as a calibration method, formaldehyde is known to stick to metal surfaces, such as the gas delivery lines, the ballast tank, the pulsed valves and the nozzle itself. This would create contamination issues and so the branching ratio obtained via this method would be subject to great uncertainty.

6.4 Summary

The first studies of alkoxy radical reactions kinetics below 284 K have been reported in this work. The rate coefficients for both the NO + methoxy radical and NO + ethoxy radical reactions were found to exhibit modest pressure dependencies, which is consistent with the previous higher temperature observations. The pressure dependent component of the rate coefficients corresponds to the formation of an alkyl nitrite (RONO) which is collisionally stabilised into a deep well (~ 164-177 kJ mol^{-1} for CH_3ONO). Extended Lindemann-Hinshelwood fits to the rate coefficients obtained for both reactions revealed pressure independent components, which are consistent with the bimolecular reaction yielding molecular products (HNO + aldehyde). The low pressure limiting rate coefficient for the ethoxy radical reaction has not previously been reported and so no direct comparisons can be made to the literature. However, the pressure independent component at 89 K is higher than any rate coefficient previously reported for this reaction over the temperature range studied, confirming the inverse temperature dependence of this reaction. For the methoxy radical reaction, the low pressure limiting rate coefficient at 89 K was found to be around an order of magnitude greater than that obtained by Caralp *et al.* at 298 K.[28] Extrapolation of the temperature dependence expression for the low pressure limiting rate coefficient derived by Caralp *et al.* was in good agreement with the experimentally obtained value reported here, suggesting that the reaction indeed proceeds via a submerged barrier to reaction and that the mechanism operating at low temperatures is the same as at higher temperatures.

Further analysis of the extended Lindemann-Hinshelwood fits to the data reveal that at 88 K and a total gas density of 3.5×10^{16} molecule cm^{-3}, the

yields of the bimolecular products for both reactions are high : 0.70 for the methoxy radical reaction and 0.67 for the ethoxy radical reaction.

Detection of the formaldehyde product from the methoxy radical reaction via laser induced fluorescence spectroscopy acted as an additional confirmation that the bimolecular reaction is indeed operating at these low temperatures.

This work has demonstrated that at very low temperatures, the reaction of NO with alkoxy radicals is fast, and the low pressure limiting rate coefficient is active and, compared to the 298 K value, is significantly enhanced. Therefore, in the low temperature and low pressure interstellar environments where alkoxy radicals and NO have been detected, the reaction of NO with alkoxy radicals may be operating, and yielding bimolecular products such as HCHO and HNO. Given that CH_3O, NO, HCHO and HNO have all been observed in Barnard-1 molecular cloud, the reaction of NO and CH_3O should be considered for inclusion in astrochemical models.[42,46,63]

6.5 References

1 Dupeyrat, G., Marquette, J. B. & Rowe, B. R. Design and testing of axisymmetric nozzles for ion–molecule reaction studies between 20 °K and 160 °K. *Physics of Fluids (1958-1988)* **28**, 1273-1279 (1985).

2 Rowe, B., Dupeyrat, G., Marquette, J. & Gaucherel, P. Study of the reactions $N^+2 + 2N_2 \rightarrow N^+_4 + N_2$ and $O^+_2 + {}^2O_2 \rightarrow O^+_4 + O_2$ from 20 to 160 K by the CRESU technique. *The Journal of chemical physics* **80**, 4915-4921 (1984).

3 Sims, I. *et al.* Ultralow temperature kinetics of neutral–neutral reactions. The technique and results for the reactions CN+ O_2 down to 13 K and CN+ NH_3 down to 25 K. *The Journal of chemical physics* **100**, 4229-4241 (1994).

4 Nizamov, B. & Leone, S. R. Kinetics of C_2H reactions with hydrocarbons and nitriles in the 104-296 K temperature range. *The Journal of Physical Chemistry A* **108**, 1746-1752 (2004).

5 Soorkia, S. *et al.* Reaction of the C_2H Radical with 1-Butyne (C_4H_6): Low-Temperature Kinetics and Isomer-Specific Product Detection. *The Journal of Physical Chemistry A* **114**, 3340-3354 (2010).

6 Vakhtin, A. B., Heard, D. E., Smith, I. W. & Leone, S. R. Kinetics of reactions of C_2H radical with acetylene, O_2, methylacetylene, and allene in a pulsed Laval nozzle apparatus at T= 103K. *Chemical Physics Letters* **344**, 317-324 (2001).

7 Vakhtin, A. B., Heard, D. E., Smith, I. W. & Leone, S. R. Kinetics of C_2H radical reactions with ethene, propene and 1-butene measured in a pulsed Laval nozzle apparatus at T= 103 and 296 K. *Chemical Physics Letters* **348**, 21-26 (2001).

8 Vakhtin, A. B., Lee, S., Heard, D. E., Smith, I. W. & Leone, S. R. Low-temperature kinetics of reactions of the OH radical with propene and

1-butene studied by a pulsed Laval nozzle apparatus combined with laser-induced fluorescence. *The Journal of Physical Chemistry A* **105**, 7889-7895 (2001).

9 Vakhtin, A. B., McCabe, D. C., Ravishankara, A. & Leone, S. R. Low-temperature kinetics of the reaction of the OH radical with hydrogen peroxide. *The Journal of Physical Chemistry A* **107**, 10642-10647 (2003).

10 Vakhtin, A. B., Murphy, J. E. & Leone, S. R. Low-temperature kinetics of reactions of OH radical with ethene, propene, and 1-butene. *The Journal of Physical Chemistry A* **107**, 10055-10062 (2003).

11 Daranlot, J. *et al.* Gas−Phase Kinetics of Hydroxyl Radical Reactions with Alkenes: Experiment and Theory. *ChemPhysChem* **11**, 4002-4010 (2010).

12 Daugey, N. *et al.* Kinetic measurements on methylidyne radical reactions with several hydrocarbons at low temperatures. *Phys Chem Chem Phys* **7**, 2921-2927 (2005).

13 Taylor, S. E., Goddard, A., Blitz, M. A., Cleary, P. A. & Heard, D. E. Pulsed Laval nozzle study of the kinetics of OH with unsaturated hydrocarbons at very low temperatures. *Phys Chem Chem Phys* **10**, 422-437 (2008).

14 Caravan, R. L., Shannon, R., Lewis, T., Blitz, M. A. & Heard, D. E. Measurements of Rate Coefficients for Reactions of OH with Ethanol and Propan-2-ol at Very Low Temperatures. *The Journal of Physical Chemistry A* (2014).

15 Shannon, R. J., Taylor, S., Goddard, A., Blitz, M. A. & Heard, D. E. Observation of a large negative temperature dependence for rate coefficients of reactions of OH with oxygenated volatile organic compounds studied at 86-112 K. *Phys Chem Chem Phys* **12**, 13511-13514 (2010).

16 Shannon, R. J., Blitz, M. A., Goddard, A. & Heard, D. E. Accelerated Chemistry in the Reaction between the Hydroxyl Radical and Methanol at Interstellar Temperatures Facilitated by Tunnelling. *Nature Chem.* **5**, 745-749 (2013).

17 Shannon, R. J., Caravan, R. L., Blitz, M. & Heard, D. E. A combined experimental and theoretical study of reactions between the hydroxyl radical and oxygenated hydrocarbons relevant to astrochemical environments. *Phys. Chem. Chem. Phys.* **16**, 3466-3478 (2014).

18 Gomez Martin, J. C., Caravan, R. L., Blitz, M. A., Heard, D. E. & Plane, J. M. C. Low Temperature Kinetics of the CH_3OH + OH Reaction. *J. Phys. Chem. A* **118**, 2693-2701 (2014).

19 Sims, I. R. & Smith, I. W. Rate constants for the radical-radical reaction between CN and O_2 at temperatures down to 99 k. *Chemical Physics Letters* **151**, 481-484 (1988).

20 Sims, I. *et al.* Ultra−low temperature kinetics of neutral–neutral reactions: The reaction CN+ O_2 down to 26 K. *The Journal of chemical physics* **97**, 8798-8800 (1992).

21 Carty, D., Goddard, A., Köhler, S. P. K., Sims, I. R. & Smith, I. W. M. Kinetics of the Radical−Radical Reaction, $O(^3P_J)$ + $OH(X^2\Pi_\Omega)$ → O_2+ H, at Temperatures down to 39 K. *The Journal of Physical Chemistry A* **110**, 3101-3109 (2005).

22 Hickson, K. M. & Bergeat, A. Low temperature kinetics of unstable radical reactions. *Phys Chem Chem Phys* **14**, 12057-12069 (2012).
23 Daranlot, J. *et al.* Elemental nitrogen partitioning in dense interstellar clouds. *Proceedings of the National Academy of Sciences of the United States of America* **109**, 10233-10238 (2012).
24 Daranlot, J. *et al.* Revealing atom-radical reactivity at low temperature through the N + OH reaction. *Science* **334**, 1538-1541 (2011).
25 Bergeat, A., Hickson, K. M., Daugey, N., Caubet, P. & Costes, M. A low temperature investigation of the N(^{4}S°) + NO reaction. *Phys Chem Chem Phys* **11**, 8149-8155 (2009).
26 Fittschen, C., Frenzel, A., Imrik, K. & Devolder, P. Rate constants for the reactions of C_2H_5O, i-C_3H_7O, and n-C_3H_7O with NO and O_2 as a function of temperature. *International Journal of Chemical Kinetics* **31**, 860-866 (1999).
27 Daele, V., Laverdet, G., Le Bras, G. & Poulet, G. Kinetics of the Reactions CH_3O + NO, CH_3O + NO_3, and CH_3O_2 + NO_3. *The Journal of Physical Chemistry* **99**, 1470-1477 (1995).
28 Caralp, F. *et al.* Kinetic and mechanistic study of the pressure and temperature dependence of the reaction CH_3O + NO. *Journal of the Chemical Society, Faraday Transactions* **94**, 3321-3330 (1998).
29 Frost, M. J. & Smith, I. W. Rate constants for the reactions of CH_3O and C_2H_5O with NO_2 over a range of temperature and total pressure. *Journal of the Chemical Society, Faraday Transactions* **86**, 1751-1756 (1990).
30 Dobe, S., Lendvay, G., Szilagyi, I. & Bérces, T. Kinetics and mechanism of the reaction of CH_3O with NO. *International Journal of Chemical Kinetics* **26**, 887-901 (1994).
31 Ohmori, K., Yamasaki, K. & Matsui, H. Pressure Dependence of the Rate Constant for the Reaction of CH_3O+ NO. *Bulletin of the Chemical Society of Japan* **66**, 51-56 (1993).
32 Daele, V., Ray, A., Vassalli, I., Poulet, G. & Bras, G. L. Kinetic study of reactions of $C_2H_5O_2$ and C_2H_5O with NO at 298 K and 0.55–2 torr. *International Journal of Chemical Kinetics* **27**, 1121-1133 (1995).
33 Baker, G. & Shaw, R. Reactions of methoxyl, ethoxyl, and t-butoxyl with nitric oxide and with nitrogen dioxide. *J. Chem. Soc.*, 6965-6970 (1965).
34 Fernández-Ramos, A. *et al.* Direct dynamics study of the dissociation and elimination channels in the thermal decomposition of methyl nitrite. *Journal of the American Chemical Society* **120**, 7594-7601 (1998).
35 Zhu, R., Raghunath, P. & Lin, M.-C. Effect of Roaming Transition States upon Product Branching in the Thermal Decomposition of CH_3NO_2. *The Journal of Physical Chemistry A* **117**, 7308-7313 (2013).
36 Suits, A. G. Roaming Atoms and Radicals: A New Mechanism in Molecular Dissociation. *Accounts of Chemical Research* **41**, 873-881 (2008).
37 Herath, N. & Suits, A. G. Roaming radical reactions. *The Journal of Physical Chemistry Letters* **2**, 642-647 (2011).

38 Harding, L. B. & Klippenstein, S. J. Roaming Radical Pathways for the Decomposition of Alkanes. *The Journal of Physical Chemistry Letters* **1**, 3016-3020 (2010).

39 Bowman, J. M. & Shepler, B. C. Roaming radicals. *Annual Review of Physical Chemistry* **62**, 531-553 (2011).

40 Bowman, J. M. Roaming. *Molecular Physics* **112**, 2516-2528 (2014).

41 Prozument, K. *et al.* A Signature of Roaming Dynamics in the Thermal Decomposition of Ethyl Nitrite: Chirped-Pulse Rotational Spectroscopy and Kinetic Modeling. *The Journal of Physical Chemistry Letters* **5**, 3641-3648 (2014).

42 Cernicharo, J. *et al.* Discovery of the Methoxy Radical, CH_3O, toward B1: Dust Grain and Gas-phase Chemistry in Cold Dark Clouds. *The Astrophysical Journal Letters* **759**, L43 (2012).

43 Öberg, K. I., Bottinelli, S., Jørgensen, J. K. & Van Dishoeck, E. F. A cold complex chemistry toward the low-mass protostar B1-b: evidence for complex molecule production in ices. *The Astrophysical Journal* **716**, 825 (2010).

44 Goodman, A., Crutcher, R., Heiles, C., Myers, P. & Troland, T. Measurement of magnetic field strength in the dark cloud Barnard 1. *The Astrophysical Journal* **338**, L61-L64 (1989).

45 Acharyya, K. *et al.* The Importance of OH Radical-Neutral Low Temperature Tunneling Reations in Interstellar Clouds Using a New Model. *Molecular Physics* **Accepted** (2015).

46 Cernicharo, J. *et al.* Tentative Detection of the Nitrosylium Ion in Space. *The Astrophysical Journal* **795**, 40 (2014).

47 Taylor, W. D. *et al.* Atmospheric photodissociation lifetimes for nitromethane, methyl nitrite, and methyl nitrate. *International Journal of Chemical Kinetics* **12**, 231-240 (1980).

48 Zhu, X., Kamal, M., M. & Misra, P. Laser-induced excitation and dispersed fluorescence spectra of the ethoxy radical. *Pure and Applied Optics: Journal of the European Optical Society Part A* **5**, 1021 (1996).

49 Foster, S. C. *et al.* Free jet-cooled laser-induced fluorescence spectrum of methoxy. 1. Vibronic analysis of the~ A and~ X states. *The Journal of Physical Chemistry* **92**, 5914-5921 (1988).

50 Atkinson, R. *et al.* Evaluated kinetic and photochemical data for atmospheric chemistry: Volume II–gas phase reactions of organic species. *Atmos. Chem. Phys* **6**, 3625-4055 (2006).

51 Co, D. T., Hanisco, T. F., Anderson, J. G. & Keutsch, F. N. Rotationally resolved absorption cross sections of formaldehyde in the 28100-28500 cm^{-1} (351-356 nm) spectral region: implications for in situ LIF measurements. *The journal of physical chemistry. A* **109**, 10675-10682 (2005).

52 Stone, D., Blitz, M., Daubney, L., Ingham, T. & Seakins, P. CH_2OO Criegee biradical yields following photolysis of CH_2I_2 in O_2. *Phys Chem Chem Phys* **15**, 19119-19124 (2013).

53 Gravestock, T. J. *A kinetic and spectroscopic study of chemistry relating to the atmopsheric role of iodine species* PhD thesis, University of Leeds, (2006).

54 Clouthier, D. & Ramsay, D. The spectroscopy of formaldehyde and thioformaldehyde. *Annual Review of Physical Chemistry* **34**, 31-58 (1983).
55 Dieke, G. H. & Kistiakowsky, G. B. The Structure of the Ultraviolet Absorption Spectrum of Formaldehyde. I. *Physical Review* **45**, 4-28 (1934).
56 Dieke, G. H. & Kistiakowsky, G. B. The Rotational Structure of the Ultra-Violet Absorption Bands of Formaldehyde. *Proceedings of the National Academy of Sciences* **18**, 367-372 (1932).
57 Gravestock, T. J., Blitz, M. A., Bloss, W. J. & Heard, D. E. A Multidimensional Study of the Reaction $CH_2I + O_2$: Products and Atmospheric Implications. *ChemPhysChem* **11**, 3928-3941 (2010).
58 Stone, D., Blitz, M., Daubney, L., Howes, N. U. & Seakins, P. Kinetics of CH_2OO reactions with SO_2, NO_2, NO, H_2O and CH_3CHO as a function of pressure. *Phys Chem Chem Phys* **16**, 1139-1149 (2014).
59 Burkert, A., Grebner, D., Müller, D., Triebel, W. & König, J. Single-shot imaging of formaldehyde in hydrocarbon flames by XeF excimer laser-induced fluorescence. *Proceedings of the Combustion Institute* **28**, 1655-1661 (2000).
60 Hottle, J. R. *et al.* A laser induced fluorescence-based instrument for in-situ measurements of atmospheric formaldehyde. *Environmental science & technology* **43**, 790-795 (2008).
61 Pilling, M. J. & Seakins, P. W. *Reaction kinetics*. (Oxford University Press, 1995).
62 McGee, T. J. & McIlrath, T. J. Absolute OH absorption cross sections (for lidar measurements). *Journal of Quantitative Spectroscopy and Radiative Transfer* **32**, 179-184 (1984).
63 Marcelino, N., Cernicharo, J., Roueff, E., Gerin, M. & Mauersberger, R. Deuterated Thioformaldehyde in the Barnard 1 Cloud. *The Astrophysical Journal* **620**, 308 (2005).

Chapter 7. Experimental determination of the high pressure limiting rate coefficient at low temperatures via the proxy method

7.1 Background and previous proxy method studies

Chapters 3-5 of this thesis have reported and discussed the kinetics of reactions of hydroxyl radicals with neutral species at low temperatures. These reactions are found to be operating via a common mechanism, which initially proceeds by the barrierless formation of a weakly bound complex. This complex has three possible fates following formation: re-dissociation back to reactants, reaction forming bimolecular products (for example via tunnelling), or collisional stabilisation into the pre-barrier well. At the high pressure limit (corresponding to k^{∞}) of these reactions, the rate determining step will be the formation of the complex, k_a as shown in Figure 7. 1.

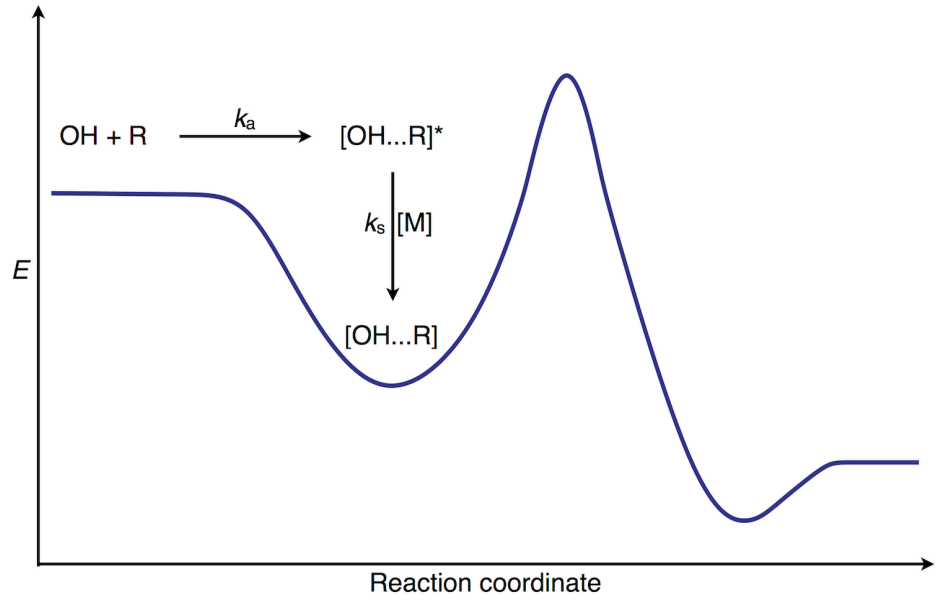

Figure 7. 1: Generic potential energy surface illustrating the microscopic processes involved in the reaction at the high pressure limit.

Obtaining the high pressure limiting rate coefficient of reactions featuring an association step is of importance to combustion and atmospheric chemistry, where reactions may be at or approaching this value. Whilst in the context of astrochemical environments it is largely the low pressure limiting rate coefficient of these type of reactions that will be relevant, the high pressure limiting rate coefficient is still an important parameter required to model these reactions via master equation calculations or by simple fitting of the

data to an extended Lindemann-Hinshelwood mechanism. Additionally, obtaining the high pressure limiting rate coefficient serves to demonstrate that the experimentally obtained rate coefficients are in the fall-off regime or low pressure limit. However, only a limited pressure range can be attained using the Laval apparatus and so, as evident from the pressure dependence studies presented in this thesis, the high pressure limiting rate coefficient may not always be obtained via conventional methods.

The proxy method, developed by Jaffer and Smith and by Quack and Troe, has been employed to obtain a lower limit to the high pressure limiting rate coefficients of some of the OH reactions studied in this work.[1,2] The theoretical basis for this method and the experimental implementation utilised here are discussed below.

If a reaction involves the formation of a complex, then providing there is no potential barrier along the path to its formation, the rate of formation of the complex is unlikely to depend on the initial vibrational states of the reactant species.[1] If there is a barrier to the formation of the complex, then vibrational excitation may enhance the rate of association.[3] Assuming that the complex is sufficiently long lived and the ergodicity principle applies (energy is randomised rapidly amongst the modes of the complex compared to reaction or redissociation), then if the complex redissociates to reactants, the reactant species will return in the vibrational ground state.[1,4] If the ergodic assumption holds, then the rate limiting step to vibrational relaxation is the formation of the complex, k_a, which is also the high pressure limiting rate coefficient, k^{∞} (see Figure 7. 1). Therefore, by producing and state selectively monitoring (via laser induced fluorescence for example) one of the reactants in a vibrationally excited state, the high pressure limiting rate coefficient can be obtained. Figure 7. 2 below illustrates the process described above for the reaction between OH and a co-reactant, R.

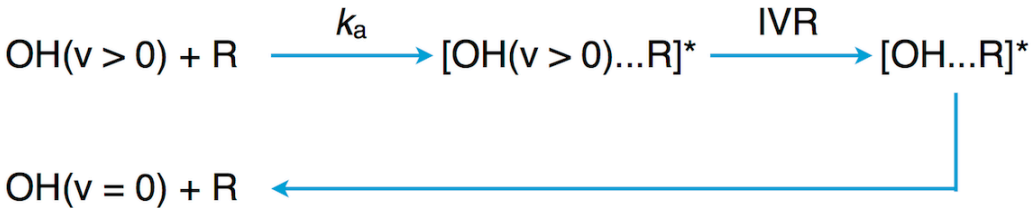

Figure 7. 2:Schematic demonstrating the principle of the proxy method for reactions of OH with R whereby a weakly bound complex is formed.

The proxy method predicts that due to the ergodicity assumption, during the lifetime of the complex, full intramolecular vibrational relaxation (IVR, as defined by Smith in the context of relaxation via the formation of a complex[5])

will occur throughout the modes of the weakly bound complex and so the rate coefficient obtained for k^{∞} should be independent of the initial vibrational state. Therefore, it would be predicted that the measured rate coefficients k(v=1)=k(v=2)=k(v=3) and so on. Whilst vibrational relaxation can occur through collisions, this process is relatively inefficient, hence fast relaxation of OH(v) will only occur through formation of the complex.

The proxy method has previously been implemented for several studies – primarily using LIF spectroscopy for the vibrational state selective monitoring of the radical reactant . A selection of these studies are summarised below. The pioneering study in this field was performed by Jaffer and Smith on the reactions of OH(v=1) with NO (R7.1) and NO_2 (R7.2) at 298 K.[1] Following the photolysis of HNO_3 in a flowtube reactor to yield OH(v=0), OH(v=1) was selectively formed via optical pumping, and subsequently monitored via LIF spectroscopy.

$$OH(v = 1) + NO \rightarrow OH(v = 0) + NO \qquad \text{R7.1}$$

$$OH(v = 1) + NO_2 \rightarrow OH(v = 0) + NO_2 \qquad \text{R7.2}$$

Good agreement was found between the OH(v=1) rate coefficients and the extrapolated high pressure limiting values obtained by Anastasi and Smith, suggesting that the reactions were indeed proceeding via a strongly bound complex facilitating redistribution of the vibrational energy.[6,7] Following this work, Smith and Williams studied the room temperature kinetics of OH(v=1) with HNO_3 and H_2O using the same experimental technique employed by Jaffer and Smith.[1,8] Fast deactivation rate coefficients on the order of 10^{-11} molecule^{-1} cm^3 s^{-1} were obtained for HNO_3 and H_2O, whereas the deactivation by Ar was found to have an upper limit of 10^{-15} molecule^{-1} cm^3 s^{-1}, providing further evidence for vibrational relaxation being promoted by the formation of a collision complex.[8]

Low temperature proxy method studies have also been performed by the group of Sims and Smith using a CRESU apparatus coupled to PLP-LIF, for example, for the reactions of CH(v=1).[9]

$$CH(v = 1) + CO \rightarrow CH(v = 0) + CO \qquad \text{R7.3}$$

$$CH(v = 1) + N_2 \rightarrow CH(v = 0) + N_2 \qquad \text{R7.4}$$

Herbert *et al.* studied the rate coefficients of CH(v=1) with CO and N_2 down to 23 K and observed a slight negative temperature dependence with room temperature values of 9 × 10^{-11} molecule^{-1} cm^3 s^{-1} for R7.3 and 3 × 10^{-11} molecule^{-1} cm^3 s^{-1} for R7.4.[9] At 584 K, the rate coefficient for reaction with N_2

(R7.4) was found to be notably slower than for the CO reaction (R7.3), suggesting that the HCN_2 complex has a lifetime that is too short for full energy redistribution from the high frequency C-H vibration to the low frequency modes of the complex to occur. Therefore on redissociation of the complex, some of the CH reactant is returned in its v=1 vibrational state. However, the values obtained above 300 K were found to be in reasonable agreement with the high pressure limiting values obtained by Fulle and Hipler for the same reaction by conventional pressure dependence studies in helium bath gas.[9-11] On consideration of these results, Smith commented that when the binding energy of the complex is less than ~ 10RT, the timescale for vibrational relaxation amongst the modes of the complex becomes comparable to the lifetime of the complex, and therefore full relaxation may not occur during the complex lifetime.[5] Therefore, for a given complex binding energy, at lower temperatures, full IVR is more likely to occur due to the extended lifetime of the complex. This is supported by the work of McCabe *et al.* on the reaction of OH(v=1) + HNO_3, who concluded that IVR was on a similar timescale as the rate of redissociation of the complex.[12]

Brownsword *et al.* performed studies of the reactions of CH(v=1) with H_2 and D_2 between 13-295 K using the same experimental methods as Herbert *et al.*[9,13] No dependence on pressure and a mild negative temperature dependence was observed, providing evidence for the formation of the complex via a purely attractive potential to form the CH_3* complex.[13] The high pressure limiting rate coefficient obtained for CH + H_2 at 295 K was found to be in good agreement with the value measured by Berman and Lin through pressure dependence studies.[14]

Not all of the existing experimental studies performed are supportive of the proxy method hypothesis whereby full vibrational relaxation via complex formation is assumed to be fast. Silvente *et al.* have performed extensive studies on the reactions of OH in several vibrationally excited states at room temperature.[4] The reactions of H_2O and CH_4 with OH (v=1,2,3) and NH_3,CS_2, $(CH_3)_2S$, CH_3SH and CH_3Br with OH (v=1,2) have been studied by using laser induced fluorescence spectroscopy of OH, where OH(v) is produced from the reaction of $O(^1D)$ with the co-reactant.[4] It was found that the deactivation rate coefficients were enhanced with increasing quanta of vibrational excitation of OH. This is inconsistent with the theoretical basis of the proxy method. A cascading effect whereby vibrational relaxation of the

hydroxyl radical occurred at single-quantum changes was observed, which is consistent with SSH theory which will be discussed below.[15]

A cascade mechanism (characterised by early time growth in the OH(v) kinetic traces) was also observed by McKee *et al*. in the study of OH(v=1,2) + C_2H_2, whereby OH(v≤4) was produced from the $O(^1D)$ + H_2 reaction and subsequently probed via LIF spectroscopy.[3] Earlier studies by Glass *et al.* examined the reactions of vibrationally excited OH with H_2O, HCl, D_2, CH_4,NH_3, HBr, O and CO.[16,17] The reactions of O with HBr and H with NO_2 were utilised to produce OH in vibrational states up to v=1 and v=3 respectively, and OH(v) was subsequently state selectively monitored by EPR (electron paramagnetic resonance) spectroscopy.[16-18] A dependence of the deactivation rate on the initial vibrational state was observed, with the deactivation rate increasing with increasing vibrational quanta. It was also noted that vibrational relaxation was most favourable where ΔE was smallest between the initial and final vibrational states of both OH and the co-reactant. Both of these observations are supportive of SSH type theory.[15]

7.1.1 SSH theory of vibrational energy transfer

Schwartz, Slawsky and Herzfeld (SSH) theory, initially developed in 1952, is a quantum mechanical theory used to treat vibrational energy transfer, where collisions are treated as de Broglie waves.[15,19] The intermolecular potential used for SSH theory is described by E7.1, where *r* is the intermolecular distance, *ϵ* is the attractive potential energy between the molecules and *α* is an experimentally derived Lennard-Jones parameter, the values of which is fitted to E7.1.

$$V(r) = Uexp(-\alpha r) - \epsilon \qquad \text{E7.1}$$

The original equation used to calculate the probability of transfer between sets of vibrational energy levels developed by Schwartz, Slawsky and Herzfeld is complicated, and has been simplified by Tancos to give two limiting cases based on the parameter ΔE.[19,20] For V-V (vibration-vibration) transfer, between two molecules, denoted ‘a’ and ‘b’, from vibrational levels *i* to *j* and *k* to *l* respectively. ΔE is the energy distributed to translational energy and is the difference between the energies of the initial and final vibrational states (E7.2) of both a and b.

$$\Delta E = hv_a(i-j) + hv_b(k-l) \qquad \text{E7.2}$$

For V-T transfer, where only molecule a undergoes a change in vibrational level, ΔE is described by E7.3.

$$\Delta E = h\nu_a(i-j) \qquad \text{E7.3}$$

where ν is the frequency of a given vibrational mode. When ΔE is large (> 200 cm^{-1}) the probability of energy of transfer between the levels is described by E7.4. When ΔE ≤ 50 cm^{-1}, the frequencies are considered to act as if resonant and the probability of transfer is described by E7.5.[19,20]

$$P_{k-l(b)}^{i-j(a)} = P_o(a)P_o(b)\left(\frac{r_c}{\sigma}\right)^2\left[V^{ij}(a)\right]^2[V^{kl}(b)]^2\,8\left(\frac{\pi}{3}\right)^{0.5} \qquad \text{E7.4}$$
$$\times\left[\frac{8\pi^3\mu\Delta E}{\alpha^2h^2}\right]^2\left(\frac{\Delta E^2\mu\pi^2}{2\alpha^2\hbar^2k_BT}\right)^{\frac{1}{6}}$$
$$\times exp\left[-\left(\frac{3\Delta E^2\mu\pi^2}{2\alpha^2\hbar^2k_BT}\right)+\frac{\epsilon}{k_BT}+\frac{\Delta E}{2k_BT}\right]$$

$$P_{k-l(b)}^{i-j(a)} = P_o(a)P_o(b)\left[V^{i-j}(a).V^{k-l}(b)\right]^2.\frac{64\pi^2\mu k_BT}{\alpha^2h^2}exp\left[\frac{-\epsilon}{k_BT}\right] \qquad \text{E7.5}$$

The parameters used in E7.4 and E7.5 are as follows: P_0 are the steric factors which account for the efficiency of different collision orientations. The vibrational factor, $[V^{ij}(a)]^2$, indicates the coupling between states *i* and *j*, and is described below for transitions of different vibrational quanta. k_B, μ ,T and h are the Boltzmann constant, reduced mass of colliding species, temperature and Plancks constant respectively. r_c is the turning point of the intermolecular potential described in E7.1 and σ is a Lennard-Jones parameter also derived from experimental data.

The expression for the vibrational factors, $[V^{ij}(a)]^2$, is dependent on the change in vibrational quanta. The expressions for quanta changes of 0,1 and 2 are given in E7.6-E7.8 accordingly.

$$\left[V^{i-i}\right]^2 = 1 \qquad \text{E7.6}$$

$$\left[V^{(i+1)-i}\right]^2 = \left[V^{i-(i+1)}\right]^2 = \alpha^2(\overline{A^2})(i+1)/2(4\pi^2v/h) \qquad \text{E7.7}$$

$$\left[V^{(i+2)-i}\right]^2 = \left[V^{i-(i+2)}\right]^2 = \alpha^4(\overline{A^4})(i+1)(i+2)/16(4\pi^2v/h)^2 \qquad \text{E7.8}$$

where $(\bar{A}^2)$ is the vibrational amplitude coefficient which is the displacement of an atom from the normal co-ordinate for a given vibration. From E7.6-E7.8, it can be seen that the value of the vibrational factor decreases with increased quanta jumps, and so SSH theory predicts that for V-V transfer, single quanta jumps are most probable. The probability of transitions

between the vibrational levels has an inverse dependence on ΔE, as shown in E7.4, and so IVR will be more effective between modes with similar vibrational frequencies.

E7.5 describes the probability of transfer between resonant states and so does not have a ΔE parameter. Resonant transfer is predicted to be much faster than the non-resonant case. Therefore IVR involving resonant modes is more likely to approximate the proxy method so that the rate coefficient becomes independent of the quanta of vibrational excitation, as IVR is assumed to be fast with respect to the rate of dissociation of the complex.[19] However, there is an inverse dependence on the frequency of the vibrational level, which comes from the vibrational factor (E7.6-7.8). As the frequency of the mode which vibrational energy is to be transferred from increases, the vibrational factor decreases. Thus for resonant transfer, transition between low frequency modes will have the highest probability.[19]

For a set of one quanta vibrational deactivations, for example OH(v=3→2), OH(v=2→1) and OH(v=1→0), a first approximation of the relative rate coefficients of these processes can be obtained from E7.7, as $[V^{(i+1)-i}]^2$ is proportional to (i+1)/2. Ratios of k(v=3)=1.5k(v=2)=3k(v=1) are predicted, which is in contrast to the k(v=3)=k(v=2)=k(v=1) ratios predicted by the proxy method. What is evident from this is that the limiting step in the mechanism for OH(v) + R according to the proxy methodology is the formation of the complex. In SSH theory, given that the rate coefficient for vibrational relaxation increases with increasing vibrational excitation, it may be the rate coefficient for vibrational relaxation that is the limiting step. Therefore, if the rate coefficients are observed to increase with increasing vibrational excitation, the rate coefficient obtained at the highest vibrational excitation is the lower limit to the association rate coefficient and hence k^{∞}.

The probability of transition (E7.4, E7.5) exhibits a dependence on the reduced mass of the species (a and b) between which energy transfer occurs, and so the probability of energy transfer will increase for larger species. Therefore, for increasingly large species, it is anticipated that the obtained rate coefficients for OH(v) + R via the proxy method will tend more towards the high pressure limiting rate coefficient for the OH + R reaction as IVR within the weakly bound complex is no longer rate limiting.

The proxy method has been implemented for the first time for OH reactions at low temperatures by Shannon.[21] Shannon studied the reactions of OH(v=1,2,3) with acetone, dimethyl ether and acetylene at 93 K, and with methanol at 93 K and 63 K, using $O(^1D)$ + H_2 as a precursor of vibrationally

excited OH radicals. Shannon found that the obtained rate coefficients exhibited a positive dependence on the vibrational excitation of OH. However, the ratios of the rate coefficients for the reaction of OH in different quanta of vibrational excitation (in other words k(v=1)/k(v=3)) did not adhere to the ratios predicted by SSH theory for any of the reactions studied.[15,19,21] Two overall trends were observed by Shannon: as the temperature was decreased, and as the co-reagent size was increased, the values of k(v=1) and k(v=3) converged. This is rationalised by the extended lifetime of the complex between OH and the co-reactant, therefore enhancing the probability of full vibrational relaxation amongst the modes of the complex.[21]

Higher temperature proxy method studies have mostly been conducted for reactions where the complex is relatively strongly bound (≤ 45 kJ mol^{-1}) as the longer the lifetime of the complex, the more likely that vibrational relaxation will be competitive with the redissociation of the complex.[5] Shannon obtained the lifetime of some OH-R complexes with respect to redissociation using master equation calculations. For the OH-methanol complex (binding energy of 20-24 kJ mol^{-1}) the 93 K lifetime is enhanced by over 5 orders of magnitude compared to room temperature with a lifetime of ~ 2 × 10^{-7} s at 93 K.[21-23] For the OH-DME complex (binding energy of ~ 29.8 kJ mol^{-1}) , the lifetime is enhanced by over 6 orders of magnitude with a 93 K lifetime of ~ 1 × 10^{-4} s.[21,24,25] The lifetime of the OH-acetone complex (binding energy ~ 18.4-22.2 kJ mol^{-1}) is enhanced by nearly 7 orders of magnitude with ~1 × 10^{-3} s lifetime at 93 K.[21,25-27] Whilst it is anticipated that the lifetime of the complex will be significantly shorter for complexes where the hydroxyl radical is vibrationally excited, owing to the additional energy the vibrational excitation brings, the significant enhancement of the lifetimes at low temperatures for these weakly bound complexes illustrates that despite the complexes having only a relatively small binding energy, they have a significant lifetime compared to the vibrational period of the OH stretch (~3828 cm^{-1} according to the calculations of Xu and Lin,[23] giving a period of ~ 1 × 10^{-14} s). Hence IVR throughout the modes of the weakly bound complex should be competitive with the redissociation of the complex for low temperature reactions where complexes of this nature are formed.[23] Prior to the work of Shannon, Smith commented that for vibrational relaxation to compete with redissociation of a weakly bound complex, the complex should have a lifetime sufficient that it will survive many vibrational periods, and this may only be achieved at very low temperatures.[5] However, Smith also added that if vibrational relaxation occurs at one quanta steps, in other words via a SSH mechanism, then the complex lifetime may not be

sufficient to allow full vibrational relaxation due to the enhanced internal energy of the complex, and therefore only partial vibrational relaxation may be observed.[5]

In this work, the kinetics of OH(v=1,2,3) with ethanol and propan-2-ol at 89 K, OH(v=1) with methanol at 88 K, and OH(v=1) with ammonia at 56 K have been studied.

$$OH(v>0) + CH_3CH_2OH \xrightarrow{k_{7.6}} OH(v=0) + CH_3CH_2OH \quad \text{R7.6}$$

$$OH(v>0) + CH_3CH(OH)CH_3 \xrightarrow{k_{7.7}} OH(v=0) + CH_3CH(OH)CH_3 \quad \text{R7.7}$$

$$OH(v>0) + CH_3OH \xrightarrow{k_{7.8}} OH(v=0) + CH_3OH \quad \text{R7.8}$$

$$OH(v>0) + NH_3 \xrightarrow{k_{7.9}} OH(v=0) + NH_3 \quad \text{R7.9}$$

Given the enhanced lifetimes of comparable complexes calculated by Shannon and the comments by Smith, it is anticipated that at least partial vibrational relaxation will occur and so a lower limit to the high pressure limit may be obtained.

7.1.2 Data fitting

Prior to presenting the experimental methods utilised for this work, the rationale behind the data fitting method will first be discussed in light of previous experimental observations, The cascade effect observed by McKee *et al.*,[3] Silvente *et al*.[4] and Shannon[21] leads to complications in data fitting. To fully account for the energy transfer processes involved, including reaction of the complex to yield bimolecular products, requires a multi-exponential fitting equation to be deduced. Considering only one quanta changes, Shannon and Silvente *et al*. utilised the integrated solution to E7.9 for fitting.[4,21] Note that the rate coefficients given below are pseudo first order, as the co-reactant is assumed to be in great excess of OH(v).

$$\frac{d[OH(v=i)]}{dt} = k_w'[OH(v=i+1)] + \phi k_x'[O(^1D)] - \left(k_y' + k_z'\right)[OH(v=i)] - k_{loss}[OH(v=i)] \quad \text{E7.9}$$

The parameters of E7.9 are as follows: k_w' is the pseudo first order rate coefficient for vibrational relaxation from OH(v=i+1) to the level of interest (bimolecular reaction is R7.10).

$$OH(v=i+1) + R \xrightarrow{k_w} OH(v=i) + R \quad \text{R7.10}$$

k_x' is the pseudo first order rate coefficient for the initial formation of OH into the level of interest from the reaction of $O(^1D)$ with H_2 (which in excess of $O(^1D)$), with yield ϕ (bimolecular reaction is R7.11).

$$O(^1D) + H_2 \xrightarrow{k_x} \phi OH\ (v = i) + H \qquad \text{R7.11}$$

k_y' is the pseudo first order rate coefficient for the relaxation of OH(v=i) to the level below (bimolecular reaction is R7.12).

$$OH(v = i) + R \xrightarrow{k_y} OH(v = i - 1) + R \qquad \text{R7.12}$$

k_z' is the pseudo first order rate coefficient for loss of OH(v=i) via reaction with the co-reagent following the formation of the complex to yield bimolecular products.

$$OH(v = i) + R \xrightarrow{k_z} products \qquad \text{R7.13}$$

k_{loss} is the rate coefficient for the diffusional loss of OH(v=i) (R7.14)

$$OH(v = i) \xrightarrow{k_{loss}} loss \qquad \text{R7.14}$$

The integrated solution to the differential equation can be seen in the work of Silvente *et al*. or Shannon.[4,21]

To obtain a rigorous fit of this equation to the data requires the measurement of rate coefficients for all of vibrational redistribution processes accounted for. For the reaction of $O(^1D)$ + H_2, utilised by Shannon to produce OH(v), OH can be produced in vibrationally excited states up to v=4.[21,28] To obtain a robust fit to the data would require measurement of the vibrational deactivation of OH(v=4), and then utilising that value in the fitting of the OH(v=3) data and so on and so forth. Furthermore, whilst SSH theory states that vibrational energy transfer by one quanta is most probable (as shown in E7.6-E7.8), there is also the possibility of multiple quanta energy jumps which is not accounted for in this fitting equation.[15]

Given that SSH theory predicts faster relaxation of higher vibrational levels, if a cascade mechanism is operating, it will be predominantly the early time data of lower vibrational levels that is perturbed by growth from the relaxation of higher levels.[3,15,21] Attempting to fit a single-exponential decay trace to the full temporal profile of OH(v) would retrieve a rate coefficient that is lower than the true value.[3] However, by fitting the data with a single-exponential decay trace from sufficiently long delay times, the decay component is no longer significantly perturbed by the cascade of higher vibrational levels into the probed vibrational level.

$$[OH(v = i)] = [OH(v = i)]_0 \exp(-k_{obs}t) \qquad \text{E7.10}$$

where

$$k_{obs} = (k_y{}' + k_z{}') + k_{loss} = (k_y + k_z)[R] + k_{loss} \qquad \text{E7.11}$$

k_y is the rate coefficient for the relaxation of OH(v=i) to the level below (R7.12), k_z is the rate coefficient for loss of OH(v=i) via bimolecular reaction with the co-reagent (R7.13), and k_{loss} is the diffusional loss of OH(v=i) (R7.14).

To deduce the robustness of the values obtained from the fit of the integrated solution of E7.9 to the temporal profile of OH(v), Shannon also fitted E7.10 to the data from 75 μs onwards. Agreement between the two fitting equations within the errors of the retrieved values was seen by Shannon, demonstrating that that fitting an exponential loss equation at long times is satisfactory. Additionally, this supported by the work of McKee *et al*. who utilised E7.10 to fit to their OH(v=2) and OH(v=1) data from the reaction of OH(v) with acetylene, and through modelling, demonstrated that the fitted traces were not significantly perturbed by the cascade of higher levels, with a maximum of ~ 10 % effect.[3,29] Silvente *et al.* reported that this fitting method would perturb the retrieved rate coefficient by a maximum of ~ 5 %.[3,4,29]

7.1.3 Reaction versus relaxation

From the fitting of the data, the loss components of OH(v) from vibrational relaxation (k_y) or reaction (k_z) to yield bimolecular products following the formation of the complex cannot easily be resolved. For the purpose of obtaining the rate coefficients for IVR, this presents some complications and so the experiments at 89 K have been performed at the highest possible gas density to promote the stabilisation of the complex rather than the bimolecular reaction. With regards to obtaining the high pressure limiting rate coefficient, the inability to disentangle the rate coefficients for relaxation (k_y) and reaction (k_z) is effectively irrelevant ,as these processes both proceed via the initial formation of the complex (k_a) at low temperatures, and it is the rate coefficient for the formation of the complex which is the high pressure limiting rate coefficient (k^{∞}).

7.1.4 Enhancement of reaction by provision of vibrational energy

Since the publication of the Polanyi rules in 1972, there has been a great deal of research into mode selectivity and promoting a reaction pathway by the provision of vibrational energy into a particular mode of a reactant.[30] Whilst a discussion of the large body of work conducted in this field is beyond the scope of this thesis, there are a number of reviews including those by Crim and by Zare.[31-33] The challenge in mode selectivity is that IVR is often fast so the excess vibrational energy provided to a particular bond can be redistributed amongst the modes of the molecule or complex. Where mode selectivity has been successful, the vibrational modes of the molecule are uncoupled due to sufficiently different vibrational frequencies, and so IVR is uncompetitive. An example of this is the H + HOD reaction, where the O-H stretch is selectively vibrationally excited to promote the breaking of the O-H bond.[33,34] It might be suggested that vibrational excitation of the hydroxyl radical may enhance the bimolecular reaction, but this excess energy is in the incorrect mode to do so as the O-H vibration is orthogonal to the reaction coordinate.

The co-reactants of OH(v) contain either OH bonds or NH bonds, both of which have vibrational frequencies close enough to be coupled to the hydroxyl radical vibration, and so the probability IVR should be increased.[23,35] However, the provision of additional energy to the reactants may also pose the problem to whether the reaction rate coefficient is enhanced simply by having sufficient energy to transcend the relatively low barriers to reaction (maximum ~ 13 kJ mol^{-1}). McKee *et al*. discussed the possibility of vibrational excitation enhancing the bimolecular H-abstraction rate coefficient for the reaction of OH(v=1,2) with acetylene.[3] The minimum energy pathway for the reaction of OH with acetylene features a deep well (131 kJ mol^{-1}) corresponding to the stabilisation of the OH-acetylene complex, proceeded by a barrier to H-abstraction (59 kJ mol^{-1}).[3] The internal energy of OH(v=1) is not sufficient to overcome this barrier, but the energy of OH(v=2) lies 24 kJ mol^{-1} above the barrier.[3,29] The OH bond is a spectator of the reaction and the rate coefficients for both the OH(v=1) and OH(v=2) + acetylene reactions were found to exhibit the same temperature dependence, thus it was concluded by the authors that the excess energy from OH(v=2) did not enhance the rate coefficient. McKee *et al.* state that for this vibrational excitation to enhance the reaction, the excess energy must not be distributed amongst the modes of the complex (HOC_2H_2) and so for this to occur IVR must be slow, which the authors concluded unlikely.[3]

In the systems studied in this work, the vibrational energy of OH(v=1,2 and 3) are all sufficient to transcend the relatively low barriers to reaction and so such comparisons cannot be made. However, the experiments are carried out so that the other reactant species and bath gas are in great excess of the OH(v). OH is produced with a concentration on the order of ~ 10^{11} molecule cm^{-3} in a total gas density jet of 1.1×10^{17} molecule cm^{-3}. Using the concentration of OH, the relative energies of OH(v) in all the vibrational states (1,2,3 and 4) and the vibrational distributions from the reaction of $O(^1D) + H_2$, the total excess energy of the system can be calculated.[28] If it is assumed that the vibrational energy can be distributed to all species (including the bath gas, N_2), then the total additional energy transferred to each molecule is on the order of 0.09 J, which in terms of temperature is ~ 0.01 K. Therefore, vibrational excitation of the O-H stretch of the hydroxyl radical will not enhance the reaction rate coefficient by thermal means. In the case of the ammonia reaction where OH(v) is produced up to v=3, assuming that the excess vibrational energy cannot be transferred to rotational modes or translational energy of the bath gas (for example, when the bath gas is Ar, which has no vibrational or rotational degrees of freedom) then the maximum change in temperature would be ~ 7 K. The work presented in this thesis has demonstrated at low temperatures, the rate coefficient for the OH + R reactions exhibit an inverse temperature dependence and therefore, if the temperature was raised by 7 K, this would only serve to reduce, rather than enhance, the rate coefficient.

7.2 Experimental procedure

The general experimental procedure for kinetic studies is outlined in Chapter 2 and so only a brief description is given here. The vapour pressure of the reactant (ethanol (Sigma Aldrich ≥ 99.8 %), propanol-2-ol (Fischer scientific > 99.5 %), methanol (Sigma-Aldrich ≥ 99.9 %) or ammonia (BOC 99.8 %)) was admitted to an evacuated cylinder and diluted with the bath gas (nitrogen (BOC, OFN) or argon (BOC, 99.8 %)) then allowed to mix overnight. Vibrationally excited OH was formed via the 248 nm photolysis of ozone in the presence of hydrogen, or just in the presence of ammonia for the OH(v>0) + ammonia reaction. Ozone was produced from the electrical discharge of O_2 (BOC, 99.999 %) using an ozone generator (Fischer technology, OZ 500). The O_2/O_3 mixture was admitted into an evacuated cylinder where it was diluted with the bath gas (nitrogen or argon as before). After a mixing period, the O_3/O_2/bath gas mixture, H_2 from the cylinder

(BOC) (with the exception of the ammonia reaction) and the alcohol/bath gas mixture were flowed through calibrated mass flow controllers into a stainless steel 2 L ballast tank where the reagent gases were allowed to mix. The gas mixture was expanded through the Laval nozzle via two pulsed solenoid (Parker series 9) valves at a rate of 5 Hz with ~ 20 ms pulse duration. For the 89 K experiments, the total flow rate of the gases was chosen to produce the highest density stable expansion (1.06×10^{17} molecule cm^{-3}) so that the direct bimolecular channel will be less competitive. The vibrationally excited OH was formed from the pulsed laser photolysis of ozone via a 248 nm excimer laser (Lambda-Physik LPX) along the axis of the jet and the subsequent reaction of the photolytically produced $O(^1D)$ atoms with molecular hydrogen or ammonia.

$$O_3 \xrightarrow{248\,nm} O(^1D) + O_2 \qquad \text{P7.1}$$

$$O(^1D) + H_2 \longrightarrow OH\ (v > 0) + H \qquad \text{R7.10}$$

$$O(^1D) + NH_3 \longrightarrow OH\ (v > 0) + NH_2 \qquad \text{R7.11}$$

Aker and Sloan have demonstrated that R7.10 yields OH in vibrational states of v=4,3,2 and 1, with ratios of 13:25:32:29.[28] Cheskis *et al*. have determined that from R7.11, OH is produced in vibrational states v=3,2,1 and 0 with ratios 0.14:0.34:0.32:0.20.[36] However Silvente *et al.* have shown that ammonia is a very efficient deactivator of vibrationally excited OH and IVR is rapid at 298 K (on the order of 10^{-10} molecule^{-1} cm^3 s^{-1}), therefore the cascade effect may be less pronounced for the OH + ammonia reaction.[4] For the OH + ammonia reaction, rate coefficients were obtained only for OH(v=1) as higher vibrational levels of OH could not be easily observed from R7.11.

Experiments were performed under pseudo first order conditions, so that [R]>>[OH]. The relative OH concentration in a given vibrational state was monitored via LIF spectroscopy using a Nd:YAG (Litron LPY 664-10) pumped dye laser (Sirah Gmbh Cobra stretch) tuned to a wavelength resonant with a transition of a specific vibrational state of OH. For v=2 and v=3, the $P_1(1.5)$ rotational transition of the Δv=-1 vibronic band, as employed by Silvente *et al.*, was utilised using the frequency doubled output of the laser using Pyridine dye .[4] For the v=1 work, the $Q_{21}(1.5)$ Δv=1 rovibronic transition was utilised for a matter of experimental convenience, as this excitation wavelength could be readily obtained with the laser dye (Rhodamine-6G) utilised for the v=0 kinetic studies, and the frequency doubled output of the Pyridine dye is poor at the wavelength corresponding

to Δv=-1 for v=1. The transitions and corresponding excitation wavelengths used for this work are summarised in Table 7. 1 and example LIF spectra with the rotational transitions utilised for the v=2 and v=3 kinetics are shown in Figure 7. 3 and Figure 7. 4, respectively.

Table 7. 1:Summary of laser induced fluorescence transitions and excitation wavelengths utilised in this work.

OH(v)	Transition	Excitation wavelength/ nm
1	$A^2\Sigma \leftarrow X^2\Pi$ (2,1)	~287.7
2	$A^2\Sigma \leftarrow X^2\Pi$ (1,2)	~350.9
3	$A^2\Sigma \leftarrow X^2\Pi$ (2,3)	~356.8

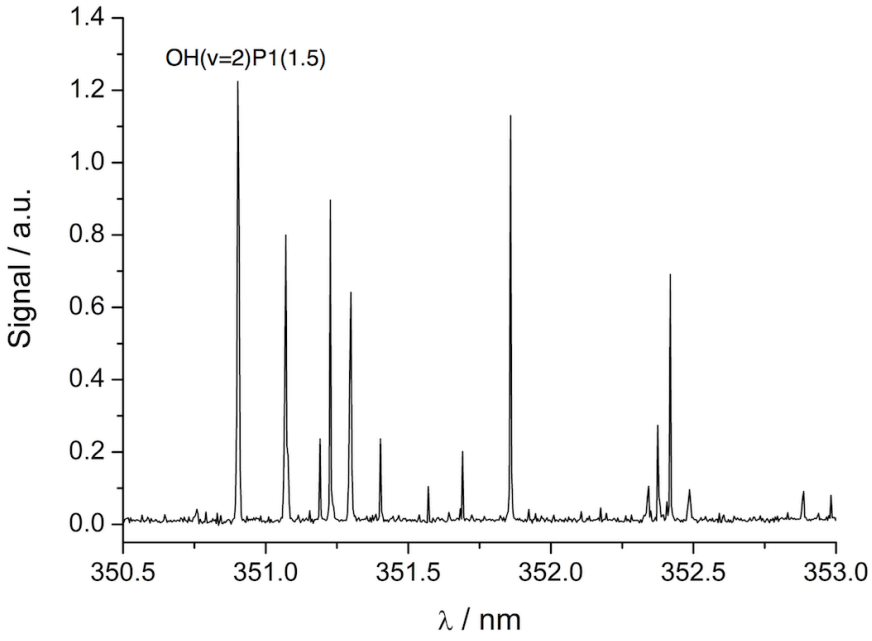

Figure 7. 3: Laser excitation spectrum of OH(v=2) formed from the reaction of $O(^1D)$ + H_2 following 248 nm photolysis of O_3 with 280 mJ pulse energy. Recorded at T = 88 ± 4 K and a total gas density of (1.1 ± 0.1) × 10^{17} molecule cm^{-3}. The assigned rotational transition is the line utilised for kinetic studies in this work.

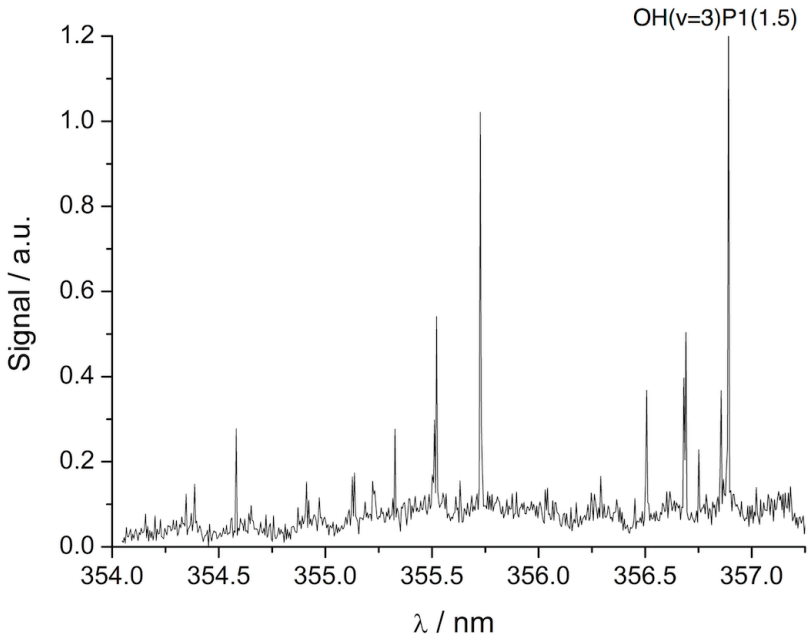

Figure 7. 4: Laser excitation spectrum of OH(v=3) formed from the reaction of $O(^1D)$ + H_2 following 248 nm photolysis of O_3 with 280 mJ pulse energy. Recorded at T = 88 ± 4 K and a total gas density of (1.1 ± 0.1) × 10^{17} molecule cm^{-3}. The assigned rotational transition is the line utilised for kinetic studies in this work.

Following excitation, the off-resonance fluorescence (~ 308 nm via the (0,0) transition or ~312 nm via the (1,1) transition) was monitored using a PMT (Thorn EMI 9813QB) fitted with an interference filter (Barr Associates λ_{max} = 308.5 nm , 5 nm FWHM for v=1 and Barr Associates λ_{max} = 309.0 nm , 8 nm FWHM for v =2,3). By varying the co-reagent concentration, several pseudo first order decay rate coefficients were obtained and the bimolecular rate coefficient for a given vibrationally excited state of OH deduced by the gradient of a plot of k_{obs} versus the co-reactant concentration.

$$k_{obs} = (k_{7.6} + k_z)[CH_3CH_2OH] + k_{loss} \quad \text{E7.12}$$

$$k_{obs} = (k_{7.7} + k_z)[CH_3CH(OH)CH_3] + k_{loss} \quad \text{E7.13}$$

$$k_{obs} = (k_{7.8} + k_z)[CH_3OH] + k_{loss} \quad \text{E7.14}$$

$$k_{obs} = (k_{7.9} + k_z)[NH_3] + k_{loss} \quad \text{E7.15}$$

7.3 Results and discussion

Examples of the temporal evolution of the OH(v=1), OH(v=2) and OH(v=3) LIF signals following production from the reaction of $O(^1D)$ with H_2 (R7.10) or NH_3 (R7.11) in the presence of a co-reagent are shown in Figures 5-8. Fitting of the pseudo first order traces was attempted using the multi-exponential solution to E7.9, however, given that rate coefficients for the

$O(^1D) + H_2$ (or $O(^1D) + NH_3$) reaction and for the vibrational relaxation of OH(v=4) were unknown, and following on from the work of Shannon and McKee *et al*., the single exponential loss function (E7.10) to the data at later times was instead utilised.[3,21] To minimise the effect of the cascade mechanism on the obtained value of k_{obs}, the data were fitted from sequentially long delay times until the retrieved rate coefficient was found not to increase further. This method was also utilised by McKee *et al*. and in this work it was found that the data could be fitted with E7.10 from 80 μs onwards for all vibrational levels for OH(v) + methanol, ethanol and propanol and from 50 μs onwards for OH(v=1) + ammonia. Bimolecular plots for each reaction at each vibrational level, constructed from k_{obs} versus co-reagent concentration, are shown in Figures 5-8. For the OH(v=1) + ammonia reaction, it was not possible to measure the loss rate coefficient of OH(v=1) in the absence of ammonia due to the method of production of OH(v=1). Given that the intercepts obtained in the bimolecular plots for OH(v=1) + R of the other reactions yielded intercepts within error of the OH(v=0) bimolecular plot intercepts obtained at the same temperature and density conditions, the intercept obtained from the OH(v=0) + ammonia bimolecular plot obtained under the same jet conditions was utilised.

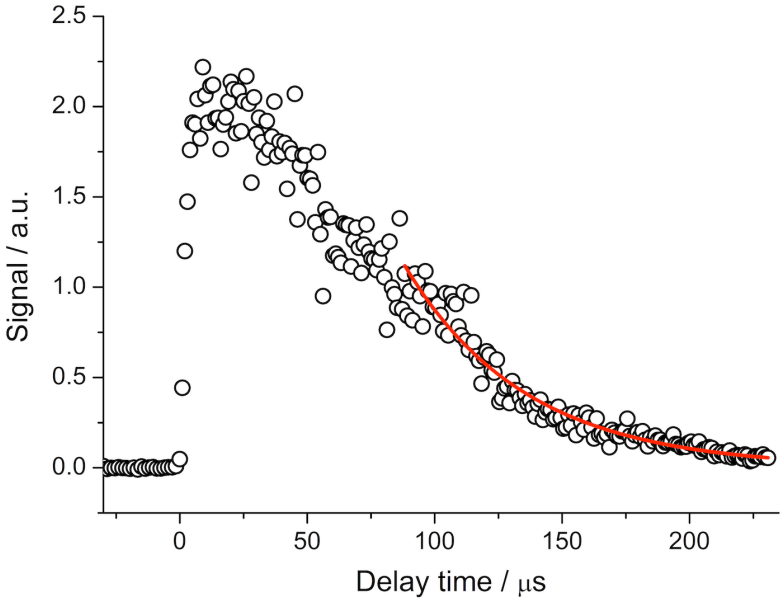

Figure 7. 5: Pseudo first order LIF trace of OH(v=1) together with the non linear least squares fit of E7.9 to the data (from t = 80 μs onwards) from the reaction of $O(^1D) + H_2$ in the presence of methanol (1.08×10^{14} molecule cm^{-3}) at 88 ± 4 K and a total gas density of (1.1 ± 0.1) × 10^{17} molecule cm^{-3}. The least squares fit of E7.10 to the data yields a pseudo first order rate coefficient of 21050 ± 586 s^{-1}.

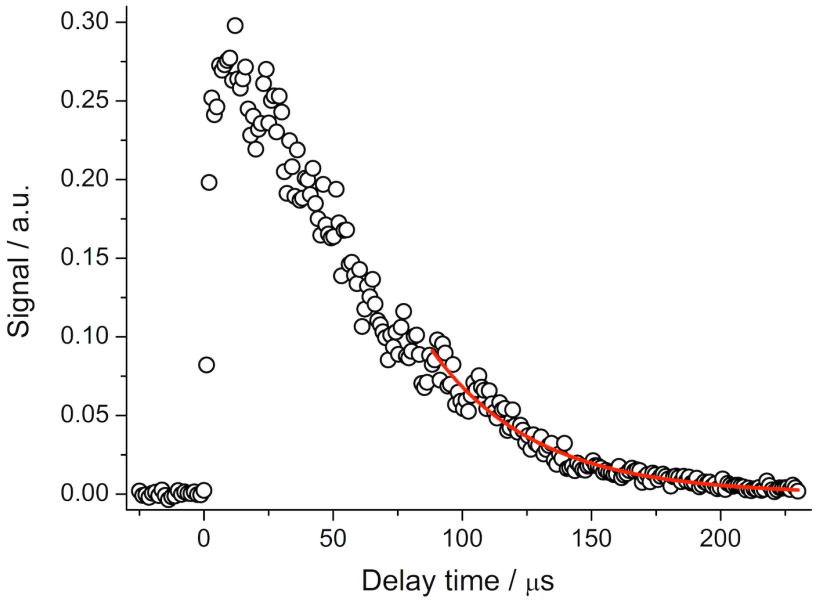

Figure 7. 6: Pseudo first order LIF trace of OH(v=2) together with the non linear least squares fit of E7.9 to the data (from t = 80 μs onwards) from the reaction of $O(^1D) + H_2$ in the presence of ethanol (6.13×10^{13} molecule cm^{-3}) at 88 ± 4 K and a total gas density of $(1.1 \pm 1) \times 10^{17}$ molecule cm^{-3}. The least squares fit of E7.10 to the data yields a pseudo first order rate coefficient of 24931 ± 662 s^{-1}.

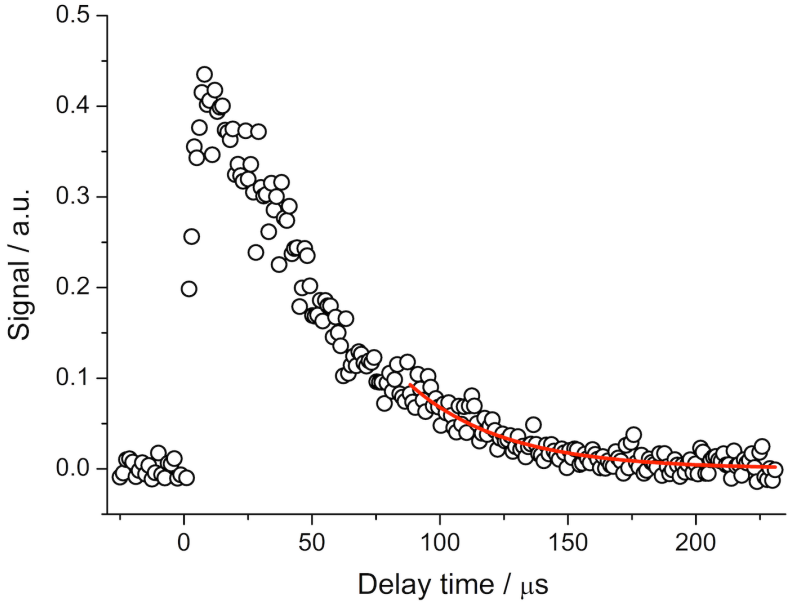

Figure 7. 7: Pseudo first order LIF trace of OH(v=3) together with the non linear least squares fit of E7.9 to the data (from t = 80 μs onwards) from the reaction of $O(^1D) + H_2$ in the presence of propanol (3.95×10^{13} molecule cm^{-3}) at 88 ± 4 K and a total gas density of (1.1 ± 1) × 10^{17} molecule cm^{-3}. The least squares fit of E7.10 to the data yields a pseudo first order rate coefficient of 27024 ± 1493 s^{-1}.

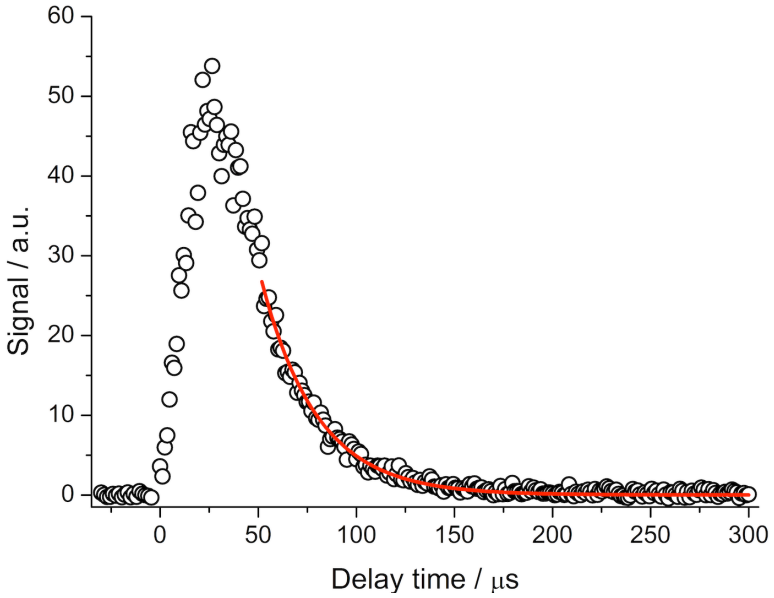

Figure 7. 8: Pseudo first order LIF trace of OH(v=1) together with the non linear least squares fit of E7.9 to the data (from t = 50 μs onwards) from the reaction of $O(^1D)$ + NH_3 (2.31×10^{14} molecule cm^{-3}) at 56 ± 4 K and a total gas density of (4.4 ± 0.5) × 10^{16} molecule cm^{-3}. The least squares fit of E7.10 to the data yields a pseudo first order rate coefficient of 35189 ± 518 s^{-1}.

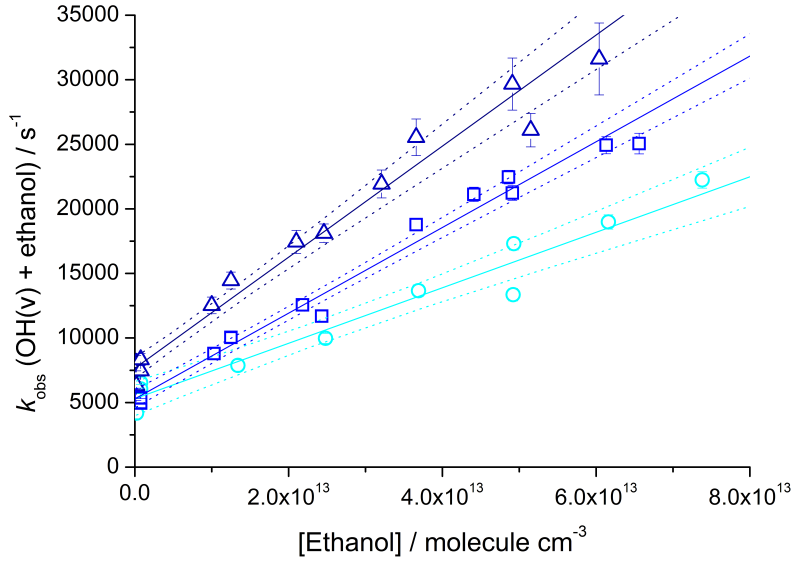

Figure 7. 9: Variation of k_{obs} with ethanol concentration for OH(v=1) (light blue open circles), OH(v=2) (mid blue squares) and OH(v=3) (dark blue triangles) obtained at 88 ± 4 K and a density of (1.1 ± 1) × 10^{17} molecule cm^{-3} using N_2 bath gas. Each data set is fitted with a weighted linear least squares fit of E7.12 (full lines) to the data the gradient of which yields the bimolecular rate coefficient. The dashed lines represent the upper and lower 95 % confidence limits. The error bars on the pseudo first order rate coefficients result from the error in the fit of E7.10 to the data, and in this case the error bars are obscured by the symbol. The overall error in the bimolecular rate coefficient is the 95% confidence limits propagated with the error in the determination of the total density from the impact pressure measurements.

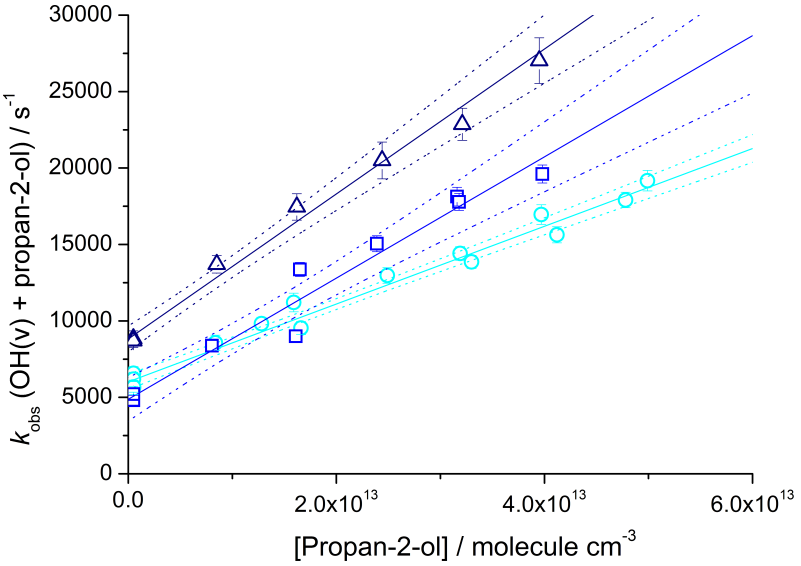

Figure 7. 10: Variation of k_{obs} with propanol concentration for OH(v=1) (light blue open circles), OH(v=2) (mid blue squares) and OH(v=3) (dark blue triangles) obtained at 88 ± 4 K and a density of (1.1 ± 1) × 10^{17} molecule cm^{-3} using N_2 bath gas. Each data set is fitted with a weighted linear least squares fit of E7.13 (full lines) to the data the gradient of which yields the bimolecular rate coefficient. The dashed lines represent the upper and lower 95 % confidence limits. The error bars on the pseudo first order rate coefficients result from the error in the fit of E7.10 to the data, and in this case the error bars are obscured by the symbol.

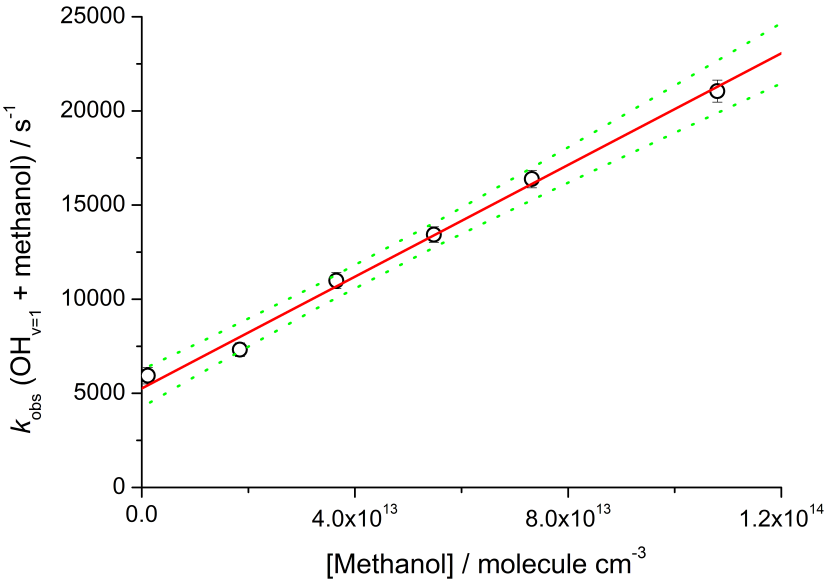

Figure 7. 11: Variation of k_{obs} with methanol concentration for OH(v=1) (black open circles) obtained at 88 ± 4 K and a density of (1.1 ± 1) × 10^{17} molecule cm^{-3} using N_2 bath gas. Each data set is fitted with a weighted linear least squares fit of E7.14 to the data the gradient of which yields the bimolecular rate coefficient .The green dashed lines represent the upper and lower 95 % confidence limits. The error bars on the pseudo first order rate coefficients result from the error in the fit of E7.10 to the data, and in this case the error bars are obscured by the symbol. The overall error in the bimolecular rate coefficient is the 95% confidence limits propagated with the error in the determination of the total density from the impact pressure measurements.

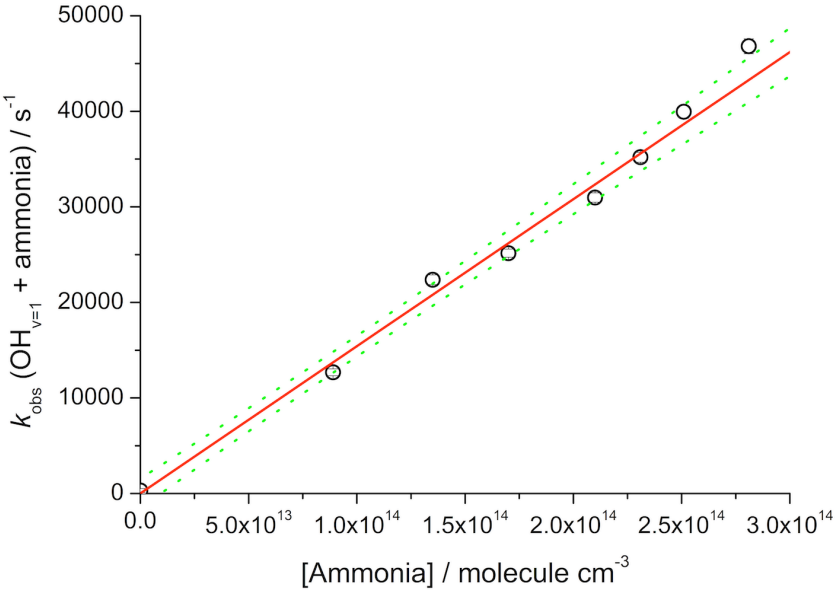

Figure 7. 12: Variation of k_{obs} with ammonia concentration for OH(v=1) obtained at 56 ± 4 and a density of (4.4 ± 0.5) × 10^{16} molecule cm^{-3} using Ar bath gas. Each data set is fitted with a weighted linear least squares fit of E7.15 to the data the gradient of which yields the bimolecular rate coefficient The green dashed lines represent the upper and lower 95 % confidence limits. The error bars on the pseudo first order rate coefficients result from the error in the fit of E7.10 to the data, and in this case the error bars are obscured by the symbol. The overall error in the bimolecular rate coefficient is the 95% confidence limits propagated with the error in the determination of the total density from the impact pressure measurements.

Table 7. 2: Measured rate coefficients of the reactions of vibrationally excited OH obtained in this study, together with the temperatures of the flows generated by the pulsed Laval nozzles. Errors have been calculated by propagation of the 95 % confidence limits in the bimolecular rate coefficients with the errors in the expansion densities.

R	*T*/K	M	$k_{(v=0)}$ / 10^{-10} molecule^{-1} cm^3 s^{-1} #	$k_{v=1}$ / 10^{-10} molecule^{-1} cm^3 s^{-1}	$k_{v=2}$ / 10^{-10} molecule^{-1} cm^3 s^{-1}	$k_{v=3}$ / 10^{-10} molecule^{-1} cm^3 s^{-1}
Methanol	88 ± 4	N_2	0.38 ± 0.04*	1.5 ± 0.21	-	-
Ethanol	88 ± 4	N_2	0.55 ± 0.06	2.15 ± 0.24	3.32 ± 0.33	4.50 ± 0.51
Propanol	88 ± 4	N_2	0.7 ± 0.1	2.54 ± 0.28	3.96 ± 0.45	4.74 ± 0.75
Ammonia	56 ± 4	Ar	0.14 ± 0.02	1.54 ± 0.18	-	-

#Rate coefficients obtained at the same density and temperature as the OH(v) data. The ethanol and propanol values comprise a component from the pressure dependent channel.*Obtained in Ar jet, however the rate coefficient found was found by Shannon *et al.* to be independent of pressure, so this is insignificant.[37]

The bimolecular rate coefficients obtained in this work for OH(v) + methanol, ethanol, propanol and ammonia are summarised in Table 7. 2, and are shown alongside the OH(v=0) + R rate coefficients for comparison.

The rate coefficients for the OH(v) + R reactions were found to be significantly faster than measured for OH(v=0), providing evidence that the measured rate coefficients for OH(v=0) are either at the low pressure limit (in the case of methanol and ammonia) or in the fall off region (in the case of ethanol and propanol). To aid comparison, the rate coefficients for OH(v) + ethanol, propan-2-ol and ammonia are shown alongside the OH(v=0) values in Figure 7. 13, Figure 7. 14 and Figure 7. 15 respectively.

In the cases of the reactions of ethanol and propanol, for which the rate coefficients with OH(v=2) and OH(v=3) were measured, it can be seen that the rate coefficient increases with higher vibrational excitation, as shown in Figure 7. 13 and Figure 7. 14. This observation is at odds with the proxy method hypothesis which assumes that IVR is fast with respect to redissociation of the complex, and thus the measured rate coefficient should be independent of initial vibrational excitation. The enhancement of the rate coefficient with vibrational excitation suggests that the lifetime for the complex (OH(v)-R) is insufficient to allow full IVR.

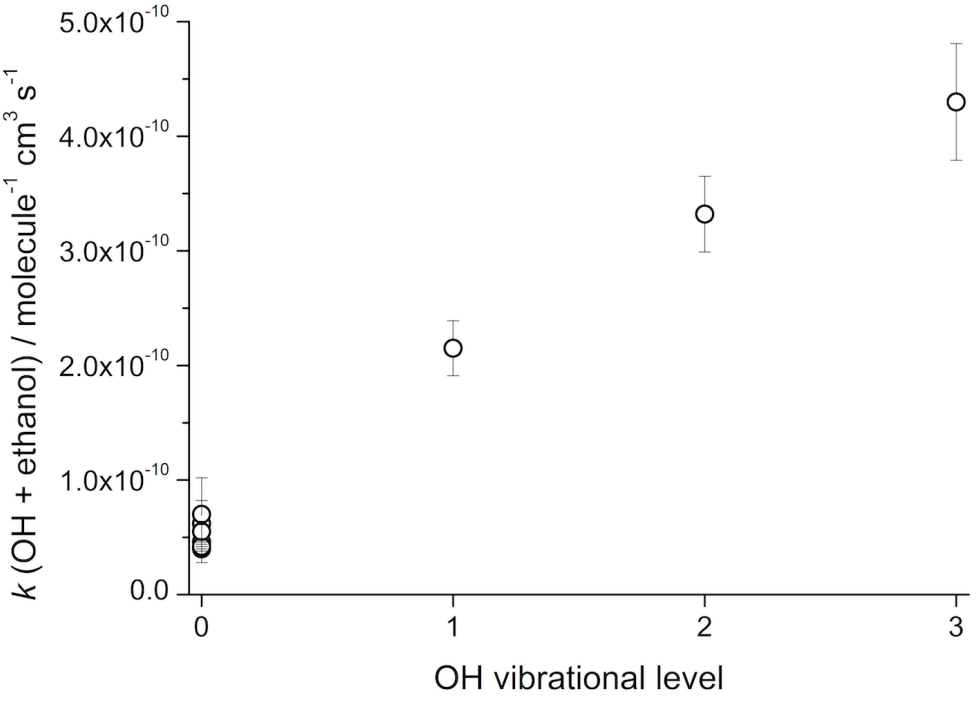

Figure 7. 13: Bimolecular rate coefficients for OH + ethanol obtained in this work at a temperature of 88 ± 4 K and a total gas density of (1.1 ± 1) × 10^{17} molecule cm^{-3} using N_2 bath gas as a function of OH vibrational excitation quanta.

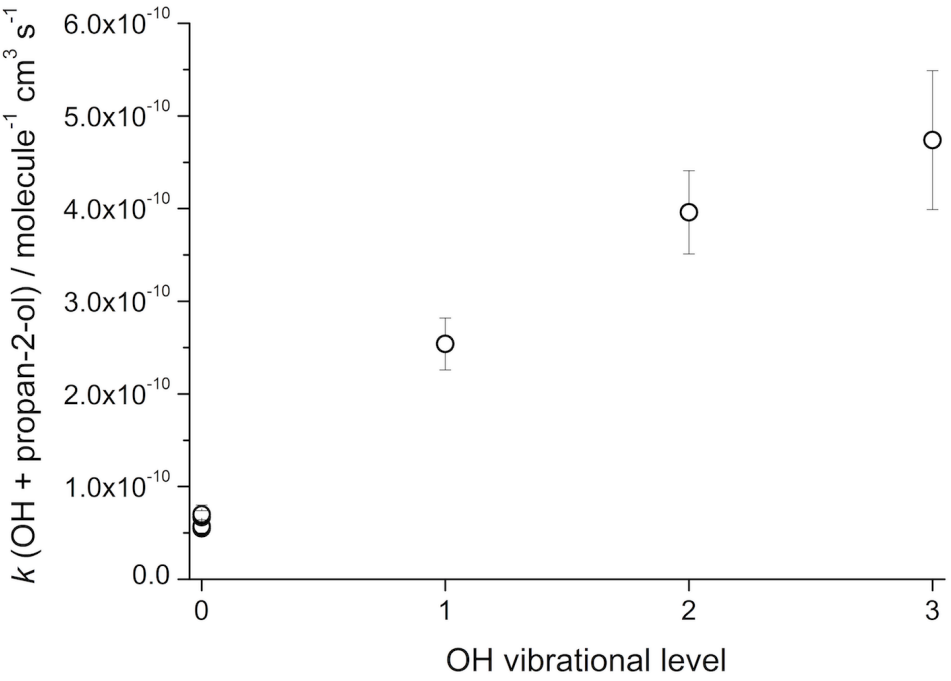

Figure 7. 14: Bimolecular rate coefficients for OH + propanol obtained in this work at a temperature of 88 ± 4 K and a total gas density of (1.1 ± 1) × 10^{17} molecule cm^{-3} using N_2 bath gas as a function of OH vibrational excitation quanta.

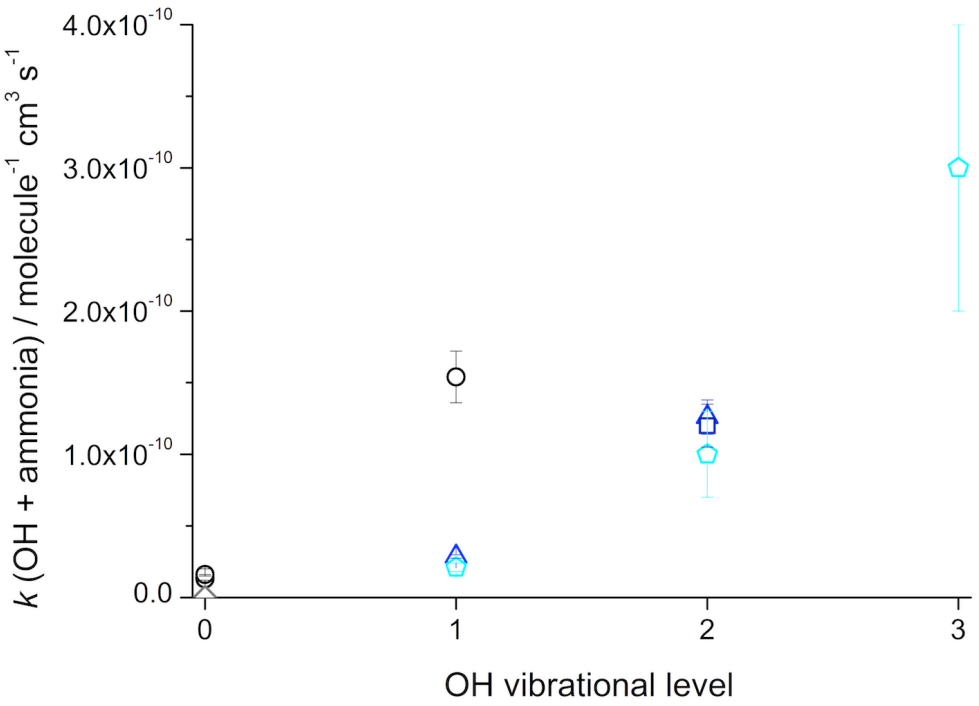

Figure 7. 15: Bimolecular rate coefficients for OH + ammonia as a function of OH vibrational excitation quanta. Black open circles: This work at a temperature of 56 ± 4 K and a total gas density of (4.4 ± 0.5) × 10^{16} molecule cm^{-3} using Ar bath gas. Blue triangles: Silvente *et al*. at 298 K.[4] Dark blue squares: Rensberger *et al.* at 298 K.[38] Light blue pentagons: Cheskis *et al*. at 298 K.[36] Grey diamond: Diau *et al.* at 298 K.[39]

For the OH(v) + ammonia reaction, rate coefficients obtained at 298 K are plotted alongside those obtained in this work.[4,36,38,39] It can be seen in Figure 7. 15 that the OH(v=1) + ammonia rate coefficient at 56 K is significantly faster than at room temperature. Given the weak binding energy of the OH + ammonia complex (7.5 kJ mol^{-1} according to the calculations Monge-Palacios *et al.*[35]), it would seem unlikely that vibrational relaxation of OH(v) would be occurring via the formation of the OH-ammonia complex as its lifetime will be reduced with increasing temperature. However, at 298 K Silvente *et al.* noted that OH(v) deactivation by ammonia was highly efficient and suggested the role of an OH-ammonia complex.[4] The vibrational frequency of N-H (3598 cm^{-1}) and the energy difference between OH (v=1-0) (3570 cm^{-1}) are sufficiently close so that IVR may be enhanced through resonant transfer (see section 7.1.1). [19,20,35,40] Resonant transfer is unlikely to be contributing for the ethanol reaction as the nearest vibrational frequency is ~ 300 cm^{-1} greater than the energy difference between OH(v=1) and OH(v=0).[19,20,23,40] As resonant IVR is much more efficient, the complex may not require a long lifetime for vibrational relaxation to occur and so the high pressure limiting rate coefficient may be obtainable at lower vibrational excitation of OH. At 298 K, the high pressure limit has evidently not be obtained as the rate coefficients reported in the literature increase with higher vibrational levels, suggesting that the complex lifetime is insufficient for full vibrational relaxation.[4,36,38] However, at 56 K, the complex lifetime will be longer therefore the OH(v=1) + ammonia rate coefficient may be an appropriate representation for the high pressure limiting rate coefficient. To establish this, further experiments at higher quanta of OH vibrational excitation, or trajectory calculations would need to be performed. Hence the rate coefficient obtained in this work should be regarded as a lower limit to k^{∞}.

To the authors best knowledge there are no other OH(v) rate coefficient measurements for the ethanol and propanol reactions and so the corresponding comparisons cannot be made. The ratios of the rate coefficients (k(v=3)/k(v=1)) are presented in Table 7. 3, alongside results previously obtained by Shannon for the methanol, DME and acetone reactions.[21]

Table 7. 3: Ratios of rate coefficients for OH + R reactions obtained at different vibrational excitations of OH from this work and by Shannon, shown alongside the predicted ratios from the proxy method and SSH theory.[21] The co-reactants are ordered in increasing molecular size for ease of intercomparison.

R	Well depth* / kJ mol^{-1}	T/K	k(v=1)/k(v=3)	k(v=2)/k(v=3)	k(v=1)/k(v=2)
Proxy method[#]			1	1	1
SSH theory[#]			0.33	0.67	0.5
Methanol[§]	24	93 ± 4	0.34		
DME[§]	22	93 ± 4	0.42		
Ethanol	27	88 ± 4	0.47	0.74	0.64
Acetone[§]	22	93 ± 4	0.58		
Propanol	27	88 ± 4	0.53	0.83	0.64

* Values from *ab initio* stationary point calculations by Galano *et al.*, Henon *et al.* and Carr *et al.*[22,24,27] # Theoretical values. § By Shannon.[21]

It can be seen from Table 7. 3 that with increasing molecular size, the ratio of k(v=1)/k(v=3) approaches the proxy limit predicted values. The enhanced density of states for the complex of larger co-reactants with respect to the separated OH and co-reactant species leads to an enhanced lifetime of the complex with respect to redissociation.[41] Therefore, vibrational relaxation amongst the modes of the complex is increasingly competitive with redissocation, and therefore on redissociation of the complex, OH is more likely to return in the ground vibrational state. This in agreement with the hypothesis of Smith and also with the previous low temeprature proxy method work of Shannon.[5,21] The observation that the rate coefficients increase with higher vibrational excitation of OH is indicative that IVR is not 'instantaneous' with respect to the rate of re-dissocation of the complex, and so the limiting step in the loss of OH(v) is not the formation of the complex, but the rate of IVR. Therefore the values obtained for OH(v) + R are the lower limits of the high pressure limiting rate coefficient. This is supported by the conclusions of McCabe *et al* on their work on OH(v=1) + HNO_3 at 256-373 K. Given that SSH theory states that the probabilty, and therefore rate coefficient, for IVR increases with increasing vibrational excitation, the rate coefficients for OH(v) + R acquired at the highest vibrational excitation are the lower limits to k_a, and thus the high pressure limit, k^{∞}.

7.4 Summary

The proxy method of Quack, Troe, Jaffer and Smith has been implemented in this work to attempt to obtain the high pressure limiting rate coefficients for the reactions of OH with ethanol, propanol, methanol and ammonia at low temperatures.[1,2] The proxy method utilises the ergodicity assumption (that energy redistribution is fast) to deduce the high pressure limiting rate coefficient for a reaction whereby a complex is formed, by the rate coefficient for the loss of a vibrationally excited reactant. Vibrationally excited OH(v) was produced and monitored state selectively by laser induced fluorescence spectroscopy, and rate coefficients for the loss of OH(v) in the presence of the co-reactants was obtained. At low temperatures, the formation of the weakly bound complex between OH and the co-reactant has been shown to enhance the rate coefficients for bimolecular reaction, and it is the formation of the weakly bound complex which facilitates IVR of the vibrational energy from the OH vibrational mode amongst the modes of the complex. The proxy method predicts that if the complex has a sufficient lifetime, full IVR should occur and the OH(v) should be returned vibrationally cold on redissociation of the complex. However, SSH theory for vibrational energy transfer states that vibrational relaxation is dependent both on the change in vibrational quanta, and also on the initial vibrational state. From SSH theory, it would be expected that the rate coefficient would increase with higher quanta of vibrational excitation.[15] Therefore, the rate coefficient for OH(v) + R closest to the high pressure limiting rate coefficient for OH + R would be the value measured for the highest vibrational level of OH. Alternatively, the proxy method predicts that the rate coefficients obtained should be independent of the level of vibrational excitation.

The rate coefficients obtained in this study for OH(v) + R were on the order of 10 times greater than the values obtained for OH(v=0) + R , which reinforces the pressure dependence studies reported earlier in this thesis which determined that the rate coefficients obtained for OH(v=0) + R are in the fall off regime or at the low pressure limit. It was found that the rate coefficients for OH(v) were enhanced by increasing the quanta of vibrational excitation, which is in (qualitative) agreement with predictions of SSH theory. The ratios of the rate coefficients for OH(v=1) + R and OH(v=3) + R suggest that the mechanism is somewhere between the assumptions made by the proxy method and SSH theory. The ratio k(v=1)/k(v=3) was found to increase with the size of the co-reactant, R. This provides evidence for the complexes of OH(v)-R being shorter lived for the smaller reactants, and so

full IVR is does not occur before redissociation. Even for the largest reactant (propanol) full IVR had not been achieved. In the case of OH(v=1) + ammonia, it is postulated that resonant IVR may be occurring and so the obtained rate coefficient may be a good proxy of the high pressure limiting rate coefficient. However, to ascertain that it is not a lower limit further experiments would need to be performed at higher vibrational quanta of excitation or trajectory calculations performed to investigate the rate of IVR.

The lower bounds of the high pressure limiting rate coefficients obtained in this study for OH + ethanol and OH + propanol have been utilised in the extended Lindemann-Hinshelwood fits to the pressure-dependence data in Chapter 3 to obtain the low pressure limiting rate coefficients, and hence obtain the contribution of the bimolecular channel to the overall rate coefficient at low temperatures. Using the values reported in this chapter, it was found that the rate coefficients corresponding to the bimolecular channel of both of these reactions were significantly enhanced with respect to the room temperature values.[42]

The data reported in this chapter can be used as lower bound to the barrierless association rate coefficient in future master equation calculations. This will aid further understanding of the temperature and pressure dependence of these reactions which is imperative for ascertaining the potential impact of such reactions in the low temperature interstellar regions where these species are found.

7.5 References

1 Jaffer, D. H. & Smith, I. W. M. Time-Resolved Measurements on the Relaxation of OH(v=1) by NO, NO_2 and O_2. *Faraday Discuss.* **67**, 212-220 (1979).

2 Quack, M. & Troe, J. Complex Formation in Reactive and Inelastic Scattering: Statistical Adiabatic Channel Model of Unimolecular Processes III. *Berichte der Bunsengesellschaft für physikalische Chemie* **79**, 170-183 (1975).

3 McKee, K. W. *et al.* Experimental and Master Equation Study of the Kinetics of OH + C_2H_2: Temperature Dependence of the Limiting High Pressure and Pressure Dependent Rate Coefficients. *The Journal of Physical Chemistry A* **111**, 4043-4055 (2007).

4 Silvente, E., Richter, R. C. & Hynes, A. J. Kinetics of the vibrational deactivation of OH X ^{2}II (v= 3, 2, 1) with hydrides and reduced sulfides. *J. Chem. Soc., Faraday Trans.* **93**, 2821-2830 (1997).

5 Smith, I. W. M. Collisional energy transfer, intramolecular vibrational relaxation and unimolecular reactions. *Journal of the Chemical Society, Faraday Transactions* **93**, 3741-3750 (1997).

6 Anastasi, C. & Smith, I. W. Rate measurements of reactions of OH by resonance absorption. Part 6.—Rate constants for OH+ NO (+ M)→ HNO_2 (+ M) over a wide range of temperature and pressure. *Journal of the Chemical Society, Faraday Transactions 2: Molecular and Chemical Physics* **74**, 1056-1064 (1978).

7 Anastasi, C. & Smith, I. W. Rate measurements of reactions of OH by resonance absorption. Part 5.—Rate constants for OH+ NO_2 (+ M)→ HNO_3 (+ M) over a wide range of temperature and pressure. *Journal of the Chemical Society, Faraday Transactions 2: Molecular and Chemical Physics* **72**, 1459-1468 (1976).

8 Smith, I. W. & Williams, M. D. Vibrational relaxation of OH (v=1) and OD (v=1) by HNO_3, DNO_3, H_2O, NO and NO_2. *Journal of the Chemical Society, Faraday Transactions 2: Molecular and Chemical Physics* **81**, 1849-1860 (1985).

9 Herbert, L. B. *et al.* Rate Constants for the Relaxation of CH ($X^2\Pi$, v= 1) by CO and N_2 at Temperatures from 23 to 584 K. *The Journal of Physical Chemistry* **100**, 14928-14935 (1996).

10 Fulle, D. & Hippler, H. The high−pressure range of the reaction of CH ($^2\Pi$) with N_2. *The Journal of Chemical Physics* **105**, 5423-5430 (1996).

11 Forster, R. *et al.* High pressure range of the addition of HO to HO, NO, NO_2, and CO. I. Saturated laser induced fluorescence measurements at 298 K. *The Journal of Chemical Physics* **103**, 2949-2958 (1995).

12 McCabe, D. C. *et al.* Kinetics of the Removal of OH (v=1) and OD (v=1) by HNO_3 and DNO_3 from 253 to 383 K. *The Journal of Physical Chemistry A* **107**, 7762-7769 (2003).

13 Brownsword, R. A. *et al.* Kinetics over a wide range of temperature (13–744 K): Rate constants for the reactions of CH(v=0) with H_2 and D_2 and for the removal of CH(v=1) by H_2 and D_2. *The Journal of Chemical Physics* **106**, 7662-7677 (1997).

14 Berman, M. R. & Lin, M. Kinetics and mechanisms of the reactions of CH and CD with H_2 and D_2. *The Journal of Chemical Physics* **81**, 5743-5752 (1984).

15 Schwartz, R., Slawsky, Z. & Herzfeld, K. Calculation of vibrational relaxation times in gases. *The Journal of Chemical Physics* **20**, 1591-1599 (1952).

16 Spencer, J. E. & Glass, G. Some reactions of OH (v= 1). *International Journal of Chemical Kinetics* **9**, 111-122 (1977).

17 Glass, G., Endo, H. & Chaturvedi, B. Vibrational energy transfer from OH to other gaseous hydrides. *The Journal of Chemical Physics* **77**, 5450-5454 (1982).

18 Spencer, J. E. & Glass, G. The production and subsequent relaxation of vibrationally excited OH in the reaction of atomic oxygen with HBr. *International Journal of Chemical Kinetics* **9**, 97-109 (1977).

19 Lambert, J. D. *Vibrational and rotational relaxation in gases*. (Oxford University Press, USA, 1977).

20 Tanczos, F. I. Calculation of vibrational relaxation times of the chloromethanes. *The Journal of Chemical Physics* **25**, 439-447 (1956).

21 Shannon, R. J. *Experimental and computational studies of hydroxyl radical kinetics at very low temperatures* PhD thesis, University of Leeds, (2012).

22 Galano, A., Alvarez-Idaboy, J. R., Bravo-Pérez, G. & Ruiz-Santoyo, M. E. Gas Phase Reactions of C1–C4 Alcohols with the OH Radical: A Quantum Mechanical Approach. *Phys. Chem. Chem. Phys.* **4**, 4648-4662 (2002).

23 Xu, S. & Lin, M. C. Theoretical Study on the Kinetics for OH Reactions with CH_3OH and C_2H_5OH. *P. Combust. Inst.* **31**, 159-166 (2007).

24 Carr, S. *et al.* Experimental and Theoretical Study of the Kinetics and Mechanism of the Reaction of OH Radicals with Dimethyl Ether. *The Journal of Physical Chemistry A* **117**, 11142-11154 (2013).

25 Vandenberk, S., Vereecken, L. & Peeters, J. The acetic acid forming channel in the acetone + OH reaction: A combined experimental and theoretical investigation. *Physical Chemistry Chemical Physics* **4**, 461-466 (2002).

26 Yamada, T., Taylor, P. H., Goumri, A. & Marshall, P. The reaction of OH with acetone and acetone-d6 from 298 to 832 K: Rate coefficients and mechanism. *Journal of Chemical Physics* **119**, 10600-10606 (2003).

27 Henon, E., Canneaux, S., Bohr, F. & Dóbé, S. Features of the potential energy surface for the reaction of OH radical with acetone. *Physical Chemistry Chemical Physics* **5**, 333-341 (2003).

28 Aker, P. M. & Sloan, J. J. The initial product vibrational energy distribution in the reaction between $O(^1D)$ and H_2. *The Journal of Chemical Physics* **85**, 1412-1417 (1986).

29 McKee, K. W. *Laser studies of chemical reactions of importance in atmospheric and combustion systems*, University of Leeds, (2003).

30 Polanyi, J. C. Concepts in reaction dynamics. *Accounts of Chemical Research* **5**, 161-168 (1972).

31 Crim, F. F. Bond-selected chemistry: vibrational state control of photodissociation and bimolecular reaction. *The Journal of Physical Chemistry* **100**, 12725-12734 (1996).

32 Crim, F. F. Vibrational state control of bimolecular reactions: Discovering and directing the chemistry. *Accounts of Chemical Research* **32**, 877-884 (1999).

33 Zare, R. N. Laser control of chemical reactions. *science* **279**, 1875-1879 (1998).

34 Sinha, A., Hsiao, M. C. & Crim, F. F. Bond−selected bimolecular chemistry: H + HOD (4vOH)→ OD + H_2. *The Journal of Chemical Physics* **92**, 6333-6335 (1990).

35 Monge-Palacios, M., Rangel, C. & Espinosa-Garcia, J. Ab initio based potential energy surface and kinetics study of the OH + NH_3 hydrogen abstraction reaction. *The Journal of Chemical Physics* **138**, 084305 (2013).

36 Cheskis, S., Iogansen, A., Kulakov, P., Sarkisov, O. & Titov, A. Laser photolysis of ozone in the presence of ammonia: Vibrationally excited OH radicals. *Chemical Physics Letters* **143**, 348-352 (1988).

37 Shannon, R. J., Blitz, M. A., Goddard, A. & Heard, D. E. Accelerated Chemistry in the Reaction between the Hydroxyl Radical and

Methanol at Interstellar Temperatures Facilitated by Tunnelling. *Nature Chem.* **5**, 745-749 (2013).

38 Rensberger, K. J., Jeffries, J. B. & Crosley, D. R. Vibrational relaxation of OH (X $^2\Pi_i$, v= 2). *The Journal of Chemical Physics* **90**, 2174-2181 (1989).

39 Diau, E. W. G., Tso, T. L. & Lee, Y. P. Kinetics of the reaction hydroxyl + ammonia in the range 273-433 K. *The Journal of Physical Chemistry* **94**, 5261-5265 (1990).

40 Raiche, G. A., Jeffries, J. B., Rensberger, K. J. & Crosley, D. R. Vibrational energy transfer in OH X $^2\Pi_i$, v= 2 and 1. *The Journal of Chemical Physics* **92**, 7258-7263 (1990).

41 Gilbert, R. G. & Smith, S. C. Theory of unimolecular and recombination reactions. (1990).

42 Caravan, R. L., Shannon, R., Lewis, T., Blitz, M. A. & Heard, D. E. Measurements of Rate Coefficients for Reactions of OH with Ethanol and Propan-2-ol at Very Low Temperatures. *The Journal of Physical Chemistry A* (2014).

Concluding remarks

The rate coefficients for a range of OH + oxygenated volatile organic compound (oVOC) reactions have been measured at low temperatures – in the cases of the OH + ethanol and OH + propanol reactions, these are the first measurements below 200 K.[1] Measurements of the OH + acetone and dimethyl ether (DME) reaction rate coefficients obtained at ~ 140 K are complemented by master equation calculations and previous experimental results by Shannon.[2] Rate coefficients of the OH + methanol reaction obtained in this work build on previous work reported by this research group and extend the measured temperature range down to 56 K and up to 138 K.[3,4] Additionally, these measurements are additionally supported by experiments performed in a cryogenically cooled flow tube apparatus by Gomez-Martin.[4]

The rate coefficients for the OH + oVOC reactions are found to be significantly enhanced at low temperatures despite barriers to hydrogen abstraction. A common mechanism is found to be operating in the these reactions involving the formation of a weakly bound complex (15-25 kJ mol^{-1}) prior to the hydrogen abstraction barrier. At lower temperatures the complex is longer lived and has three possible fates: redissociation, collisional stabilisation into the pre-barrier well or quantum tunnelling through the H-abstraction barrier. The postulated mechanism is similar to that proposed for the CN + C_2H_6 reaction though low temperature experiments by Sims *et al.* and theoretical work by Georgievskii and Klippenstein, and the OH + HNO3 reaction by Brown *et al*.[5-8] The contributions of the stabilisation and tunnelling channels are assessed through pressure dependence studies and it is found that quantum tunnelling contributes to the overall rate coefficient for all of the reactions. The master equation calculations performed by Shannon for the OH + acetone and DME systems are supportive of the postulated mechanism. The potential interstellar impact of these reactions has been assessed in collaboration with Acharyya and Herbst (U. Virginia) and it was found that the OH + methanol reaction had the greatest impact.[9]

A dramatic upturn in the rate coefficient for OH + ammonia is also observed despite the complex being very weakly bound. At 54 K the rate coefficient was found to be two orders of magnitude faster than at room temperature. Pressure dependence studies provided evidence for the reaction operating purely via the tunnelling channel to yield bimolecular products. The NH_2 product of the OH + ammonia reaction was temporally detected via laser

induced fluorescence spectroscopy at 54 K and using an internal standard, the yield of the bimolecular channel was found to be ~ 100 %. Ammonia and OH are both abundant in low temperature interstellar environments and modelling efforts by Acharyya and Herbst (U. Virginia) have demonstrated that their reaction may lead to a significant reduction in modelled interstellar ammonia. Around a 40 % reduction in ammonia concentration is calculated at 10 K and 10^5 years compared to the model calculated abundance when the OH + ammonia is excluded.

The high pressure limiting rate coefficients at low temperatures were explored for these reactions using the proxy method of Jaffer, Smith, Quack and Troe. OH was produced in vibrationally excited states and the rate coefficients for the reactions of OH(v) with ammonia, methanol, ethanol and propanol were state selectively measured via laser induced fluorescence spectroscopy. The proxy method postulates that the rate coefficient for a reaction featuring an association step measured with the radical in its vibrationally excited state should be equal to the high pressure limiting rate coefficient, as the ergodicity principle states that intramolecular vibrational redistribution of the excess vibrational energy should be rapid on the timescale of redissociation or reaction. It was found that the measured rate coefficients increased with quanta of vibrational excitation of OH, which is not consistent with the ergodicity principle and is in agreement with SSH theory. The rate coefficients obtained at the highest quanta of vibrational excitation of OH are concluded to be a lower limit to the high pressure limiting rate coefficient for these reactions at low temperature. The obtained rate coefficients should aid future master equation calculations performed on the OH + oVOC and OH + ammonia reactions.

The first low temperature study of the reactions of alkoxy radicals (RO) with NO was performed and a negative temperature dependence consistent with previous literature observations was observed. Measurements of the rate coefficients for the reactions of NO + methoxy radicals and NO + ethoxy radicals over a pressure range revealed two components to the overall rate coefficient: a pressure dependent channel consistent with collisional stabilisation of the RONO complex into a deep well, and a pressure independent channel consistent with bimolecular product formation. The formaldehyde product was temporally detected from the methoxy radical + NO reaction and found to be formed with a rate coefficient consistent with the value obtained by LIF monitoring of the methoxy radical reactant.

The significant enhancement of the rate coefficients at low temperature for many hydrogen abstraction reactions studied in this and previous work suggests that the postulated mechanism, whereby the formation of the complex enhances the probability of tunnelling through the abstraction barrier, may be general for hydrogen transfer reactions at low temperature where a complex can be formed. The OH + ammonia results obtained in this work demonstrate that this is possible even for very weakly bound complexes. Further low temperature work should be carried out on other reactions of this type, including the OH + methane reaction which was briefly discussed in Chapter 5.

The inability of current theoretical work to reproduce the sharp turnaround between the apparent Arrhenius-type behaviour and the inverse temperature dependence at low temperatures for the reactions of OH + ammonia and OH + methanol points to interesting potentially non-statistical behaviour which could be explored further through trajectory calculations. The continued synergy between experimental and theoretical work and the on-going advancement of both disciplines will enhance our understanding of complex kinetic behaviour for reactions in this class. Collaboration with other CRESU research groups to enable a greater temperature range to be achieved and utilisation of alternative detection techniques (such as quadrupole mass spectrometers with tuneable synchrotron ionization radiation) would be highly beneficial. In particular, alternative detection techniques would be valuable for product detection and branching ratio assignments, which are of importance for use in astrochemical models.

Efforts to collaborate with the astrochemical community to assess the ultimate implications of the laboratory data obtained should be sustained. Such co-operation is mutually beneficial and provides guidance for future kinetic measurements to be performed to gain a better understanding of complex molecule formation in interstellar environments.

1 Caravan, R. L., Shannon, R., Lewis, T., Blitz, M. A. & Heard, D. E. Measurements of Rate Coefficients for Reactions of OH with Ethanol and Propan-2-ol at Very Low Temperatures. *The Journal of Physical Chemistry A* (2014).

2 Shannon, R. J., Caravan, R. L., Blitz, M. & Heard, D. E. A combined experimental and theoretical study of reactions between the hydroxyl radical and oxygenated hydrocarbons relevant to astrochemical environments. *Phys. Chem. Chem. Phys.* **16**, 3466-3478 (2014).

3 Shannon, R. J., Blitz, M. A., Goddard, A. & Heard, D. E. Accelerated Chemistry in the Reaction between the Hydroxyl Radical and

Methanol at Interstellar Temperatures Facilitated by Tunnelling. *Nature Chem.* **5**, 745-749 (2013).

4 Gomez Martin, J. C., Caravan, R. L., Blitz, M. A., Heard, D. E. & Plane, J. M. C. Low Temperature Kinetics of the CH_3OH + OH Reaction. *J. Phys. Chem. A* **118**, 2693-2701 (2014).

5 Georgievskii, Y. & Klippenstein, S. J. Strange Kinetics of the C_2H_6 + CN Reaction Explained. *The Journal of Physical Chemistry A* **111**, 3802-3811 (2007).

6 Brown, S. S., Burkholder, J. B., Talukdar, R. K. & Ravishankara, A. R. Reaction of Hydroxyl Radical with Nitric Acid: Insights into Its Mechanism. *The Journal of Physical Chemistry A* **105**, 1605-1614 (2000).

7 Brown, S. S., Talukdar, R. K. & Ravishankara, A. Reconsideration of the rate constant for the reaction of hydroxyl radicals with nitric acid. *The Journal of Physical Chemistry A* **103**, 3031-3037 (1999).

8 Sims, I. R. *et al.* Rate constants for the reactions of CN with hydrocarbons at low and ultra-low temperatures. *Chemical Physics Letters* **211**, 461-468 (1993).

9 Acharyya, K. *et al.* The Importance of OH Radical-Neutral Low Temperature Tunneling Reations in Interstellar Clouds Using a New Model. *Molecular Physics* **Accepted** (2015).

Appendix A

A.1 Inverse Laplace transform method

Dr Robin Shannon (University of Leeds) and Dr Arne Bunkan (University of Leeds / University of Oslo) have performed master equation calculations on the reactions of OH with acetone and DME, and OH with ammonia the results of which are presented in Chapters 4 and 5 of this thesis respectively.[1] For this purpose, the procedure which Shannon and Bunkan employed for the master equation treatment of the barrierless association reactions (RA.1) will be briefly outlined.

$$A + B \xrightarrow{k_a} AB^* \qquad \text{RA.1}$$

$$AB^* \xrightarrow{k_{-a}} A + B \qquad \text{RA.2}$$

To calculate the microcanonical rate coefficient of a barrierless process, k(E), from first principles requires a variational approach which is computationally demanding as vibrational frequencies and energies are required to be known along the whole potential energy surface.[2]

It was first proposed by Slater that the canonical high pressure limiting rate coefficient for a unimolecular reaction, $k^{\infty}_{-a}(T)$ (such as RA.2), can be related to the microcanonical rate coefficient of the process, k(E) via an inverse Laplace transform.[3] However, the research of the group of Michael Pilling has been fundamental for the application of this method to master equation calculations and was first implemented by Robertson *et al.* using the relationship shown in E1.30.[4]

$$k^{\infty}{}_{-a}(T) = \frac{1}{Q(T)} \int_0^{\infty} k(E)\, \rho(E) exp\left(\frac{-E}{k_B T}\right) dE \qquad \text{EA.1}$$

However, an association reaction between two species A and B (RA.1) is the reverse of a unimolecular reaction (RA.2) and the corresponding rate coefficients are related to one another through detailed balance (EA.2).

$$k^{\infty}{}_{a}(T) = k^{\infty}{}_{-a}(T) K_{eq} \qquad \text{EA.2}$$

where $k^{\infty}_{a}(T)$ and $k^{\infty}_{-a}(T)$ are the high pressure limiting canonical rate coefficients for RA.1 and RA.2, respectively and K_{eq} is the equilibrium constant for the processes. Therefore, the microcanonical rate coefficient can be expressed in terms of $k^{\infty}_{a}(T)$ as shown in EA.3.

$$k(E) = \ell^{-1} \frac{Q(T) K_{eq}(T) k^{\infty}{}_{-a}(T)}{\rho(E)} \qquad \text{EA.3}$$

where ℓ^{-1} symbolises an inverse Laplace transform. Using the work of Davies *et al.* for the temperature dependent expression of $k^{\infty}_{a}(T)$,[5] Robertson *et al.* are able to yield a complex expression for the microcanonical rate coefficient, which is shown in EA.4 and EA.5.[4]

$$k(E) = \frac{A^{\infty}C}{\rho(E)\Gamma(n^{\infty}+1.5)} \int_0^{E-E^{\infty}-\Delta H} \rho_{prod}(E)[(E - E^{\infty} - \Delta H) - x]^{n^{\infty}+0.5} dx \quad \text{EA.4}$$

where

$$C = \frac{2\pi m_a m_b}{h^2(m_a m_b)} \quad \text{EA.5}$$

A^{∞}, n^{∞} and E^{∞} are experimentally obtained parameters, Γ is a mathematical function known as the gamma function, h is Planks constant, $\rho(E)$ is the density of states of the reactant, $\rho_{prod}(E)$ is the convoluted density of states of the products, ΔH is the energy difference between reactants and products, and m_a and m_b are the masses of the product species. For further details about this method and a full derivation see Davies *et al.*[5] Robertson *et al.*[4] and Glowacki *et al.*[6]

A.2 References

1 Shannon, R. J., Caravan, R. L., Blitz, M. & Heard, D. E. A combined experimental and theoretical study of reactions between the hydroxyl radical and oxygenated hydrocarbons relevant to astrochemical environments. *Phys. Chem. Chem. Phys.* **16**, 3466-3478 (2014).

2 Shannon, R. J. *Experimental and computational studies of hydroxyl radical kinetics at very low temperatures* PhD thesis, University of Leeds, (2012).

3 Slater, N. New formulation of gaseous unimolecular dissociation rates. *The Journal of Chemical Physics* **24**, 1256-1257 (1956).

4 Robertson, S., Pilling, M., Baulch, D. & Green, N. Fitting of pressure-dependent kinetic rate data by master equation/inverse Laplace transform analysis. *The Journal of Physical Chemistry* **99**, 13452-13460 (1995).

5 Davies, J. W., Green, N. J. & Pilling, M. J. The testing of models for unimolecular decomposition via inverse Laplace transformation of experimental recombination rate data. *Chemical Physics Letters* **126**, 373-379 (1986).

6 Glowacki, D. R., Liang, C.-H., Morley, C., Pilling, M. J. & Robertson, S. H. MESMER: an open-source master equation solver for multi-energy well reactions. *The Journal of Physical Chemistry A* **116**, 9545-9560 (2012).

Appendix B

B.1 Temperature profiles of the jets utilised in this study obtained via impact pressure measurements.

Below are the temperature profiles of the stable expansions utilized in this study. Black circles denote the stable jet, red circles denote where the jet was considered to lose stability. The nozzle was positioned at the distance from the impact pressure transducer indicated by the position of the last black circle in each plot for the kinetics experiments.

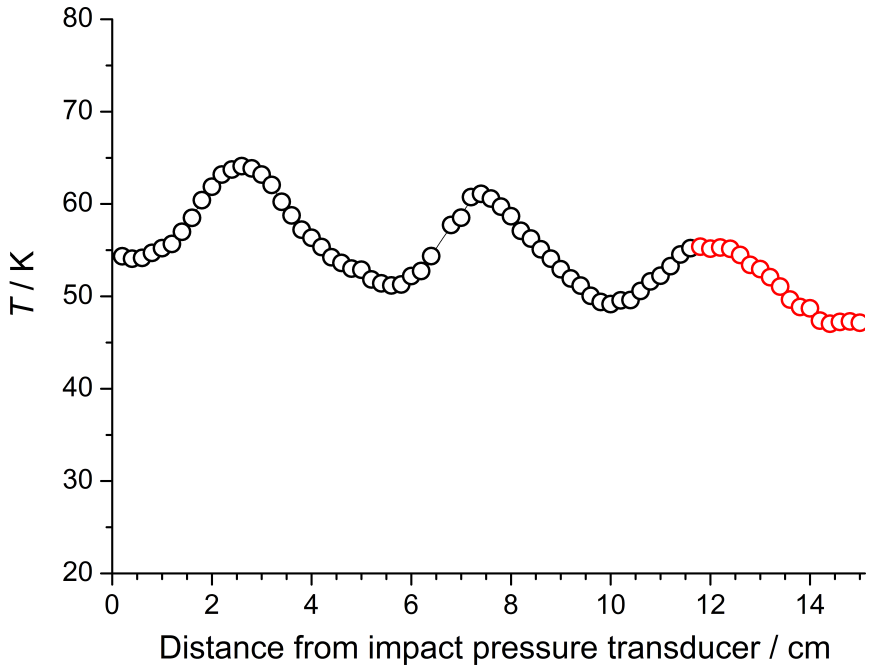

Figure 1: T = 56 ± 4 K. Total gas density = (4.4 ± 0.5) × 10^{16} molecule cm^{-3}. Bath gas = Ar. Stable jet length = 11.6 cm. Chamber pressure = 0.46 Torr. M = 3.62 ± 0.17.

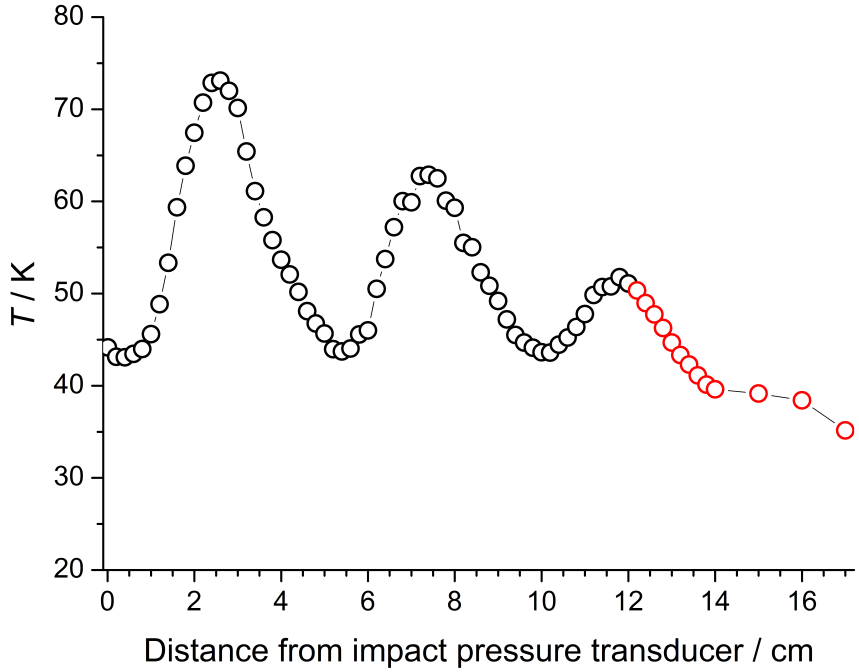

Figure 2: T = 54 ± 6 K. Total gas density = (8.0 ± 1.4) × 10^{16} molecule cm^{-3}. Bath gas = Ar. Stable jet length = 14.2 cm. Chamber pressure = 0.90 Torr. M = 3.70 ± 0.30.

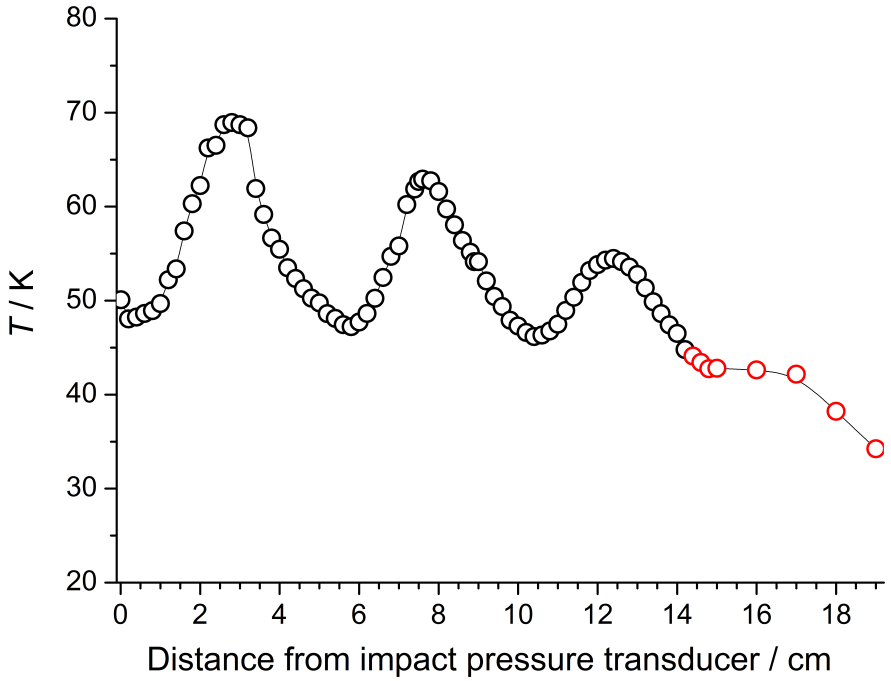

Figure 3: T = 53 ± 9 K. Total gas density = (15 ± 4) × 10^{16} molecule cm^{-3}. Bath gas = Ar. Stable jet length = 12.0 cm. Chamber pressure = 1.8 Torr. M = 3.76 ± 0.35.

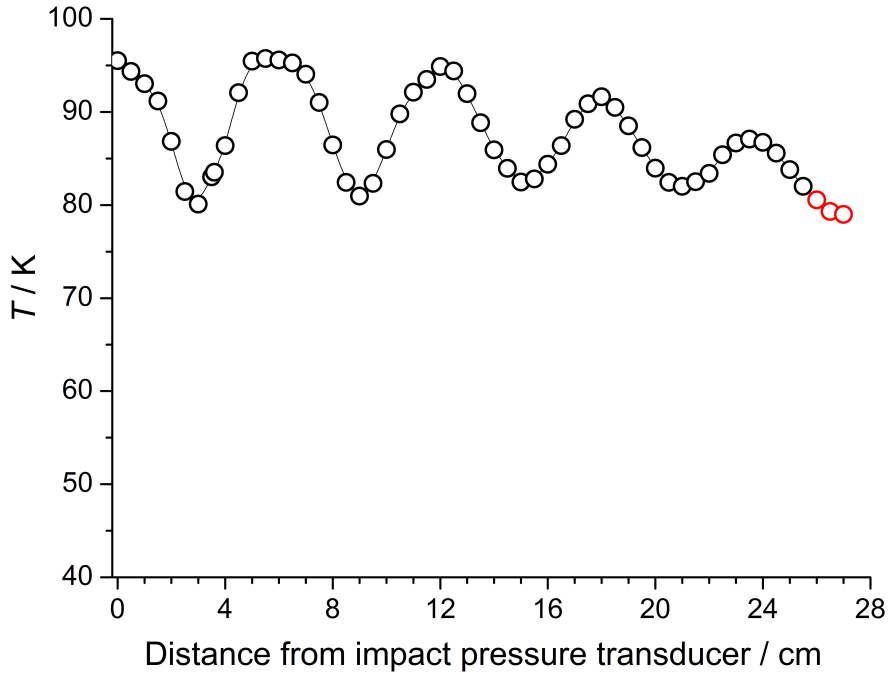

Figure 4: T = 88 ± 5 K. Total gas density = (3.5 ± 0.5) × 10^{16} molecule cm^{-3}. Bath gas = N_2. Stable jet length = 25.5 cm. Chamber pressure = 0.47 Torr. M = 3.49 ± 0.47.

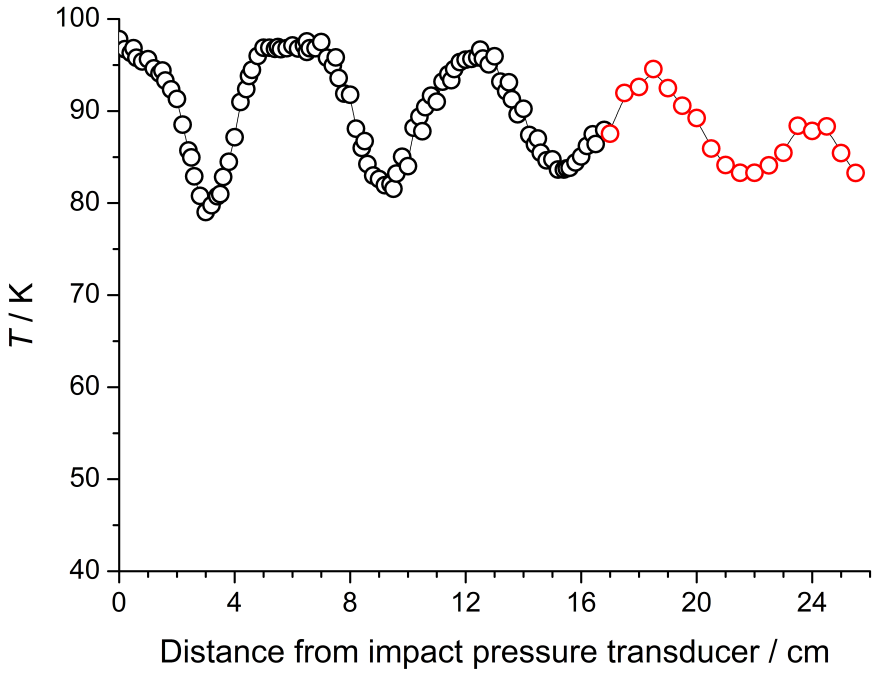

Figure 5: T = 90 ± 6 K. Total gas density = (4.1 ± 0.6) × 10^{16} molecule cm^{-3}. Bath gas = N_2. Stable jet length = 16.8 cm. Chamber pressure = 0.38 Torr. M = 3.39 ± 0.15.

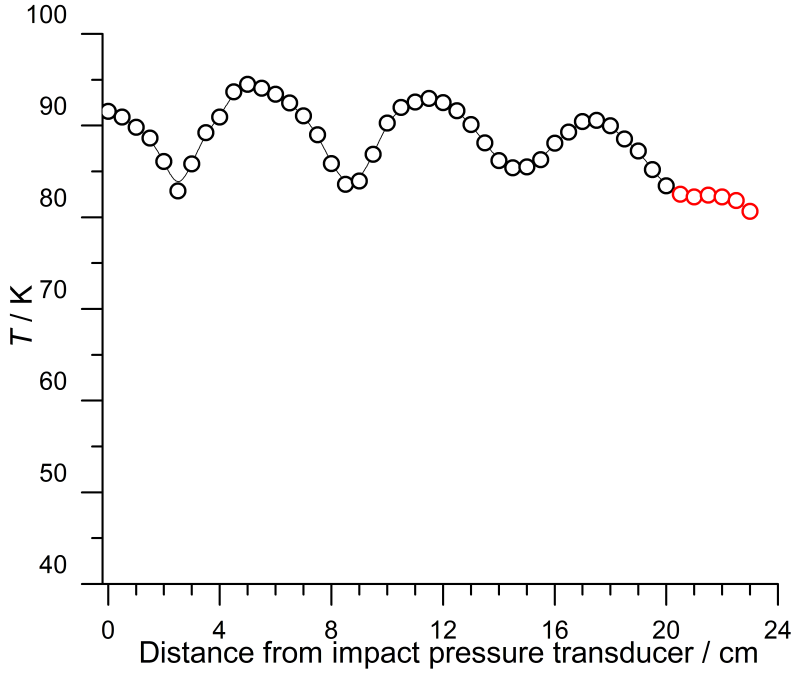

Figure 6: T = 89 ± 3 K. Total gas density = (6.5 ± 0.6) × 10^{16} molecule cm^{-3}. Bath gas = N_2. Stable jet length = 20.0 cm. Chamber pressure = 0.81 Torr. M = 3.43 ± 0.09.

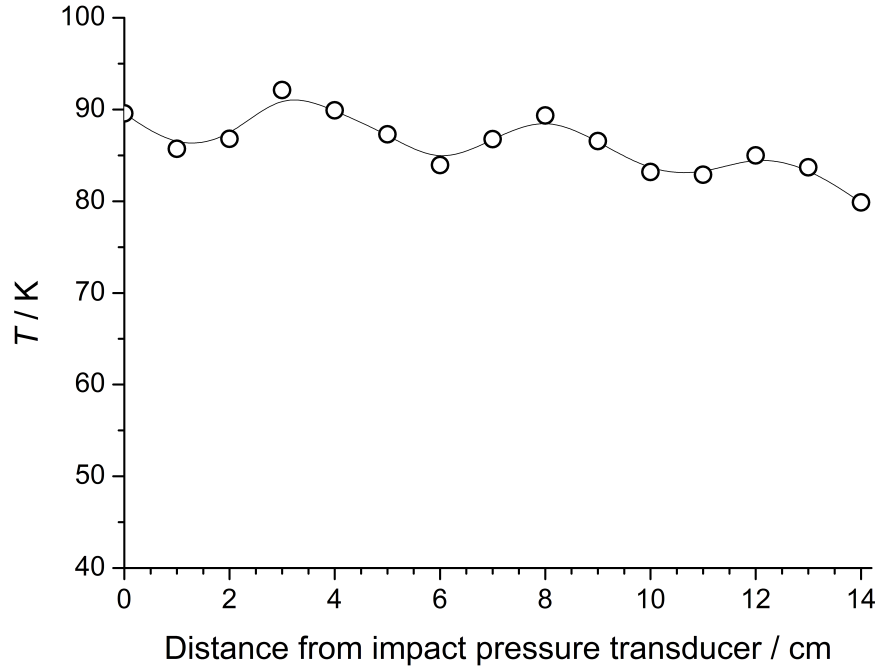

Figure 7: T = 86 ± 3 K. Total gas density = (6.8 ± 0.6) × 10^{16} molecule cm^{-3}. Bath gas = N_2. Stable jet length = 14.0 cm. Chamber pressure = 0.86 Torr. M = 3.51 ± 0.09.

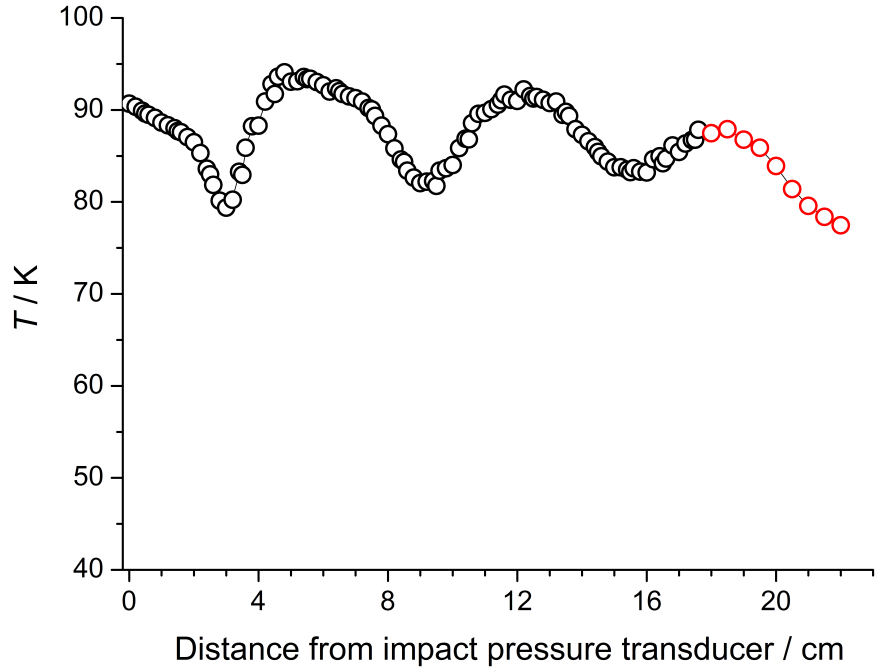

Figure 8: T = 88 ± 4 K. Total gas density = (7.4 ± 0.8) × 10^{16} molecule cm^{-3}. Bath gas = N_2. Stable jet length = 17.6 cm. Chamber pressure = 0.77 Torr. M = 3.47 ± 0.10.

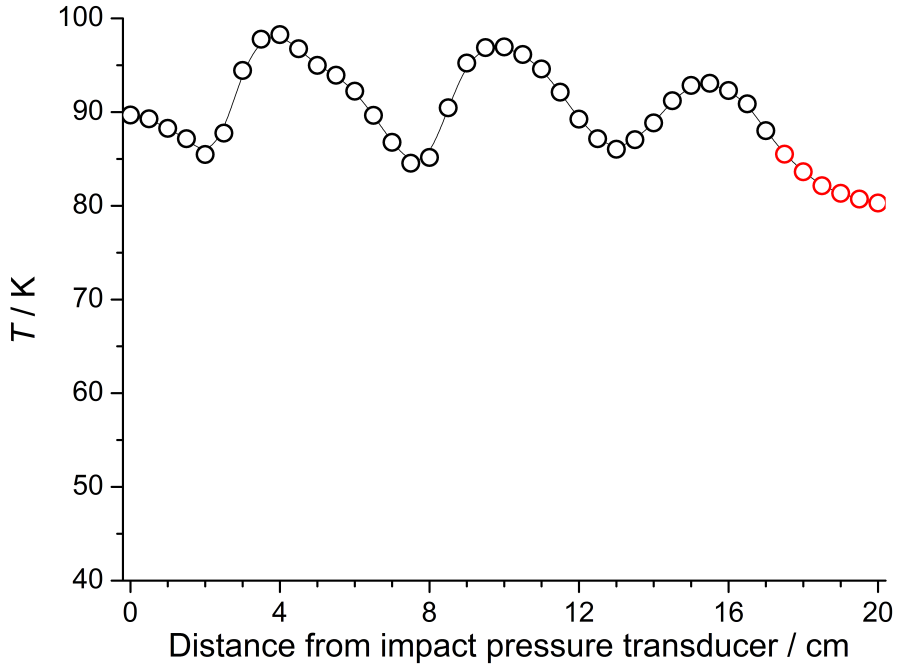

Figure 9: T = 91 ± 4 K. Total gas density = (8.3 ± 0.9) × 10^{16} molecule cm^{-3}. Bath gas = N_2. Stable jet length = 17.0 cm. Chamber pressure = 1.10 Torr. M = 3.37 ± 0.11.

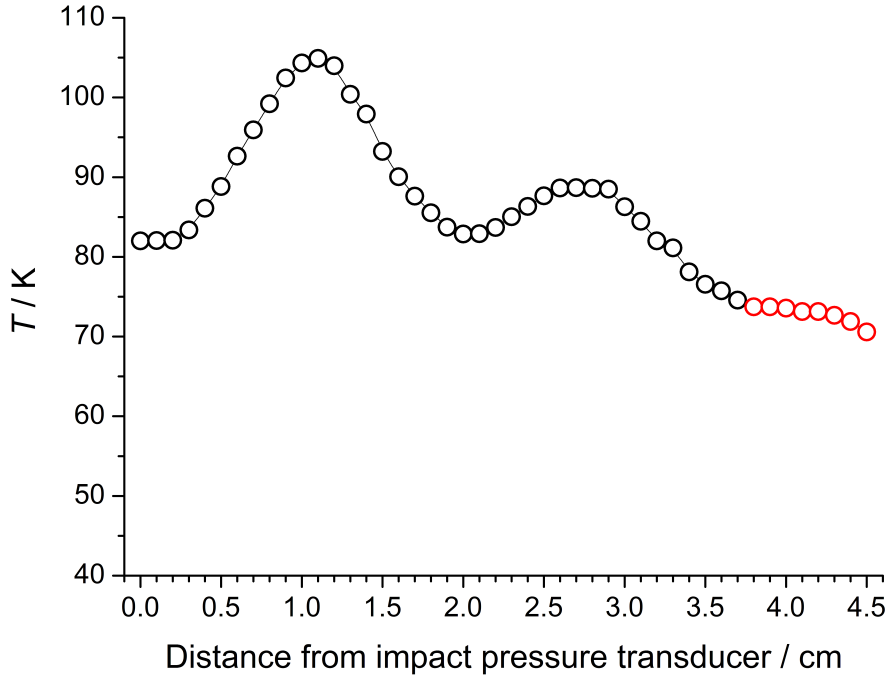

Figure 10: T = 88 ± 8 K. Total gas density = (9.4 ± 1.3) × 10^{16} molecule cm^{-3}. Bath gas = Ar. Stable jet length = 3.7 cm. Chamber pressure = 2.25 Torr. M = 2.68 ± 0.17.

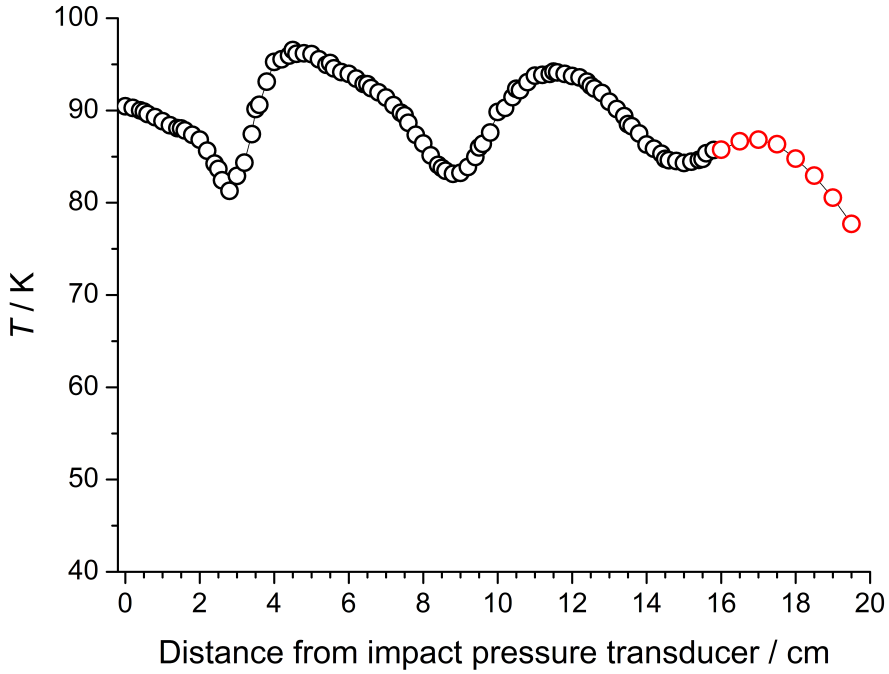

Figure 11: T = 89 ± 4 K. Total gas density = (11 ± 1) × 10^{16} molecule cm^{-3}. Bath gas = N_2. Stable jet length = 16.0 cm. Chamber pressure = 1.13 Torr. M = 3.42 ± 0.11.

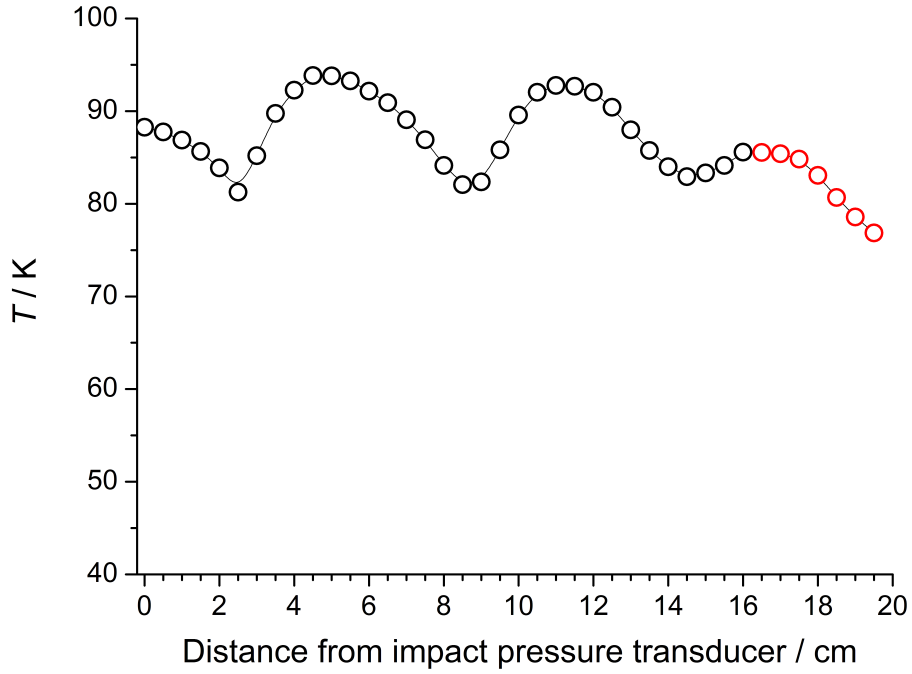

Figure 12: T = 88 ± 4 K. Total gas density = (11 ± 1) × 10^{16} molecule cm^{-3}. Bath gas = N_2. Stable jet length = 16.0 cm. Chamber pressure = 1.31 Torr. M = 3.46 ± 0.11.

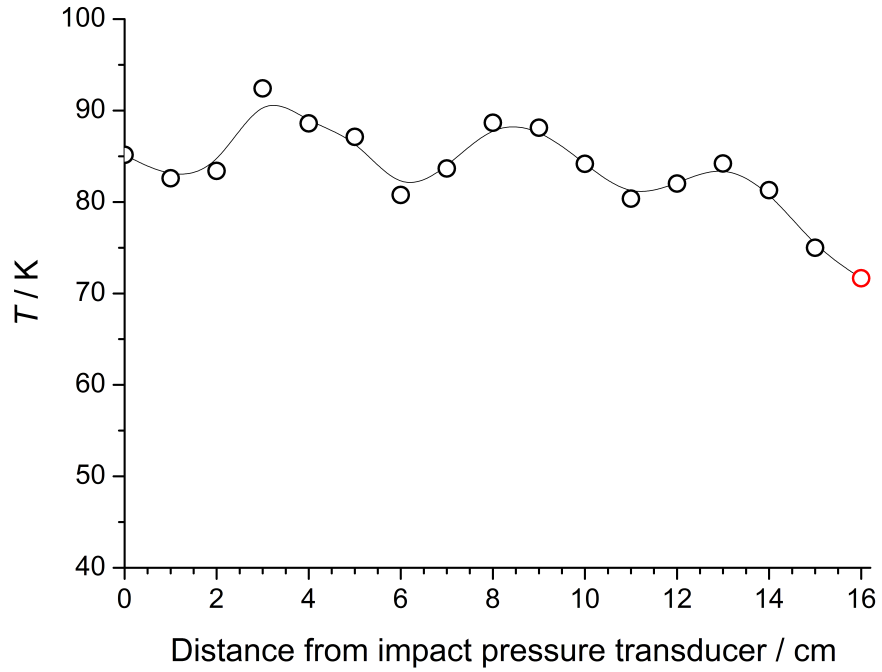

Figure 13: T = 84 ± 4 K. Total gas density = (16 ± 2) × 10^{16} molecule cm^{-3}. Bath gas = N_2. Stable jet length = 15.0 cm. Chamber pressure = 1.42 Torr. M = 3.57 ± 0.12.

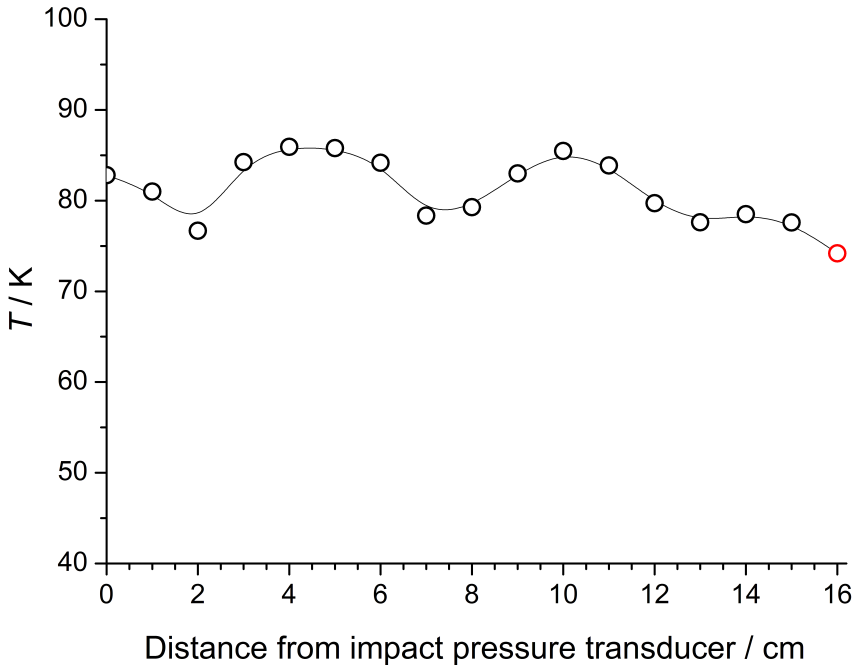

Figure 14: T = 82 ± 3 K. Total gas density = (16 ± 2) × 10^{16} molecule cm^{-3}. Bath gas = N_2. Stable jet length = 15.0 cm. Chamber pressure = 1.72 Torr. M = 3.65 ± 0.10.

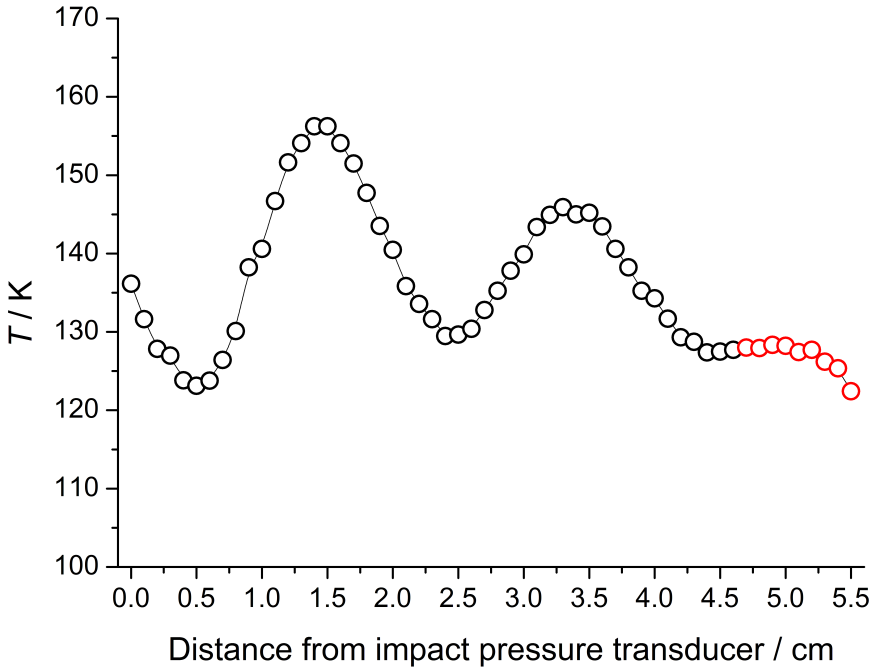

Figure 15: T = 138 ± 9 K. Total gas density = (8.0 ± 1.0) × 10^{16} molecule cm^{-3}. Bath gas = N_2. Stable jet length = 4.6 cm. Chamber pressure = 2.25 Torr. M = 2.42 ± 0.15.

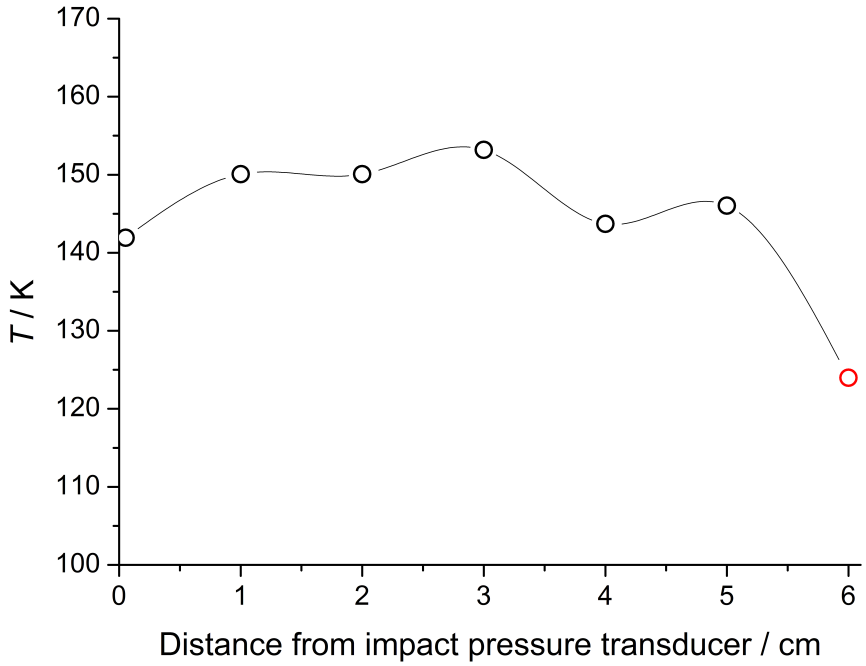

Figure 16: T = 148 ± 15 K. Total gas density = (10 ± 2) × 10^{16} molecule cm^{-3}. Bath gas = N_2. Stable jet length = 5.0 cm. Chamber pressure = 2.90 Torr. M = 2.26 ± 0.23.

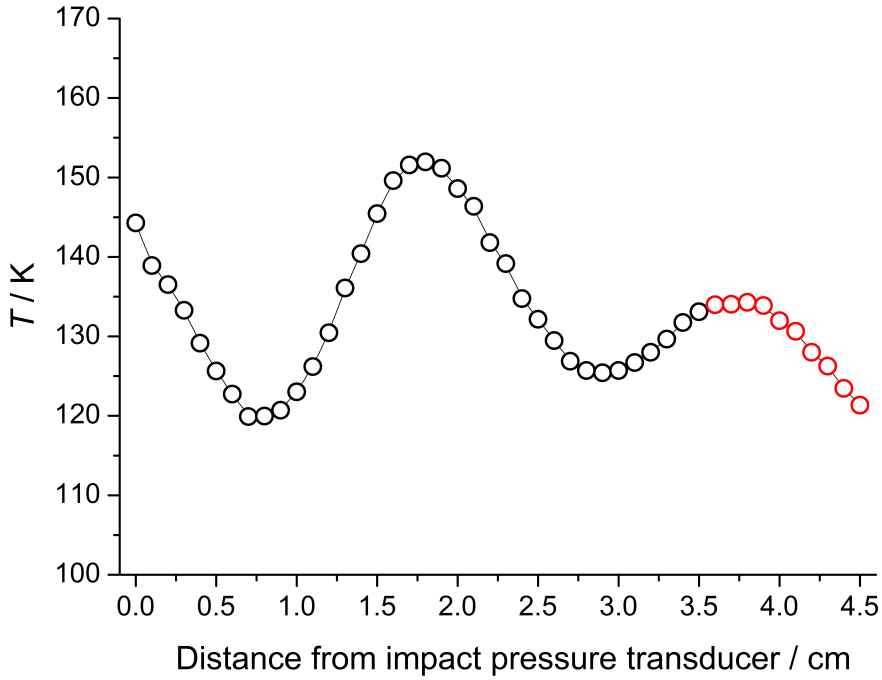

Figure 17: T = 133 ± 10 K. Total gas density = (13 ± 3) × 10^{16} molecule cm^{-3}. Bath gas = N_2. Stable jet length = 3.5 cm. Chamber pressure = 3.64 Torr. M = 2.49 ± 0.17.

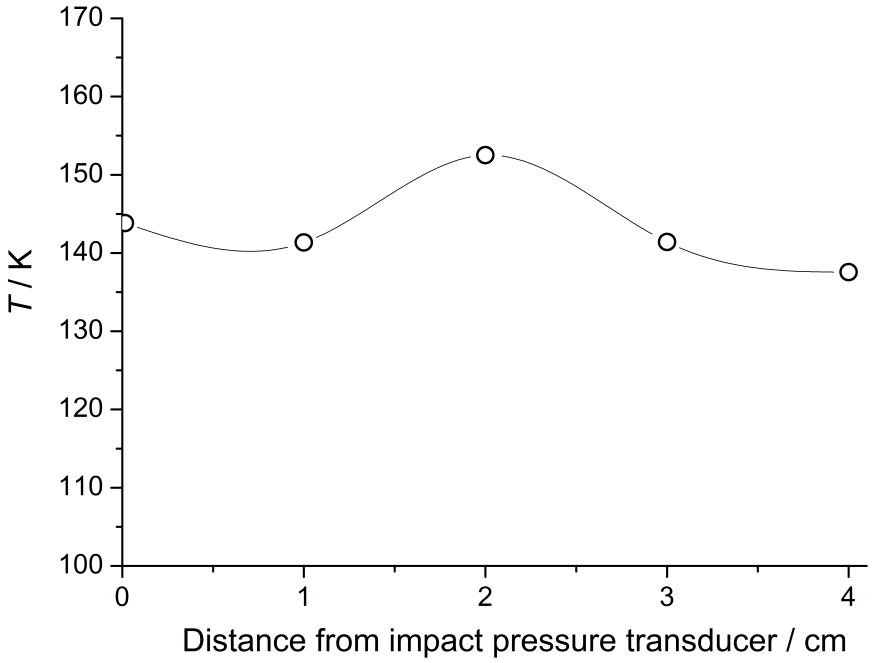

Figure 18: T = 144 ± 15 K. Total gas density = (18 ± 2) × 10^{16} molecule cm^{-3}. Bath gas = N_2. Stable jet length = 4.0 cm. Chamber pressure = 5.16 Torr. M = 2.32 ± 0.24.

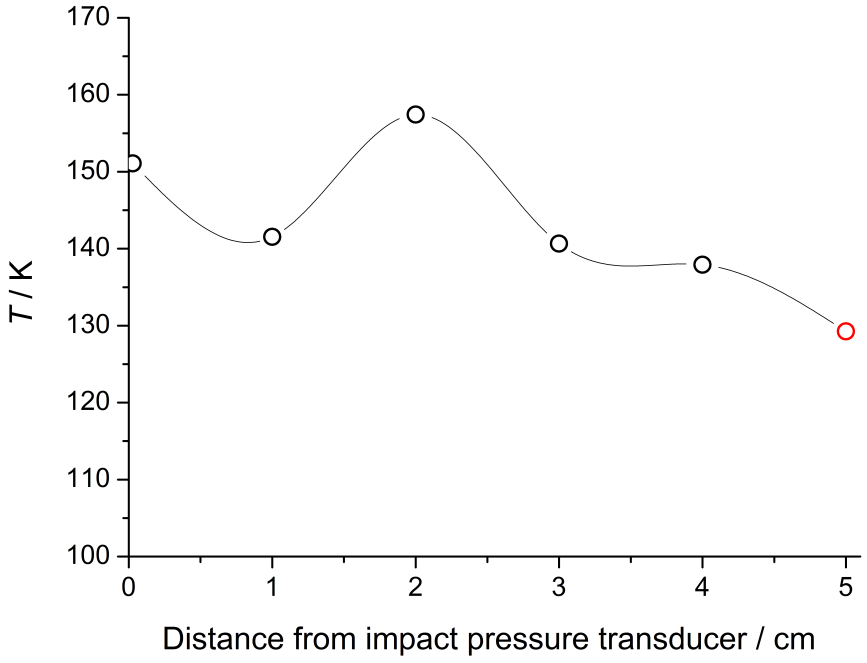

Figure 19: T = 146 ± 15 K. Total gas density = (26 ± 4) × 10^{16} molecule cm^{-3}. Bath gas = N_2. Stable jet length = 4.0 cm. Chamber pressure = 7.36 Torr. M = 2.29 ± 0.24.

Appendix C

For a linear first order differential equation such as EC.1, the general solution is obtained from EC.2 using the integrating factor method. From the basis of these equations, the derivations for the fitting equations used in this work will be presented.

$$\frac{dx(t)}{dt} + P(t)x(t) = Q(t) \qquad \text{EC.1}$$

$$x(t) = \frac{\int (Q(t)\, e^{\int P(t)dt})dt + c}{e^{\int P(t)dt}} \qquad \text{EC.2}$$

where c is a constant.

C.1 Derivation of the single exponential loss fitting equation

For a reaction with a schematic k→l, where k is the species of interest, then the following schematic is employed. The example used here is the loss of the hydroxyl radical, OH.

Assuming an instantaneous production of OH, such as by PC.1, and the reaction scheme RC.1 and RC.2 where the co-reagent R is assumed to be in great excess (so that the reaction is under pseudo first order conditions), the differential equation is given below in EC.3.

$(CH_3)_3COOH + hv \rightarrow OH + co - products$ (instantaneous) PC.1

$OH + R \rightarrow products$ (k_r) RC.1

$OH \rightarrow loss$ (k_{loss}) RC.2

$$\frac{d[OH]}{dt} = -(k_r' + k_{loss})[OH] = -k_{obs}[OH] \qquad \text{EC.3}$$

where k'_r is the pseudo first order rate coefficient for RC.1 when R is in great excess and k_{obs} is the experimentally observed rate coefficient.

Rearranging yields EC.4, and integration between time *t* and time 0 yields the fitting equation, EC.5.

$$\frac{d[OH]}{[OH]} = -k_{obs}dt \qquad \text{EC.4}$$

$$[OH]_t = [OH]_0 \exp(-k_{obs})t \qquad \text{EC.5}$$

C.2 Derivation of the exponential growth-exponential loss fitting equation

For a reaction with a schematic of j→k→l, where the species of interest is k, then the following equation is derived. The example used here is the formation of the hydroxyl radical and its subsequent loss.

From the production scheme P1.2 and the reaction schemes RC.1-RC.4 the differential equations for OH* (EC.6) and OH (EC.7) are obtained.

$(CH_3)_3COOH + hv \rightarrow OH, OH^* + co - products$ (instantaneous) PC.2

$OH^* + M \rightarrow OH + M$ (k_{rel}) RC.3

The bath gas, M, is in great excess of OH* under experimental conditions and so the RC.3 can be considered pseudo first order (RC.4).

$OH^* \rightarrow OH$ (k'_{rel}) RC.4

$OH + R \rightarrow products$ (k_r) RC.1

$OH \rightarrow loss$ (k_{loss}) RC.2

$$\frac{d[OH^*]}{[OH^*]} = -k'_{rel}dt$$ EC.6

$$\frac{d[OH]}{dt} = -(k'_r + k_{loss})[OH] + k'_{rel}[OH^*] = -(k_{obs})[OH] + k'_{rel}[OH^*]$$ EC.7

The integrated solution to EC.6 is EC.8

$$[OH^*]_t = [OH^*]_0 exp\,(-k'_{rel}t)$$ EC.8

which can then be inserted into EC.7

$$\frac{d[OH]}{dt} = -(k_{obs})[OH] + k'_{rel}[OH^*]_0 \exp\,(-k_{rel}t)$$ EC.9

Applying EC.1 and EC.2 using the parameters shown in EC.10 and EC.11, the expression shown in EC.12 is obtained.

$$P(t) = -(k_{obs})$$ EC.10

$$Q(t) = [OH^*]_0 \exp\,(-k'_{rel}t)$$ EC.11

$$[OH]_t = \frac{\frac{[OH^*]_0 k_{rel}}{k_{obs} - k_{rel}} exp(k_{rel} - k_{obs})t + c}{e^{k_{obs}t}}$$ EC.12

simplifying yields EC.13.

$$[OH]_t = \frac{[OH^*]_0 k_{rel}}{k_{obs} - k_{rel}}\ e^{-k'_{rel}t} + ce^{-k_{obs}t}$$ EC.13

C is obtained from the expression for [OH] at time zero (EC.14, EC.15).

$$[OH]_0 = \frac{[OH^*]_0 k'_{rel}}{k_{obs} - k'_{rel}} + c$$ EC.14

$$c = [OH]_0 - \frac{[OH^*]_0 k'_{rel}}{k_{obs} - k'_{rel}} \quad \text{EC.15}$$

Substituting into EC.13 yields EC.16, which is then simplified to obtain the fitting equation EC.17.

$$[OH]_t = \frac{[OH^*]_0 k'_{rel}}{k_{obs} - k'_{rel}} e^{-k_{rel} t} + \left([OH]_0 - \frac{[OH^*]_0 k'_{rel}}{k_{obs} - k'_{rel}}\right) e^{-k_{obs} t} \quad \text{EC.16}$$

$$[OH]_t = \frac{[OH^*]_0 k'_{rel}}{k_{obs} - k'_{rel}} \left(e^{-k'_{rel} t} - e^{-k_{obs} t}\right) + [OH]_0 e^{-k_{obs} t} \quad \text{EC.17}$$

An equivalent expression is also used for the some of alkoxy radical loss traces and the HCHO product traces (Chapter 6).

C.3 Derivation of the biexponential growth-exponential loss fitting equation

For the product detection of NH_2 from the reaction of OH + ammonia (Chapter 5) a tri-exponential equation was utilised to fit the data owing to the complicated reaction scheme which is given below. Assuming pseudo first order conditions so that [NH_3] >> [OH], then $k_{5.2}$ becomes k_x and $k_{5.1}$ becomes k_y, the pseudo first order rate coefficients.

$O_3 + hv \rightarrow O(^1D) + O_2$	(instantaneous)	PC.3
$O(^1D) + NH_3 \rightarrow OH + fNH_2$	($k_{5.2} \rightarrow k_x$)	RC.5
$OH + NH_3 \rightarrow H_2O + NH_2$	($k_{5.1} \rightarrow k_y$)	RC.6

f signifies the yield of NH_2 produced from RC.3, so that in the solution to the differential equation, the relative yields of NH_2 from RC.3 and RC.4 can be compared. It is assumed that both OH and NH_2 are lost with the same first order loss rate coefficient, k_{loss}, via diffusion.

$OH \rightarrow loss$	(k_{loss})	RC.2
$NH_2 \rightarrow loss$	(k_{loss})	RC.7

The following differential equations are constructed for O(^{1}D) (EC.18) OH (EC.19) and NH_2 (EC.20), with the solution for O(^{1}D) also given in EC.18.

$$\frac{d[O(^1D)]}{dt} = -k_x[O(^1D)] \xrightarrow{yields} [O(^1D)]_t = [O(^1D)]_0 exp\,(-k_x t) \quad \text{EC.18}$$

$$\frac{d[OH]}{dt} = k_x[O(^1D)] - k_y[OH] - k_{loss}[OH] = k_x[O(^1D)] - k_{obs}[OH] \quad \text{EC.19}$$

$$\frac{d[NH_2]}{dt} = f.k_x[O(^1D)] + k_y[OH] - k_{loss}[NH_2] \quad \text{EC.20}$$

The integrated solution to EC.19 is analogous to the solution obtained in section C.2, however the second term is removed given that at time zero, there is no OH, as shown in EC.21.

$$[OH]_t = \frac{[O(^1D)]_0 k_x}{k_{obs}-k_x}\ (e^{-k_x t} - e^{-k_{obs} t}) \quad \text{EC.21}$$

Therefore the differential equation for NH_2 can now be expressed by EC.22

$$\frac{d[NH_2]}{dt} = f.k_x\{[O(^1D)]_0 e^{-k_x t}\} \quad \text{EC.22}$$
$$+k_y\left\{\frac{[O(^1D)]_0 k_x}{k_{obs}-k_x}\ (e^{-k_x t} - e^{-k_{obs} t})\right\} - k_{loss}[NH_2]$$

which can be rearranged to:

$$\frac{d[NH_2]}{dt} + k_{loss}[NH_2] = k_x[O(^1D)]_0 \quad \text{EC.23}$$
$$.\left[e^{-k_x t}\left\{f + \frac{k_y}{k_{obs}-k_x}\right\} - \frac{k_y}{k_{obs}-k_x} e^{-k_{obs} t}\right]$$

which can then be simplified for ease of calculation to EC.24

$$A = f + \frac{k_y}{k_{obs}-k_x} \qquad B = \frac{k_y}{k_{obs}-k_x}$$

$$\frac{d[NH_2]}{dt} + k_{loss}[NH_2] = k_x[O(^1D)]_0[A.e^{-k_x t} - B.e^{-k_{obs} t}] \quad \text{EC.24}$$

The general solution to a first order differential equation is

$$P(t) = k_{loss} \quad \text{EC.25}$$

$$Q(t) = k_x[O(^1D)]_0(Ae^{-k_x t} + Be^{-k_{obs} t}) \quad \text{EC.26}$$

$$\frac{d[NH_2]}{dt} + P(t)[NH_2](t) = Q(t) \quad \text{EC.27}$$

$$\int P(t)\,dt = \int k_{loss}\,dt = k_{loss} t \quad \text{EC.28}$$

$$\int Q(t)e^{k_{loss} t}\,dt = k_x[O(^1D)]_0\left(\frac{A}{k_{loss}-k_x} e^{(k_{loss}-k_x)t} - \frac{B}{k_{loss}-k_{obs}} e^{(k_{loss}-k_{obs})t}\right)$$

EC.29

$$[NH_2]_t = k_x[O(^1D)]_0\left(\frac{A}{k_{loss}-k_x} e^{(-k_x)t} - \frac{B}{k_{loss}-k_{obs}} e^{(-k_{obs})t}\right) + Ce^{-k_{loss} t} \quad \text{EC.30}$$

$$C = -k_x[O(^1D)]_0\left(\frac{A}{k_{loss}-k_x} - \frac{B}{k_{loss}-k_{obs}}\right) \quad \text{EC.31}$$

$$[NH_2]_t = k_x[O(^1D)]_0 \quad \text{EC.32}$$
$$.\left\{\left(\frac{A}{k_{loss}-k_x} e^{(-k_x)t} - \frac{B}{k_{loss}-k_{obs}} e^{(-k_{obs})t}\right) - \left(\frac{A}{k_{loss}-k_x} - \frac{B}{k_{loss}-k_{obs}}\right) e^{-k_{loss} t}\right\}$$

Rearrangement of EC.32 and substitution of EC.24 EC.25, and $k_{obs}=k_y+k_{loss}$ into the solution yields the final fitting equation, EC.3

$$[NH_2]_t = \frac{k_x[O(^1D)]_0}{k_y+k_{loss}-k_x}$$
$$\times\left[\frac{f(k_y+k_{loss}-k_x)+k_y}{k_{loss}-k_x}\{e^{-k_x t} - e^{-k_{loss} t}\} + \{e^{(-k_y-k_{loss})t} - e^{-k_{loss} t}\}\right] \quad \text{EC.33}$$

Appendix D

D.1 Concentration of CH_3O radicals generated from the 248 nm photolysis of methyl nitrite.

$$[CH_3O] = \phi_{248\,nm}.\sigma_{248\,nm}.\ n^o photons. \qquad \text{ED.1}$$
$$area\ of\ photolysis\ laser.[\,CH_3ONO]$$

Percentage of methyl nitrite in jet = 0.035%.

Concentration of methyl nitrite = 1.2×10^{13} molecule cm^{-3}.

$\sigma_{248\ nm}$ ~ 1.6×10^{-18} $molecule^{-1}$ cm^2 (interpolated from measurements at 245 and 250 nm by Sander *et al.*[1])

$\phi_{248\ nm}$ estimated as 1.

Area of photolysis laser beam = 0.28 cm^2.

Photolysis laser energy = 303 mJ/pulse.

Number of photolysis photons = 3.8×10^{17}.

$[CH_3O] = 1 \times (1.6 \times 10^{-18}) \times (3.8 \times 10^{17}) \times 0.28 \times (1.2 \times 10^{13})$.

$[CH_3O] = 2.2 \times 10^{12}$ molecule cm^{-3}.

D.2 Concentration of C_2H_5O radicals generated from the 248 nm photolysis of methyl nitrite.

$$[C_2H_5O] = \phi_{248\,nm}.\sigma_{248\,nm}.\ n^o photons. \qquad \text{ED.2}$$
$$area\ of\ photolysis\ laser.[C_2H_5ONO]$$

Percentage of ethyl nitrite in jet = 0.0234%

Concentration of ethyl nitrite = 8.3×10^{12} molecule cm^{-3}.

$\sigma_{248\ nm}$ ~ 2.38×10^{-18} $molecule^{-1}$ cm^2 (interpolated from measurements at 245 and 250 nm by Maricq and Wallington[2]).

$\phi_{248\ nm}$ estimated as 1.

Area of photolysis laser beam = 0.28 cm^2.

Photolysis laser energy = 327 mJ/pulse.

Number of photolysis photons = 4.1×10^{17}.

$[C_2H_5O] = 1 \times (2.38 \times 10^{-18}) \times (4.1 \times 10^{17}) \times 0.28 \times (8.3 \times 10^{12})$

$[C_2H_5O]$ = 2.3 × 10^{12} molecule cm^{-3}.

D.3 CH_3O versus OH detection

Methoxy radicals from photolysis of methyl nitrite (off resonance detection ~ 309.5 nm): $[CH_3ONO]$ in the jet = 1.2 × 10^{13} molecule cm^{-3}, yielding 2.2 × 10^{12} molecule cm^{-3} methoxy radicals, as shown in section D.1. Figure 17 of Chapter 3 shows that this yields a maximum fluorescence signal height of 3 (arb. units) from the wavelength scan, with PMT voltage of 1969 V.

OH radicals from O_3 photolysis in the presence of excess H_2 (on resonance detection at ~ 308 nm):

$$[OH] = \frac{\phi_{248\,nm}.\sigma_{248\,nm}.\ n^o photons.}{area\ of\ photolysis\ laser.[O_3]} \qquad \text{ED.3}$$

Concentration of ozone in the jet = 2.3 × 10^{12} molecule cm^{-3}.

$\sigma_{248\ nm}$ ~ 1.07 × 10^{-17} $molecule^{-1}$ cm^2.

$\phi_{248\ nm}$ =0.9.

Area of photolysis laser beam = 0.28 cm^2.

Photolysis laser energy = 303 mJ/pulse.

Number of photolysis photons =3.8 × 10^{17}.

[OH] = 0.9 × (1.07 × 10^{-17}) × (3.8 × 10^{17}) × 0.28 × (2.3 × 10^{12})

[OH] = 2.3 × 10^{12} molecule cm^{-3}.

A laser excitation wavelength scan yields a maximum fluorescence signal height of 18 (arb. units) with PMT voltage of 1666 V. The specifications of the PMT (Thorlabs 9813 B) indicate that there is factor of ~ 50 increase in the gain between 1666-1969 V, therefore the equivalent methoxy signal is 0.06 (3/50 = 0.06). Therefore the signal for OH compared to methoxy radicals is 18/0.06 = 300 times larger.

D.4 References

1 Sander, S. *et al.* Chemical Kinetics and Photochemical Data for use in Atmospheric Studies–Evaluation Number 17, JPL Publication 10–6. (JPL, 2011).

2 Maricq, M. M. & Wallington, T. J. Absolute UV cross sections of methyl and ethyl peroxy radicals. *The Journal of Physical Chemistry* **96**, 986-992 (1992).

Appendix E

E.1 List of *ab initio* abbreviations

CCSD	Coupled cluster theory with singles and doubles excitations
CCSD(T)	Coupled cluster theory with singles and doubles excitations and with estimated triples contributions
UCCSD(T)	Open shell unrestricted coupled cluster theory with singles and doubles excitations and with estimated triples contributions
QCISD	Quadratic configuration interaction with singles and doubles excited determinants
QCISD(T)	Quadratic configuration interaction with singles and doubles excited determinants and with estimated triples contributions
MP2	Møller-Plesset perturbation theory with 2^{nd} order correction for overcounting electron-electron repulsion.
MP4	Møller-Plesset perturbation theory with 4^{th} order correction for overcounting electron-electron repulsion.
CASSCF(8,8)	Complete active space self consistent field theory with 8 electrons distributed in all possible ways in 8 orbitals
CASPT3(8,8)	Third order multireference perturbation theory with complete active space reference and with 8 electrons distributed in all possible ways in 8 orbitals
ROHF	Restricted open-shell Hartree-Fock theory
B3LYP	A density functional theory exchange-correlation hybrid functional: Becke 3 parameter functional with Lee Yang Parr
BHandHLYP	A density functional theory exchange-correlation hybrid functional: Becke half and half Lee Yang Parr
MPW1K	A density functional theory exchange-correlation hybrid functional: Modified Perdew Wang 1 parameter model for kinetics.
AVDZ	see aug-cc-pVDZ
M06-2X	A Minesota exchange-correlation functional for density

	functional theory published in 2006 with 54 % Hartree-Fock exchange.
aug-cc-pVDZ	A Dunning type basis set: augmented correlation-consistent polarised double zeta basis set
aug-cc-pVTZ	A Dunning type basis set: augmented correlation-consistent polarised triple zeta basis set
FC	Using the frozen core approximation
CBS	Complete basis set
BAC	Bond-additivity corrected basis set
EB	Extended basis set
6-311G	Pople type basis set with no diffuse or polarization functions
6-311G**	Pople type basis set with no diffuse functions but a single polarization function on the d orbitals of heavy atoms and p orbitals on hydrogen
6-311G(d,p)	see 6-311G**
6-311+G(2d,2p)	Pople type basis set with one set of diffuse functions on the s and p orbitals to heavy atoms and 2 polarisation functions on the d orbitals of heavy atoms and 2 polarisation functions on the p orbitals of hydrogen.
6-311+G(3df,2p)	Pople type basis set with one set of diffuse functions on the s and p orbitals to heavy atoms and 3 and 1 polarisation functions on the d and f orbitals respectively on the heavy atoms, and 2 diffusive functions on the p orbitals of hydrogen
6-311++G(d,p)	Pople type basis set with one set of diffuse functions on the s and p orbitals to heavy atoms and diffuse functions added to hydrogen on the s orbital with one polarisation function on the d orbitals of heavy atoms and one polarisation function on the p orbitals of hydrogen